Departamento de Física de la Materia Condensada
Facultad de Ciencias
Universidad Autónoma de Madrid

Instituto de Ciencias de Materiales de Madrid
Consejo Superior de Investigaciones Científicas

SURFACE NANOSTRUCTURATION AND ENGINEERING BY COARSENING MECHANISMS

Memoria presentada para optar al grado
de Doctor en Ciencias Físicas por
Alejandro González González

Dirigida por Dr. Enrique Vasco Matías

Tutor: Celia Polop Jordá

Madrid, Abril 2013

Prólogo

Esta tesis es el resultado del trabajo llevado a cabo en el Departamento de Nanoestructuras y Superficies del Instituto de Ciencia de Materiales de Madrid, el cual se encuentra adjunto al Consejo Superior de Investigaciones Científicas (CSIC). Parte de este trabajo fue realizado en colaboración con otros grupos nacionales e internacionales, entre ellos: Laboratorio de Óptica de Metales del Instituto de Física Aplicada "Leonardo Torres Quevedo" (CETEF-CSIC) (Madrid, España), el Departamento de Física de la Materia Condensada de la Universidad Autónoma de Madrid, Facultad de Ciencias (Madrid, España) y el Laboratorio de Microscopía del Centro de Investigación y Estudios Avanzados (CINVESTAB-IPN) (Mérida, México).

M.Sc. Alejandro González González

Fecha: 08/04/2013

Miembros del Tribunal evaluador: Prof. María Teresa Cuberes, Prof. Enrique García Michel, Prof. Rodolfo Cuerno, Prof. Vicente Muñoz Sanjosé, Prof. José María Gómez Gutiérrez, Dr. Juan de la Figuera, and Dr. Jorge Iribas Cerdá

Director de Tesis: Dr. Enrique Vasco Matías
Tutor: Dr. Celia Polop Jordá

(Este document fué escrito en MS. Word)

Dedicado a *Jannett*
quien ha decidido compartir junto a mí este intenso camino
y que lleva en su vientre nuestro pequeño gran regalo de vida,
Leonardo

IMPACTO CIENTIFICO DE ESTE TRABAJO DE INVESTIGACION

El desarrollo de esta tesis ha permitido la publicación de un total de 9 artículos de investigación científica en revistas internacionales de impacto tecnológico, la asistencia a más de 10 conferencias tanto nacionales como internacionales y la participación en 3 proyectos de investigación. Las publicaciones con correspondencia de autor más recientes se muestran a continuación, junto con algunas de las ponencias desarrolladas.

Publicaciones recientes en revistas internacionales de impacto

- **A. González-González**, C. Polop and E. Vasco, "*Columnar growth and intrinsic stress in polycrystalline films*", Physical Review B: Rapid Communications (in progress)

- **A. González-González**, C. Polop and E. Vasco, "*Post-coalescence evolution of growth stress in polycrystalline films*", Physical Review Letters **110**, 053101 (2013)

- **A. González-González**, C. Polop and E. Vasco, "*Slope selection-driven Ostwald ripening in ZnO thin-film growth*", Physical Review B **86**, 045434 (2012)

- **A. González-González**, *et al.*, "*Morphology evolution of thermally annealed polycrystalline thin films*", Physical Review B **84**, 155450 (2011)

- **A. González-González**, *et al.*, "*Morphology analysis of Si island arrays on Si(001)*", Nanoscale Research Letters **5**, 1882 (2010)

- **A. González-González**, *et al.*, "*Surface slope distribution with mathematical molding on Au(111) thin film growth*", Journal Vacuum Science & Technology A: Vacuum, Surfaces, and Films **27**, 1012 (2009)

Ponencias en conferencias nacionales e internacionales

- Seminario en la Jornada Científica sobre Técnicas de Caracterización de Superficie, bajo el título: "Slope-selection driven Ostwald ripening in ZnO thin film growth". Valencia (España). Noviembre 2012

- Seminario de línea del departamento de Nanoestructuras, Superficies y Recubrimientos del Instituto de Ciencia de Materiales de Madrid, bajo el título: "*Morphology analysis of nanoscale island arrays grown by MBE on flatten and pit-patterned Si(001) substrates*". Madrid (España). Febrero 2012

- American Vacuum Society: Science and Technology of Materials, Interfaces and Processing (AVS 58th International Symposium & Exhibition). Nashville, (E.E.U.U.), Noviembre 2011

- Nanoscale Patterns at Surfaces. Madrid (España), Septiembre 2011

- 8th International Workshop on Epitaxial Semiconductors on Patterned Substrates and Novel Index Surfaces. Como (Italia) Junio 2010

- Charla en el programa de Master inter-universitario de Física de la Materia Condensada y Nanotecnología, curso "Morfologías Funcionales por Nanoestructuración". Tópico: "*Thin film growth mechanisms: Late Selected Slope-driven Ostwald ripening case".*
  Periods: 2009-2010, 2010-2011. Madrid (España)

RESUMEN

El objetivo de esta tesis es investigar las interacciones locales entre entidades superficiales que constituyen sólidos estructuralmente heterogéneos y parcialmente confinados, conocidos como láminas delgadas policristalinas, a fin de estudiar cómo influyen dichas interacciones en la evolución de la morfología de las láminas durante su preparación. En este sentido, se prepararon láminas policristalinas de metales (Au) y óxidos metálicos (ZnO) mediante el uso de métodos físicos en fase vapor y recocido térmico. Las láminas así preparadas fueron caracterizadas por microscopías de proximidad y de barrido electrónico, técnicas de difracción de rayos X, y procedimientos de tratamiento digital de imágenes discretas, a fin de analizar tanto cualitativa como cuantitativamente la evolución morfológica y estructural de las láminas preparadas. La evolución morfológico-estructural de las láminas fue interpretada mediante el uso de novedosos modelos teóricos de crecimiento, apoyados a su vez por simulaciones numéricas basadas en aproximaciones mesoscópicas de diversos tipos, a saber: escalado dinámico (descripción de procesos como la difusión atómica en superficie), sistemas de ecuaciones en derivadas parciales (difusión a través de defectos) y elementos finitos (interacciones elásticas). Los modelos propuestos permitieron la identificación y predicción del origen, naturaleza, distribución espacial y evolución de las principales fuerzas que dan lugar tanto a la formación de entidades superficiales individuales como al desencadenamiento de diversos procesos de agregación entre ellas. En base a dichas interpretaciones ha sido posible explicar la evolución de diversos procesos de impacto tecnológico como la generación y relajación de esfuerzos mecánicos y las deformaciones a las que dan lugar en superficies de láminas delgadas policristalinas.

ABSTRACT

The objective of this thesis is to investigate the local interactions between those surface entities composing solids that are structurally heterogeneous and partially confined, well-known as polycrystalline thin films, to study how these interactions affect the film morphology evolution during the preparation of the films. In this context, we grew polycrystalline thin films of metal (Au) and metal oxides (ZnO) materials by means of the physical vapor deposition methods and annealing. These films were characterized by means of scanning probe and scanning electron microscopies, x-ray diffraction and image processing procedures in order to analyze qualitative and quantitatively their morphological and structural evolution of the prepared films. The structural and morphological evolution of the films was interpreted by means of novel theoretical models of growth that were supported by numeric simulations based on mesoscopic approaches as: dynamic scaling (to describe atomic diffusion at surfaces), systems of partial differential equations (diffusion through defects) and finite elements (elastic interactions). The proposed models allowed the identification and prediction of the origin, nature, space distribution and evolution of the main driving forces for the formation of surface entities and the coalescence among them. Based on these interpretations, it has been possible to explain the evolution of diverse processes of technological impact as the evolution of the intrinsic stress and the surface nanostructuration of film surfaces.

CONTENTS

LIST OF TABLES

CHAPTER 1

CHAPTER 2

CHAPTER 3

CHAPTER 4

LIST OF FIGURES

CHAPTER 1

CHAPTER 2

CHAPTER 3

CHAPTER 4

CHAPTER 5

CHAPTER 1

INTRODUCTION AND THEORETICAL BACKGROUND

1.1 Thermodynamics foundations of thin film growth: energy minimization processes

In this work we investigate the origin, nature and evolution of the intrinsic[1] interactions happening between the different entities (namely: atoms, islands, mounds and grains) that compose a solid, during the growth and processing of such a solid in the form of thin film[2]. From a thermodynamic viewpoint, these interactions intend to minimize the total energy of the system by leading the solid into structural transformations towards close-to-the-equilibrium configurations, as stated by the principle of minimum energy[3]:

"For a closed system with constant external parameters and entropy, the internal energy will decrease and approach to a minimum value at equilibrium".

The viability of such an energy minimization is usually quantified through the variation of thermodynamic potentials like the Gibbs free energy $G(\Theta)$ during the transformations undertaking in the solid. In terms of $G(\Theta)$, such a minimization implies:

$$\Delta G \equiv G\left(\Theta_f\right) - G\left(\Theta_i\right) < 0\,, \tag{1.1}$$

Where $G(\Theta_i)$ and $G(\Theta_f)$ correspond to the energies ascribed to the initial and final configurations Θ of the solid (i.e., before and after the transformation), respectively. From Eq. 1.1, the minimum-energy configurations Θ_0 are defined as:

$$\Delta G(\Theta_0 + \Delta\Theta) > 0 \tag{1.2}$$

Where $\Delta\Theta$ denotes how much the system is shifted out from the equilibrium. Unlike the gases where a thermodynamic state is described commonly through a set of state

[1] "Intrinsic" is referred here how "inherent in", i.e., in absence of external fields and forces.

[2] A thin film is the shallow layer of a solid having a high surface-bulk ratio. For thin films, thicknesses are in ranged from fractions of (monolayer) to a few hundreds of nanometers. As a consequence of the surface tension, uncoordinated atoms at the thin film surface have higher out-of-plane lattice parameters (lower in-plane ones) in comparison with the bulk, which is known as buckling.

[3] This principle is essentially a reformulation of the second law of thermodynamics.

variables (e.g., temperature T, volume V, pressure P, entropy S) able to modify the energy balance, for the special case of thin film we prefer to talk of system configurations Θ described in terms of structural and morphological parameters such as: entity sizes λ, shapes (regarding faceting and misorientation) and space correlation; this latter one referred to inter-entity spacing, number of neighbors and ordering at different length scales. Table 1.1 depicts several energy minimization processes happening during the development of a thin film.

For the specific case of nucleation and growth (first row in Table 1.1), the initial system configuration is formed by a high density of monomers (individual adatoms) coming from a supersaturated flux, with an initial energy $G(\Theta_i)$, i.e. $G(t \rightarrow 0\ \text{s})$ (for early growth times at which nucleation events take place).

Energy minimization processes	Analytical formulation and description	Description
Nucleation and growth of atomic entities from vapor phase	$\Delta G(\lambda / \Omega^{1/3}) = \Delta G_{surface} + \Delta G_{bulk}$ $\propto \lambda^2 \gamma_s - \lambda^3 \gamma_{cond.}$ where: the first term denotes the increase in the surface energy of the system per formed λ-sized nucleus (with γ_s being the surface energy per area and Ω the atomic volume); and the second one accounts for the decrease by nucleus condensation from a supersaturated vapour phase (with μ the thermodynamical potential describing the equilibrium between a solid and its vapor, being realized as a measure of the condensation energy, γ_{cond}: $\mu \propto \ln(P_{vapor}^{growth} / P_{vapor}^{equilibrium})$ under supersaturation conditions, i.e., for $P_{vapor}^{growth} > P_{vapor}^{equilibrium}$. For nucleus growing from the aggregation of adatoms on the surface, the vapour supersaturation is translated into a supersaturation of adatom density. Typical behavior found in Volmer-Weber-type metal thin films.	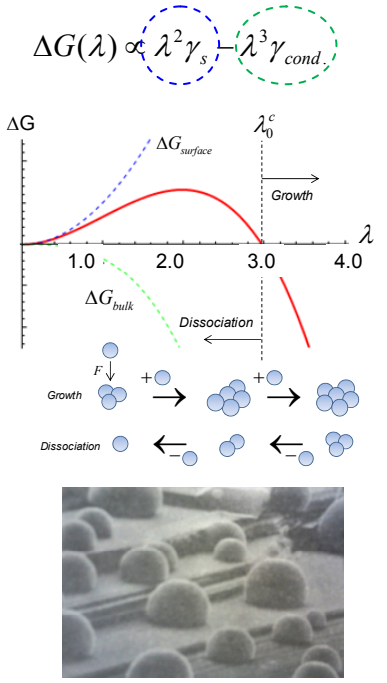 Typical behavior used for preparation of quantum dots in massive semiconductor (e.g., Si/Ge alloy films). SEM image taken from A. Pimpinelli and J. Villain "*Physics of Crystal Growth*" Cambridge University Press, United Kindomg (1998) Page 72.

Formation of a λ -rippled wetting layer (Stransky-Kastranov growth mode) 2D→3D

$$\Delta G(\lambda) = \Delta G_{surface} + \Delta G_{elastic}$$
$$\propto \pi\lambda_{\perp}\delta\gamma_s - \tfrac{1}{2}\lambda_{\perp}\lambda\delta\gamma_e$$

where: the first term corresponds to the increase in the surface energy γ_s by the generation of surface λ-spaced ripples with amplitude and length of $\lambda_{\perp}$ and δ, respectively; the second one corresponds to the decreases in the elastic energy γ_e due to the formation of ripples with unstrained tops.

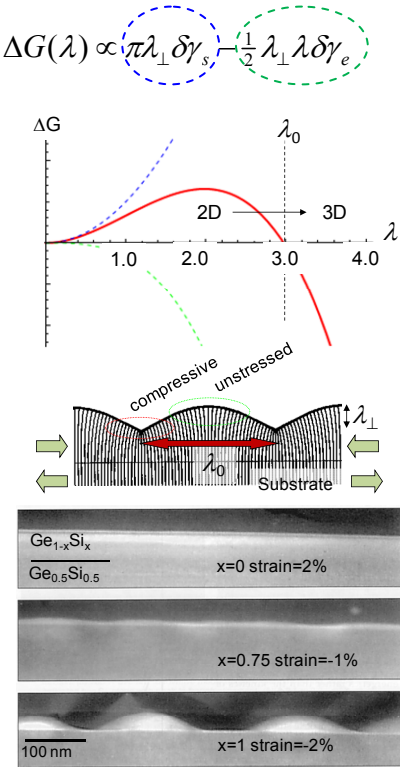

Typical behavior observed in films with epitaxial stress due lattice mismatch at the interface. Typically observed in Semiconductors (Si/Ge) and oxide ($CoCrO_4/MgAl_2O_4$) systems. Cross sections profiles were taken from C. Roland, MRS Bulletin 21, 27 (1996)

Faceting

$$\Delta G(\theta^{(hkl)}, \lambda^3) = \Delta G_{surface} + \Delta G_{elastic}$$
$$\propto \left[\gamma_s^{(hkl)} \csc\theta - \gamma_s \cot\theta\right]\lambda^2 \tan^{1/3}\theta$$
$$-\gamma_e \lambda^3 \tan\theta$$

where: the first terms account of the variation of surface energy by replacing a section of average surface with a certain facet (*hkl*) of lower energy ($\gamma_s > \gamma_s^{(hkl)}$) which is $\theta^{(hkl)}$-tilted from basal plane (001); the second one describe the decrease of the elastic energy generated during heteroepitaxial growth; which happens preferentially at the steps whose density is $\propto \tan\theta$.

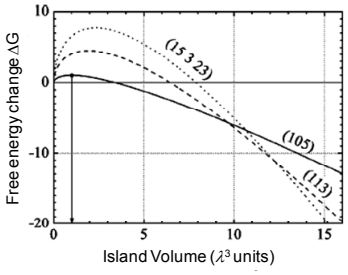

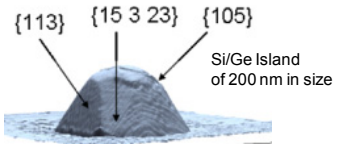

Adapted from J. Tersoff, and F. K. LeGoues, Phys. Rev. Lett. 72, 3570 (1994) and M. Bollani et al., Nanotechnology 23, 045302 (2012)

Typical behavior observed on strained films and during thermal annealing of semiconductors.

Table 1.1 Examples of energy minimization processes during film growth: (row 1) entity nucleation and growth. (Row 2) Stranski-Kastranov mode (from wetting layer (2D)→ 3D growth). (Row 3) Kinetic faceting.

In this stage, the nucleation of small species (e.g., dimers from the attachment of two adatoms) results in a thermodynamic unfavorable process as $G(\Theta_f) > G(\Theta_i) \Rightarrow \Delta G > 0$, and so the opposed process (the dissociation of dimers into monomers) has a high occurrence probability. If the size of the resulting species reaches a threshold size λ_0^c (in the example shown in Table 1.1, $\lambda_0^c \equiv$ three-atom sized species, or trimers), $G(\Theta_f) = G(\Theta_i) \Rightarrow \Delta G = 0$, which means that both processes (namely the coarsening and desorption) happen with equal probabilities. Such threshold size λ_0^c, termed critical size, allows to separate the surface species into subcritical and supercritical one for $\lambda < \lambda_0^c$ and $\lambda \geq \lambda_0^c$, respectively. Thus the coarsening of supercritical species becomes thermodynamically favorable $G(\Theta_f) < G(\Theta_i) \Rightarrow \Delta G < 0$ (i.e., more probable than desorption), and then the supercritical species evolve to large coarse-grained structures of thousands of atoms. The key aspects of other relevant processes involved in later growth stages (rows 2 – 3) are outlined in Table 1.1 and Fig. 1.1. Fig. 1.1 shows a generic picture of the energy minimization processes happening at dissimilar length and timescales of the thin film growth process. At first stages of growth the development of nuclei occurs, causing a reduction in the system energy as described in the first row of Table 1.1.Once grains are close enough to touch each others, i.e., at a size λ_1^c, they can merge each other (i.e., coalesce) forming larger structures. In order to minimize the energy cost of the new surfaces, grains can develop facets. Such process implies an energy cost for the development of facets, but for a certain threshold size λ_2^c, the energy is reduced by elastic contribution, as described in Table 1.1 (second row).

The minimum-energy configurations Θ_0, defined as $\partial_\Theta G\big|_{\Theta_0} = 0$, with $\partial_\Theta G\big|_{\Theta_0 \pm \Delta\Theta} > 0$ can be classified into global[4] (or local) minima in the energy configuration map as a function of $\Delta\Theta$ range (Fig. 1.2a). The minimum energy required to move the system between different (local) minimum-energy configurations through paths going by saddle points is termed activation energy $\Delta G = G(\Theta^{\#}) - G\left(\Theta_i\right)$. As $\Delta G(\Theta^{\#})$ is higher, the process rate $v = v_0 \exp[-\Delta G(\Theta^{\#}) + T\Delta S / k_B T]$ (with $v_0 \propto \nabla_\Theta^2 G(\Theta)$ denoting the attempt

[4] The global minimum is defined as the configuration with the lowest G in the set of minima of the potential energy landscape of a system with thermal energy $k_B T$, with k_B being the Boltzmann constant.

frequency, $k_B T$ the thermal energy [1], and ΔS the entropy variation) decreases as well as its occurrence probability for a given time t', $v\int_0^{\tau} \exp(-vt)\partial t$ (Fig. 1.2b).

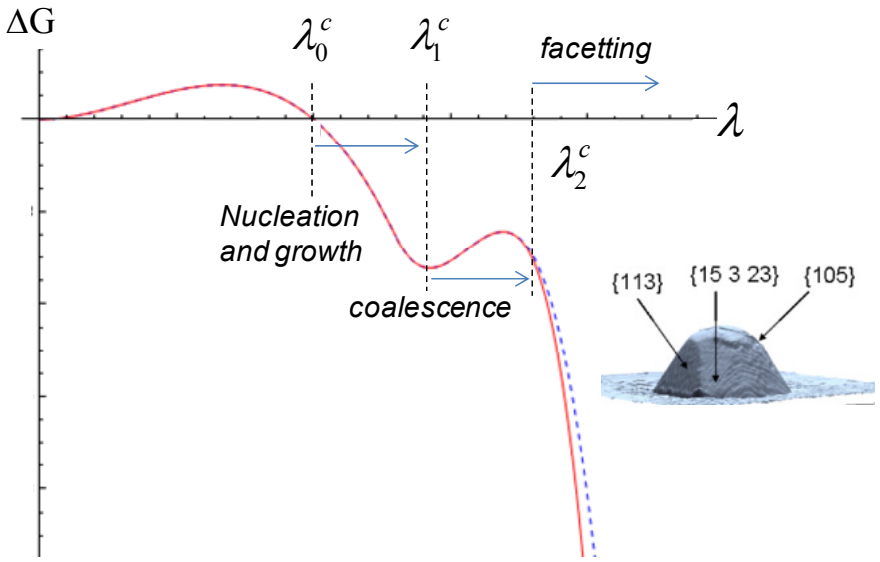

Figure 1.1 Evolution of energy minimization process during film growth. Dashed (vertical) lines indicates the grain threshold sizes for nucleation and growth, coalescence and faceting. The inset show a Si/Ge pyramid (taken from M. Bollani et al., Nanotechnology 23, 045302 (2012)). The dashed lines in the curve indicate unfavorable facets (i.e., with more energy than those developed by following the solid curve).

From the transition state theory (TST) [1], the prevalence of a specific pseudo-equilibrium configuration depends on the magnitude of both the activation energy $\Delta G(\Theta^{\#})$ and the driving force $\vec{\gamma}(\Theta)$ (with units of N/m or J/m^2) triggering the energy minimization process, as illustrated in Fig. 1.2(b), the latter defined as [2]:

$$\vec{\gamma}(\Theta) = -\vec{\nabla}_{\Theta} G(\Theta) \qquad (1.3),$$

The driving force "moves" the system toward possible lower energy configuration, or restores it from any slight displacement from the equilibrium. If $\vec{\nabla}_{\Theta} G(\Theta)$ increases (i.e. if the system is perturbed away from equilibrium), $\vec{\gamma} \neq 0$ tend to bring the system back towards the low energy (equilibrium) configuration, like a restoring force.

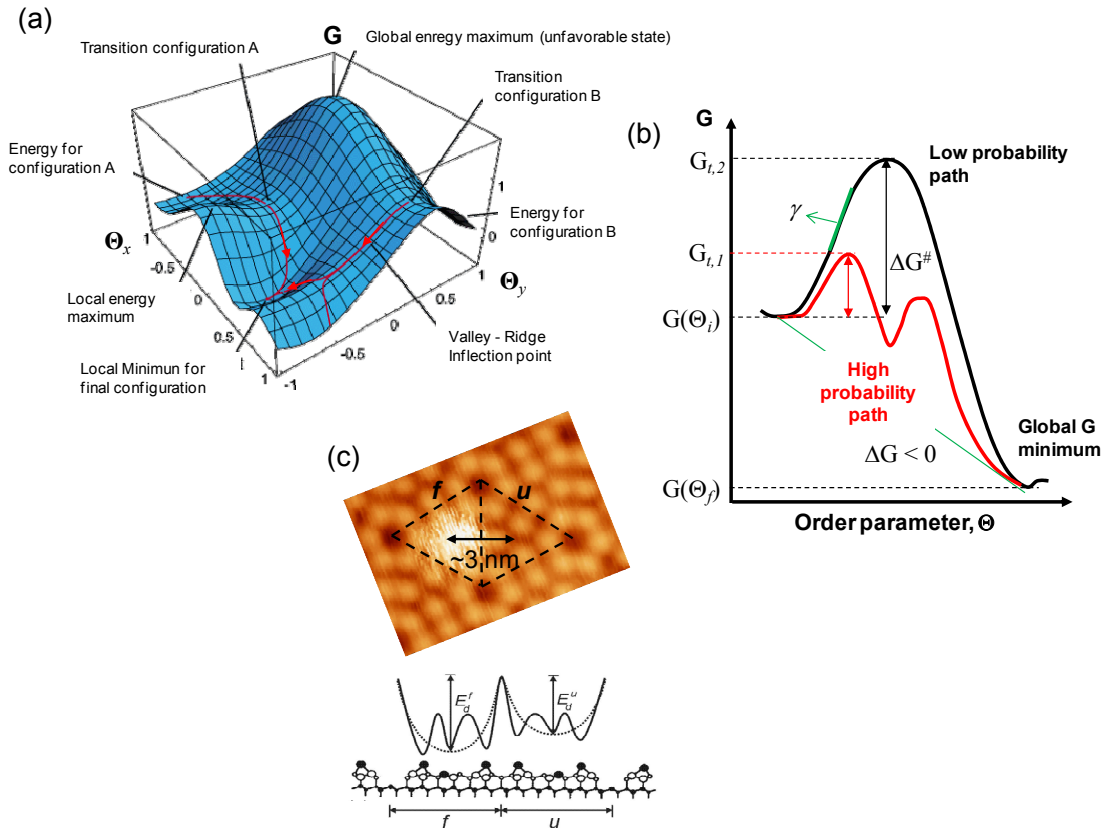

Figure 1.2 (a) Energy landscape of a generic system. (b) Cross section profile along generic spontaneous paths with different occurrence probabilities, toward a minimum-energy configuration. (c) STM image of an individual diffusing adatom on a (7x7)-reconstructed Si(111) whose potential energy surface (*PES)* showing the diffusion barriers intra- and inter-*faulted* (*f*) and *unfaulted* (*u*) half cells in depicted below

When $\vec{\gamma} = 0$, the system is in (*pseudo*-)thermodynamic equilibrium. It is worth to mention that during film growth and processing there are processes that are: (i) favorable from a thermodynamic viewpoint, but also (ii) kinetically restricted, having a low probability of occurrence in the time scale of the investigating phenomenon. Fig. 1.2 shows dissimilar minimum-energy paths for idealized growth mechanisms, both being possible from a thermodynamic viewpoint ($\Delta G < 0$) but with different $\Delta G(\Theta^{\#})$: (black line) kinetically restricted [higher $\Delta G(\Theta^{\#})$] and (red line) more favorable [lower $\Delta G(\Theta^{\#})$]. For the specific case of the surface diffusion, the (local) minimum-energy configurations correspond to the adsorption sites (i.e. locations at which atoms preferentially sticks to the surface), and the transition state correspond to the saddle points (i.e. non-preferred sites of adhesion between adsorption sites). As an example, in Fig. 1.2(c) self-diffusion on a faulted half cell of a reconstructed (7x7)-Si(111) is more favorable than in the unfaulted cells.

1.2 Kinetic paths to minimize the system energy

Once introduced the relevant thermodynamic arguments driving the growing film toward low-energy configurations, how such a morphological/structural transformation proceeds is described by the kinetics of the process[5]. Kinetic phenomena in film growth are related to active mass transport, comprising species diffusion ranging from the random walk[6] of individual atoms/point defects to biased mass transport on mesoscopic length scales (involving thousands of individual events) [3-5]. In thin film growth, the material condensation at the growing surface proceeds through a sequence of steps in which the adatoms exchange energy with the lattice vibrations (thermal phonon bath)[7] of the substrate. Once atoms are adsorbed (i.e., they become adatoms)[8], they can move by surface diffusion[9], exploring the potential energy landscape of the surface (also termed as potential energy surface, *PES*). When adatoms meet each others, they form dimers, and trimers, and so on. Stable nuclei growths until the development of grains. Once grains touch each others, they can coalesce to create larger grains, separated to each other by grain boundaries. In this stage of growth other available types of diffusive processes are the grain boundary (GB) and bulk diffusions; which involves the non-elemental movement of indistinguishable atoms at short-range scale and vacancies at long-range ones, in the opposite direction. Since the GBs are rarefied regions (in which atoms are partially coordinated), the diffusion along GBs is faster than that within the bulk, but both are slower than diffusion on the surface with the lowest atomic coordination. In terms of diffusion coefficients (that provided a measure of mobility rate in explored area by the diffusing species per time unit), it means that $\kappa_s > \kappa_{GB} > \kappa_B$, with the sub-indexes being referred to the mass diffusivities on the surface, along GBs and within the bulk, respectively.

1.2.1 Atom diffusion: stochastic approach to growth kinetics

From an atomistic viewpoint, diffusion of individual entities such as atoms and vacancies/point defects can be appropriately addressed from a random walk hopping model[3] and the transition state (TST) theory [1,6]. In the random walk model, the

[5] Kinetics refers to the relationship between the motion of entities and its causes.
[6] A random walk is a mathematical formalization of a path consisting of successive random steps.
[7] Or to the thermal bath of phonons.
[8] A diminutive of *ad*sorbed atoms, *ad*atoms.
[9] Or transient mobility for hyperthermal entities. In that case, thermalization by such transient mobility occurs.

migration of an isolated adatom corresponds to a random path between adsorption sites, the mean square displacement of the atoms being:

$$\left\langle \left(\vec{r}(t)-\vec{r}_0\right)^2 \right\rangle \equiv \left\langle \left(\Delta\vec{r}\right)^2 \right\rangle = \left(\left\langle \Gamma_x \left\langle \lambda_x^j \right\rangle^2 + \Gamma_y \left\langle \lambda_y^j \right\rangle^2 \right\rangle \right) t = \Gamma_h \left\langle \lambda^j \right\rangle^2 t \tag{1.4}$$

where $\vec{r}(t)$ describes how the atom position varies on the surface, $\vec{r}_0 = \vec{r}(0)$, and $\left\langle \lambda_k^j \right\rangle$ and Γ_h are the mean jump length and the corresponding hopping frequency along the $h = x, y$ axis, respectively (Figure 1.3a). The corresponding surface tracer diffusion coefficient, which is the explored surface area by the atom per time unit, is then defined as:

$$D_s = \lim_{t\to\infty} \frac{\left\langle \left(\Delta\vec{r}\right)^2 \right\rangle}{2d't} = \frac{1}{2d'} \left\langle \lambda^j \right\rangle^2 \Gamma_h , \tag{1.5a}$$

with

$$\Gamma_h = \nu_0 \exp[-E / k_B T] \tag{1.5b}$$

where d' is the dimensionality of the of the diffusion domain (namely, d'=1 perimeter diffusion, = 2 surface diffusion), $\nu_0 \propto k_B T / h \sim 10^{13}$ Hz is the attempt frequency, E denotes the diffusion barrier, and $k_B T$ corresponds to the thermal energy. An expression for the hopping frequency can be obtained by means of the transition state theory (TST); which assumes that there is a thermal equilibrium between the atom/vacancy populations in the adsorption well and the saddle point (the activated state), this activated state being a point of no return.

Then, regarding atomic diffusion on singular surfaces (just considering surface corrugation), the rate of diffusion is proportional to the ratio of the partition functions of the two states, expressed as:

$$\Gamma_h^{TST} = \frac{k_B T}{h} \frac{Z^{\#}}{Z_i} \exp\left[-\frac{E}{k_B T} \right] = D_s \frac{\left\langle \lambda^j \right\rangle^2}{2d_D} \tag{1.6a}$$

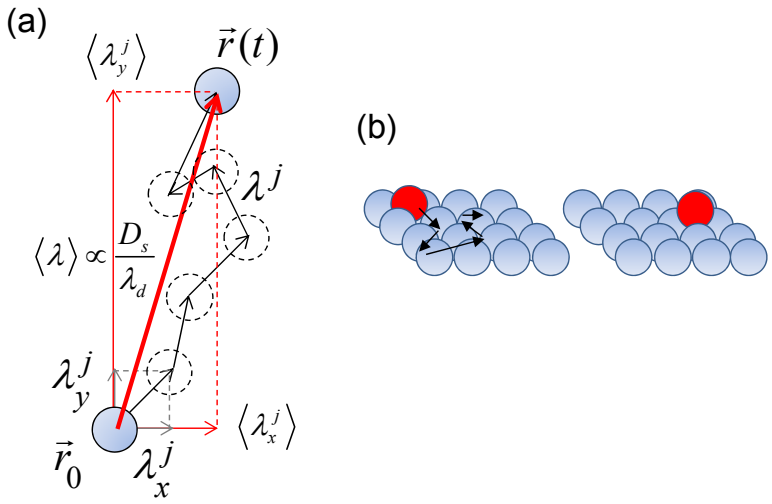

Figure 1.3 Surface diffusion by random walk model. (a) Sketch of random walk concepts (Eq. 1.6 – 1.7) for an isotropic surface. λ_d corresponds to the diffusion length. (b) Sketch of the random walk diffusion of an atom on a cubic crystalline surface

with,
$$D_s = \frac{k_B T}{2hd'} \left\langle \lambda^j \right\rangle^2 \exp[\Delta S^{\#} / k_B] \exp[-E / k_B T] \tag{1.6b}$$

where $Z^{\#}$ and Z_i are the partition functions of the ground and transition state, respectively, such that $Z^{\#} / Z_i \approx \exp[T\Delta S / k_B T]$ with $\Delta S = S^{\#} - S_i$ denoting the entropy change, and h the Planck's constant [5,6]. In its conventional form, TST considers the Gibbs free energy of the system along a minimum-energy path that leads from the initial state to a final one, as sketched in Figure 1.2. From TST principles, atoms diffuse between adsorption sites by surpassing higher-energy transition states (that corresponds to saddle points in the *PES*), the energy difference between both states being to the barrier of the process. Figure 1.4 summarizes several atomic diffusion processes on film surfaces, in which only short-range jumps towards the nearest adsorption sites are considered. However large jump events like leap-frog, although plausible, are less probable) [7].

Figure 1.4 (*inset, upper ball model*) shows a type of diffusion by atomic exchange that is different from that of hopping. In this process, the adatom pushes a neighbour one out from the surface lattice to occupy its position [5]. The exchange diffusion is feasible for self-diffusion where the substrate takes active part, and it has a high occurrence probability in vicinal surfaces as a mechanism of inter-layer mass transport (Figure 1.4,

inset in the lower ball model), which is hindered otherwise by step-edges barriers that prevent partially the hopping diffusion [5].

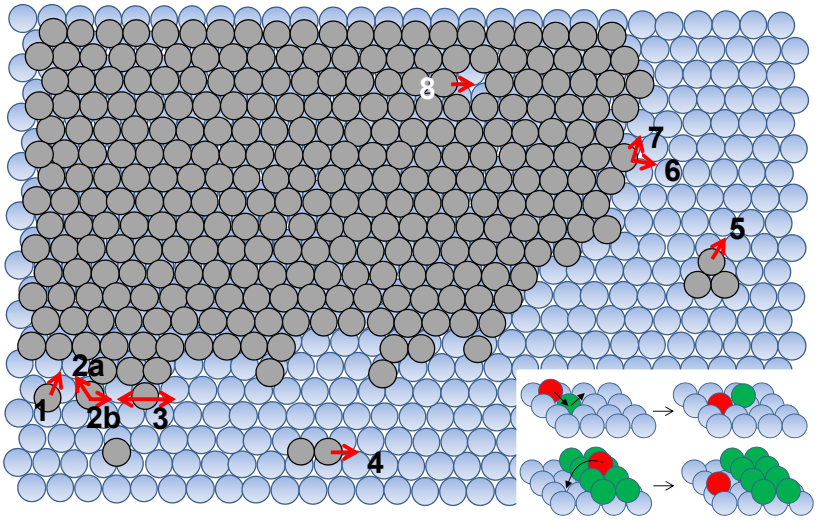

Figure 1.4 Several intralayer layer diffusion processes during film growth. The figure shows a ball model of diffusive atomic processes on a Pt(111) surface, among them: (1) Diffusion and attachment to step-edge sites (0.29 eV). (2a) diffusion along the step-edge around a corner position (0.45 eV), (2b) diffusion of atom at a corner to step-atom position (0.40 eV), (3) diffusion of step atom along step edge (0.84 eV), (4) dimer dissociation (0.81 eV), (5) trimer dissociation (1.28 eV), (6) diffusion of kink atom to corner site (1.32 eV), (7) kink detachment (1.72 eV), (8) vacancy diffusion (0.80 eV). The value inside brackets indicates the activation energies for each process. Insets at the lower-right side show interlayer diffusion by exchange (*upper inset*) and hopping (*lower inset*) diffusion. The figure was adapted from T. Michely and J. Krug "*Islands, Mounds and Atoms: Pattern and Processes in Crystal Growth far from Equilibrium*", Springer Verlag, Germany 2004 (Fig. 3.2, page 64).

Individual atoms can also move along planar defects (like grain boundaries) and within the bulk (e.g. involving the movement of point defects within the crystal lattice). As a first approach Equations 1.5 and 1.6 (which are Arrhenius law-based equations) are also valid to address such kinds of diffusion processes, by replacing the activation energy E and geometrical constants as it proceeds. As a rule of thumb: $E_{bulk} > E_{GB} > E_s$, (where E_{bulk}, E_{GB}, and E_s are the barriers for diffusions in bulk, along grain boundaries, and on surfaces, respectively) which sets a hierarchy for kinetic processes during growth, the more probable (around 10^{10} times faster) being those happening in "dilute" configurations with lower coordination [5].

A fact to stress is that the movement of individual entities from their *pseudo*-equilibrium positions induces slight displacements of the neighbouring atoms in the crystal lattice because restoring forces (stresses) that appear in order to minimize the local energy by shifting the system near the unperturbed lattice parameter. Examples of

displacements taking place in several characteristic situations are shown in Figure 1.5; among them: (*a*) displacements around a vacancy;

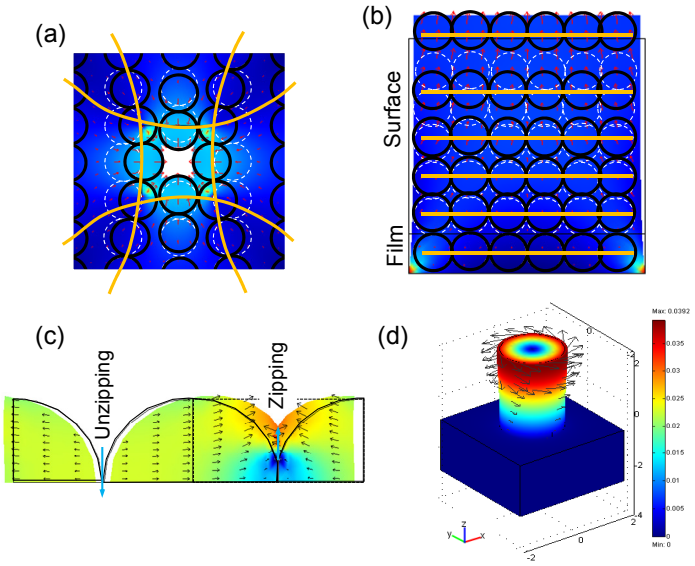

Figure 1.5 Finite element simulations showing slight displacements causing strain fields. (a) Strain field by vacancy generation. Black circles correspond to final lattice configuration, whereas dashed (white) ones correspond to initial lattice structure. Arrows points towards the direction of displacement. The color scheme indicates local displacements from the equilibrium position, i.e. strain fields or regions with: (dark) unperturbed and (light) perturbed lattice parameter. (b) Buckling on a cross-section profile of a thin film, in which a strain field is developed after removing the atom layer of the surface. (c) Traction by grain boundary zipping. (d) Columnar grain torsion by in-plane reorientation.

(ii) Buckling of the surface of a solid since the periodicity of the crystal lattice is broken at the surface; (c) traction and (d) torsion in misorientated grain boundaries that are rarefied solid regions. Such displacements correspond to the system response at atomic timescale ~10^{-12} s, in the range of the attempt frequency, reason why they are "static" at the diffusion timescale.

1.2.2 Concerted atom diffusion

From the consideration of single adatoms moving by hopping between neighboring adsorption sites on a homogeneous surface, relevant mechanisms governing surface migration were described. However, in real systems the surface is covered by a finite adatom concentration ρ, which comes from the supersaturated flux of material. In such a scenario, the diffusion coefficient for an ensemble of adatoms can be formulated straightforwardly by using Equation (1.5a), as [6]:

$$\tilde{D}_s = \lim_{t\to\infty} \frac{1}{2d'nt} \sum_{i=1}^{n} \left\langle \left(\Delta \vec{r}_i\right)^2 \right\rangle \qquad (1.7a),$$

where n is the total number of entities in the ensemble. $\tilde{D}_s$ can be reconciled with the hopping model by associating an effective coverage-dependent jump rate to the motion of single adatoms. Thus, collective diffusivity may be expressed by [6]:

$$\tilde{D}_s = \bar{D}_s \Lambda = \frac{a^2}{2d'} \bar{\Gamma}_h(\rho) \Lambda \qquad (1.7b),$$

where $\bar{D}_s$ is an average jump diffusion coefficient and $\Lambda = \partial\left(\mu / k_B T\right) / \partial \ln \rho\big|_T$ is a thermodynamic factor [6] that considers the fluctuation with μ and $\rho\big|_T$ denoting the chemical potential and the local adatom density at an area element of the ensemble, $\rho\big|_T \propto e^{\Lambda\mu/k_B T}$, and ρ is the density of adatoms in equilibrium with surface entities). Actually, adatoms are furthermore subject to lateral interactions, which result in the deformation of the potential energy landscape (*PES*) experienced by an adatom in the vicinity of another one [6] and that may lead to correlated motions, as those depicted in Figure 1.6.

Depending on the nature of the adatom-substrate configuration, the lateral interactions can be either repulsive or attractive. This is illustrated in the diagram in Figure 1.5(a), where it is assumed that only the nearest-neighbor ground state is affected. A direct consequence of these deformations is that for interacting adatoms the energy barrier for diffusion is locally reduced (or increased) in the case of repulsions (or attractions). When the interactions are small, i.e., $|\Delta E| \ll E$ the attempt frequency is strongly affected, whereas substantial changes in the respective hopping rate due to a modification of the Boltzmann factor are expected, as $\exp\left(-E / k_B T\right) \to \exp\left(-(E \pm \Delta E) / k_B T\right)$.

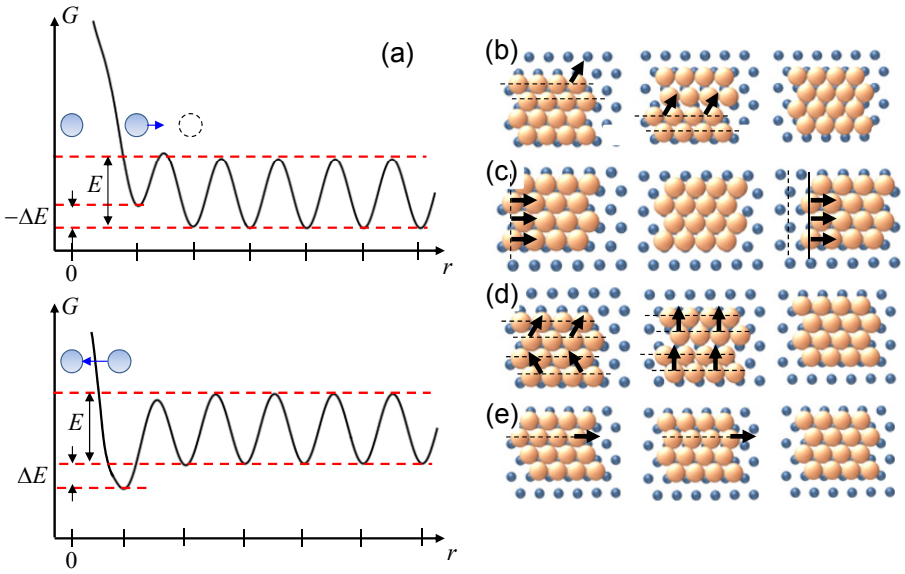

Figure 1.6 Basics of collective atom diffusion. (a) Schematic of the deformation of the potential energy landscape due to: repulsive (up) and attractive (down) interactions for an adatom interacting with another adatom at the origin (here position label as "0"). E is the diffusion barrier and ΔE is the additional interaction energy.

1.2.3 Mass transport phenomena: mesoscopic approach to diffusion

Diffusion is usually described in mesoscopic terms by using Langevin-type continuity equations [4-6]:

$$\frac{\partial \rho}{\partial t} = -\vec{\nabla}_{\vec{r}} \vec{j}(\vec{r},t) + \Phi - \Psi \qquad (1.8),$$

where $\vec{\nabla}\vec{j}(\vec{r},t)$ is the divergence of the surface current, Φ is a term describing potential sources of adatoms (e.g. from the impinging flux), and Ψ denotes potential sinks (e.g. via thermal re-evaporation). By using the Fick's second law [1, 4, 5],

$$j(\vec{r},t) = -\tilde{D}\vec{\nabla}_{\vec{r}}\mu(\vec{r},t) \qquad (1.9a),$$

with $\mu(\vec{r},t)$ being the chemical potential or the thermodynamic potential proportional to the density of adatoms, and $\tilde{D}$ a collective diffusion coefficient and upon combination with the continuity equation expressed in Equation 1.8 (neglecting sources and sinks), we get:

$$\frac{\partial \rho}{\partial t} = \tilde{D}\vec{\nabla}^2_{\vec{r}}\mu(\vec{r},t) \qquad (1.9b),$$

For the classical mechanism of surface diffusion, usually known as Mullins (MBE)-type surface diffusion $\mu(\vec{r},t)$ represents the chemical potential, being $\nabla_{\vec{r}}\mu(\vec{r},t)$ a driving force biasing surface currents towards preferred (minimum energy) paths along the film. Because the gradient in ρ at the surface can be correlated with the surface density of dangling bonds because they are sinks (Fig. 1.6e), $\nabla\rho \to \nabla^2 h$ and $\mu \propto \nabla\rho \to k\nabla^2 h$. Besides, due to the fact that $h(r')$ (the local height of the surface at a point r') depends on the probability of nucleation and attachment in this point $\propto \rho(r')$, we can approach that $\partial_t \rho \to \partial_t h$. By using a chemical potential $\mu(\vec{r},t) \propto -\nabla^2_{\vec{r}}\rho(\vec{r},t)$ in a special case in which the $\tilde{D}$ constant is space independent, Equation 1.9b transforms into:

$$\frac{\partial \rho(\vec{r},t)}{\partial t} = -\tilde{D}\vec{\nabla}^4_{\vec{r}}\rho(\vec{r},t) \qquad (1.10)$$

Figsures 1.7(a)-(c) show the result of a simulation over a three dimensional surface entity with an analytical Gaussian-like shape supporting mass transport/relaxation by MBE diffusion. As observed, the initial shape is relaxed (i.e. it volume spreads on the surface), which is highlighted by cross-section profiles in Figure 1.7(d) taken over the surface entity for different runtimes of the simulation. So far, we consider surface diffusion only. However, processes of atomic desorption may be also present. Such process are governed by the surface gradient in the vapour pressure of an surface in equilibrium with the vapour phase; these gradients being caused by the local variation in the density of dangling bonds estimated in terms of surface curvature, and thus $\Phi - \Psi \propto -\nu\nabla^2 h$. In addition to diffusion along surface, a consequence of chemical potential-biased mass transport is the rising of phenomena like grain rotation, in which atoms flows along peripheral trajectories of the surface entities, to form pseudo-coherent low-energy GBs as depicted in Figure 1.8(a).

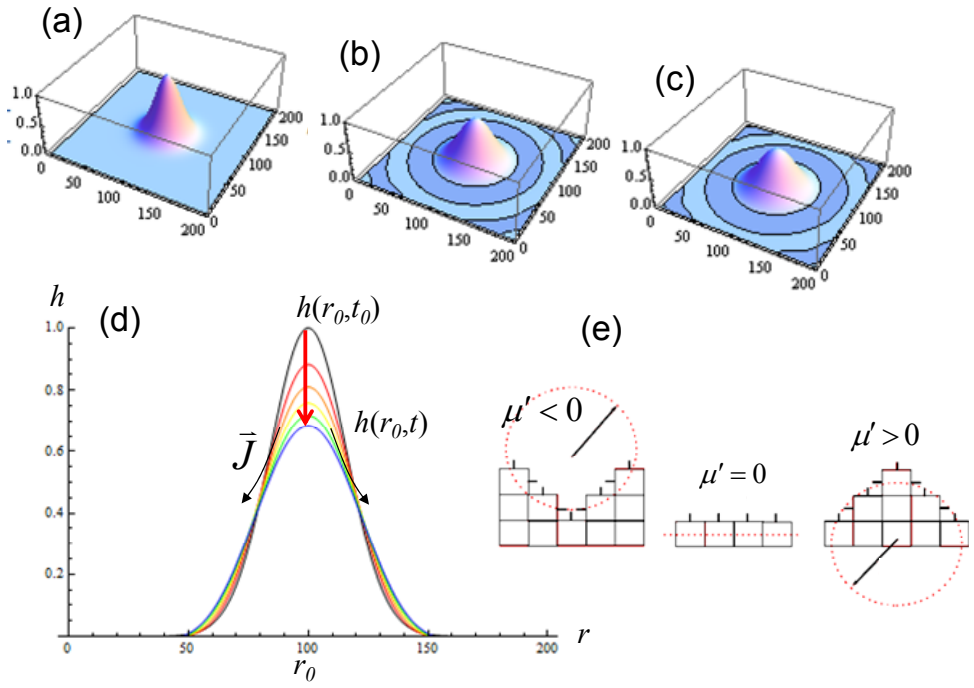

Figure 1.7 (a-d) Evolution of a generic gaussian-shaped entity by Mullins-type diffusion. (e) Curvature dependence of the surface chemical potential.

Other chemical potential-driven diffusion processes cause the filling of the gaps between surface entities (details in §4, Figure 1.8b), the grain boundary mobility (Figure 1.8c) and competitive coalescence like Ostwald ripening (details in §5 and sketch in Figure 1.8d) All them described below.

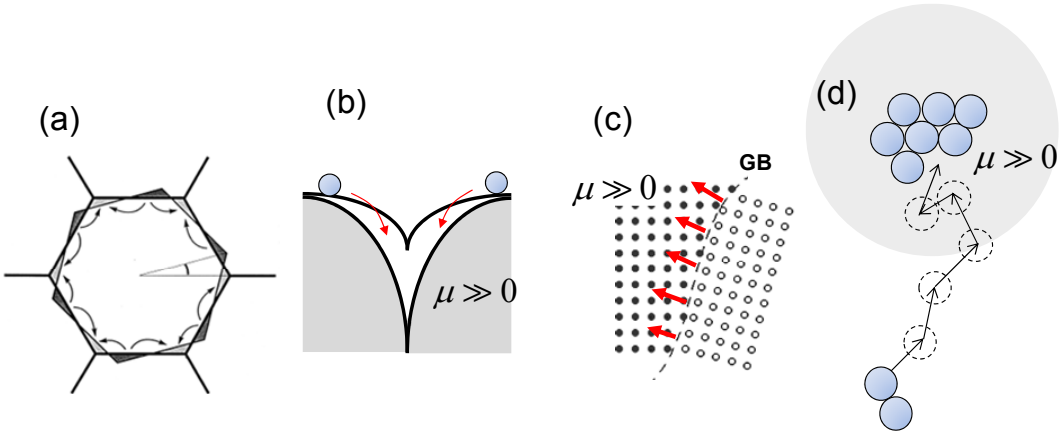

Figure 1.8 Chemical potential gradients driven diffusion processes, sketched of (a) rotation of an hexagonal grain to create low-angle and/or coincident-site-lattice grain boundaries , (b) filling of the gap between two grains (shadow ⇒ grains, white space ⇒ gap), (c) grain boundary motion in grain growth, and (d) Ostwald ripening.

1.3 Polycrystalline films and nanostructures

Along this work, we deal with the growth of solid films taking place by the condensation of an impinging supersaturated flux of atoms (without involved chemical reactions) above a rigid substrate of other (or same) material, as sketched in Figure 1.8(a), which is known as Physical Vapor Deposition (PVD) growth method. Thin film growth proceeds in different "modes" in dependence of the hierarchy of interactions between the adsorbed atoms (or adatoms) and the substrate. Such interactions can be described —in a first approach— by the energies of cohesion, γ_s and adhesion, γ_a, as sketched in Figure 1.9(b). The forces of adhesion, cohesion and surface tension contribute to the total energy of the system, as [3]:

$$\partial_{\Theta} G \equiv \gamma \propto \gamma_a - (\gamma_s + \gamma_f \cos[\theta]) \qquad (1.11),$$

where θ is the wetting angle. The mechanical equilibrium $\gamma = 0$ defines the following growth modes from the condition:

$$\cos(\theta) = \frac{\gamma_a - \gamma_s}{\gamma_f} \qquad (1.12)$$

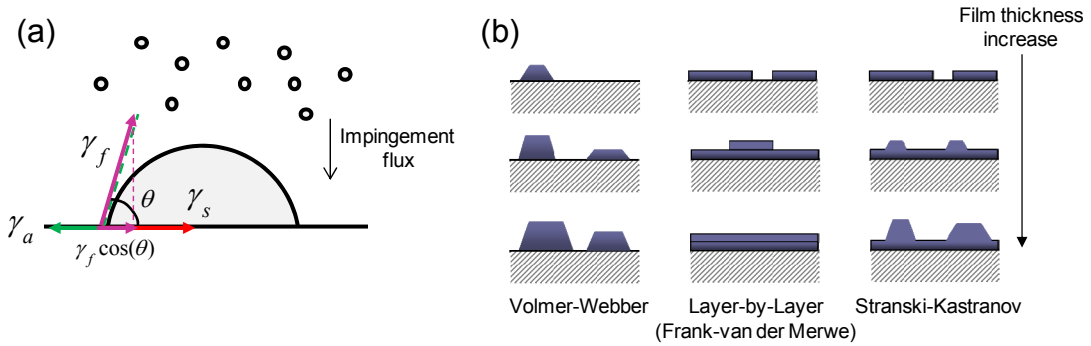

Figure 1.9 (a) Cross-section view of the scheme of the system considered along this work, formed by a grained film attached to a rigid substrate immersed in a material flux. (b) Growth modes in dependence on the force balance between the forces of: adhesion γ_a, cohesion γ_s, and the film surface tension γ_f.

Thus, films with high surface tensions and/or unable to form stable interfaces with the substrate (i.e., that do not wet, which implies low $\gamma_a - \gamma_s$) tend to growth in a three

dimensional manner according to the *Volmer-Weber* mode (that is characterized by $\theta \to \pi/2$). Otherwise, the growth takes place in a two-dimensional layer-by-layer fashion on singular surfaces, and by step-flow on vicinal ones (*Frank-van der Merwe* mode with $\theta \to 0$). A mixed mode (termed *Stranski-Krastanov* mode) is available when the interface stability drops (i.e., $\gamma_a - \gamma_s$ decreases) as the film thickness increases (for example, due to the elastic energy ascribed to the heteroepitaxial strain) [8,9]. This gives rise to a mutation in the growth mode from two-dimensional layer-by-layer one (during the early stages in which a wetting layer is deposited) to three-dimensional mode for later stages. In general, both VW and SK produce polycrystalline films (with lower and higher degree of in-plane crystalline coherence, respectively). In the VW mode, the nucleated grains are uncorrelated to each other during an early pre-coalescence stage that extends beyond the completion regime of a film growing layer-by-layer. Thus, when the VW grains become in touch, they are large enough to produce grain coalescence involving crystalline reorientation. On the other hand, the SK wetting layer imposes a local order to the grain nucleated above, which are broken by defect generation.

In general, the growth of metals and oxides proceeds by VW and SK modes. In such modes three-dimensional surface entities like islands, mounds, and grains separated to each other by grain boundaries (i.e. polycrystalline films) are usually developed. At this point, it deserves to define a polycrystalline film as: (i) —*pure polycrystalline*, if there is not any crystalline coherence within the whole space scale of analysis, which rarely occurs in solid films because the role played by the substrate and the in-plane interactions between grains, Figure 1.10. (ii), —*textured*, if there is in-plane or out-of-the plane coherence by competitive interactions between grains that leads, for example, to a preferred growth of a specific crystal orientation among others. Such competitive interactions can be driven by surface energy minimization processes like those exposed in Table 1.1 (third and fourth rows); and (iii) —*single crystalline*, in which crystalline coherence is preserved within the whole spacescale of analysis. Table 1.2 summarizes a general classification of defects in polycrystalline films.

The size of grains (crystallites) is typically in the range of 1–500 nm, reason why sometimes we term grains as *nanostructures*, and straightforwardly to the polycrystalline solid film as *nanostructured* system [10,11]. Nanostructuration is the process of breaking up the film into nanometer-sized structures, which is interesting

because (a) the viability of scaling volumetric functional properties down to the nano-micrometer scale (and then the possibility to built devices with ultra-high level of integration) [12,13], and (b) the tailoring of such functional properties via the manipulation of quantum confinement effects, which rise as a consequence of the small size of nanostructures [4, 5, 14, 15]. In this case, nanostructuration requires well-defined spacing, symmetry, and narrow entity-size and –shape distributions in order to prevent the dispersion of the tailored properties. Some examples of improved functional properties are better catalytic yield and surface sensibility, superhydrophobicity, plasmon resonance, superconductivity, luminescence, among others.

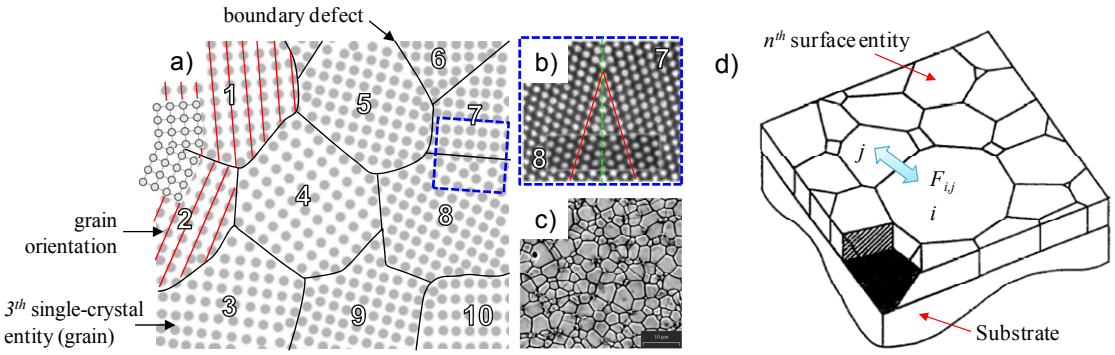

Figure 1.10 Polycrystalline films: (a) Ball model (top view) of a polycrystalline solid material with a cubic crystal lattice. Single-crystalline domains (surface entities) are labeled from 1 to 10. Insets: red lines in "1" and "2" depict crystalline orientations. Curved contours correspond to the boundary defects. (b) High resolution image of a low-angle GB in a polycrystalline Ni film. (c) Granular surface of a SnO polycrystalline film. (d) Sketch showing a polycrystalline thin film clamped by a rigid substrate. The film is formed by n partially confined surface entities separated by boundary defects. $F_{i,j}$ denotes the interaction between entities.

It is worth noting that the growth of polycrystalline solid films by PVD is in fact a non-equilibrium (irreversible) process, mainly in the cases of high growth rates and low-moderate growth temperature.

1.4 Functional properties of nanostructured thin films

As a consequence of the crystalline coherence, the functional properties of single and polycrystalline materials are in general quite different. Functional properties of single-crystalline thin films are dependent on the crystal anisotropy[10], as example the

[10] The crystal anisotropy is a consequence of the variation of the lattice parameter with the crystallographic direction.

mechanical properties in metals [2]. However, the random orientation of grains in polycrystals confers an isotropic behavior to the film properties.

Location in crystal domains	Dimension	Crystal lattice defect	Description
Intra granular structure	0D	-Intrinsic Point defects like vacancies, and interstitials -Extrinsic defects like impurity atoms	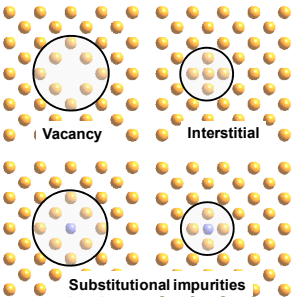
	1D	Surface steps, Edge and Screw dislocations	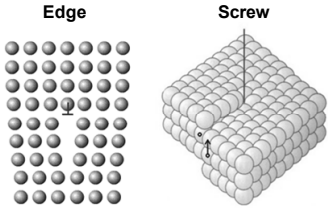
Inter granular structure	2D	-Stacking faults and grain boundaries (in crystals of one material or phase) -(Anti)phase boundaries	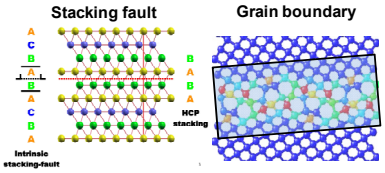
	3D	-Precipitates formed by impurity atoms -Voids, which are agglomerates of vacancies and film discontinuities -Stacking fault tetrahedral and clusters of dislocations	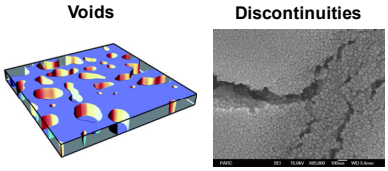

Table 1.2 Main classes of crystal defects.

The absence of planar defects like grain boundaries provides single-crystal interesting properties, because diffusion of carriers (particles, *quasi*-particles responsible of material's) is in general better than in polycrystals. It is due to the inelastic scattering of such carriers with the GBs, such that the carrier mobility $\propto 1/\rho_{GB}$, with ρ_{GB} being the GB density. As example, in conductive metal films like Cu, GBs contribute to hinder the mobility of the charge carriers, reducing the electrical conductivity of materials. GBs also pin the dislocation motions, improving the mechanical strength of the materials. Regarding optical properties, in $SrTiO_3$ films it have been demonstrated that

both the local reflectivity and valence electron densities are reduced in a 30-50% near the cores of GBs, in comparison with the single-crystalline material. It happens as a consequence of the variation in the local mass density along GBs, which goes down into a 20-40% with respect to that of the bulk [16], which induces differences in the electronic structure and medium polarizability. Single crystal materials are also useful for lasing, being used (e.g. sapphire and Nd:YAG crystals) as gain medium in most lasers. The reduction of the mobility of carriers in polycrystals results convenient in several applications, as example, protective coatings to prevent mechanical damage (dislocations and cracks are frozen along grain boundaries, the material mechanical resistance being improved), thermal isolating coatings and so on [17, 18]. While bulk properties of single/polycrystalline materials degrade in nanostructured systems, surface properties strengthen and quantum ones, which are inherent to the discrete band structure of the atoms, appears [13, 19-27]. Therefore, considerable efforts have been prompted[11] in the development of novel bottom-up nanostructuring strategies. Complementary to the experimental procedures, numerical simulations and theoretical models based on grain interactions have been developed, which were aimed to extract detailed information concerning underlying atomistic processes in nanostructuration experiments [5, 8, 9, 28]. As an example of such efforts in the understanding of local grain interactions, the role of the principal mechanisms responsible of the generation/relaxation of compressive stress and selected shapes during film preparation (both topics approached in this work) is nowadays matter of an intense debate [10, 11, 29].

[11] The national nanotechnology initiative of the National Science Foundation (at E.E.U.U.) supports the research in the areas of Fundamental Nanoscale Phenomena & Processes, Nanomaterials, Nanoscale Devices and Systems and Nanomanufacturing with total investments of 319.93 million $ in 2010, 297.41 million $ in 2011 and 344.3 million $ in 2012 (see http://www.nsf.gov/about/budget/fy2012/pdf/35_fy2012.pdf).

1.5 Scope and work structure

In order to investigate the main local interactions between surface entities that take place during polycrystalline film preparation and processing —and the role of such interactions in the surface nanostructuration—, it is necessary to analyze the structure evolution of thin films under preparation. With this knowledge, we hope to gain insight in controlling, manipulate and tailor the surface morphology in order to achieve nanostructured polycrystalline films with desired functional properties by using a bottom-up strategy [30, 31]. There is a variety of processes that leads to thin film surface nanostructuration. Two of them are of special interest in thin films: (a) grain coalescence, including peer-to-peer (short range) entity interactions by material sharing, and (b) grain coarsening, in which long range entity interactions cause the lateral expansion of grains, as an example by hierarchical mechanisms. Peer-to-peer coalescence lead (in general) to percolate and melted-like nanostructured surfaces and the rising of intrinsic stress in thin films. On the contrary, coarsening usually develop films with well-shaped surface entities distributed along the surface following a specific pattern. To explore these opposite processes, the objectives of this work are:

(I) Investigate peer-to-peer coalescence by elucidating the origin, nature, spatial distribution, evolution and flux dependence of the postcoalescence growth stress caused by intrinsic interactions between surface entities during thin film preparation and,

(II) Investigate the increment of the surface entities (coarsening) by Ostwald ripening in thin films with postcoalescence-like surface morphology, caused and maintained by kinetic limitations due to low mobility experimental conditions.

This work approaches these issues through the investigation of the multiscale evolution of the structure and morphology of the polycrystalline films. Model materials (namely metals and single-metal oxides —Au and ZnO, respectively) were used to prepare the films investigated at the coarse-grained scale. To achieve these objectives, the work is organized as follows: *Chapter 2 —Experimental and theoretical methods*, is devoted to provide a brief description of the experimental techniques and theoretical methods employed along this work, among them: film deposition by thermal

evaporation and post-processing by in-situ thermal annealing, characterization by scanning probe microscopies, x-ray diffraction and novel image processing procedures, and classical growth models based on dynamic scaling, mesoscopic partial-differential equation systems and finite element approaches.

Chapter 3 —"*Coarsening phenomena during polycrystalline thin film preparation: Experimental evidences"* presents experimental findings concerning the evolution of the structure of Au-polycrystalline films during growth and processing, obtained by scanning probe microscopies and x-ray diffraction. By using novel a multi-scale statistical analysis, we recognize several phenomena like grain reorientation and shape selection during film growth and processing.

Chapter 4 —*"Peer-to-peer coarsening: intrinsic stress generation and relaxation during polycrystalline thin film preparation"* addresses the key role of the balance of intrinsic forces between surface entities during peer-to-peer coarsening and post-coalescence stages in thin film growth, which enables the nanostructuration of surface entities through stress-driven and kinetic-limited phenomena. A novel mechanism including classical aspects of grain growth as reorientation, zipping and slope selection is described for the case of metal films. This model is supported by comprehensive multi-scale simulations combining continuum and finite element approaches, which offers a successful explanation of the structural evolution reported here.

In *Chapter 5* —"*Hierarchical coarsening: A late slope selection-driven Ostwald ripening in polycrystalline thin film preparation"*, the lateral expansion o between surface structures is investigated. We revise recent results of the growth by pulsed laser deposition of single-metal oxide films, finding that an Ostwald ripening phenomenon can be atypically preserved for late growth times even at moderate temperatures by selected-slope-driven surface diffusion. We also demonstrate, by using continuum approaches, the manner in which that kind of mechanism can organize randomly-located surface entities into well-ordered arrays. Once the principal mechanisms of self-organization of surface entities in thin films have been elucidate, general conclusions are proposed.

CHAPTER 2

EXPERIMENTAL AND THEORETICAL METHODS

2.1 Film preparation and processing

2.1.1 Film growth by thermal evaporation

Throughout this work, we deal with films grown as a result of the condensation of a given material on solid substrates from its supersaturated vapor phase. This method of film preparation is termed physical vapor deposition (PVD). An example of PVD set-up for thermal evaporation in vacuum conditions is outlined in Figure 2.1 [5, 18, 32-34], which was used for film preparation purposes in this study.

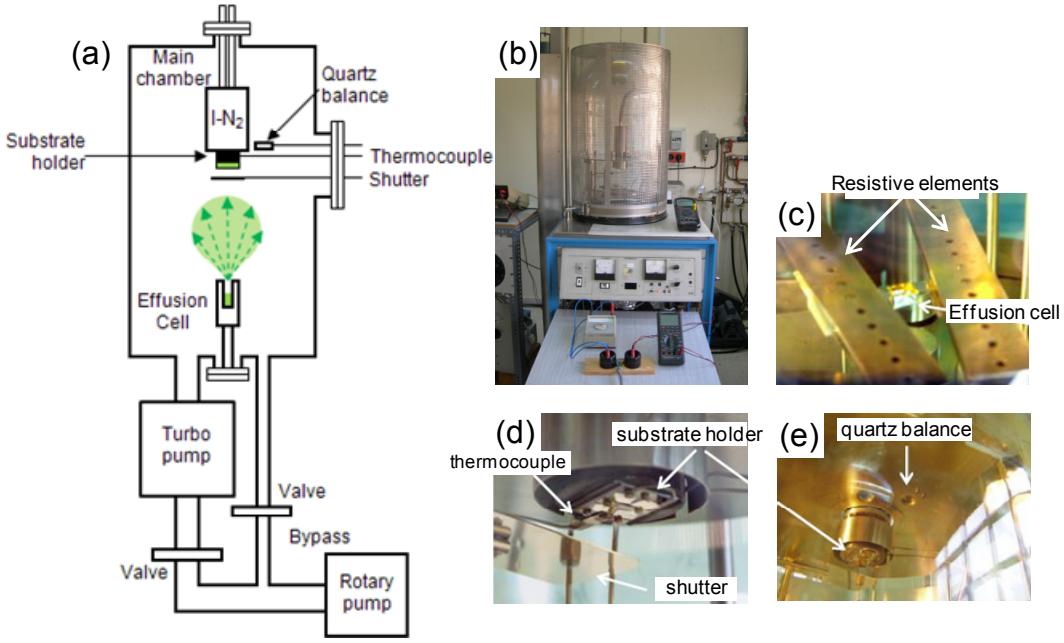

Figure 2.1 Components of the TE equipment used for film preparation: (a) General scheme showing the basic features of the TE system located at the Institute of Applied Physics "Torres Quevedo" ascribed to the Spanish National Research Council (CSIC). (b) Overview of the vacuum chamber, (c) Effusion cell made of Mo, (d) substrate holder, and (e) quartz balance.

Among the diverse techniques comprised in PVD (e.g., pulsed laser deposition, sputtering, molecular beam epitaxy, flash evaporation and others), thermal evaporation (TE) was chosen because it is the simplest one to evaporate non-refractory single-element films within controlled environment (namely, vacuum or inert atmospheres for highly-reactive single elements, e.g., metals; or oxidant atmosphere for single-metal oxides). In TE, the heating of a source by electron bombardment or through an attached

resistance (as it is in our set-up) supplies enough energy for the massive evaporation (or sublimation) of the material to deposit. The thus-generated vapor, which is equilibrium with the source, expands within the background before condensing on a cooler substrate, where it sticks, forming a thin film. Figure 2.1 shows the main components of our TE set-up as sketched in (a) that includes: (b) vacuum system; (c) multi-substrate holder assembly and evaporation source based on resistive elements; and (d and e) control systems for monitoring both the growth rate (quartz balance) and the deposition temperature T_{growth} (thermocouple).

Parameter	Description/values
Set-up	- High vacuum system (base pressure): 10^{-7} - 10^{-8} mbar equipped with turbo molecular and rotary vane pumps - Evaporator-substrate distance: 12 cm - Shutter: square-like shaped Ta sheet
Evaporator	- Effusion cell: Mo cubic crucible (melting point 2893 K) of 1 cm^3 and wall thickness of 0.05 mm, acting as a resistive element - Evaporant: Au wires of 99.99% purity (diameter of 0.1 mm) - Temperature: aprox. 1800 K - Angular distribution of gas phase: Cosine law distribution of particles with angular dispersion of ± 10º - Rate of evaporation: F_0 =1 nm/s
Substrate holder	- Stainless steel frame in thermal contact with a heating/cooling system for substrate holding - Resistive heating controlled by a temperature ramp with feedback monitor
Deposition	- Deposition rate of 1 nm/s - Film thicknesses in the range of 2 – 1200 nm ± 10 % monitored by a quartz balance - Temperatures within the range of 373-673 K ± 4-6 K, controlled by K-type thermocouples (Chromel-Alumel) fixed at substrate backside as temperature monitor - Cooling: Slow cooling –1 ^{o}C/min with thermal inertia, and fast one –10 ^{o}C/min through a reservoir in thermal contact with dynamic flux of water
Post-deposition treatment	- Annealing at the substrate temperature in the presence of dynamic flux of Ar (if required)

Table 2.1 Growth parameters used for film preparation by thermal evaporation.

Table 2.1 summarizes the growth parameters used for the film deposition by TE. The Au vapor pressure is ~0.1 mbar at the crucible temperature (~1800 K), which means that during growth the chamber base pressure of ~10^{-7} mbar contributes to a negligible density of contaminants (e.g. water, carbon,…) of <1 ppm. The substrate holder was placed in close contact with both the resistive heater and the cooling reservoir, in order

to maintain a near-constant (± 1.5 K) temperature during growth (inset of the Figure 2.2a).

The exposure of the growth flux to the substrates is controlled by a shutter. Until the effusion cell reaches a stationary regime (i.e., a constant flux is emitted) the shutter is placed above the effusion cell, hindering any evaporation on the substrate (growth flux is OFF). Once the stationary emission is achieved, the shutter is retired and the flux is ON. The angular distribution of the flux is described typically as $F(\Theta) = F_0(\cos^n(\Theta)/\psi)$ where: F_0 is the plane flux; the power n gets values that depend on the flux-source characteristics (e.g., for thermal fluxes originated by near-field evaporators $n = 3$ while for "forward peak" fluxes ejected from collimated massive sources $n \to \infty$ and thus $\cos^n\Theta \to$ Kronecker delta δ_ϕ); and $\psi = \int_{-\pi/2}^{\pi/2} \cos^n(\Theta)\partial\Theta$ corresponds to a normalization constant. We estimated a maximum lateral dispersion of the flux of $\Theta < 20^0$ by taking advantage of the W clips attaching the substrates the holder. These clips mask the growth flux, and leave a slope in the edge of the film after deposition whose slope is an estimate of the lateral dispersion of the flux. That means a $\langle F \rangle \leq 0.8\,F_0$, where $\langle \ldots \rangle$ refers to the value averaged upon the film surface. Several technical magnitudes and functions are available to quantify the uniformity of the spatial distribution of the atom flux. From such a cosine law, the ratio between the thickness at the center of the sample (opposite the evaporation source) and the film thickness dispersion along the substrate surface can be estimated from considering a point source λ_{source}-spaced from a l_{sample}-sized sample by $\delta d / \max(d) \approx \left\{1 - \left[1 + \left(l_{sample} / \lambda_{source}\right)^2\right]^{-1}\right\}$. Due to the large source-substrate distance, $\lambda_{source} = 12$ cm and the sample size $l_{sample} = 1$ cm, $\delta d \sim 10^{-3} F_0$ [32].

According to the kinetic theory of gases, thermal atoms in the vapor phase (~1800 K) have a distribution of speeds described by $\Phi(c) = 4\pi\sqrt[3]{\left(m_a / 2\pi k_B T_{gas}\right)^2}\, c^2 \exp\left(-m_a c^2 / 2k_B T_{gas}\right)$ (where c is the atom speed, m_a the atomic mass and, T_{gas} the temperature of the gas). In the case of Au growth experiments, it implies an average speed of ~440 cm/s, with an kinetic (thermal) energy $\frac{3}{2} k_B T_{gas}$ of 227 meV. Although atoms in the gas move at high speeds, they do not travel large distances because of frequent collisions and deflections from their course. Taking into account the vapor pressure P_{gas} of ~0.1 mbar, the mean

free path of the evaporant atoms in Au growth experiments, i.e. the average distance traveled by atoms between subsequent collisions $\lambda_{path} = \left(k_B / \sqrt{2}\pi\sigma_a^2\right) T_{gas} / P_{gas}$ is ~2 cm (with k_B, $\sigma_a = \pi r_a^2$ and r_a being the Boltzmann constant, the atom collision cross-section and the atomic radii, respectively). Note that λ_{source} ~$6\lambda_{path}$ and then the probability that two atoms meet in the vacuum before they condense is no negligible. However, such probability is reduced up to ~10^{-5} by considering elastic collisions and events of re-evaporation in the case of inelastic ones ($T_{gas} \geq T_{melting}$), avoiding the formation of aggregates in the vapor phase.

Figure 2.2 shows the temperature profile used during a two-step deposition of an Au/Au(111)/mica(*v*-5) film by TE.

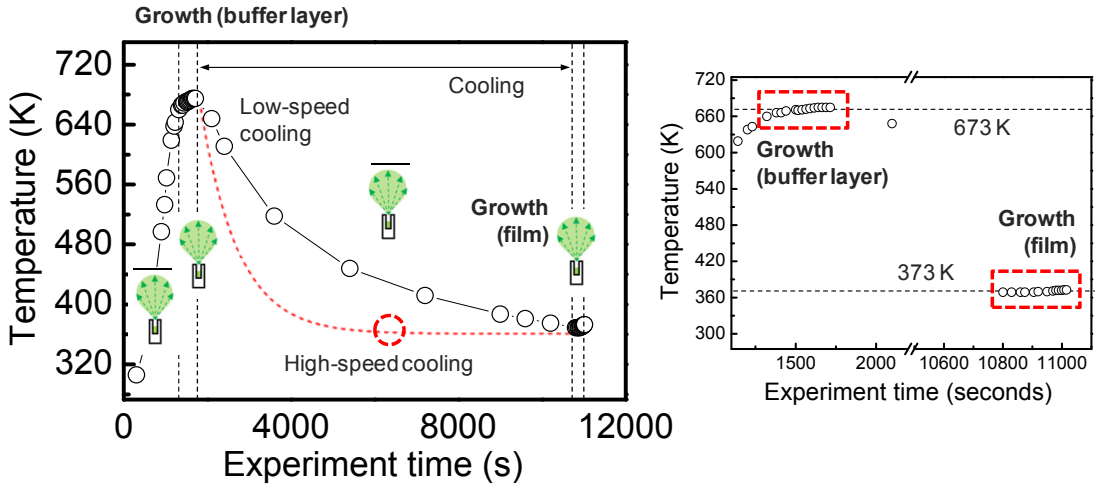

Figure 2.2 Substrate temperature evolution during growth experiments. Au/Au/mica films were grown in a two-step deposition procedure: the first one consists in the growth of an Au(111)/mica(v-5) buffer layer. In the second step, the 60-nm thick polycrystalline Au film is deposited. Dashed lines limit the periods in which the growths were carried out, whereas insets sketch the effusion cell. The line above each effusion cell indicates that the shutter is active and the flux is off. The low speed cooling ramp corresponds to thermal inertial (○), whereas the high speed cooling corresponds to the sample quenching by refrigerants (dashed). If fast cooling is accomplished, the thin film growth process would be developed at shorter experimental times, near the region marked by a dashed circle. The inset (plot at the right-hand side) highlights the thermal behavior during the growth of: Au/mica (buffer layer) and Au/Au/mica film. In the case of growths of Au/Si, the growth was developed in one step

In such case, the buffer Au(111) layer (d = 200 nm) and the outer Au films (d = 60 nm) were deposited at T_{growth} = 673 ± 6 K and 373 ± 4 K, respectively. After the growth, the temperature decays at spontaneous rate with thermal inertial (low speed cooling) or quenching (high speed cooling) with refrigerant agents if required (water flowing through a reservoir that is in close contact with the substrate holder). When the desired

substrate temperature of the next growth step is reached, the feedback system controlling the growth temperature is turned on, enabling the growth of the polycrystalline Au films at a constant deposition temperature. To monitor both film thickness and growth flux, a calibrated quartz balance placed near the substrate holder was used during TE experiments [35]. The value of the thickness obtained from the quartz balance were confirmed ex-situ by AFM tip scratching of the sample surfaces: Some scratches develop cracks whose depths (measured by cross-section scanning electron, as discussed below in Figure 2.11, or by scanning probe microscopies) provide us an estimation of the film thickness.

2.1.2 Film processing by post-deposition annealing

Once films were grown, they were subjected to continuous thermal annealing. For this purpose, the flux was stopped and samples were held at the growth temperature by *in-situ* annealing. Thermal annealing is used here for several purposes: (i) in order to smooth the rough surface morphology of films typically observed after growth experiments, and (ii) in order to investigate the mechanisms controlling the film nanostructuration.

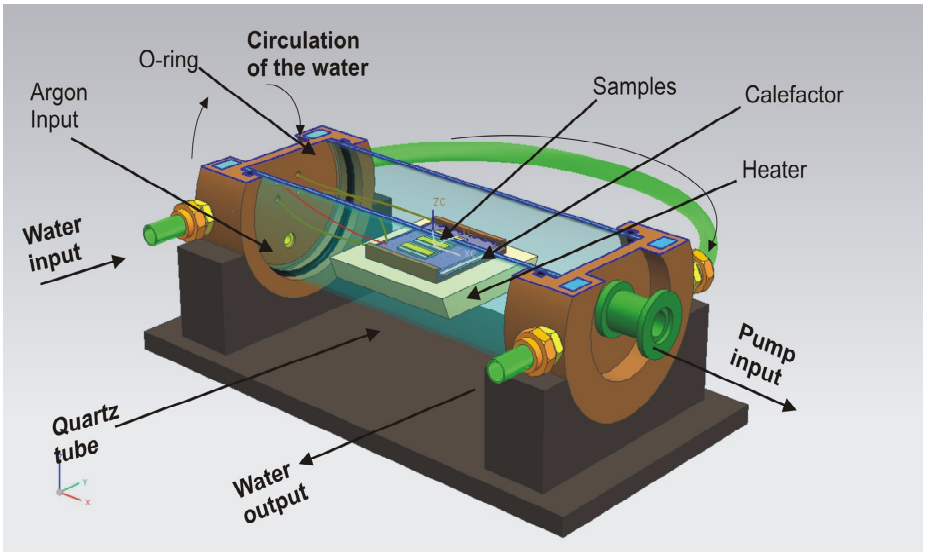

Figure 2.3 High-vacuum furnace for film processing. Several components are showed.

The annealing was also carried out in a constant Ar flux with dynamic $P_{Ar} = 1$ atm for times ranged between 120 and 1.2×10^5 s. *Ex-situ* annealing experiments were also performed in HV-furnaces (scheme in Fig. 2.3) installed at the Center of Applied

Physics at CINVESTAV-Mexico (collaboration); the conditions of such *ex-situ* annealing experiments being similar to those used in the *in-situ* ones. By using AFM microscopy it was demonstrated the annealing of samples *in-situ* and *ex-situ* showed no noticeable changes in the film surface morphology. The advantage of the *ex-situ* chamber resides in the fact that this is smaller than the growth chamber, thermal fluctuations are reduced. Besides, this small furnace enables the possibility to introduce constant pressure of gases during thermal annealing, and samples are easy to handle.

2.2 Atomic Force Microscopy (AFM)

In AFM, the mapping of the film morphology is carry out by tracking the interactive forces between a mechanical probe (a sharp tip separated a few angstroms from the surface) and the film surface [36-40]. As sketched in Figure 2.4(a), an AFM microscope briefly consists in a tip fixed to the end of a cantilever, the latter attached to an electronic interface (comprising a piezoelectric plus a control unit) able to detect changes in the dynamical properties of such cantilever caused by tip-sample interactions (e.g. deflection, and modification of the oscillation features, such as amplitude and frequency, Figures 2.4c and 2.4d) [36, 40].

Usually, an optical deflection system was used for detection. Such an optical system included: (i) a collimated laser beam focused on the rear side of the cantilever that holds the tip, and (ii) an optical position-sensitive detector consisting in a split photodiode [with four segments: *top* (A and B), and *bottom* (C and D)], which receives the intensity of the laser beam from the rear side of the cantilever once focused by a concave lens. Such a four-segment photodiode collects the laser intensity in each segment. The voltage difference from the top, bottom, left and right segments, $(V_T - V_B) + (V_L - V_R) = 0$ (Figure 2.4b) provides the AFM signal which is a sensitive measure of the cantilever vertical and lateral deflection during scanning via the *x*,*y* piezo's, whereas the *z*-piezo is connected to a feedback system. The feedback is used to keep the differential detector signal at a constant value V_0 by adjusting the vertical *z* position of the sample to achieve (almost) constant deflection z_0 of the cantilever. z_0 corresponds to a constant force F_0, ($F_0 = -kz_0$ from the Hooke's law and k is the spring constant of the cantilever). The output signal of the feedback circuit U_z (*z*-piezo signal) is recorded as a function of

(*x*,*y*) coordinates which are determined by the voltages U_x and U_y applied to the *x* and *y*-piezodrives. The two-dimensional array $U_z\left(U_x,U_y\right)$ can be transformed to "topography" $z\left(x,y\right)$ described in term of a matrix of local surface heights once the piezo coefficients (nm/V) are known. This mode of AFM operation is denominated “constant force” or “constant cantilever deflection mode”.

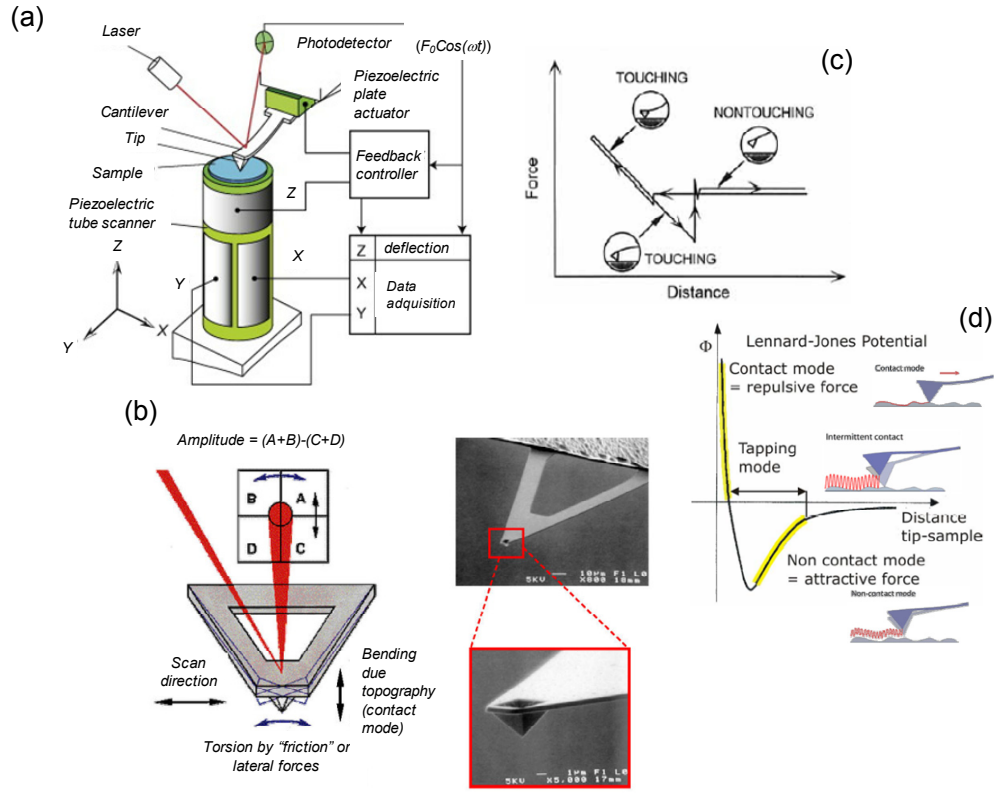

Figure 2.4 (a) AFM basics. In the case of contact mode, the feedback in z direction is deflection. In dynamic ones, it is the amplitude or the frequency. (b) A triangle-like cantilever-tip probe in the beam deflection system. (c) Typical force-distance curve due to tip-sample interactions: at a large tip-sample distance, the cantilever does not deflect (non-touching). At a distance of several nanometers, the tip jumps into contact, and the cantilever deflects (touching). During withdraw; the cantilever deflects in the opposite direction by capillary forces (touching) until it is pulled-off. (d) Sketch of a typical Lennard-Jones potential showing tip-sample interactions regimes in dependence of the AFM scanning mode.

On the other hand, the dynamic mode of amplitude modulation AM-AFM, (frequently known as “tapping”) involves the sinusoidal oscillation of the cantilever to produce an intermittent contact between tip and surface with the oscillation period. This can be realized whether the rest probe position is sufficiently far away from the sample surface while the driving amplitude is chosen to be sufficiently large to establish the intermittent contact.

AFM feature	Description	Instrumentation/Description
Relevant Forces	Electrostatic Origin	- van der Waals interactions $F(z_c, z) = -HR / 6(z_c + z)^2$ - Short-range repulsion $F(z) = -k_c z$ - Mechanical load $\sigma_{ij} = \eta\varepsilon_{ll}\delta_{ij} + G\varepsilon_{ij}$ - Capillary forces $F = 4\gamma\pi R\cos(\pi\theta) / (1 + (z_c + z) / d_{wetting})$
AFM modes	Contact mode Dynamic modes: - Amplitude modulation (tapping, jumping) - Frequency modulation	- Tip and sample are in continuous contact in repulsive regime (Fig. 2.5d). Normal and lateral forces are recorded simultaneously, resulting in topographic and friction images, respectively. SetPoint (deflection) = 0.2 – 1 V - The cantilever oscillates close to the film surface excited by an external acoustic source at a frequency close to its resonance close to that of resonance. The amplitude and frequency of oscillation are modified as a result of the tip-sample interactions. The tip separation from the surface is used as feedback to maintain the amplitude (taping mode) or frequency constants upon the scanning - Set-Point (amplitude) = 0.2 – 1 V- Scanning frequency 0.2 kHz - Excitation frequency range = 194 – 330 kHz
External conditions	-Temperature, pressure, humidity	293 K (Room Temperature), 1 ATM (atmospheric pressure) and humidity controlled by desiccants (Silica-Gel)
Image resolution	Number of image pixels in the digital matrix and size	- Images of 512x512 pixels of surface areas of 10x10 μm^2 - Pixel-size range=1 nm – 19.5 nm
Tips	Ultra-sharp silicon (Al-coated) tips	- Tip radius = 2 nm, High aspect ratio = 1:10 - Cantilevers with a spring constant of 40 N/m
Scanner system	Sectorized Piezoelectric bar	- Piezoelectric cylinders able to scan areas of 70×70 μm^2 (depth limit of 12 μm) and 10×10 μm^2 (vertical limit of 2 μm), sketch in Fig. 2.5(a) - Piezoelectric tubes have inertial movement, enabling the scanning of large areas of the sample
Sensor	Optical beam deflection system	- Beam deflection system composed of a λ = 632 nm (5 mW) He:Ne laser and a four-quadrant photodiode
Vibration isolation	Low and high frequencies isolation	- High frequencies: vertical stacked rings (small aluminum cylinders) spaced each other by Viton bearings - Low frequencies: a slap of granite and elastomers
Control interface	Dulcinea electronic control unit of Nanotec Electronica Co.	- Digital Signal Processor (DSP) card monitored by the WSxM software

Table 2.2 Operative parameters of AFM.

Thus, the tip taps the surface and experiences the full variation of the tip-sample interaction potential. The repulsive forces during intermittent contact decrease the

R.M.S oscillation amplitude, which yields a highly surface-sensitive signal that can be used as feedback. Table 2.2 summarizes specific features of AFM set-up used in this work.

AFM measurements were performed at the ICMM-CSIC by using Nanotec Electrónica equipment [12] (Figure 2.5). This microscope operates with a Dulcinea electronic control unit and the WSxM interface (windows scanning microscope, where "x" refers to force, tunneling, near optical microscopy), which is used also for data acquisition and occasional processing [37]. Once the tip was manually positioned, the fine approach towards the sample was carried out automatically by a variable-speed steeper motor. All measurements were carry out at RT (293 K), which implies a low thermal noise contribution (i.e. thermal drift of the cantilever) to the AFM vertical resolution, as $z = \sqrt{4k_B T / 3k} = 0.074nm / \sqrt{k} = 0.01nm$ (for cantilevers with spring constant of $k = 40$ N/m). The cantilever was heated by the He:Ne laser during several hours prior to measure, in order to avoid thermal drift in a humidity-controlled atmosphere.

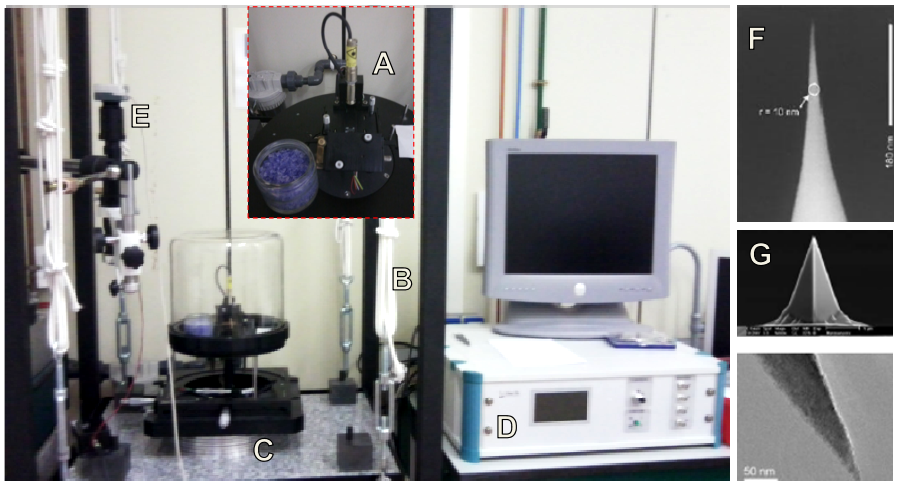

Figure 2.5 AFM equipment at ICMM-CSIC. (A) AFM head. (B and C) Mechanical noise-reduction system comprising several kinds of elastic strings. (D) Electronic interface to manipulate the feedback system and data acquisition. Several features of the tips used: (F) super-sharp silicon tips of radius=2 nm and (G-H) standard silicon tip of radius=10 nm (SEM images with different magnifications)

In room conditions with ambient humidity, a thin film of water can be absorbed on hydrophilic surfaces and therefore, close to the surface, a liquid bridge could be formed between tip and sample causing the rising of attractive forces of capillary. In order to

[12] The equipment used in this work is an AFM Cervantes Full Mode developed by Nanotec Electronica® (www.nanotec.es)

control the humidity, a crucible with desiccant agents like silica gel was placed in the closed system during measurements. Ultra-sharp silicon tips with radius of 2 nm and aspect-ratio as high as 1:10 was used in order to reduce potentials effects of tip convolution as will be discussed in §2.3.

2.3 Scanning tunneling microscopy (STM)

In STM, a fine metal tip is placed a few angstroms away from the surface of a conducting sample, so that the application of a small voltage U_t (or bias) generated a net tunneling current I_t (Figure 2.6a). This current results from the classically forbidden tunnelling of electrons close to the Fermi level of the sample (once defined its local density of states, LDOS) to unoccupied states in the tip (or viceversa, depending on the bias polarity). Such I_t current flows through the potential energy barrier of width Δ (tip-sample separation) and height Φ_w (the average work function of the electrodes), as sketched in Figure 2.6(b). The resulting I_t depends exponentially on Δ and thus it is very sensitive to changes in the tip-sample separation, as described in Table 2.3. Usually a current feedback is used to keep I_t at a constant value of a few nA (topography mode) while the tip scans the sample surface. Thus, the feedback voltages $U_{feedback}$ supplied to the piezoelectric elements to keep I_t to a constant value for each surface site are used to build the corresponding topographic map (Figure 2.6a). Table 2.3 summarizes the specific features of STM set-up used in this work. The STM measurements were carried out with a STM head Hitachi V-3000 coupled to a scanning electron microscope (SEM) Hitachi S-2700 (described in §2.4), as displayed in Figure 2.7(a). Measurements were performed in high vacuum (base pressure $<10^{-6}$ mbar) to improve the tip-sample interactions.

As shown in the inset of Figure 2.7(a), the STM head was tilted 45º with respect to the SEM electron gun and electrically isolated piezoelectric elements for STM approaching were used to make available simultaneous STM-SEM measurements. Polycrystalline Tungsten STM tips were prepared by using the DC-etched method from a W wire of 0.8 mm of diameter. Such a wire is introduced into an electrochemical bath at room temperature, in which acts as the anode, whereas a stainless steel rod is used as the cathode. Such rod has a ring-like shape, so that a layer of the electrolytic solution (KOH 6M in water, pH = 13) is developed inside the ring by hydrophilicity (Figure 2.8b).

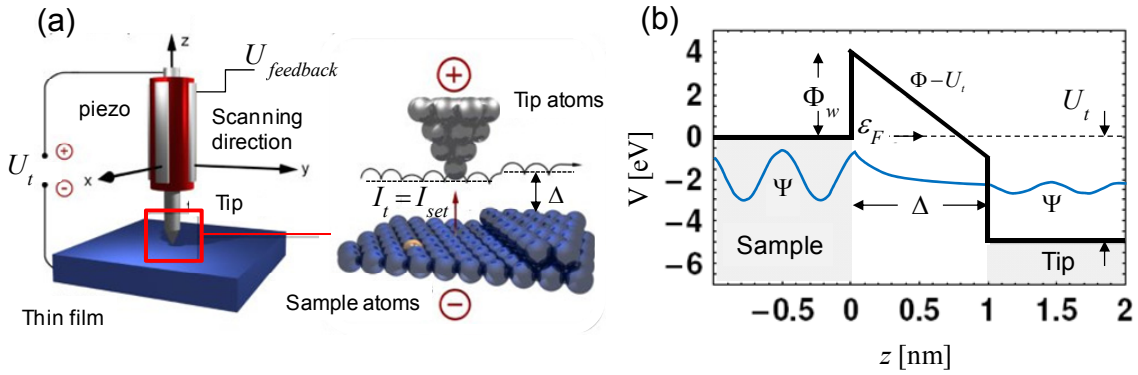

Figure 2.6 (a) STM basic principles. (b) Schematic diagram of a one-dimensional potential energy landscape, for an electron with a Ψ wavefunction in a tunnel contact between two metal electrodes separated by an insulator. In the scheme, Φ is the height barrier associated with a tunneling process between metals separated by a Δ=1-nm thick insulator (vacuum) for an applied bias of $U_t = 5$V. z denotes the tip height position.

The following chemical reactions take place [41] at:

$$\text{cathode: } 6H_2O + 6e^- \rightarrow 3H_{2(g)} + 6OH^-$$

$$\text{anode: } \frac{W_{(s)} + 8OH^- \rightarrow WO_4^{2-} + 4H_2O + 6e^-}{W_{(s)} + 2OH^- + 2H_2O \rightarrow WO_4^{2-} + 3H_{2(g)}}$$

The etching takes place at the air/electrolyte interface, and as one can learn from the reaction in the anode, the tungsten undergoes an oxidative dissolution to tungstate anions (WO_4^{2-}), which are soluble in water. However, the actual reaction is more complex than it appears: the tungsten is first oxidized to intermediate tungsten oxides; these are in turn non-electrochemically dissolved to yield these soluble tungstate anions which show greatest stability in a basic medium. The reaction also involves the reduction of water; bubbles of gaseous hydrogen and OH− ions are thus produced at the cathode. One can wonder how this reaction actually generates a tip shape out of a cylindrical wire. The explanation roots in the fact that capillary forces yield the formation of a meniscus of solution around the tip wire when it is immersed into the electrolyte. The shape of the meniscus plays a very important role in determining the final shape of the tip as the etching rate at the top of the meniscus is a lot slower than at the bottom. This can be explained by the presence of a concentration gradient due to the diffusion of OH− ions to the tip. Furthermore, the soluble tungstate produced during the reaction flows towards the lower end of the tip wire, generating a dense viscous layer which prevents this region from being etched away. Thus, a necking phenomenon is

observed in the meniscus where the etching rate is enhanced. At some point, this part of the wire becomes so thin its tensile strength cannot sustain the weight of the lower end of the wire; the latter breaks off and a sharp tip is left behind. This is commonly referred to as the "drop-off" method, and it is illustrated in Figure 2.7(b), upper schemes. During etching the current flowing through the cell decreases linearly with etching time because the cross-section of the anode (wire) decreases. The wire eventually breaks at a neck that is formed during etching, since the rate is enhanced in a region just below the KOH surface. In our cell, the ∅=10mm wires break after 100 min, and the current quickly fell below a pre-set limit, below which the supply is automatically cut off (Figure 2.7b).

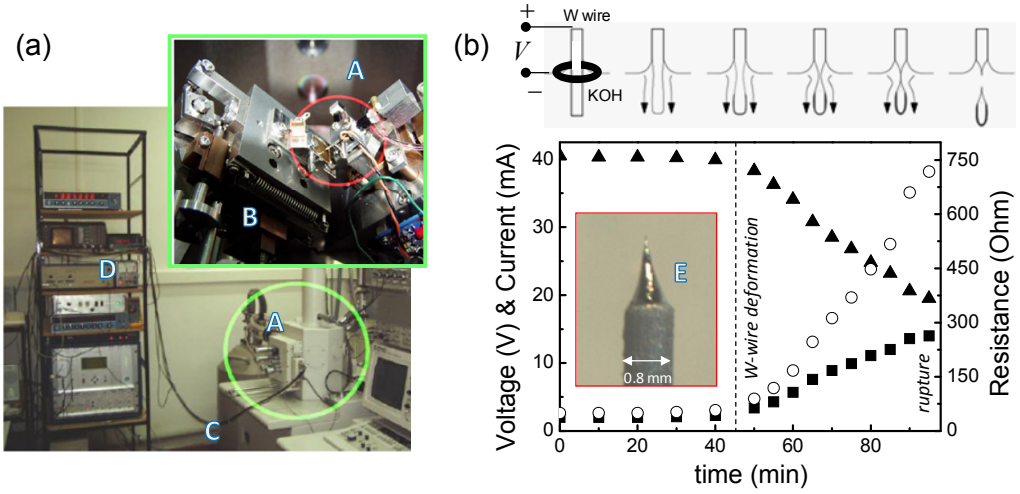

Figure 2.7 (a) SEM-assisted STM equipment at ICMM-CSIC: (A) STM head. (B and C) Mechanical noise-reduction system. (D) Electronic interface to manipulate the feedback system and data acquisition. (E) W-tips of radius <10 nm. (b) Evolution of the resistance (open circles), DC voltage (■) and current (▲) during the W-tip preparation by electrochemical etching. The upper scheme shows the drop-off method.

STM feature	Description	Instrumentation
Working principle	Tunnel effect	$I_t \propto \exp[-\Delta]$
STM Mode	Constant current (topographic mode)	- Variations in the local height of the surface produce variations in the tunnel current due to the tip-sample distance dependence. These variations are compensated by a feedback that modifies the tip-sample distance. - Tunnel current setpoint around 0.5 nA - Bias voltage around 50mV- Scanning frequency 0.2 kHz (fast axis)
Image resolution	Number of image pixels in the digital matrix and size	- Image of 512x512 of a surface area up to 1x1 μm^2

Scanner system and approaching	Sectorized piezoelectric bar	- Piezoelectric are protected with a electronic isolate coating - x,y,z scan sensibilities of 90,90,30 nm/V respectively - Approaching by piezoelectric bar system
External conditions	Temperature, pressure	- 293 K (RT), High vacuum (<10^{-6} mbar)
Vibration isolation	Low and high frequencies isolation	- High frequencies: vertical stacked rings (small aluminum cylinders) spaced each other by Viton bearings - Low frequencies: pneumatic flanges
Control interface	Dulcinea electronic control unit of Nanotec Electronica Co.	- DSP card monitored by the WSxM software

Table 2.3 Operative parameters of STM.

Several aspects to keep in mind to interpret appropriately the SPM (i.e., STM and AFM) images at mesoscopic scale (of around 1×1 μm^2) are:

Effect of the pixel size: as the size of the surface entities increases, it becomes necessary to increase also the size of the SPM images in order to have a representative statistics of the film surface morphology. However, the resolution of the AFM technique [equal to the pixel size $\Delta_{pixel} = L \times L/\Pi$, with $L \times L$ being the image area and Π, the number of image pixels (image resolution)] decrease as the image size does (if there is a limit in Π). In our experiments, Π =512×512 píxels was employed for all the images sizes, ranging from 100 nm - 5 μm of length, which means that for images of 1x1 μm^2 surface areas, the best lateral resolution achieved with the AFM is $\Delta_{pixel} \approx 2$ nm (that corresponds to ≈50 absorption sites on a flat (111)-fcc surface).

Tip radius effect: The tip (whose profile is idealized as a conical form ended in a semi-sphere of radius R) convolves the real shapes of the surface entities (Figure 2.8) [39]. The degree of convolution depends mainly on the ratio between the surface angles (also described as surface slopes) and the aperture angle of the tip. To reduce this spurious effect, both the radius and tip aperture angle must be as small as possible such that the tip aspect-ratio is higher than the average aspect ratio of the surface entities to examine [42]. The effect of convolution can be observed in Figure 2.8, where tips of different radius were used to image the morphology of Au grains. As the tip radius is higher, the grains seem to be broader. Even for STM, in which the tunnel current between the tip apex and the sample enables atomic resolution for rough (vicinal and coarse-grained) surfaces, wide tips induce convolution effects as a consequence of that tunnel current occurs also along the tip flanks. In general, for the experiments described along this

work, high aspect-ratio tips (at least higher than that of the imaged surface entities) were used to reduce accordingly the tip effects on the surface statistics. Also, slow scanning frequencies (0.1–0.5 Hz) and moderate image sizes (300 nm–2 μm) were used to avoid non-linear responses of the piezoelectric scanners.

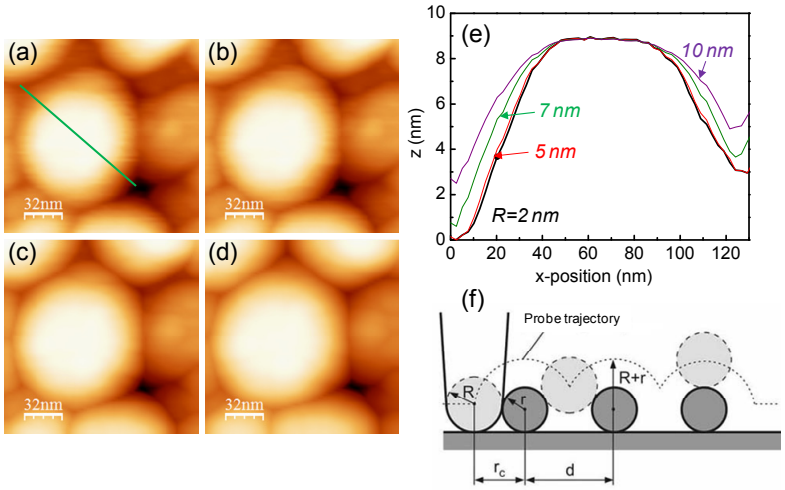

Figure 2.8 SPM tip convolution effect. (a-d) AFM images of an Au film taken with tips of different radius. (e) Profiles taken along the line showed in (a) for all the images. Tip convolution is appreciable for radius higher than 5 nm. The vertical scale is 9 nm. (f) Sketch showing the tip convolution effect, in which *R*, *r* and r_c are the tip, entity and contact radius, respectively, and d the entity spacing.

2.4 Scanning electron microscopy

In Scanning Electron Microscopy (SEM), an electron beam is emitted from a filament cathode and then collimated. Such an electron beam is focused by a condenser lense system into a spot of about 0.4–5.0 mm of diameter on the sample surface. The beam passes through pairs of scanning coils (or deflector plates), which deflect the beam in the *x* and *y* axes so that it scans in a raster manner over a rectangular area of the sample surface (Figure 2.9) [43]. Electrons scatter both elastically and inelastically with the material within the interaction volume of 10 Å – 4 μm in depth (in dependence on the acceleration voltage) and different kinds of signal result from electron scattering, among them backscattered electrons, secondary electrons, Auger electrons, X-ray… (Figures 2.9a and 2.9c).

The current of secondary electrons detected by the collectors varies in dependence of both the chemical composition of the sample and the surface topography irregularities, such that it provides direct information of the chemical nature and the surface morphology. Table 2.4 summarizes relevant information of the SEM measuring

parameters. In this study, we used two SEM equipments: a Hitachi S-2700 (thermoionic emission) and a Jeol JSM-6500 (field emission) both located at the Materials Science Institute of Madrid (Fig. 2.9c). This technique was used to acquire top-view and cross-section images of the films (the latter in fractured samples), which provide us complementary information concerning morphology and film microstructure.

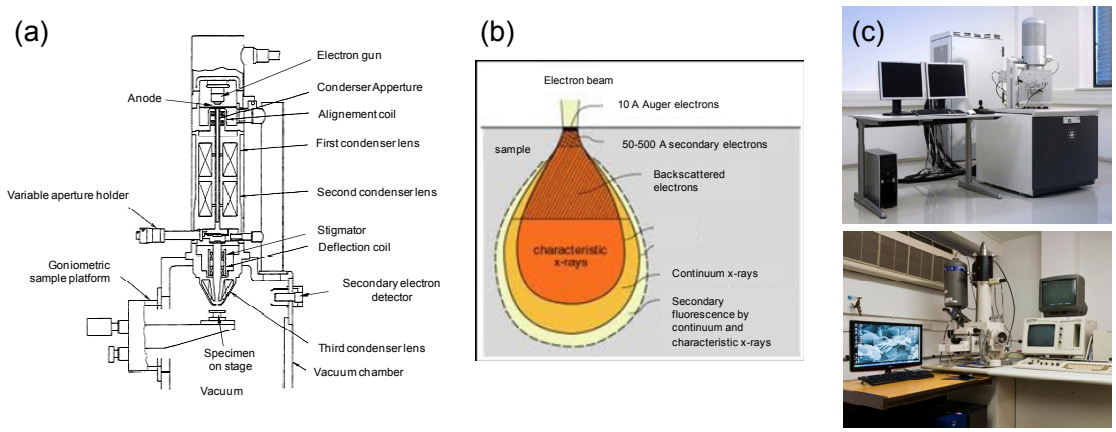

Figure 2.9 SEM basics. (a) Schematic sketch of the principle of SEM operation, showing a cross-section view of the e-beam-film interaction volume (the depth dependence of the emitted secondary electrons). (b) Scheme of a Hitachi S-2700. (c) NANOSEM 230 FEI field emission (upper) and Hitachi S-2700 (lower) microscopes used along this work.

Scanning electron parameters	Range of variation
Signal precedence	- Backscattered, Secondary electrons < 50eV, and Auger electrons, lattice vibrations (inelastic sample-*e* interactions)
Accelerating voltage	- 0.2 – 30 keV
Filament emission current	- 300 μA
Nominal lateral resolution	- 4 nm (20 nm por practical purposes)
Maximum image size	- 100 mm
Image resolution	- Max 512 x 512 pixels
Detectors	- Low-voltage high-contrast backscattered electron detector (vCD) and Secondary electron detector (SeD)
Emission cathode	- Tungsten (thermoionic emission), or LaB6 (Field Emission)

Table 2.4 Operative parameters of SEM.

However, for ductile materials like Au considerable plastic deformations of the kind of stretching and thinning were observed after fracture-by-traction procedures (Figure

2.10a) [44, 45], and the film microstructure is distorted within regions under deformation. Exploiting the fact that we have a columnar-like microstructure instead of a laminar one (which has a soft axe in the plane of the film), we overcome the disadvantage of film distortion by scratching intentionally the film with STM W tips (applying a shear load), and then observing the cross-section profile on the crest of the folds where the film breaks "occasionally" without apparent plastic deformation, as shown in Figs. 2.10(b) and 2.10(c).

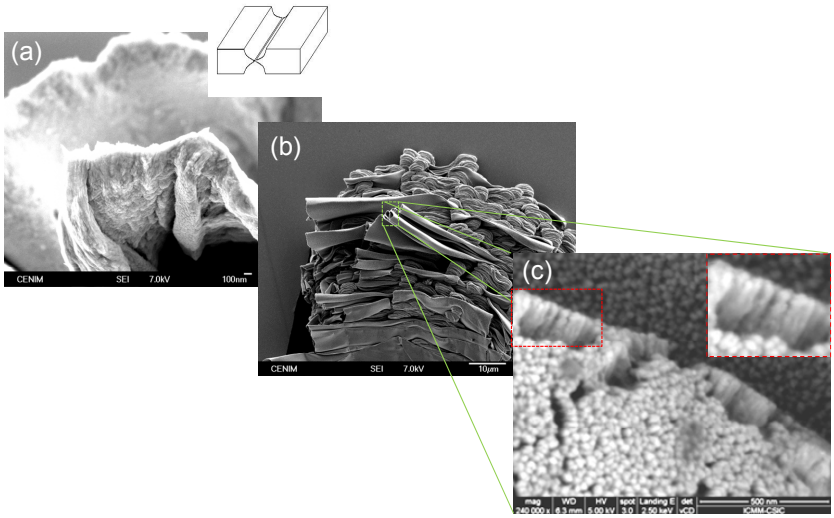

Figure 2.10(a) Au/Si(111) SEM cross-section image showing a typical stretching/thinning deformations (sketched in the insets) of the film during fracture. (b) Scratches developed on the film surface with STM tips applying a shear load. (c) Thus-obtained folds whose crests maintain the microstructure almost intact where a clear columnar microstructure is disclosed.

2.5 X-ray diffraction (XRD)

X-ray diffraction (XRD) was used to determine the crystal structure of films, textures, lattice parameters, crystalline domain sizes and chemical composition [46]. In XRD, a monochromatic beam of x-ray radiation, with wavelengths $\lambda_{x\text{-}ray}$ ranging from 0.01 to 10 nm (fitting the interatomic distances d_{hkl} in crystals and molecules, ranging 0.15–0.4 nm), scatters both elastically an inelastically[13] on the sample. For crystal structure analysis elastic scattering is the relevant phenomenon to be investigated [46, 47]. In the elastic scattering the conservation of the momentum of photons and the lattice vector of the crystal planes that diffract is accomplished. When X-rays scatters with a group of

[13] Inelastic scattering promotes photoionization and Compton scattering. Only it is the Thompson component in the scattering x-rays that is made use of in structural investigations by XRD [M. Birkholz, "*Thin Film Analysis by X-Ray Scattering*" pages 1-2].

atoms that are arranged in a periodically ordered array like a crystal lattice (Figure 2.11a), such interaction generates a diffraction (or interference) pattern, the crystal acting as a diffraction grating. A regular array of scatter atoms produces a regular array of spherical waves that, although they cancel one another out in most directions through destructive interference, they add constructively in a few specific directions, determined by Bragg's law (Equation. 2.1a). Then, maxima of intensity $\mathrm{Max}[I(\vec{r})]$ (with $\vec{r}$ a vector position) will be observed due to constructive interference. The position of such peaks in the space of interferences is described by the Bragg's law (Figure 2.11b):

$$2d_{hkl}\sin(\theta) = n\lambda_{x-ray} \qquad (2.1a),$$

where d_{hkl} is the interplanar spacing, i.e. the distance between planes of a same family with Miller indexes (h,k,l), n is the interference order, and θ is the Bragg angle. For cubic-symmetry crystals like those here analyzed, $d_{hkl} = a/\sqrt{h^2+k^2+l^2}$ (Figure 2.12b).

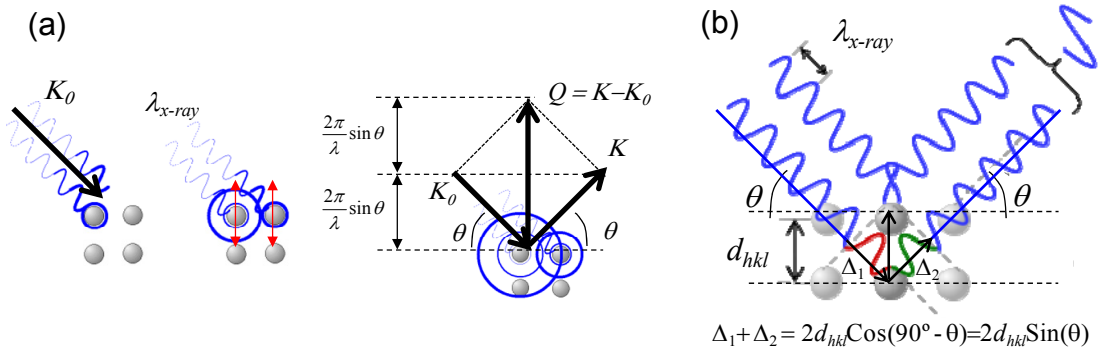

Figure 2.11 Basic principles of XRD. (a) Sketch of the elastic interaction between the x-ray beam and atoms in a crystal (left) and vector representation of the scattering vector (right). (b) Bragg's law. Δ_1 and Δ_2 are phase shifts due to the optical path difference.

2.5.1 θ-2θ scans

In the analysis of the crystal structure of materials by XRD, the objective is to measure Bragg's reflections, i.e. their angular position, peak shape and intensity in order to derive microstructural information from them. One way to achieve that is by θ-2θ scans, whose working principle is depicted in Figure 2.12(a).

The sample is positioned in the center of the instrument, the probing x-ray beam is directed to the sample at an angle θ with respect to the sample surface, and the detector monitors the scattered radiation at 2θ with respect to the incidence direction in the plane defined by K_0 and K. During the scan both the incidence and detection angles of x-ray beam are continuously varied keeping the ratio $\theta/2\theta$ constant. This geometry imposes the constriction that the Bragg law is satisfied only for the planes with the lattice vector $Q = K - K_0$ being directed along the out-of-the film plane direction (Figures 2.12b to 2.12c).

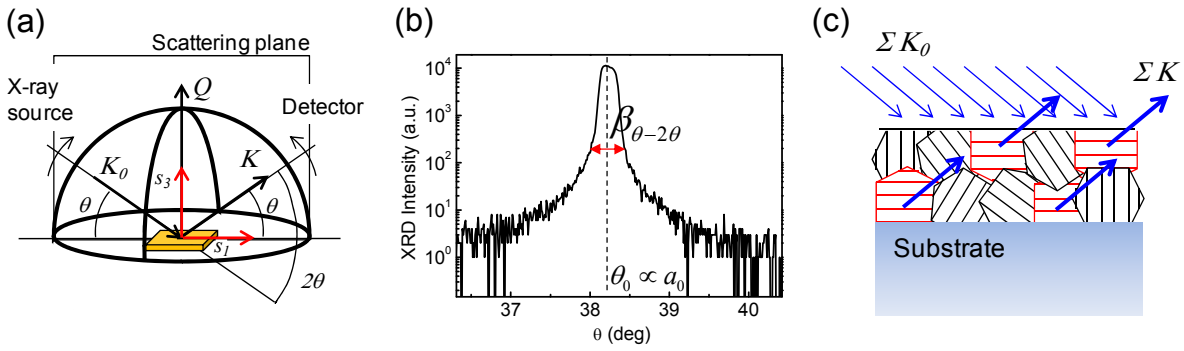

Figure 2.12 *θ-2θ* scans. (a) Scheme representation of a *θ-2θ* scan. (b) *θ/2θ* scan around an Au(111) peak. (c) Selection principle for exclusive measurement of surface-parallel lattice planes in a *θ/2θ* scan on a polycrystalline films, which enable the determination of the grain size (b) of the mean size population.

For polycrystalline films like those investigated in this work, the distribution of the crystal orientation of grains certain crystallographic direction [*hkl*] was found to be preferentially oriented with respect to the sample reference frame. This anisotropy in the crystal orientation of grains/crystallites is termed "texture". This effect may easily be recognized in symmetric θ-2θ diffraction patterns and rocking curves, by a pronounced enhancement of certain Bragg reflections when compared with a powder spectrum, as summarized in Table 2.5 where the θ-2θ XRD configuration is outlined.

Besides, θ-2θ scans are commonly used for investigation of polycrystals, because it enables to determine the average out-of-plane crystallite size $\lambda_\perp$ by Scherrer's formalism, inspecting the width of the peaks in the spectra (Fig.2.12b):

$$\lambda_\perp = \frac{0.94\lambda_{x-ray}}{\beta_{\theta-2\theta}\cos(\theta)} \qquad (2.1b),$$

X-ray feature	Range of variation	Description
Geometry configuration	Bragg-Brentano Four circle goniometer	- Bragg's law: $2d_{hkl}\sin\theta = n\lambda_{xray}$, with $d_{hkl} = a/\sqrt{h^2+k^2+l^2}$ -cubic symmetry
Wavelength	1.54056 Å	- CuKα line (Kα1)
Detector	LinxEye and Scintillator	- Sensibility up to 0.01 deg
Source	CuKα filament	- Fixed - Acceleration voltage = 40 kV - Electron current = 30mA
Scan modes	$\theta/2\theta$ ϕ-scan ψ-scan	- Out-of-plane texture (angular displacement from 0 –π) - In-plane texture (angular displacement from 0 – 2π) - Dispersion in 2θ of a plane family (angular displacement from 0 –π/2)

Table 2.5 Operative parameters of XRD.

Where 0.94 is the Scherrer constant for crystals with cubic symmetry, and $\beta_{\theta\text{-}2\theta}$ is the full-with-at-half-maximum of the given peak in the θ-2θ scan. Also, because peaks in such scans correspond to lattice parameters by the Bragg's law (Equation 2.1a), scans enable a rough estimation of the strains ε (small displacements of atoms in the crystal lattice), by using the Hooke's law:

$$\sigma = M\varepsilon = M\frac{a-a_0}{a_0} \qquad (2.1c),$$

where M is the biaxial modulus of stress and a_0 the unstrained lattice parameter.

However, the determination of the residual stress by Equation 2.1c results in an inexact method, reason why more sophisticated X-ray stress analyses must be achieved, as will be discussed below.

2.5.2 Azimuthal ϕ-scans

In a conventional θ-2θ scan the lattice planes contributing to a Bragg reflection are all oriented (near-) parallel to the film surface (Figure 2.12c). Thus, only a subset of grains is monitored, for which the plane normal lies in a cone of a miscut angle (which is estimated by rocking curve) around the substrate normal. If the orientation distribution is required, however, the reflections of all grains in the sample must be recorded. This is performed by scanning selected reflections under various orientations, which is accounted by the azimuthal ϕ and the tilt angle ψ. The geometry of the experimental set-up is shown in Figure 2.13(a). The angle of rotation ϕ measures the azimuth of the

sample in the surface plane, whereas the tilt angle ψ quantifies the amount of tilting of the sample normal with respect to the scattering vector. Such scans enable us to measure the in-plane texture of the film, by inspecting azimuthal (in-plane) grain orientations [46]. Figure 2.13(b) shows a ϕ-scan taken from an Au(111) film, showing a considerable degree of in-plane texture.

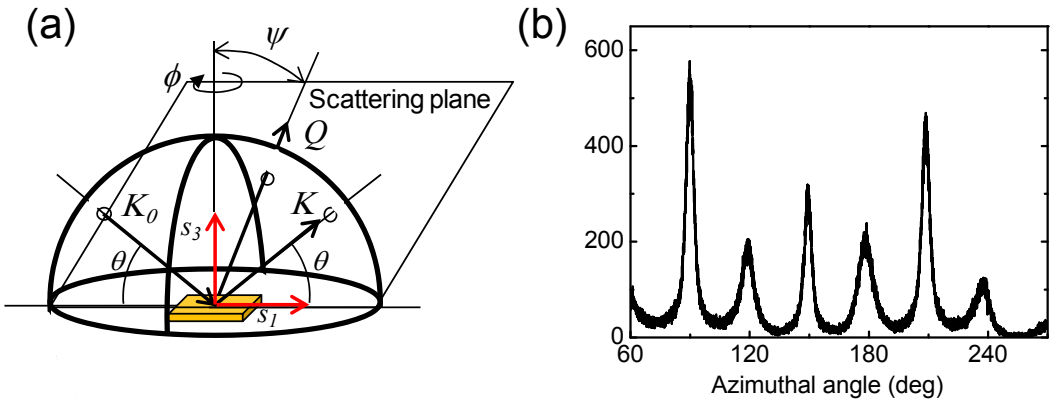

Figure 2.13 ϕ and ψ scans. (a) Schematic representation of a ϕ and ψ scan configurations. (b) ϕ-scan measured around an Au(420) peak.

2.5.3 X-ray stress analysis

XRD is also useful to determine strains caused by mechanical stresses in thin films by using the x-ray stress analysis (XSA). Strains in solid films can be a consequence of lattice mismatch between substrate and sample, thermal expansion, external forces or internal defects, it being then a powerful tool to disclose processes during growth and annealing. As observed in Figure 2.14(a) when a film fixed to a massive substrate supports an average load (external or internal) it shrinks or elongates, in dependence of the type of load (stress) σ: compressive ($\sigma < 0$, contraction) or tensile ($\sigma > 0$, elongation); which cause a film-substrate system deflection. As mentioned previously, in order to determine how much a film is elastically deformed, we can estimate the strain $\varepsilon = (a - a_0) / a_0$ by θ-2θ scan [46]. By using a modified Hooke's law taking into account for shear stress contribution with the tilt angle to the strain, this can be determined (Figure 2.14b) as:

$$\varepsilon_{\psi} = \left(\frac{1+\nu}{E}\right)\sigma_{\parallel}\sin^2\psi - \frac{2\nu}{E} \qquad (2.1\text{d}),$$

As observed from the 422 reflection from XSA investigation of a TiN film, the Bragg peaks exhibit a pronounced shift down to higher 2θ as the tilt ψ increases in both directions. The slope of the d_{hkl} – $\sin^2\psi$ provides an accurate estimation of the strain in the solid films [46].

Table 2.5 briefly summarizes some basic XRD features. We used the conventional Bragg-Brentano geometry configuration, as sketched in Figure 2.15.

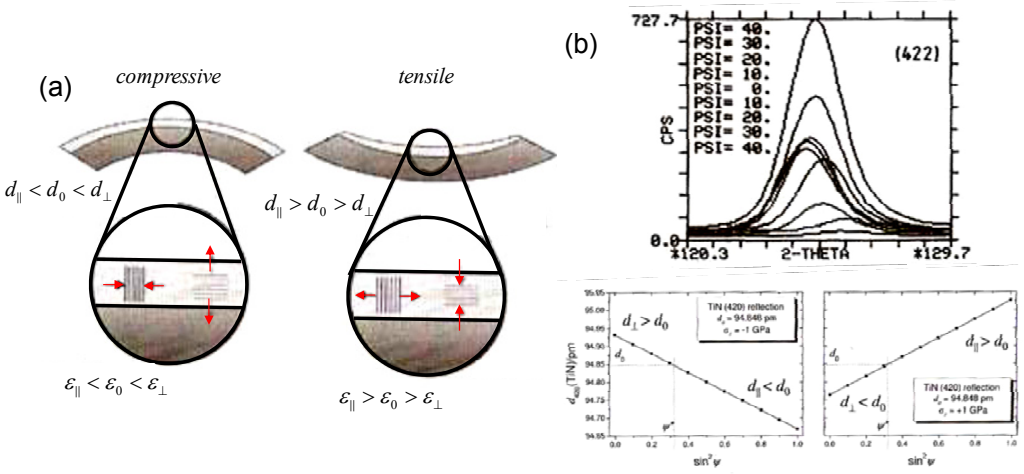

Figure 2.14 (a) Typically bended film-substrate system under compressive (left) and tensile (right) stress in the film plane (magnified deformation). (b) Working principles of XSA for a 422 reflection of a TiN film deposited on stainless steel. Peak shifts for various tilts ψ in accordance to the strain to what lattice planes are subjected. (c) Simulations of the ψ-dependence of d_{hkl} in thin TiN film under compression (left) and tensile (right) stress. Taken from M.Birkholz, "*Thin Film Analysis by X-Ray Scattering*" Wiley-VCH Verlag GmbH & Co. KGaA, Great Britain, 2006 (Pages 245-247).

Using different XRD scan types, we are able to characterize the degree of crystallinity (crystal quality) along the in-plane and out-of-plane directions of the film (i.e., texture analyses). For conducting such experiments, a four-circle diffractometer has to be used. Figure 2.15 provides scheme and picture of a D8 Bruker-AXS four-circle diffractometer at the Materials Science Institute of Madrid, which was used in the measurement conditions summarized in Table 2.5.

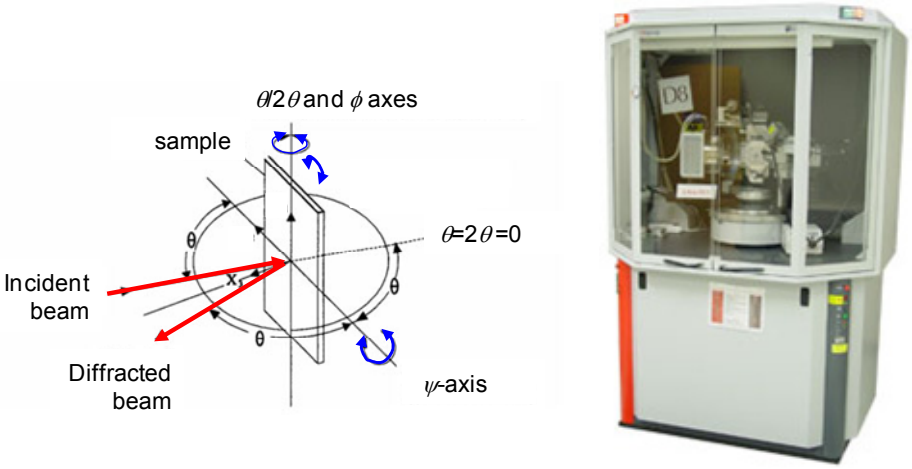

Figure 2.15 Scheme of x-ray diffraction fundaments. Bragg-Brentano geometry and a picture of the D8 Bruker AXS x-ray diffractometer used in this work.

2.6 Image Processing: Quantitative description of the morphology of a film by statistical procedures

In order to approach the morphology evolution of a thin film (which is realized as the time-dependence of its growth front in close connection with the operative atomistic mechanisms during deposition), several statistical functions and image-processing algorithms are used. Such procedures allow us to obtain the shape parameters (as defined below) that characterize to the morphologies under investigation.

2.6.1 Discrete procedures

The film topography imaged by AFM correspond to square matrices of $\Pi=N\times N$ discrete elements (pixels) whose values corresponds the local heights $h_{\vec{r}}$ of the surface averaged over areas Δ^2_{pixel} that are located at $\vec{r}=(n_1\Delta)\vec{v}_1+\ldots+(n_D\Delta)\vec{v}_D=r_{n_1,\ldots,n_D}$ (where $\{\vec{v}_i\}$ with $i = 1\ldots D$ denotes a set of orthogonal unitary vectors that describes the pixel position in a D-dimensional system). The fact that $h_{\vec{r}}(t)$ depends on the time within the timescale of film deposition and annealing defines the growth kinetics of the film, and therefore $h_{\vec{r}}(t)$ is considered as a "growth front" rather that steady surface. Relevant statistical and shape parameters are sketched in Figure 2.16. Among them, we have [4]:

- ***The average height***, $\bar{h}(t)=\langle h_{\vec{r}}(t)\rangle=\frac{1}{N^2}\sum_{i,j}^{N,N}h_{i,j}(t)$, where $\langle\ldots\rangle=\frac{1}{N^2}\sum_{i,j}^{N,N}\ldots$ denotes the space average
- ***The interface width*** or ***surface roughness***, usually defined as the root-mean-square deviation of $h_{\vec{r}}(t)$ population for a given *t*: $w(t)=\sqrt{\frac{1}{N^2}\sum_{i,j}^{N,N}\left(h_{i,j}(t)-\bar{h}(t)\right)^2}$
- ***The surface correlation length*** $\lambda(t)$, that determines how far is the correlation between neighboring surface sites with λ being the correlation cut-off; and so $\langle h_r(t)h_{r+l}(t)\rangle=0$ only for $l\geq\lambda$. In grained morphologies, $\lambda(t)$ is ascribed to the (*lateral) size* of the surface structures, and thus for a compact population (without voids in between) of N' structures with a density $\rho=N'/L\times L$, $\bar{\lambda}=\sqrt{1/\rho}$

To determine these magnitudes, statistical functions are commonly employed [4, 44, 48] among them: (*i*) the Fast Fourier Transform X(*k*,*t*), (*ii*) the Power Spectral Density (PSD), and (*iii*) Height-to-Height Correlation Function $G(\lambda,t)$. The typical features of these functions are summarized in Table 2.6, which outlines (by column sort): the name of the statistical function to use, its analytical expression, and its range of application, providing a brief comment on its utility.

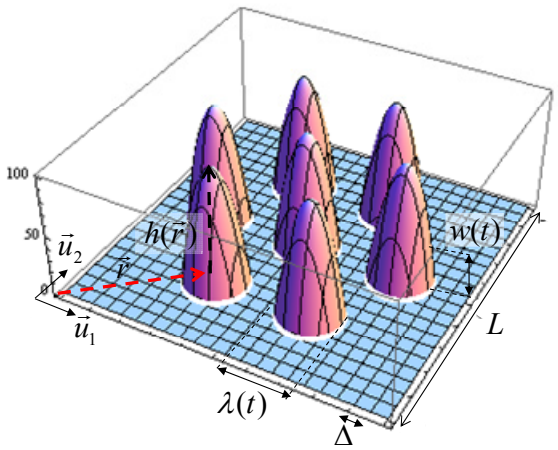

Figure 2.16 Model surface in which several statistical magnitudes are sketched.

Because mesoscopic models based on Langevin-type and continuity equations predicts the mass transport as a function of gradients and curvatures of the surface potentials, it is required to employ continuum functions of the surface morphology.

Statistical function	Formulation	Processing results	Provided data
***Fast Fourier transform* (FFT)**	$\mathrm{X}(k,t) = \left(\frac{\Delta}{2\pi}\right)^{D} \sum_{n,m,\ldots}^{L/\Delta} h(t)_{\vec{r}_{n,m,\ldots}} \exp[-i(n\Delta \cdot k_x + m\Delta \cdot k_y + \ldots)]$ $k = 2\pi / L \Rightarrow$ $\vec{k} \approx k_{n_1,\ldots,n_D} = \frac{2\pi}{n_1\Delta}\vec{v}_1 + \ldots + \frac{2\pi}{n_D\Delta}\vec{v}_D$ Allows to express a function $h(r_{x,y,\ldots},t)$ in the direct space (e.g.) into a function $\mathrm{X}(k,t)$ in the reciprocal space. The separation between zeros and/or minima of the FFT in a map modulus of $\sqrt{\mathrm{X}\cdot\mathrm{X}^*}$ corresponds to $2\pi/\lambda$, which allows to determinate of the size of the surface structures	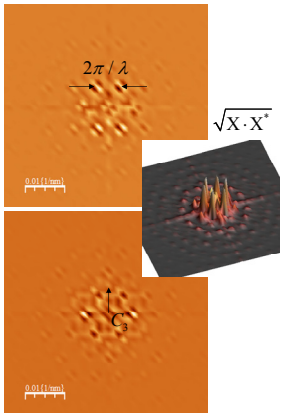	Size of the structure (corresponding to spacing of function zeros) and surface symmetry
***Power spectral density* (PSD)**	$PSD(k,t) = \left(\frac{2\pi}{L}\right)^{D} \left(\mathrm{X}\cdot\mathrm{X}^*\right)$ $PSD_{iso}(k,t) = \left(\frac{2\pi}{L}\right)^{D} \left\langle \mathrm{X}\cdot\mathrm{X}^* \right\rangle_{\left\|\vec{k}\right\|=constant}$ Allows using the *Fourier transform* to compute spatial-resolved surface roughness. It means that different contribution to w can be spatially decomposed by range of correlation length of surface entities, as: $w^2_{total} = w^2_{\Delta\to\lambda} + w^2_{\lambda\to L}$	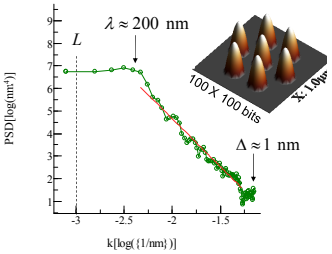	Size of the structure, determined by changes of the slope in the $PSD_{iso}(k, t)$ dependence (see Figure at the left)
Height-to-height correlation function $G(l,t)$	$G(l,t) = \left(\frac{\Delta}{L}\right)^{D} \sum_{x,y,\ldots}^{L/D} \left(\left(h_{r_{x,y,\ldots}+l_{x,y,\ldots}}(t) - \bar{h}(t)\right)\left(h_{r_{x,y,\ldots}}(t) - \bar{h}(t)\right)\right)$ Allows to determine the lateral size of surface structures as the FWHM of central peak that results from the shifting of the $h(\vec{r},t)$ function a distance $\vec{l} = \left(m_1\Delta\right)\vec{v}_1 + \ldots + \left(m_D\Delta\right)\vec{v}_D = l_{m_1,\ldots,m_D}$ The spatial distribution of the patterns of $G(l,t)$ allows us to realize the in-plane order of the surface structures	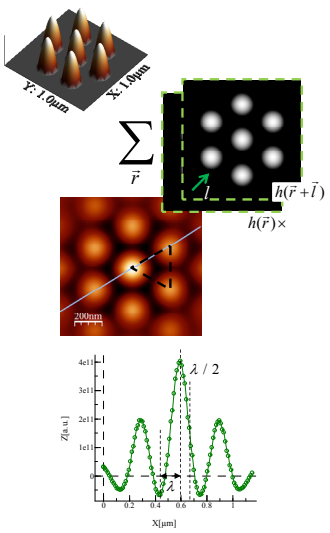	Size of the structure (determined by the full width at half central maxima) and surface symmetry

Table 2.6 Classical statistical functions commonly used to determine shape parameters. The statistical functions were probed by using an artificial surface generated by $f(\vec{r},t) = \mathrm{UnitStep}[-r^2 + z](-r^2 + z)$ and $h(\vec{r},t) = f(\vec{r}_0,t) + \sum_{i=1}^{6} f(\vec{r} - (r_x\cos[i\pi/3], r_y\sin[i\pi/3]), t)]$, which is plotted in Fig. 2.17

2.6.2 Continuum (interpolating-based) procedures

Instead of using discrete functions of the surface, we can choose to replace them by interpolating (continuum) ones by using an interpolation procedure. The interpolating function represents a "mold" of the raw (discrete) data that also make easy the development of several image processing procedures like tessellation and the determination of the local in-plane texture of the surface (the azimuthal distribution of the local slopes) [48-52]. The continuous surface methods employed along this work are based on Lagrange's interpolation algorithms [53, 54]. In such algorithms, the discrete matrix of image pixels obtained from AFM measurements $h_{\vec{r}}$ is transformed into a continuum function $h(\vec{r})$, with a four derivative in the whole domain. Once the $h(\vec{r})$ function is obtained and accurately tested, it can be used to carry out several spatially resolved analyses, among them: (*i*) the determination of local slope maps and therefore the construction of slope distributions, (*ii*) the determination of the local in-plane texture and (*iii*) image segmentation (or tessellation). The image interpolation process was achieved by using the Lagrange's interpolation formalism based on successive fitting to p^{th}-order polynomial functions as described below:

$$h(\vec{r}) = \sum_{\vec{r}_o}^{\vec{r}_{L\times L}} \sum_{i=0}^{p} L_i(\vec{r}) \cdot h_{\vec{r}_i} \qquad (2.2a),$$

with

$$L_i(\vec{r}) = \prod_{\substack{j=0 \\ j\neq i}}^{p} \frac{\vec{r} - \vec{r}_j}{\vec{r}_i - \vec{r}_j} \qquad (2.2b),$$

where $\vec{r}_i - \vec{r}_j$ is the distance between successive pixels and p the polynomial order that coincides with the highest no-null space derivative, i.e., $\nabla^p h(\vec{r})$. Thus, the chosen p values depend on the specific morphology features (how sharp it is), the density of image pixels (how many points are interpolated) and the kind of analysis to perform (namely, ∇ slope, ∇^2 saddle points for tessellation and surface curvature, and ∇^4 likes input data for simulations of surface relaxation by Mullin´s-type diffusion). Cubic and higher order $p \geq 3$, were usually employed to assure the following conditions: (*i*) continuity in $h(\vec{r})$ and $\nabla^2 h(\vec{r})$, and (*ii*) the best fitting function taking into account the

tip-convolution effects in the raw AFM images. Under these conditions, minimum deviations estimated as $\varepsilon_{\vec{r}} = \sqrt{(h_{\vec{r}} - h(\vec{r}))^2}$ of the polynomial function $h(\vec{r})$ to the raw data $h_{\vec{r}}$ were attained during the interpolation. $\varepsilon_{\vec{r}}$ deviations were demonstrated to be lower than the error taken during AFM image acquisition, as $\varepsilon_{\vec{r}} < 0.1$ nm.

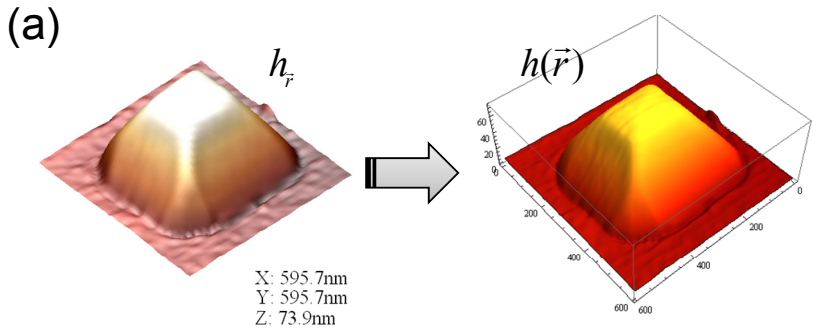

Figure 2.17 Interpolation of a discrete matrix of image pixels obtained from AFM measurements on a Si/Si(001) surface (*right*) into a continuum function (*left*).

These continuous images can be considered like a topography "mold" (denoted as a continuous "growth front" $h(\vec{r},t)$ that in general reproduces $h_{\vec{r}}(t)$ with a good agreement) of the AFM data, as shown in Figure 2.17(a) for the case of an individual Si square-fold pyramid on Si(100) [54]. The fitting using cubic interpolation produces, in general, a suitable "mold" of the SPM images. This assertion was verified by means of the $\varepsilon_{\vec{r}}$ deviation map (one example is showed in Figure 2.17(a) (but also in general for all the AFM images measured along this work). In general, maximum values of $\varepsilon_{\vec{r}}$ were found around several orders of magnitude below the systematic error inherent to the SPM technique, around 0.1 angstroms for p values ranging $1 < p < 10$ (Figure 2.17b). In the specific case of the AFM image of Figure 2.17(a), interpolation orders $p = 1$ or $p > 20$ presented discontinuities and artifacts close to "sharp" regions (e.g. with high local slopes $m > 0.8$), and also in the borders of the image (size effects) due to the low density of points in such zones, as can be observed in Figures 2.18(a–d). It is worth to remember that the conventional AFM scanning process does not distinguish local sharp features of the surface: the pixel size remains constant, at a different of a hypothetical "dynamic Fourier-resolved" AFM (adaptative mode) in which larger pixel densities would be taken at sharp surface regions in order to account for the higher local slopes.

The chosen of the best interpolation order was accomplished by using plots of $\mathrm{Max}[\varepsilon_{\vec{r}}]$ vs p as showed in Figure 2.17(b). In the case of several values were viable, cubic interpolation was chosen, in general, to guarantee the continuity in $\nabla^2 h(\vec{r})$ derivates with the lowest p value. It produces, in general, $h(\vec{r})$ functions with deviations of $\ll 0.01$ % of the real local slope values, which guarantees the reliability of such slopes obtained from this method. However, the exact % of deviation cannot be determined because slope deviations lower than 5 % are included in the systematic AFM error, estimated to be ±5% of the real value in sharp regions.

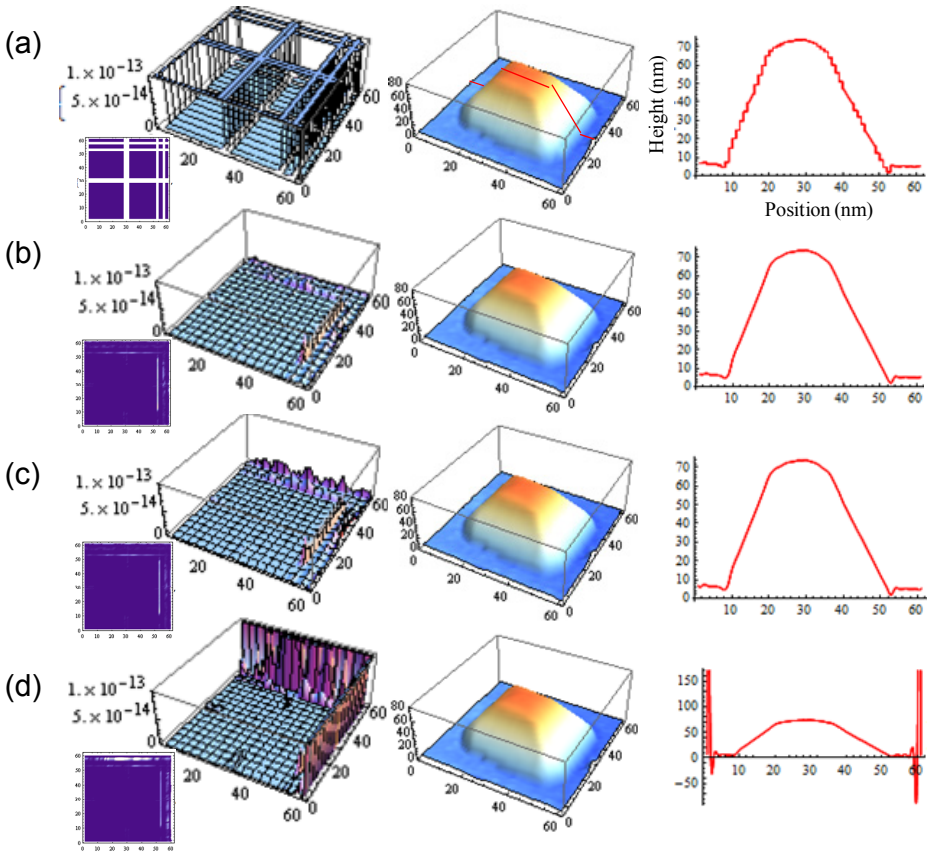

Figure 2.18 AFM image interpolation. The image to be interpolated corresponds to the Si pyramid-like grain showed in Fig. 2.18(a). Interpolation functions of several polynomial orders ranging from p = 0 (a), p = 3 (b), p = 6 (c), and p = 18 (d) are showed in the middle of the figure, together with error maps at the left side. Error maps are developed by evaluating ε_r along the film surface. At the right side cross section profiles of the AFM functions are shown.

In rare cases, specifically when low density AFM images are taken, the method of Lagrange polynomial interpolation was subjected to certain limitations, mainly regarding to effects in convoluting due to a non-suitable interpolation order that, as an

example, could cause the smoothening of the local slope values, and also distort of the in-plane slope orientations. As mentioned below, the cubic interpolation is in general the best solution, reducing surface smoothening and producing an appropriate mold of the AFM image. Similar procedures have been employed for the identification of surface facets belonging to pyramid-like surface features, (e.g. $Si_{1-x}Ge_x$ [49, 51], CdTe [53], Si/Si(001) [55], and ZnO/InP(001) [56], in which surface features have a well-known symmetry) and also in systems with less-evident symmetry such as: Au(111)/Au/mica and Au/SiOx/Si(111), in which surface features exhibiting round-like shapes.

2.6.3 Local slope/terrace width maps and distributions

By using the interpolated function of the surface $h(\vec{r})$ it is possible to determine another relevant shape parameter, that is the local slope value $m(\vec{r})$. Local slope values will be used here extensively for the analysis of the local advance of growth fronts (among others), and therefore it is worth to briefly describe some details of the procedure used to determine them. The term "local" refers to $m(\vec{r})$ values can be taken at any surface site $\vec{r}$, and it means that each slope value can correspond to the faceted section of a particular surface entity (i.e., a straight (or curved) "flanks") and top or bottom regions of such surface entities.

To determine $m(\vec{r})$ values from $h(\vec{r})$ functions, we used the dot product between the normal unit vectors $\hat{n}(\vec{r})$ at each surface site $\vec{r}$, and the vector $\hat{z} = (0,0,1)$; as [48, 49, 53-55]:

$$m(\vec{r}) = \tan(\cos^{-1}[\hat{n}(r)\cdot\hat{z}]) \qquad (2.3),$$

being $\hat{n}(\vec{r}) \equiv [n_x, n_y, n_z] = [-\nabla_x h(\vec{r}), -\nabla_y h(\vec{r}), 1] / \sqrt{(\nabla_x h(\vec{r}))^2 + (\nabla_y h(\vec{r}))^2 + 1}$, with $n_{xy}(\vec{r}) = n_x(\vec{r})\hat{x} + n_y(\vec{r})\hat{y}$ and $n_z(\vec{r})\hat{z}$ the in-film and the out-of-film plane components in the global film/substrate system $\{\hat{x}, \hat{y}, \hat{z}\}$, respectively. We can evaluate Eq. 2.3 at Δ_{pixel} -spaced surface sites and build a matrix of slope pixels, termed hereafter "*surface slope map*" (Figure 2.19). Using interpolating functions to obtain local slope values rather than discrete ones is a better methodology. The fact supporting this assertion is

that for the case of discrete functions we need (at least) two pixels to determine one local slope value. Therefore, the spatial resolution for local slope determination has a maximum limit of $2\Delta_{pixel}$ for 1D cross sections, or $(3\Delta_{pixel})^2$ in 3D (in 3D the local slope corresponds to an average taken over the slopes obtained along orthogonal and diagonal directions for each $3\Delta_{pixel}$-spaced pixels). Despite using continuum functions one can take slope values at any surface site (without limitation), it has no sense exploring surface sites in areas $< \Delta_{pixel}^2$ (i.e., with a spatial resolution better than the experimental technique): the excess of "slope pixels" would correspond to artificial (interpolated) sites of the surface. Then, the maximum resolution (in slope) is increased from the $(3\Delta_{pixel})^2$ obtained by using discrete procedures to the Δ^2 obtained when interpolating functions are used.

Once local slope maps are built, surface slope distributions $M(m)$ can be determined by the classification of the $m(\vec{r})$ values into Δm-differentiated categories (or bins), to be plotted in the form of histograms. From $M(m)$ distributions we are able to obtain statistical quantities describing probability distributions like the normal (Gaussian) one, among them: the mode (the local slope value that appears most often in the dataset, Figures 2.19f to 2.19i) and the variance.

2.6.4 Local in-plane texture

By using the interpolated function of the surface $h(\vec{r})$ it is also possible to performance local in-plane texture analyzes. In-plane texture analyses will be used here extensively for the analysis of reorientation and faceting phenomena during the advance of growth fronts, and therefore it is worth to briefly describe some details of the procedure used to achieve them. It is worth to clarify that the term "local" in this case refers that in-plane texture is monitored over a small area of the thin film surface, extending from few nanometers to several microns (the spatial range of SPM operation). Therefore, the word "local" for in-plane texture analyses based on interpolating functions is useful to differentiate them from those achieved by using X-ray ϕ-scans (§2.5.2). To perform a local in-plain texture analysis, we used the azimuthal angle $\phi(\vec{r})$ of each local slope value $m(\vec{r})$, which indicates the in-plane orientation of each $m(\vec{r})$ value (Figure 2.19j). The azimuthal angle is defined by [48, 49, 53-55]:

$$\phi(\vec{r}) = \tan^{-1}\left(n_y / n_x\right) \qquad (2.4),$$

where $n_x(\vec{r})$ and $n_y(\vec{r})$ are the components of the $\hat{n}_{xy}$ vector, that is, the orthogonal projection of the normal vector in the x,y plane. Then, similar to the case of the development of local slope maps (§2.6.3), we can build "azimuth angle maps, or ϕ-maps", as observed in Figures 2.20(c) and 2.20(g).

Once local slope maps and ϕ-maps were developed, we choose slope intervals Δm and angular dispersions $\Delta\phi$ in order to classify the $m(\vec{r})$ and $\phi(\vec{r})$, respectively; and we finally construct a 3D surface orientation map $M(m,\phi)$. Usually the values $\Delta m = 0.15$ and $\Delta\phi = 5°$ are employed in order to take into account the angular fluctuations ascribed to small distortions in the AFM measurement. The $M(m,\phi)$ maps are polar plots whose radial coordinate (radius) corresponds to m categories and the angular (polar[14]) coordinate (angle) corresponds to the ϕ values (Figure 2.19a). The intensity in the maps indicates the probability to find a specific slope in a orientation ϕ. Therefore, $M(m,\phi)$ maps allow a quantitative description of the distribution of in-plane orientations (or texture) of surface entities. Such a method had been used extensively in the past, in some cases termed "nanogoniometer" to point out the length scale of the analysis [48, 49, 53-55]. By using the definition of $M(m,\phi)$ maps, we can write $M(m)$ distributions as $M'(m) = \int_{2\pi} M(m,\phi)\partial\phi$. Several $M(m,\phi)$ maps taken from surface entities of different materials are showed in Figures 2.19(a), 2.20(d) and 2.20(h). It is worth to mention that in cases when surface tension does not control the surface entities shape's, $M(m_{fixed},\phi)$ [$M(m,\phi)$] and XRD ϕ-scan [XRD ϕ-polar map] can be compared, which is useful to develop dissimilar length-scale texture analyses.

[14] Remember that in In a spherical coordinate system the polar angle is defined by Eq. 2.3, whereas in a polar coordinate system it corresponds to the azimuthal angle

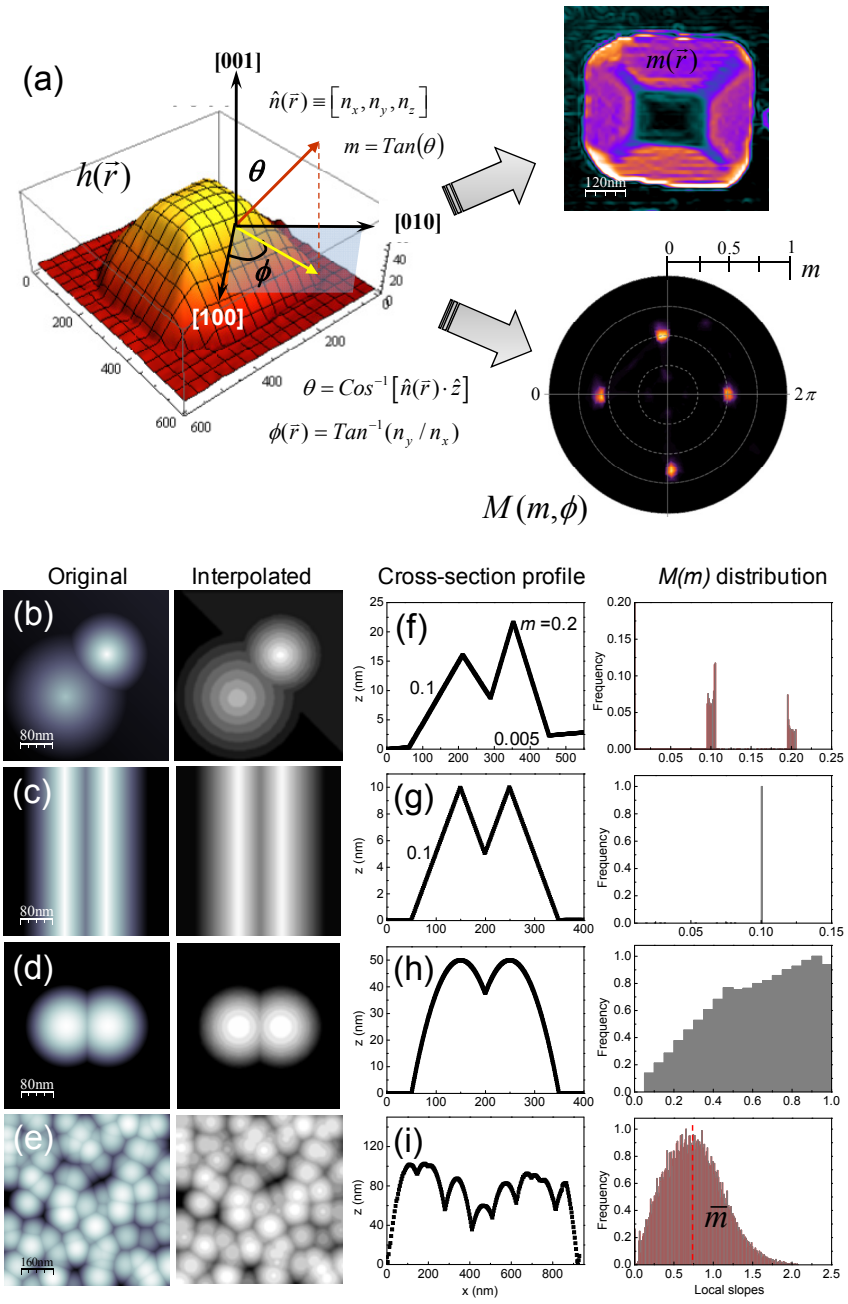

Figure 2.19 (a) Process of determination of surface slope maps. At the left-side, it is shown the AFM image function. Normal vectors and in-plane projections can be obtained, which allows us to determine the local slope values, the local slope map and the orientation maps (right). (b-e) Canonical geometries: (b) cone junction, (c) ripples, (d) paraboloid junction and (e) random-located paraboloids (left) and it respective interpolated functions (right). (f-i) Cross-section profiles of each geometry showing some local slope values (left) and it corresponding local slope distribution (right).

It is worth to mention that, in some cases, we employ a local surface coordinate system $\{\hat{n}, \hat{T}, \hat{\nabla}_S\}$ in which the unit vector $\hat{n}(\vec{r})$ is directly one of the orthogonal vector

defining the system, whereas $\hat{T}$ and $\hat{\nabla}_S$ are the tangent vector to the level curves $h(\vec{r}) = ctte.$ and the surface gradient vector, respectively.

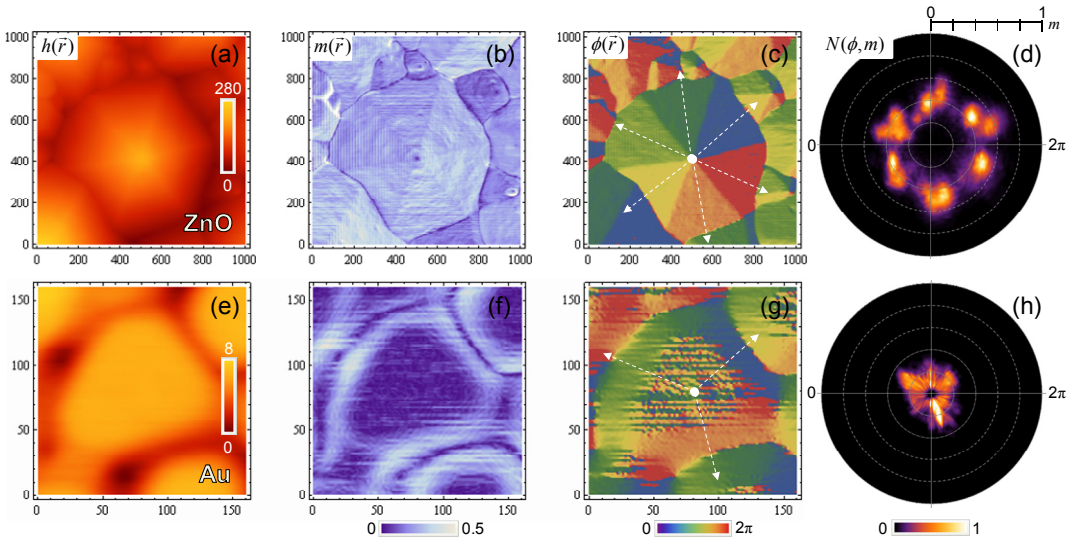

Figure 2.20 Typical surface orientation maps. (a,e) AFM images of ZnO and Au surfaces. (b,f) Surface slope maps. (c,g) ϕ-maps. (d,h) Radial slope distributions, or surface orientation maps.

2.7 Image tessellation procedures: multiscale determination of grain sizes, surface slopes and fractal dimension

Taking advantage from the interpolated function $h(\vec{r})$, we can break up the surface morphology into the individual elements (surface entities) that compose it (Figure 2.21). This procedure is termed here *image tessellation*, and we used it to determine the entity-size distribution, average fractal dimensions, and spatial-resolved analyses like the determination of local slopes close to the grain boundaries, reason why it is worth to briefly describe some details of the procedure used to achieve tessellation [50, 52, 54].

To perform surface tessellation, $\vec{\nabla}h(\vec{r},t)$ and $\vec{\nabla}^2 h(\vec{r},t)$ values are inspected with the aim to obtain closed contours. Closed contours are defined as: (i) local minima $[\nabla h(\vec{r}_i) = 0$ and $\nabla^2 h(\vec{r}_i) < 0$ (concave curvature)] or (ii) saddle points $[\nabla_x^2 h(\vec{r}_i)\nabla_y^2 h(\vec{r}_i) < \nabla_{xy}^2 h(\vec{r}_i)]$. The thus-defined contours are considered surface entity boundaries. High quality AFM images are required in order to get reliable image tessellations; otherwise contours comprising spurious points and discontinuities were

obtained. Several statistical parameters can be achieved by means of the image tessellation, we stress:

The *fractal dimension of the entity boundary* ζ (Figure 2.22), which is used to quantify the fractal behavior and the shape homogeneity of the surface entities. ζ is a function of the perimeter-to-grain area ratio, $\zeta = (n-p)/(n-2\sqrt{n\pi})\,Log_p^{2\sqrt{n\pi}} + 1$, where the grain area and perimeter correspond to $A(l) \xrightarrow[l\to 0]{} n$ and $P(l) \xrightarrow[l\to 0]{} p$, respectively [4, 56]. $A(l)$ [$P(l)$] denotes the number of partially or fully filled elements of the embedded cubic lattice (of parameter l) employed to cover the grain surface.

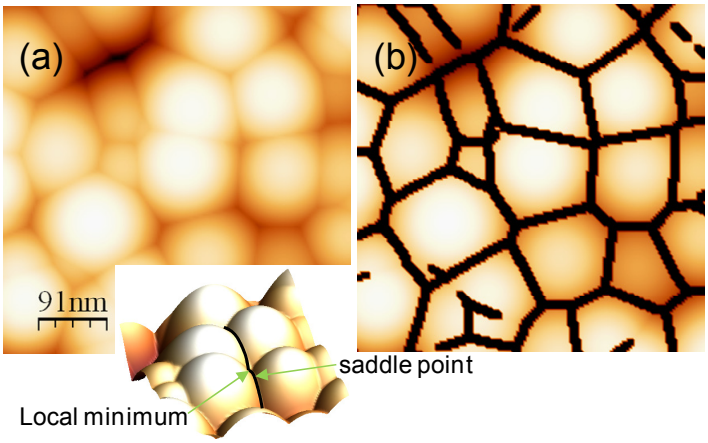

Figure 2.21 (a) Topography of a canonical surface formed by randomly located spheres. (b) Image tessellation procedure. The contours, defined as local minima and saddle points of the surface (see inset) are showed in dark. The inner structure of enclosed contours corresponds to surface tessellas (the inner region of a surface entity). The complete "puzzle" of tessellas built up the film surface.

- The above relation was built to fulfill the following conditions: For an n-sized grain, ζ drops with increasing p at a rate $\propto 1/\ln(p)$ from $\zeta = 2$ for $p \to 2\sqrt{n\pi}$ (the shortest perimeter of a compact grain with radial symmetry) down to $\zeta \to 1$ for $p \to n$ (the longest perimeter of a fractal grain). On the basis of this definition, we can determine the fractal dimension as the ratio between the image pixels at the contour region of a given entity and those belonging to its inner part.

- The *entity-size distributions* (statistical functions described in Table 2.6), we are able to determine the average sizes of the surface entities without developing explicitely size distributions. However, especially when coarsening of surface structures is

analyzed; it is necessary investigate not only the average values, but also the shape-of the size-distributions.

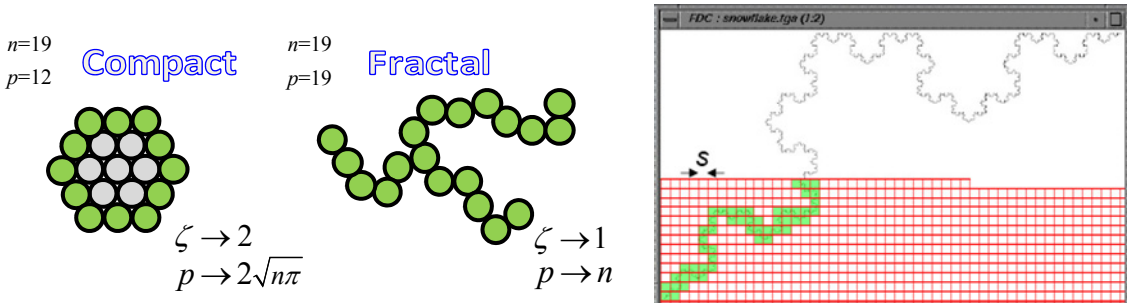

Figure 2.22 Fractal dimension fundaments (left), and window showing a tessellation code identifying contour points on ib a hypothetical fractal structure.

- As observed in Figure 2.23, to obtain the size distributions first it is necessary to define a criterion for determining the in-plane sizes of non-compact entity. For this purposes, the size of an entity was taken here (in a first approach) as the length of the largest straight-line enclosed within the contour. For highly irregular shapes, a second approach consisting in averaging the sizes measured along the main global axes ($\hat{x}$ and $\hat{y}$) avoids to overestimated the entity sizes.

- The *local slope distribution at entity borders*: in order to obtain the slopes at the borders of the surface entities, the slope map is overlaid (that corresponds to the logic operation “and”) with the tessellation map whose contours have be thickening by 4-8 image pixels around the real boundaries by defining nearest-neighboring pixels and next nearest-neighboring ones, as displayed in Figure 2.23(f).

2.8 Theoretical methods: Growth simulations

In an attempt to address the mechanisms that rule the surface nanostructuration of thin films, that is, the morphology evolution of the growth fronts, numerical simulations were carried out. Because the nanostructuration processes investigated here involve interactions between surface entities with sizes ranged between a few tenths and hundreds of nanometers (including thousands of atoms), such simulations are based on mesoscopic and continuum approaches, among them: (*i*) partial differential Langevin-

type equations to explain interaction driven mass transport phenomena, (*ii*) finite element analysis to describe elastic interactions between grains and (*iii*) hybrid simulations comprising (*i*) and (*ii*) that are linked by means of partial differential equation systems when phenomena taking place at different timescale are present. With the results of such simulations we intend: (a) to reproduce the experimental results getting insights from the degree of agreement between them; and going beyond toward a surface engineering, (b) to predict new results for tailored conditions with the goal of manipulating the growth toward nanostructuration processes.

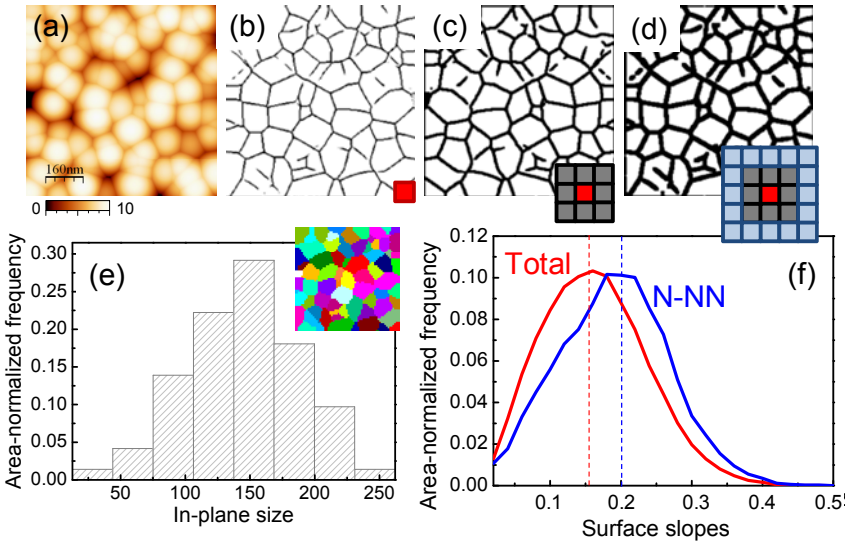

Figure 2.23 Basics and applications of image tessellation. (a) Topography of a canonical surface formed by randomly located spheres. (b-d). Image tessellations by using: (b) local minimum, (c) nearest-neighboring pixels (NN) from local minimum and (d) next-nearest neighboring pixels (N-NN). *Insets*: the red square represents a local minimum (contour) are the close shade ones to NN and N-NN pixels. (e) Entity-size distribution obtained from the contour map. *Inset*: image showing the inner domain of a canonical surface entity defined by the close contour. Each color represents a different entity. (f) Comparison between slopes obtained from the total image and the N-NN tessellation map (total = N-NN + slopes from the inner regions of the spheres). As observed, the N-NN slope distribution shows a shift in the direction of higher slopes because low slope values are not considered.

2.8.1 Continuum approach to film growth

Simulations leading with film growth mechanisms at the mesoscopic scale were carried out by using the Dynamic Scaling Theory. Dynamic scaling is supported by Langevin-type equations predicting the evolution of the "growth front" $h(\vec{r},t)$ from separable contributions per mechanisms (as mentioned before in §1.4.2). Such equations are presented on their generic form [4, 5]:

$$\frac{\partial h}{\partial t} = F - \nabla \vec{J} - \Psi \qquad (2.4),$$

where the right-side terms correspond to:

- F is a generic term comprising flux-related phenomena, such as: (*i*) the average deposition rate due to the plane flux F_0 with $\bar{h} = F_0 t$, and (*ii*) the local variations of surface heights (kinetic roughening) with respect to $\bar{h}$ (i.e., $h' = h - \bar{h}$) due to phenomena related with the inhomogeneous natures of both the flux (for example, since its angular distribution) and its incidence on the growth front. Among these phenomena, we found: (a) the stochastic flux fluctuation, which is described as an uncorrelated Gaussian noise $\eta(\vec{r},t)$ of strength of $\eta_F \propto \sqrt{F_0}$ as a consequence of the dependence of F on both the incidence angle Φ and the local aperture angle $\varphi(\vec{r})$. One of those effects is the *geometric shadowing*, which is determined mainly by $\varphi(\vec{r})$ ($0 \le \varphi < \pi$ —geometric shadowing of grazing incident particles in the flux) [4]. As described in §2.1, the angular distribution of the flux is described typically as $F(\Phi) = F_0(\cos^n(\Phi)/\psi)$ where the power n gets values that depend on the flux-source characteristics and $\psi = \int_{-\pi/2}^{\pi/2} \cos^n(\Phi)\partial\Phi$ corresponds to a normalization constant. Then, the local advance of the growing films dominated by shadowing effects can be expressed as $\partial_t h = \frac{1}{\psi}\int_{-\varphi/2}^{\varphi/2} F_0 \cos^n(\Phi)\partial\Phi + \eta(\vec{r},t)$, with Ψ being the normalization constant. Another effect considering is the mechanism of *steering*, which occurs due to the attractive interaction of Van der Waals-type that an atom approaching to the surface feels. This mechanism is the responsible for the deflection of oblique incidence trajectories towards the higher surface features. normal for [5, 57]. Steering is similar but stronger that the geometric shadowing. The higher surface features collect incident atoms within a wider aperture angle of $0 \le \varphi < 2\pi$. While the steering effect has not effect on depositions onto singular substrates, this induces lateral surface inhomogeneities in vicinal morphologies with trains of steps and 2D-3D surface entities [58]. Steering may play a role in the formation of 3D surface entities (mounds) on metal films [59], and it appears to provide an important roughening mechanism in metal homoepitaxy at very low

temperatures, where the thermal mobility is negligible [60, 61]. The deflection probability by steering (and consequently the roughening that this induces) decreases as the kinetic energy of the incident atoms rises.

- $\nabla\vec{J}$ corresponds to a generic term describing the conservative contributions related to the surface mass transport driven, according to the Fick's law: $J = -k\nabla\mu$, by:

(a) Gradients of the surface chemical potential μ, realized as the spatial variation of the density of dangling bonds. A generic chemical potential including several diffusion processes can be expressed as $\mu \approx \Omega\left\{\gamma_s\left[\nabla^2 h + \left(\nabla h\right)^2\right] - \sigma\left(h\right)\right\}$ (where Ω is the atomic volume, γ_s the surface energy and $\sigma\left(h\right)$ the local stress). Among the diffusion processes, there are: (*i*) —*Mullins-type diffusions*: $\mu \propto \nabla^2 h$ (where the dangling-bond density is assumed to be described through the surface curvature) [4, 5], (*ii*) —*Nonlinear Mullins-diffusion* between facets with different miscut angles, in which the surface potential is taken to be dependent on the step density ($\rho_{step} = 1/w$) as: $\mu \propto \left(\nabla h\right)^2$; and (*iii*) *Stress-biased diffusion*: in which surface currents $J_s = -k\nabla_s\mu$ (with k the surface diffusion coefficient, ∇_s the surface gradient and μ the chemical potential) that are driven by the μ resulting from the competition between (non)linear Mullins terms and the surface stress. Thus-defined J_s flows toward sites with higher curvatures and slopes (which implies higher densities of dangling bonds and steps, respectively) and/or under traction (those with lower film densities) [62-64].

(b) Gradients of the thermodynamic potential ascribed to the spatial variation of the density of deposited adatoms, among them: (*i*) *Diffusion bias*: in which the probability for interlayer mass transport in vicinal surfaces, that is, the diffusion (or jumping) of atoms towards lower/upper terrace step edges, is reduced by the existence of additional potential energy barriers (Ehrlich-Schwoebel ESB barriers) at the step edges [4, 5, 65]. Such effect can cause, as example, mound formation in film growth due to the presence of "uphill" surface currents J^{up} leading the fraction of adatoms reflected by the step-edge barriers and those

deposited preferentially on the upper terraces, by steering, into the ascending steps. The uphill surface currents compete with downward ones J^{down}, which are given by the fraction of atoms crossing the step-edges (e.g., via atomic exchange) plus those deposited downwards, by funnelling [5, 65]. The balance between uphill and downhill surface currents typically leads to a stabilizing downhill surface current, which tends to develop films composed by surface entities with selected shapes (or facets with selected angles or slopes m_s). The net surface current that results from this balance must satisfy the stability conditions for the selected slope m_s: $J_s(m_s)=0$, $J_s(m_s-\delta m)>0$, and $J_s(m_s+\delta m)<0$ for $\delta m \ll m_s$. Therefore, $\partial_t h' = -\langle k \rangle \nabla^2 \mu$ where $\langle k \rangle$ is space averaged to consider any anisotropy with μ the local chemical potential (Table 2.7, fourth row). (*ii*) Ψ generic terms comprising phenomena of mass transport including the *Edwald-Wilkinson* (EW, in which $\partial_t h' \propto \nabla^2 h$ as depicted in Table 2.8, third row) and *Kuramoto-Sivashinsky* (KS, in which $\partial_t h' \propto -\nabla^2 h$) dependence of the vapour pressure/sputtering yield during a deposition with desorption/erosion on the dangling-bond density, and also the *Karard-Parisi-Zhang* (KPZ/-KPZ) –type generation of porous films by deposition /erosion in conditions of major kinetic limitations (Table 2.7, second row).

Several growth mechanisms typically used to describe the evolution of growth fronts are summarized in Table 2.7. In the table, we used a canonical Gaussian function to represent the initial configuration of an individual surface entity (or nanostructure). Such initial entity overcomes under the transformations described by Equation 2.4, in dependence of the relevant mechanism controlling the growth process that is specified in the first two columns of Table 2.7. The surface evolution of the growing film was simulated by computing Equation 2.4 (modified according the case), using iterative *Runge-Kutta* methods and periodic boundary conditions to prevent finite-size artifacts. The most relevant mechanisms considered in Equation 2.4 were: Stress-biased Mullins-type diffusion (linear and non-linear, —first row in Table 2.8), KPZ (second row), EW (third) and SS (forth row).

Input parameters for such a kind of simulation include: (*i*) the growth flux F (as addressed in §2.1, we can consider a plane flux F_0 mainly), (*ii*) kinetic coefficients to fit

the timescales (such as surface κ_s), GB (κ_{GB}) and bulk (κ_{Bulk}) diffusion coefficients), (*iii*) uncorrelated noise function $\eta(\vec{r},t)$ if required (because the influence of a stochastic fluctuation on a single entity could be frequently neglected).

Class	Langevin-type equation	Features
Mullins diffusion Conservative mechanism	Stabilizing mechanism depending on the local curvature $\propto \nabla^2 h$ $\partial_t h = -\kappa\nabla^2(\nabla^2 h) + \eta$	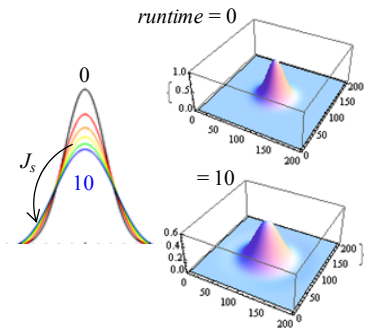 - Describes surface diffusion and MBE-type growths
Kardar-Parisi-Zhang (KPZ) Non-conservative	Stabilizing mechanism depending on the local surface slope $(\nabla h)^2$ $\partial h / \partial t = k\nabla^2 h + k'(\nabla h)^2 + \eta$ $k > 0$ and $k' > 0$ or < 0	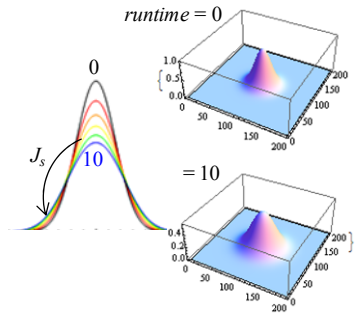 - Describes desorption and growths ruled by the film density reduction due to vacancy formation (which depends on the local slope), similar to ballistic deposition
Edwards-Wilkinson (EW) Conservative	Stabilizing mechanism depending on the local surface curvature $\propto \nabla^2 h$ $\partial h / \partial t = k\nabla^2 h + \eta$ $k > 0$ (EW); $k < 0$ (KS)	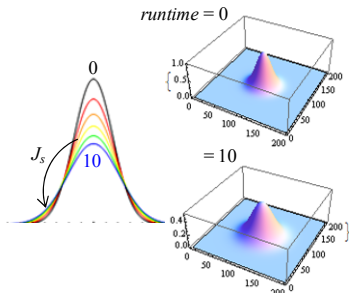 - Describes growths with desorption and downhill mass currents associated with the asymmetric spreading of clusters impacting onto inclined parts of the surface in energetic deposition by cluster impact

Slope selection (SS) Conservative in the small slope regime	Destabilizing mechanism depending on modulated local slope $\partial h/\partial t \propto \nabla\left(\frac{\nabla h}{1+(\nabla h)^2}\right) - \nabla^4 h + \eta$	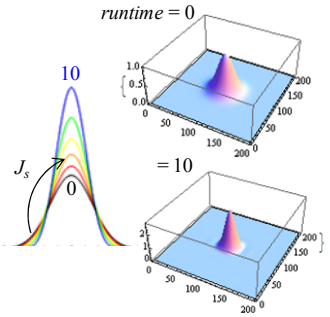 - Describe growths in which surface entities tend to develop well defined facets (conical or pyramidal-like shapes). Used to explain kinetic faceting and shape selection

Table 2.7 Relevant mechanisms involved in thin film growth.

Depending on the type of study, the morphologies that characterize the early growth stages —as measured by AFM— or those resulting from the mechanical equilibrium of inner loads (i.e., of the intrinsic stresses) —by finite element method, are used as initial conditions to compute Equation 2.4. The algorithms were developed in *Mathematica* programming environment. Calculation were performed in a cluster formed by 4 nodes (16 cores) supported in Linux Debian for intensive scientific computing using load balance. Licenced *Mathematica* 6.0–8.0 was executed in server-client scheme.

2.8.2 Finite element method

The finite element method (FEM) is a numerical technique for finding *approximate* solutions to partial differential equations (PDEs) in systems with complex geometries and infinite degrees of freedom. In this study FEM simulations will be used to investigate the mechanical response of surface grains supporting intrinsic stresses (normal and shear loads), and the strain field generated as a consequence of such intrinsic interactions. Therefore, it is worth to briefly describe some details of the FEM assumptions. The FEM method is based on the discretizing a system into a set of small elements with simpler geometries and finite degrees of freedom. These elements are coupled to each other by node points, arrayed in inhomogeneous grids with a higher node density where the geometry to mesh is more complex. The system discretization

allows to eliminate the spatial derivatives in the PDEs, and thus the equations governing the continuum problem become algebraic (or ordinary) in rate ∂_t (for stationary or transient behaviors, respectively) at the element scale. The PDEs to be solved by FEM in polycrystalline films is:

$$\varepsilon_{ij} = \frac{1}{2}\frac{\partial u_i}{\partial x_j} + \frac{1}{2}\frac{\partial u_j}{\partial x_i} \qquad (2.5a),$$

where u_i are elastic deformations or displacements along the x_i axis. Therefore, ε_{ii} corresponds to the compressive or tensile normal strain and ε_{ij} are bending strains of a x_i axis that curves in the direction x_j.

$$\sigma_{ij} = 2G\left(\varepsilon_{ij} - \frac{\varepsilon_{kk}\delta_{ij}}{3}\right) + \upsilon\varepsilon_{kk}\delta_{ij} \qquad (2.5b),$$

$$\frac{\partial \sigma_{ij}}{\partial x_j} + f_i = 0 \qquad (2.5c),$$

the force balance along x_i. which correspond to: (*Equation 2.5a*) Strain ε_{ij} definition from displacements $\vec{u}_i$ along the $\hat{i}$ axes. (*Equation 2.5b*) represents the Hooke's law for isotropic thin films under biaxial stress, with σ_{ij} being the stress tensor, G the shear modulus, υ the Lamé's first paramenter (bulk modulus), and δ_{ij} is the Kronecker delta. (*Equation 2.5c*) The Newton's second law (i.e., the equation of motion under equilibrium) with f_i denoting the body force per unit of volume that in our case (in absence of external loads) results from the balance between the surface tension-type forces involved in the growth. Once defined the appropriate mesh, the displacement in each element is approximated by the linear force-displacement equation (i.e., $\left\{\vec{f}_i\right\} = \left[\varsigma\right]^e \left\{\vec{u}_i\right\}$, with $\left[\varsigma\right]^e$ being the stiffness matrix). The basic ingredients in the FEM simulations are: (*i*) *The Mesh used to reproduce properly the system geometry*: The used finite elements correspond to Kirchoff's plates (pseudo-2D elements with 3 nodes each and uniform thickness of 1 nm), which were assembled in a numbers ranged between 100-500 elements to create optimized mesh structures (as shown in Figure 2.24). (*ii*)

model geometry: in most applications, structures with semispherical caps and gaussian-tails were used to mimic surface grains, whereas cylinders were used to model the columnar film bulk. (*ii*) *Material properties*: relevant parameters such as Young's modulus (E), Poisson ratio (v), thermal expansion coefficients (α), mass and stiffness damping (α_{dM} , α_{dK} respectively) and density (ρ) are required [summary in Table 2.8]. (*iii*) *Boundary conditions*: setting up boundary conditions implies to define both the grain-grain and grain-substrate constrains, and the body force f_i using global $\left\{\hat{R},\hat{\theta},\hat{z}\right\}$ and local $\left\{\hat{n},\hat{T},\hat{\nabla}_s\right\}$ coordinate systems, respectively. (*iv*) *Type of analysis*: we use static linear analyses in all of our FEM simulations. Static simulations describe time-independent processes, or high-speed processes, so that in the slower film growth kinetics this processes appear to be steady. In the case of elastic deformations analyzed here, this latter describes the situation in the time multiscale simulation: strain fields are created as fast as ps-ns, whereas surface-bulk diffusion occur within the range of ms-hours. Then, time scales can be decoupled, and stress generation can be treated as a static problem. The solution obtained once loads are applied (i.e. strain/stress fields) are considered in the modified potential driving the surface diffusion and so on.

Material	Property	Value
Gold (Au)	Young Modulus	78 GPa
	Poisson ratio	0.44
	Density (near 25ºC)	19300 Kg/m^3
	Thermal Expansion coefficient (25ºC)	14.6 μm/m·K
	Mass damping	1
	Stiffness damping	0.001
Silicon (Si)	Young Modulus	131GPa
	Poisson ratio	0.27
	Density (near 25ºC)	23290 Kg/m^3
	Thermal Expansion coefficient (25ºC)	2.6 μm/m·K
	Mass damping	1
	Stiffness damping	0.001

Table 2.8 Material properties used in FEM simulations.

Since the process of stress accommodation via the generation of longitudinal strain (by grain-boundary zipping) and shear strain (elastic azimuthal deformation of the type torsion) happens at the scale of atomic vibration (~few ps) before any mass transport takes place, this process can be decoupled in time from diffusion and then resolves by

FEM under statics conditions. The fact that body forces are within the elastic limits in which the Hooke's law is fulfilled, allows us to use linear Lagrangian solver. FEM simulations were carried out using the FEMLAB-COMSOL® code executed in the PC cluster for scientific computing described above.

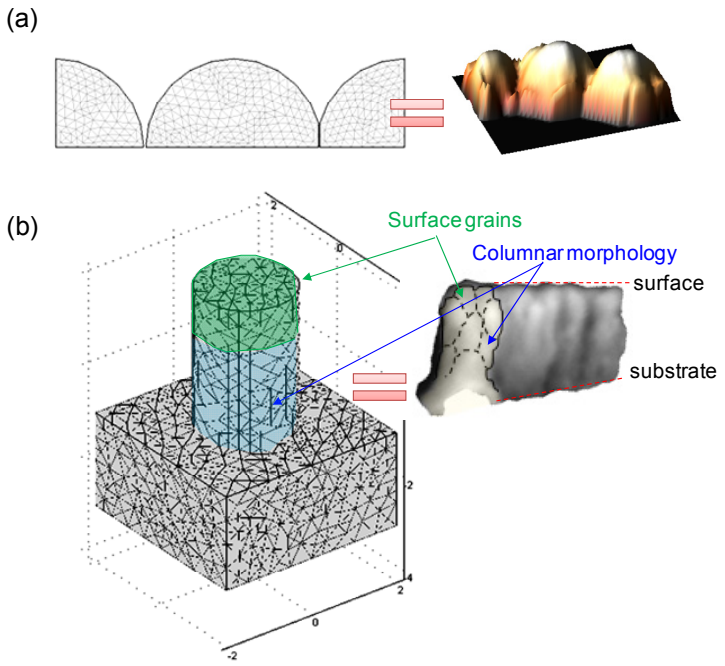

Figure 2.24 Refined mesh configuration in FEM simulations. (a) 2D-FEM simulation over a cross-section profile of three semispherical grains (for studies of grain coalescence). (b) 3D-FEM simulation over a columnar structure (for studies of grain torsion). Insets show real systems under investigation: (a) AFM image of Au/SiOx/Si(111) annealed surfaces and (b) SEM image of a cross-section profile showing the columnar microstructure of the Au/Si films.

2.8.3 Multiscale hybrid simulations

Multiscale modeling consists in the resolution of physical problems that involve key features and relevant behaviors taking place at dissimilar space and time scales, each scale being approached through specific simulations and/or theories. Typical space and time scales —and the simulations used to resolve problems in each one—, are briefly summarized in Figure 2.25, together with some practical examples. In brief, there are two basic strategies to achieve multi-scale simulations: (*i*) hierarchical (sequential) approaches, and (*ii*) hybrid (concurrent) ones [66-69].

In *hierarchical* approaches it is necessary to have a priori and complete knowledge of the fundamental processes at the lowest scale involved. This knowledge or information can then be used for modeling the system at successively coarser scales. Another

requirement is to have a reliable strategy for encompassing the lower-scale information into the coarser scales (i.e. to solve the scale linking problem).

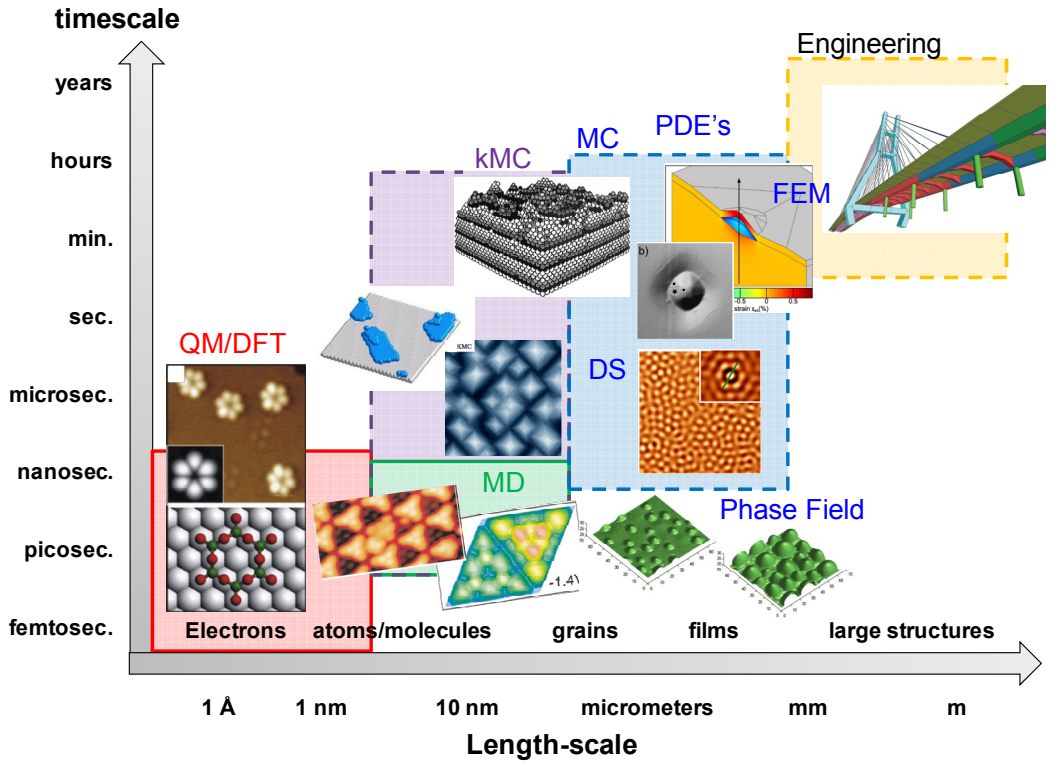

Figure 2.25 Hierarchy of multi-scale simulations. Figures in each level show examples of successively implemented simulations. Initials correspond to: Quantum Mechanics (QM), Density-Functional Theory (DFT), (Kinetic)MonteCarlo k(MC), Molecular Dynamic (MD), Partial Differential Equation Systems (PDE's), Dynamic Scaling (DS), Finite Element Model (FEM). Examples were taken from literature: QM/DFT: V_6O_{12} clusters on Rh(1 1 1) and corresponding DFT model from F. P. Netzer Surf. Sci. 604, 485 (2010); MD: Pb/Si(111)-7x7 surface from S-.C. Li Phys. Rev. Lett. 93, 116103 (2004); kMC Cu thin film growth by J. G. Amar, and P. Moskovkin; and P. Zhang Vacuum 72, 405 (2004); FEM: Strain distribution in Si capping layers on SiGe islands from N. Hrauda Nanotechnology 23, 465705 (2012); DS: Ion beam sputtering in normal incidence by E. Vasco; Phase Field: Typical evolving surface morphology with isotropic elasticity during the annealing from Y. Ni J. Crys. Growth 284, 281 (2005); Engineering: bridge by University of Zilina.

This is often accomplished by phenomenological theories, which contain a few key parameters (these can be functions), the value of which is determined from the information at the lower scale. Among the hierarchical approaches, there are: kinetic Monte Carlo coupled with *ab*-initio simulations and phase-field models. In brief, we reproduce the potential energy landscape of the system with *ab-initio* methods and then use relevant physical constants obtained in kMC simulations, and so on. Broadly speaking, a concurrent multiscale approach is more general in scope than its sequential counterpart because the concurrent approach does not rely on any assumptions (in the form of a particular coarse-graining model) pertaining to a particular physical problem.

As a consequence, a successful concurrent approach can be used to study many different problems.

In other words, the hybrid multi-scale simulation concept is based on the development of methods allowing for the consideration of multiple scales simultaneously. For example, dislocation core properties, grain boundary structure, and crack propagation could all be modeled individually or collectively by the same concurrent approach, as long as it incorporates all the relevant features at each level. What is probably most appealing, however, is that a concurrent approach does not require *a priori* knowledge of the physical quantities or processes of interest. Thus, concurrent approaches are particularly useful when exploring problems about which little is known at the atomistic level and about their connection to larger scales, and when discovering new phenomena. Among the hybrid concurrent approaches, it deserves to mention: macroscopic-atomistic *ab initio* dynamics comprising the coupling between finite element methods and molecular dynamics or molecular dynamics with tight-binding, quasi-continuum models coupling finite element methods with embedded atom potentials, and coarse-grained molecular dynamics.

In problems dealing with interactions between grains involving elastic deformations and mass transport like those investigated along this work, time and length-scales are decoupled, enabling us to apply a hierarchical strategy for multiscale modeling: while diffusion takes place in the range of ms-hours, strain generation happens as fast as ns. The same argument is valid for the corresponding length-scales: whereas the diffusion occurs at the range of the diffusion length, the strain generation can propagate along micrometers. For simulations regarding the interplay between stress relaxation and surface diffusion, liking problems were overcome by means of the fluctuations in the local density, which implies the variation of the lattice parameter a and, as a consequence, the modification of the energies involved as described by embedded atom potentials. In order to convert the local perturbations of the system density to the ascribed stress-field and vice versa, the relation $\sigma(\vec{r},t) \propto -\nabla_r U$ between the growth stress σ and the interatomic potential U of the crystal lattice were used. For fcc metals U corresponds to a manybody embedded-atom potential as that in Fig. 2.26 [[70]]. As example, in conditions of small lattice parameter perturbations $\delta a / a_0 << 1$ (with a_0 the unstrained lattice parameter and δa it perturbation) around the equilibrium one $a_0 \propto \rho_0^{-1/3}$, $U(\delta a) \propto \delta a^2$ [$\sigma \propto -\delta a$] becomes parabolic [linear] with δa and so, the

Hooke law (valid for the elastic regimes) $\sigma(\vec{r},t) \equiv M\varepsilon = M\dfrac{a-a_0}{a_0} \approx M\left[\sqrt[3]{\rho_0(\vec{r},t)/\rho(\vec{r},t)}-1\right]$ can be applied. Thus, the rarified regions of the films (with $\delta\rho<0$) would be under traction $\sigma>0$, whereas the densified regions ($\delta\rho>0$) would be under compression (Figure 2.26).

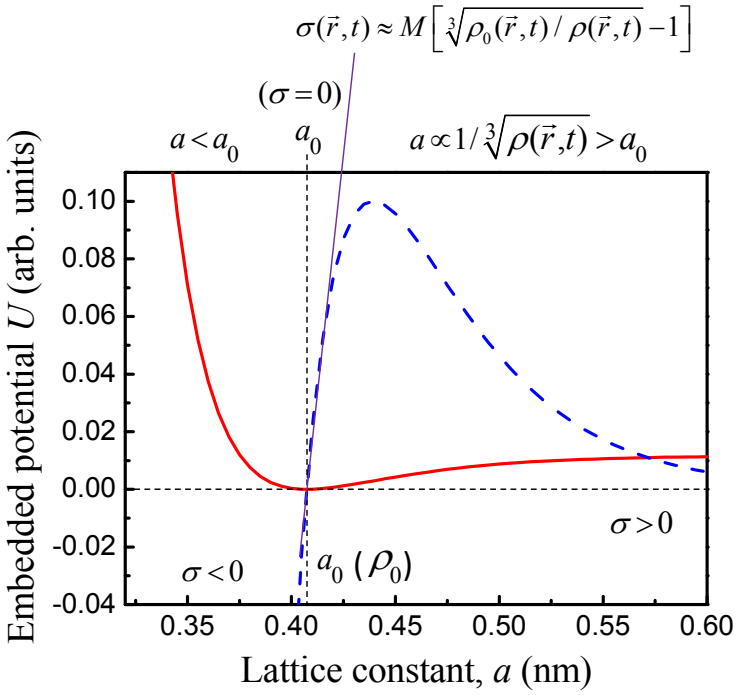

Figure 2.26 Embedded atom potential for Au films (solid, red) and the corresponding force $\propto -\nabla U$ (dashed, blue) in dependence of the lattice parameter a. In the small perturbation limit (solid line), the Hooke's law is satisfied.

CHAPTER 3

COARSENING PHENOMENA DURING POLYCRYSTALLINE THIN FILM PREPARATION: EXPERIMENTAL EVIDENCES

In this chapter, we introduce experimental evidences of the interactions between the surface entities forming thin films, namely: single-crystal domains or crystallites, grains and multigrain structures; these latter shaped as irregular bundles, columns…. Such interactions are driven by energy minimization processes taking place during growth and pots-deposition processing of the films under far-from-the equilibrium experimental conditions, e.g. under high growth rates and/or moderate temperatures giving rise to a reduced atom mobility. In order to elucidate the origin and nature of these interactions, experiments focused on the evolution of both the surface morphology and the crystal structure of the films during growth and post-deposition processing were carried out. Such an evolution was investigated by scanning probe and electron microscopies (SPM and SEM, respectively), and x-ray diffraction (XRD). These analyses allowed us to quantify the transformations of the film morphology in terms of statistical parameters such as: roughness, grain sizes, surface slopes, crystal structure and residual stresses; which all of them are used as input for modeling thin film growth.

3.1 Au thin film growth

3.1.1 Experimental details concerning thin film growth and further characterization

In order to elucidate the nature of the relevant peer-to-peer interactions between surface entities, experiments of thermal evaporation of metal Au films and post-deposition annealing were performed. Table 3.1 summarizes the experimental conditions regarding the growth by thermal evaporation (discussed also in §2.1). Here, the growth of Au thin[15] films consisted in a two steps process: in the first step, an Au layer was grown on mica substrates (being used as "buffer layers"), whereas in the second step Au thin films (overlayers) of several thicknesses were grew one-by-one above the different Au/mica films.

The Au layers were deposited at a temperature $T = 673 \pm 8$ K (0.4 $T_{melting}$) on freshly cleavage mica (*v*-5) sheets[16] (which were blew with highly pure $N_{2(g)}$ before introducing

[15] We refer "thin" to film thicknesses ≤ 1.2 μm

[16] The *v*-5 index refers to the stained A quality of the mica sheets (hard, uniformly distributed in the usable area, medium waviness), which are usually employed for thin film deposition, as indicating by recognized suppliers http://www.emsdiasum.com/microscopy/products/preparation/mica.aspx and http://www.2spi.com/catalog/submat/mic_shet.php.

them into the vacuum chamber), and at a growth rate F = 1 nm/s. The thickness d of the Au layers were remained constant, being d = 200 ± 1 nm for all samples (a total growth time of $t \cong$ 200 s). The experiments were developed in a high-vacuum environment, being the base pressure of the growth chamber $P = 8 \times 10^{-7}$ mbar. As will be mentioned before, the Au layers have a preferred (111) out-of-plane texture, reason why they can be also understood as epitaxial layers. The mica substrates were chosen by several reasons: (*i*) the ease of the cleavage process (e.g. by using an adhesive strip or cutting with a scalpel in air or vacuum), (*ii*) the low density of surface steps in comparison with other similar substrates like rocksalt, which implies to have departing atomically flat surfaces (Figure 3.1a) [71, 72], (*iii*) the good adhesion at the Au/mica interface [73], and (*iv*) the preferred (111) out-of-plane crystal texture of the fcc metal films deposited on it (e.g., Pd, Ag, Al, Au and Ni) as revealed from early growth experiments [54, 71, 72, 74-80].

The muscovite mica is a phyllosilicate mineral of potassium and aluminum [with formula $KAl_2(Al_3Si)O_{10}(OH)_2$] that exhibits a layer-like structure of aluminum silicate sheets not strongly bonded and held together by K^+ ions, as depicted in Figures 3.1(b) and 3.1(c) [81, 82]. Its crystal structure is monoclinic (lattice parameters a = 5.19 Å, b = 9.04 Å, c = 20.08 Å, y β = 95º30' [81, 82]) with a susceptible {001} basal plane of being cleavage. The surface atoms of oxygen are arranged in a hexagonal-like pattern with a lattice of 5.2 Å, which confer a negative surface polarity that results from the replacement of the Si atoms by the Al ones in a proportion of 1:4.

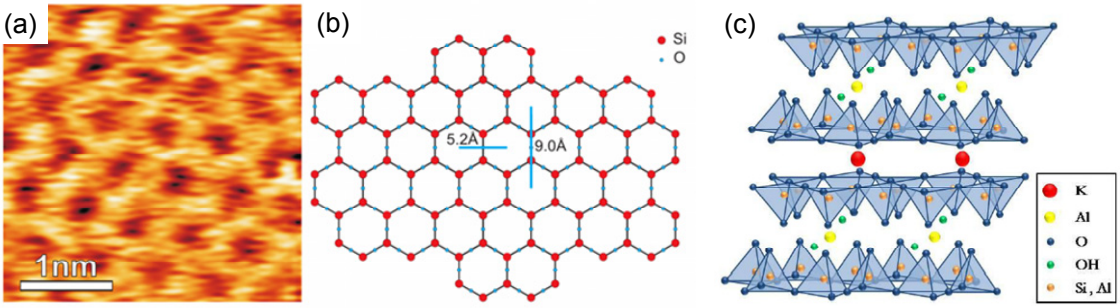

Figure 3.1 Schematic plot of the crystal structure of mica. (a) AFM image of the mica surface {0001}. Ball-based models of: (b) mica surface {0001} and (c) sheet-like structure showing that below the hexagonal array of K+ ions, there is a layer of oxygen atoms ordered in tetrahedrons.

Au overlayers (or thin films) of several film thicknesses ranged from d = 2 to 1200 nm were deposited at a temperature $T = 373 \pm 6$ K ($0.28\,T_{melting}$) above the Au(111)/mica layers at a constant growth rate $F = 1$ nm/s, under high vacuum conditions (base pressure = 8×10^{-7} mbar). As will be analyzed later, the Au overlayers also show a preferred (111) out-of-the-plane texture. The growth rate used was two orders of magnitude higher than the typical growth rates (~0.1 nm/s) [83], and the growth temperatures were low-moderate (~0.2 $T_{melting}$ [55]), ensuring a far-from equilibrium growth scenario (i.e. with low adatom mobility). As will be discussed later, such conditions promote the development of film surfaces with high density of small surface entities separated to each other by grain boundaries, reason why they could be also understood as polycrystalline overlayers, at least in a morphological sense. Under these low mobility conditions, the adatoms impinging the surface have a low diffusion length $\lambda_d \propto (D_s\tau)^{1/\text{dimension}}$, where τ is the lifetime of the diffusive species (adatoms) and D_s is the diffusion length. For different decay processes [e.g., re-evaporation, nucleation (under high fluxes), terrace step attachment and dissociation for diffusion of large-sized entities], $1/\tau = 1/\tau_{reevaporacion} + 1/\tau_{nucleacion} + 1/\tau_{attachment} + 1/\tau_{dissociation} + \ldots$, being the lower time the rate-determining step that set up the diffusion length being $\tau_{nucleation} \approx 1/\rho_1 D$, with $\rho_1 \approx \sqrt{F/D}$ [4, 5]. So, for low mobility conditions, the diffusion length is limited (it decays until $\approx$100 nm), and becomes only a fraction (<1/10) of the pseudo-thermodynamic diffusion length $\propto$ 1000 nm.

As a consequence, it was expected to obtain film microstructures ruled by kinetic limitations hindering both structural and morphological relaxations during growth. The film thickness was ranged from $d = 2$ to 1200 nm in order to develop a full-range analysis of the growth process. The surface morphology was imaged by AFM using ultra-sharp tips (see §2.3) and by SEM. X-ray diffraction experiments in θ-2θ and ϕ-scan configurations were also carry out in a Bruker D8 four-circle diffractometer using CuK_α radiation. From XRD measurements, we determine that both the intermediate Au layers and the Au polycrystalline films exhibited a preferred out-of-the-plane Au[111] texture (of around 80%) as discussed below in §3.1.3. The growth experiments were carried out in the thermal evaporation equipment of the group of *Solid State Optics* at Instituto de Física "Torres Quevedo" (ICFA-CSIC) in Madrid, Spain.

Growth Parameters	Range of variation	Instrumentation/Description
Evaporant	Au	· Au wires of 1 mm in diameter with purity of 99.99%
Coated Substrate	Au(111)/mica	· 200 nm-thick Au(111) intermediate layer grown on freshly air-cleaved high quality mica(v-5) supplied commercially in form of 0.26–0.31 mm thick sheets at $T = 673$ K (0.5 $T_{melting}$)
Evaporation process	evaporation rate 1 nm/s	Thermal evaporation in vacuum from an effusive cell source made of resistive heating of a Mo crucible of 1 cm^3 with wall thickness of 0.05 mm · Cosine law distribution of evaporated material with an angular dispersion of ± 5º
Deposition	373 ± 6 K (0.28 $T_{melting}$)	· Temperature ramp induced by resistive heating with feedback monitor · Stainless steel frame in thermal contact with a heating/cooling system for substrate holding · Thermocouples K fixed at the substrate bottom to monitor the deposition temperature
Base pressure	10^{-7} mbar (high vacuum)	· Turbo molecular an rotary vane pumps
Film thickness	2 - 1200 nm	· Quartz balance as thickness monitor ±1 nm

Table 3.1 Experimental parameters for the Au film deposition by evaporation

3.1.2 Surface morphology evolution during film growth

AFM measurements were developed to investigate the morphology evolution of polycrystalline Au(111) overlayers during film growth. Figures 3.2(a)–3.2(h) show topographies of such overlayers for several deposition times (or film thicknesses). In order to quantify such morphology evolution, Figures 3.3(a)–3.3(c) plot the deposition time-dependences of several statistical parameters, such as: in-plane grain sizes λ (Figure 3.2a), surface roughness ω (Figure 3.3b), and both local slopes m and the corresponding terrace-width values $nr \propto 1/m$ obtained at the grain border regions (Figure 3.3c-*left* and -*right* side, respectively). Because in one AFM image can be observed different length-scale entities (e.g. compare the small regular round grains of ~100 nm bundled into large irregular flat multigrain structures of ~1 μm (termed hereafter plates or domains) in Figures 3.3a to 3.3e), the morphology analysis was performed at different length scales (in connection with characteristic sizes of each).

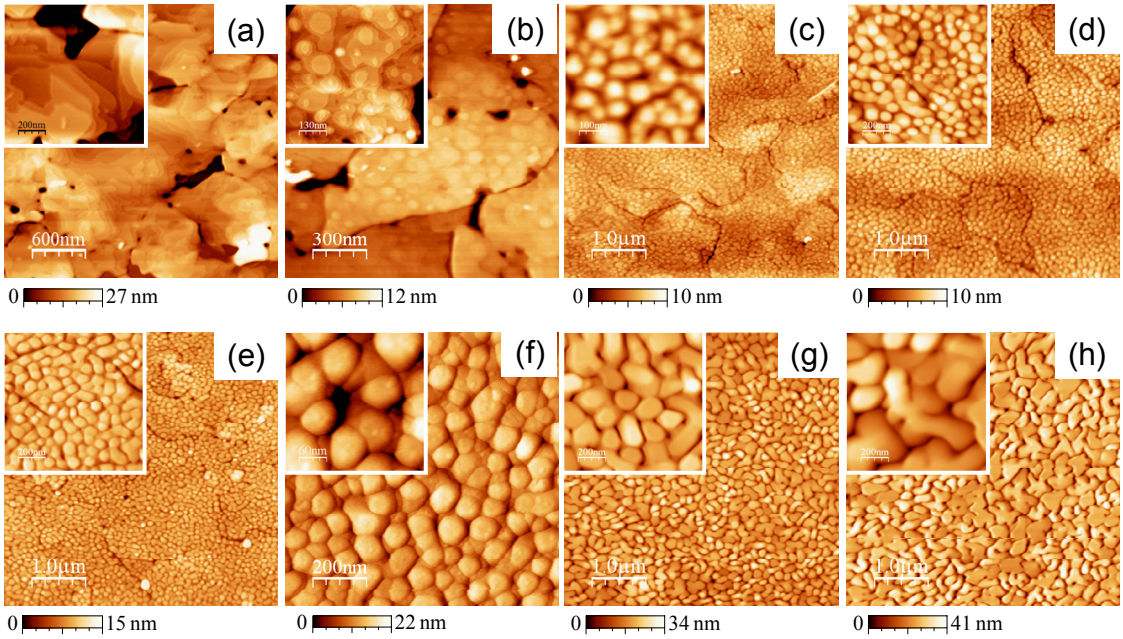

Figure 3.2 Surface morphology evolution of Au overlayers. Deposition times: (a) t=0 s, (b) 2 s, (c) 8 s, (d) 16 s, (e) 60 s, (f) 200 s (g) 600 s and (h) 1200 s. *Insets*: Specific details and short-range motif of each morphology.

Consequently, the statistic parameters were obtained for complementary length scales, and defined by using a set of indices referred to: [*no index*] —generic information obtained on the AFM images before being ascribed to a particular surface feature; sub-index *g* —local data measured on the grain-size scale (e.g., ω_g —intra-grain roughness (i.e. the roughness inside large grain structures of the substrate), λ_g —grain size and $\hat{m}_g$ —slope at the grain borders in Figures 3.3(a), 3.3(b) and 3.3(c), respectively); sub-index *s* —analogous information but referred to Au layer domains (ω_s (or the film surface ω), λ_s and $\hat{m}_s$ in Figs. 3.3(a), 3.3(b) and 3.3(c), respectively); and index "' "—data acquired on irregular (melted-like shaped) multigrain structures (λ_s' and $\hat{m}_s'$ in Figures 3.3b and 3.3c). In order to clarify such dissimilar length-scale parameters, table 3.1 illustrate their meaning.

Surface entity	Physical meaning of shape parameters	
Au layer domain (microns)	l_s = domain size m_s = slope at the outer gaps of domains	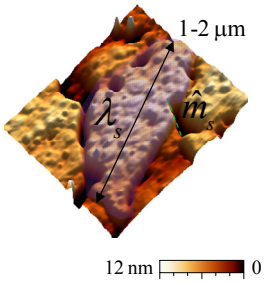
Multigrain structure (hundreds of nm)	l'_s = multigrain size m'_s = slope at the outer gaps of multigrains l'_g = grain size (referred to departing grains)	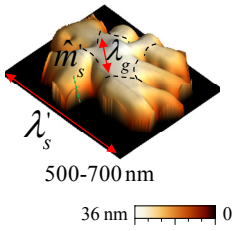
Round grain (tenths of nm)	l_g = grain size m_g = slope at the outer gaps of domains	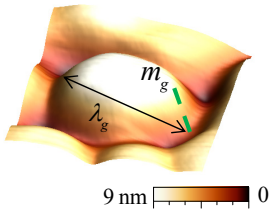

Table 3.2 Physical meaning of dissimilar length-scale shape parameters.

Considering that the GBs between touching features emerge toward the surface at a gap region confined laterally by the feature borders, a threshold border slope of $\delta m = 0.15$ was assumed to distinguish between internal GBs (those with $\hat{m} \le \delta m$) and external ones ($\delta m < \hat{m} < m_{tip}$, see §2.5 for details). On the other hand, the surface discontinuities are characterized by exhibiting $\hat{m} \ge m_{tip}$, where $2m_{tip} \approx 1.2\text{-}1.3$ corresponds to the effective aspect-ratio of the AFM tips calibrated on the surface of the roughest sample (i.e. m_{tip} is the appraisable maximum slope by AFM on continuous surfaces).

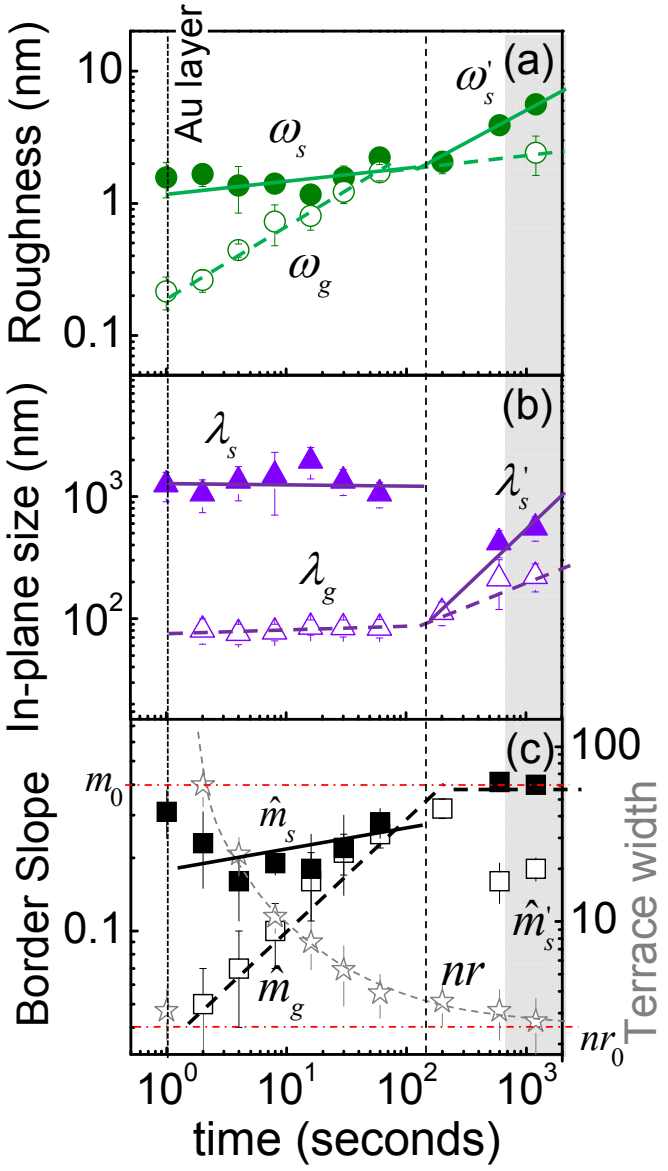

Figure 3.3 Evolution of the statistical parameters averaged on a large set of surface entities during Au(111) film growth: (a) surface roughness ω, (b) in-plane (out-of-plane) sizes λ ($\lambda_\perp$), and (c) surface slopes m and terrace width nr obtained at the entity borders.

The surface morphology of the Au layers (remembering, the intermediate Au layers grew above mica as illustrated in Figures 3.2a and 3.4a) is composed by plates or domains decorated by terraces and steps associated to screw dislocations where the round grains of the Au overlayer attach, which have an average in-plane size of $\lambda_s \approx 1250 \pm 340$ nm, as observed in Figure 3.3(b). Even for $t = 60$ s, it is still possible to distinguish this underlying structure of the Au layer, which suggests that for later growth regimes large domains are buried into the film microstructure (Figures 3.2d and 3.4c). These domains have a low intra-grain roughness of $\omega_g \approx 0.2 \pm 0.1$ nm (Figure

3.3a), a near constant in-plane size during growth, and are delimited by sharp and deep external boundaries of $\hat{m}_s = 0.3 \pm 0.1$, which confers a high inter-domains roughness of $\omega_s \approx 1.6 \pm 0.5$ nm to the film.

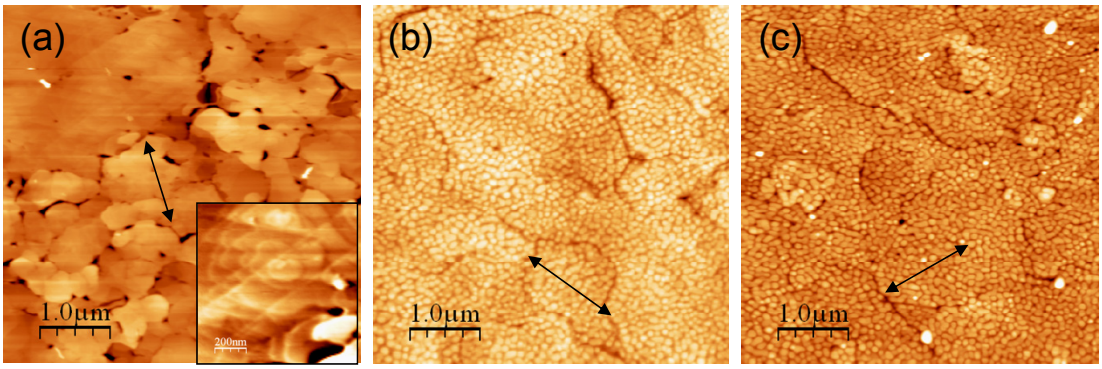

Figure 3.4 AFM topographies of large domains and round grains growing above them, taken at different growth times: (a) t = 0 s (prepared Au layer), (b) t = 16 s, and (c) t = 60 s. As observed, the morphology features of these entities remains constant during growth, supporting small changes as growth proceeds. In Fig.3.4(a) inset, a detail of the vicinal structure of the surface of a large domain of the Au layer.

During the growth of Au overlayers onto the Au layer domains, two morphology regimes with peculiar features can be distinguished:

(***Early regime***, Figures 3.2b to 3.2e): For $t < 4$ s, the nucleation of flat entities of 3–10 ML in height (islands hereafter) is observed. These islands nucleate preferably at the steps of the large terraces within the Au layer domains, as can be observed in Fig. 3.5. This fact points to an asymmetry in the interlayer mass transport phenomena caused, as a first approach, by the presence of large step energy barriers hindering interlayer diffusion. In this scenario, adatoms moving along the upper terraces (those who are in higher positions in reference to the substrate, or to the level of height = 0 nm in the SPM image) and reaching the step edge will be reflected mainly onto the upper terrace, with a low probability to diffuse towards the lower terraces. The reflected adatoms quickly find other adatoms coming from successive reflections at other positions of the step edge (especially if the step edge is curved, like in the shown in Fig. 3.5, because this configuration enables to "focalize" reflected adatoms in a specific point of the upper terrace), from diffusion towards the step edge and/or from the growth flux, and small entities like dimers are trimers develop near the step edge, forming the "seed" of the flat entities observed. The reflected adatoms therefore generates preferred "uphill" surface

currents against the "downhill" ones, which would move material towards lower terraces.

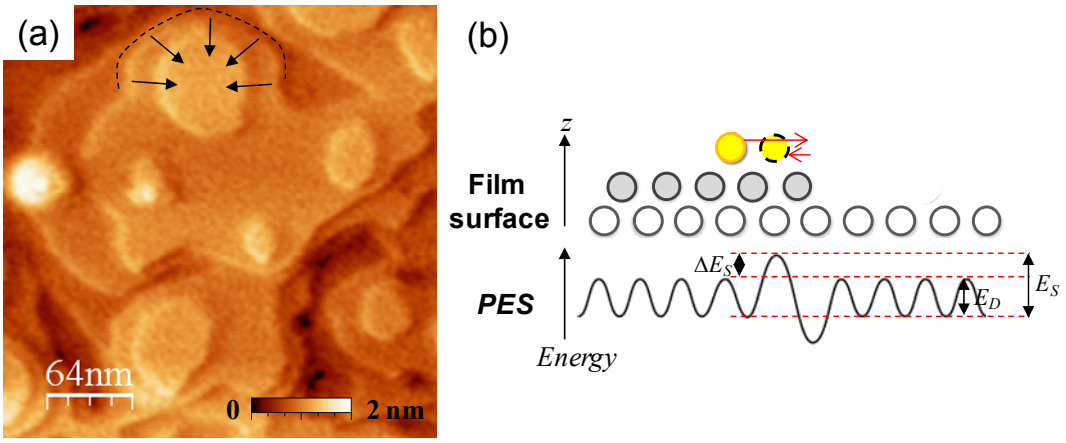

Figure 3.5 (a) AFM image of an Au film of t = 2 s. The dashed line highlights a terrace step edge of the 4th monolayer, whereas arrows indicates uphill surface currents due to adatom reflection from step edges as a consequence of high energy barriers. (b) Ball model showing an scheme of the process of reflection due to high energy barriers at step edges E_D and E_s are the diffusion and barrier energies, respectively.

For $8 < t \leq 60$ s, uphill currents and nucleation within upper terraces is observed. The surface morphology evolves into small and round grains, also termed mound-like morphology elsewhere [5, 83, 84]. These small grains have no apparent internal grain boundaries, reason why we identify them as surface single-crystal grains as we will discussed later from XRD spectra and selected area electron diffraction experiments and transmission electron microscopy images. The tendency to in-plane compact shapes indicates that intralayer diffusion is more favourable than interlayer one (i.e. jumping off step-edges is less probable), which hinders the surface morphology relaxation [4]. Then, small grains keep their lateral sizes pseudo-constant in this regime, with $\langle \lambda_g \rangle = 81 \pm 4$ nm (which agrees with a slight time-scaling dependence $\lambda_g \propto t^{p=0.02}$, Fig. 3.2(b)), and growth precedes in height preferentially inside large domains. the absence of coalescence phenomena induced by grain coarsening is evident [54]. As a consequence of such phenomenon, the intra-domain roughness increases strongly as $\omega_g \propto t^{\beta=0.52\pm0.05 \geq 1/2}$, whereas the inter-domain roughness varies slightly over time $\omega_s \propto t^{\beta=0.08\pm0.01}$ (with $\langle \omega_s \rangle = 1.6 \pm 0.3$ nm for t = 2 – 200 s). Because: $\omega_s \approx 10\omega_g$ for $t < 4$ s, $\omega = \sqrt{\omega_g^2 + \omega_s^2} \approx \omega_s$. The high values of ω_s are the consequence of the different height between domains, which also have deep GBs also with variable depths.

According to dynamic scaling, $\beta \geq 1/2$ defines a preferred growth in height of the round grains, which supports our hypothesis of the presence of high energy barriers during growth, with grains that are uncorrelated at longer-range scales (long-range here is referred to sizes larger that the terrace width) [4]. For $8 < t \leq 60$ s the flat domains of the Au layer are buried, and therefore $\omega \propto \omega_g \approx \omega_s$. This observation is also supported by the scaling dependence of the local slopes m, which follows a power-law dependence $\hat{m}_g \propto t^{z=0.7\pm0.1}$ and tends to a saturated (or selected) slope of $m_0 = 0.40$ around $t \approx 100$ s (symbol ■ in Figure 3.3c). The surface slopes of the GBs between domains keep pseudo-constant during growth, being $\langle \hat{m}_s \rangle = 0.3 \pm 0.1$. Note that $\langle \hat{m}_g \rangle \approx 0.8 \langle \hat{m}_s \rangle$ for $t < 60$ s, which indicate that strong kinetic limitations hindering surface relaxation enable small round grains of the Au overlayer to reach the slope values of the domains of the Au layer (at least until they are visible). Round grains continue growing preferably in height until reaching a slope saturation value m_0 for late growth stages (with $m_g \rightarrow m_0 = 0.4$), surpassing the m_s values while domains of the Au layer are buried. In fact, recent studies of similar Au films grown at room temperature shows that $\hat{m}_g \geq m_{tip}$, also supporting the hypothesis of a preferred growth in height ascribed to hindered interlayer mass transport due to the presence of high energy step edge barriers [71]. The presence of a no coarsening scenario [5] implies slight lateral (in-plane) interactions between grains, which causes that the grain growth will be slower that the development of preferred facets during this *Early regime*. This process delays the coarsening between surface grains until late stages of growth (for $t > 100$ s) as observed in Figures 3.6(a-c) and 3.6(d), in which AFM image and cross-section profiles showing isolated grains are depicted. In Figure 3.6 it can be observed how the average in-plane size of grains $\langle \lambda_g \rangle$ remains almost constant in this early regime while increasing the slope at the flanks of the grains. (*Late regime*, Figures 3.2f to 3.2h): For $100 < t < 1200$ s the surface morphology is dominated by a high density of rounded grains, and any apparent registry of the Au layer domains is lost in this regime, suggesting that the domains have been buried. The density of grains decreases, indicating the beginning of coalescence between them. In this beginning of the *Late regime* we are no able to discern any inner GB inside surface entities, reason why we can continue defining them as single crystals (crystallites), with $\omega = \langle \omega_g \rangle = \langle \omega_s \rangle$,

$\lambda = \langle \lambda_g \rangle = \langle \lambda_s \rangle$ and $\hat{m} = \langle \hat{m}_g \rangle = \langle \hat{m}_s \rangle$. However, for $t > 600$ s irregular shaped surface entities are observed, which have inner shallow GBs (with slopes $\approx 0.15 m_{tip}$), as shown in Figs. 3.2(h) and 3.3(e). Such surface entities will be termed hereafter "bundles" of smaller grains, or multigrain structures. At this stage of growth, the temperature surpassed in $\approx$20-30 K[17] the desired growth temperature of T = 373 K, and atom diffusion improves slightly ($\propto \exp(E_D / k_B T)$, with E_D the energy for diffusion).

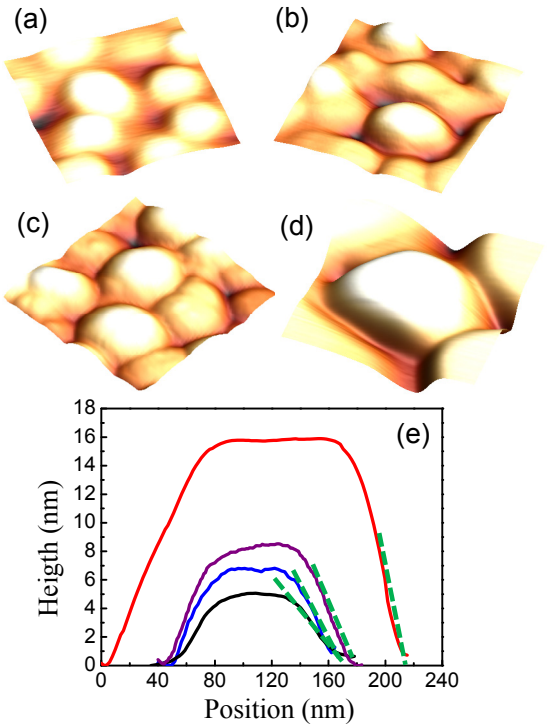

Figure 3.6 AFM image of several arrays of surface entities for different growth times: (a) 16 s, (b) 60 s, (c) 200 s and (d) 600 s. Each image has an area of 250 × 250 nm^2 and a vertical scale of 18 nm. (e) Cross-section profiles of relevant entities showing that for early regimes the grain size remains almost constant, and it coarsen for later ones. The dashed lines highlight the continuous increase in the slope values.

Because irregular-like shaped grains were observed in this stage of growth (without the presence of abnormal grain with sizes far away from the average grain size), we relate this coalescence phenomenon to the classical peer-to-peer coalescence by material sharing involving local atomic exchange to fill gaps between grains. In this stage of growth the inter-bundle roughness increased as $\omega_s' \propto t^{\beta'=0.5\pm0.1}$ (i.e., the bundles grow in height with no correlation between each other), whereas ω_g inside bundles kept almost

[17] The temperature feedback failed to maintain the temperature nearly constant for t > 1000 s.

constant. Multigrain structures coalesce at this stage, reason why they continue growing for $t > 1200$ s, following the scaling law $\lambda_s^{'} \propto t^{p'=0.6\pm0.2}$ (Figure 3.3b). Because $p' \approx \beta'$, $\partial_t \hat{m}_s^{'} \to 0$ (Figure 3.3d). During the last years several works reported similar features that had been here observed here for Au film surfaces in a wide set of experimental conditions [80, 85] but in none of them, in our knowledge, a statistical analysis taking into account the heterogeneity of the surface morphology has been developed.

3.1.3 Evolution of the film texture by XRD and AFM during growth

With the aim to investigate the degree of film crystallinity (or film texture), two experiments were carried out: on one hand, XRD scans in $\theta - 2\theta$ and ϕ- scan configurations were accomplished to explore both the out-of-plane and in-plane crystal structure in the microscale (taking information from film regions within the range of micrometers, §2.4). By other hand, the AFM nanogoniometer-like method (local in-plane texture in §2.6.4) was used to track the in-plane texture upon film regions limited to a few hundreds of nanometres.

XRD $\theta - 2\theta$ scans were taken on Au films of several chosen growth times t = 2, 16, 200 and 600 s to cover all the growth stages, that is: nucleation and grain growth, coalescence, percolation and film closure. The out-of-plane orientations of the mica(v-5) substrates correspond to the crystal directions <002n> (with n = 1,2,...,11), which is expected as the mica is cleavage along the {001} basal planes. Regarding Au overlayers, one main orientation (and therefore a preferred out-of-plane texture) corresponding to Au[111] crystal direction (and its harmonic [222]) was observed at $2\theta = 38.179 \pm 0.001^{\circ}$ (and $81.700 \pm 0.001^{\circ}$), respectively. As observed in Fig. 3.7, due to the large penetration length of XRD in gold (~1μm) θ-2θ peaks ascribed to mica orientations were observed even for films of t = 600 s, although the intensity of such peaks decreases with the growth time. The same occurs with the Au orientations corresponding to the epitaxial Au layer. As a consequence, the analysis of the evolution of film crystallinity during the growth of the Au overlayer is difficult to achieve, because the peak intensity will be unscreened by the peaks of the epitaxial Au layer. In an attempt to overcome such difficulty, grazing-incidence XRD scans were developed, but the peak intensity observed was too low. Then, peaks ascribed to Au (111) orientations were assumed to be composed by two contributions, the Au epitaxial layer

and the Au overlayer. This assertion is supported by the fact that small increments in the peak width were observed as growth proceeds. Then, two pseudo-Voigt functions were applied to fit the experimental XRD peaks. From peak fitting we determine the width of the peaks, and using Scherrer's equation (§2.5.1) we obtained the out-of-plane grain size $\lambda_{\perp}$.

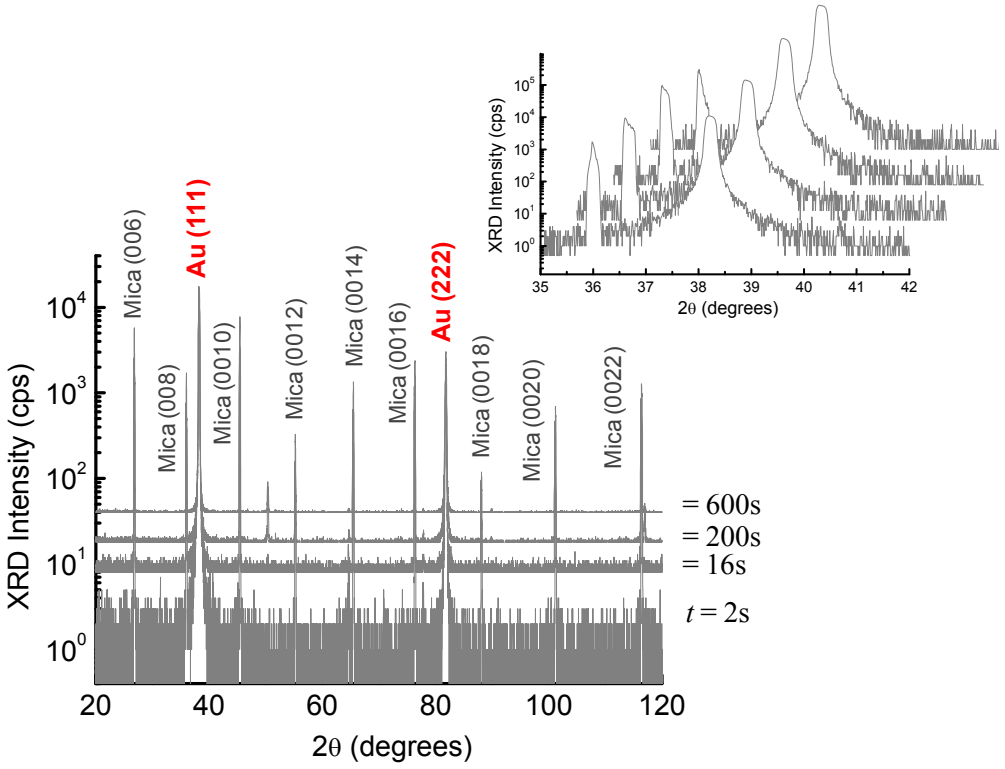

Figure 3.7 θ-2θ XRD scans for Au(111) films of several growth times: t = 2, 16, 200, and 600 s. (Inset) θ-2θ profiles of the peaks corresponding to the (111) Au crystal orientation. The profiles were shifted in a waterfall-like fashion in order to improve visibility.

From calculations, $\lambda_{\perp}$ values for the Au epitaxial layer remained almost constant, with $\lambda_{\perp} = 93 \pm 8$ nm. By other hand, the evaluation of $\lambda_{\perp}$ for peaks ascribed to the Au layer was only possible for films with thickness ≥ 60 nm (when peak spreading was appreciable), resulting in $\lambda_{\perp} = 56 \pm 10$ nm. The fact that the components of the peak ascribed to the epitaxial Au layer were wider suggest that the Au overlayer introduces noise to the measurement, which is expected if such a layer has a polycrystalline-like structure.

By measuring the interplanar spacing between planes (*hkl*) from the Bragg's law $d_{hkl} = \lambda_{XRD} / 2\sin(\theta)$ we estimate the average strain in the Au overlayers. For this purpose, the slightly shifts of the mica (000*n*) peaks from its expected positions in the

$\theta-2\theta$ scans were corrected, and then the real shifts of the Au (111) [and Au (222)] peaks from their expected positions were also determined. Once the d_{111} [d_{222}] were calculated, the lattice parameter of gold was straightforwardly obtained by using the relation $d_{hkl}=a/\sqrt{h^2+k^2+l^2}$ between the Miller index and the lattice parameters of fcc materials, with a the lattice parameter. The residual stress was determined by the tensorial form of the Hooke's law $\sigma=-\frac{E}{2\nu}(a-a_0)/a_0$ in order to relate the in-plane stress with the out-of-plane strain, where $E=$ 79 GPa is the Young's Modulus, $\nu=0.44$ the Poisson ration and $a_0=0.4078$ nm the equilibrium (unstrained) lattice parameter of gold. By using such relations, the average residual stress value was estimated to $\sigma=$ -5.3 ± 1.2 MPa, the sign ascribed to the compressive nature.

As described in §2.4, the in-plane texture of the films provides useful information concerning the spatial registry of grains during growth. The usefulness of such analysis resides in investigating the in-plane interactions along the azimuthal direction between grains that can cause, as an example, phenomena of grain reorientation via perimeter currents and shear strain with a torsion contribution. Here, the in-plane texture was investigated at dissimilar length scales by using different techniques: (*a*) in the nano and mesocale AFM-nanogoniometer was used by inspecting azimuthal ϕ-dependence of the local slope distribution $M(m,\phi)$ (§2.5.3). Such analysis assumes that for large enough single-crystal grains in which the surface tension does not control their shapes, the azimuthal distribution of their facets (a slope range can be ascribed to each facet) is connected with the in-plane orientation of the grains, and thus with the in-plane texture of the film by making statistics over representative AFM images. On these premises, the $M(m,\phi)$-based analysis has been previously used to study the in-plane texture (termed there as surface orientation map, SOM) in nanostructured systems and polycrystalline films at space scales far below the DRX lateral resolution limit [53, 86, 87].

(*b*) In the microscale range we used XRD ϕ-scans in order to determine the population of 18.4-tilted Au(420) planes [46] and to inspect the film in-plane texture at X-ray spot-size scale (macroscopic areas of few mm^2, Figure 3.9). Figures 3.8(a) to 3.8(d) show both $M(m,\phi)$ distributions and azimuthal profiles corresponding to the mode slopes of the distributions [symbol (○) in Figure 3.8 –*right*], and the ϕ-scans obtained by XRD [solid lines in Figure 3.8 –*right*].

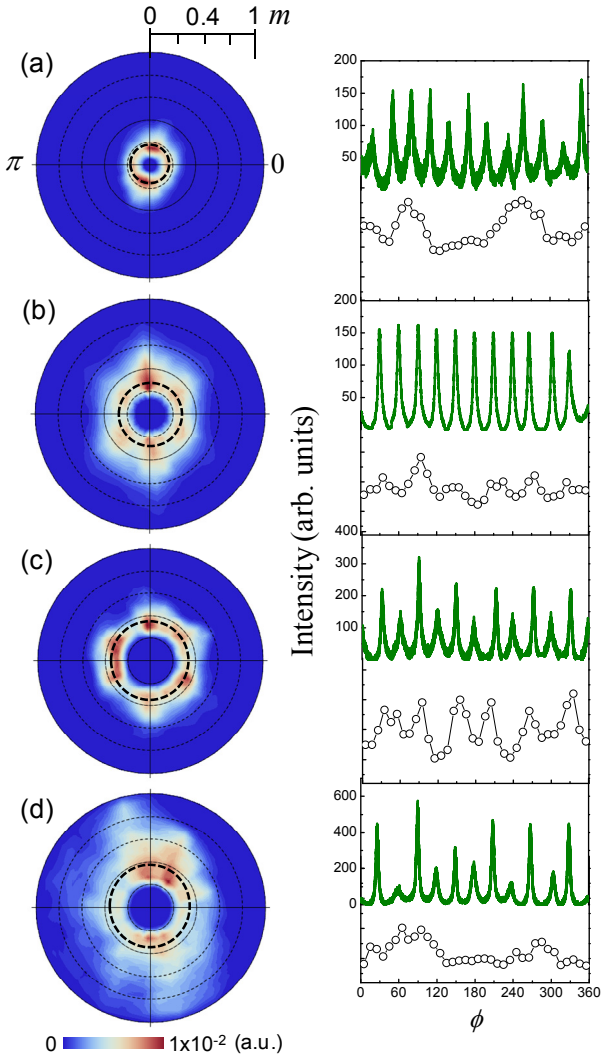

Figure 3.8 (a) Typical $M(m,\phi)$ spectra for an Au(111) films grew at several times: (a) 16 s, (b) 60 s, (c) 200 s and, (d) 1200 s.

As observed from $M(m,\phi)$ distributions, at the initial stages of the *Early regime* ($t < 2$s) small grains inside the Au-layer domains exhibit random in-plane orientations, even at the beginning of the *Late regime* ($t < 600$s). This well-defined grain orientation is distorted towards the end of the late regime of growth ($t > 600$ s) (Fig. 3.8d), where the development of large entities with a melted-like shape contributes to the distortion of the six-fold orientation even for images of reduced area (1×1 μm). Then, such a distortion could be understood as a fingerprint for interactions between small grains, promoting grain reorientation and peer-to-peer coalescence. At the microscale ϕ-scans of Au overlayers and Au layers show a well-defined twelve-fold orientation, which suggests that the crystalline coherence between domains was roughly maintained during

the growth of the overlayer. The peaks observed in the ϕ-scans correspond —in agreement with results reported in early growth studies on Au/mica films [72]—, to the $\mathrm{Au}(111)[1\bar{1}0]\,||\,\mathrm{mica}(001)[010]$ (or $\mathrm{Au}(111)[1\bar{1}0]\,||\,\mathrm{mica}(001)[100]$) orientations and it stacking-fault partner, e.g. the crystal structure developed for an inversion plane perpendicular to the "film in-plane".

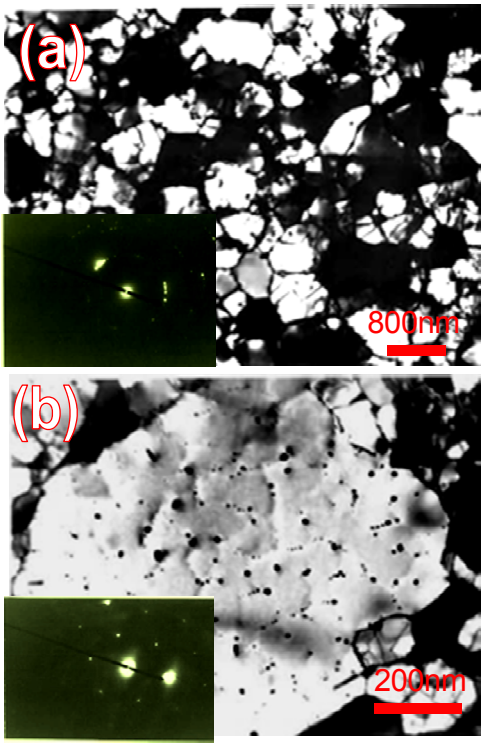

Figure 3.9 Transmission Electron Microscopy (TEM) images of Au overlayers (t = 200 s) grew at 373 K. (a) At length scales including several grains the film has a polycrystalline structure, as confirmed by the random pattern of the Selected Area Electron Diffraction (SAED) image (*inset*). (b) At contrast, individual multigrain structures of ~ 200 nm in size, which are composed by small grains separated by shallow boundaries (low contrast structures), shows a near-perfect single crystalline SAED pattern (*inset*); suggesting that they are low-angle or coincidence-site-lattice boundaries. TEM-SAED experiments were developed previously by Dr. Enrique Rodríguez Cañas at the Materials Science Institute of Madrid.

In pre-coalescence stages of growth (i.e. when grains are separated to each other by empty spaces), such orientations were ascribed to twinning (double positioning) phenomena [72, 88], in which large grain structures have two equally-probable orientations. This twelve-fold symmetry is not observed in general in the local $M(m,\phi)$ distributions because: (i) the AFM areas inspected only include the small grains inside domains of the Au layer. The fact that the twelve-fold orientation is not observed for the growing grains in the Au overlayer suggests that such films have a polycrystalline structure. Indeed, it has been shown from Selected Area Electron Diffraction (TEM-

SAED) that individual large grains have an inner high six-fold in-plane texture, which has been termed a "near-single-crystalline" structure elsewhere [84], as observed in Fig. 3.8. Another fingerprint supporting such assertion is that the twelve-fold orientation of the Au epitaxial layer is distorted as growth proceeds. The distortion observed, i.e., the variation in the intensities of the peaks, could be attributed to the development of a polycrystalline overlayer. Despite small round grains are close enough to coalesce, they develop relatively sharp gaps and deep boundaries between them during early stages of film growth (Figures 3.2 and 3.3b). However, for late stages coalescence is apparent, giving rise to the development of multigrain structures. Then, peer-to-peer coalescence phenomena is delayed until late stages of growth, which is not expected because grains are close enough to coalesce even for growth times $t < 16$ s.

3.2 Thermal processing of polycrystalline Au films

3.2.1 Experimental details concerning film processing and characterization

Au films were deposited on SiO_x–covered Si(111) substrates at a nominal temperature of $T_{growth} = 100\ ^oC$ (0.28 $T_{melting}$) and a pressure of 10^{-7} mbar. The film thickness was $d =$ 200 nm for all samples with a deposition rate of $F = 10$ Å/s. This rate is two orders of magnitude higher than the typical rates (~ 0.1 Å/s) [83], which gives rise to a film microstructure ruled by kinetic limitations that hinder both the structural and morphological relaxations during deposition [89]. Once deposited, the flux was stopped and the samples were held at the growth temperature for an *in-situ* annealing (which enables the film relaxation) during $t_a = 1.2\times10^2 - 1.2\times10^5$ s under an Ar flux (P_{Ar}=1 atm). Afterwards, the samples were cooled quickly down to room temperature and investigated by atomic force microscopy (AFM) using ultra-sharp silicon tips. Such ultra-sharp AFM silicon tips have a nominal radius of 2 nm and an estimated aspect-ratio on calibration samples of $2m_{tip} \approx 1.5$. By other hand, the crystalline structure of the thermally annealed thin films was characterized by x-ray diffraction (XRD) in θ-2θ and ϕ-scan geometries measured in a Bruker D8 four-circle diffractometer using Cu K_α radiation. The thus-prepared films exhibited an out-of-the-plane Au[111] texture.

3.2.2 Surface morphology evolution during annealing

Figures 3.10(a) to 3.10(d) show the morphology evolution of the Au films with t_a as measured by AFM. Due to the heterogeneity of the surface features, the morphology analysis was performed at different length scales by using the image tessellation procedure (as described above in §2.7) in connection with characteristic sizes of each.

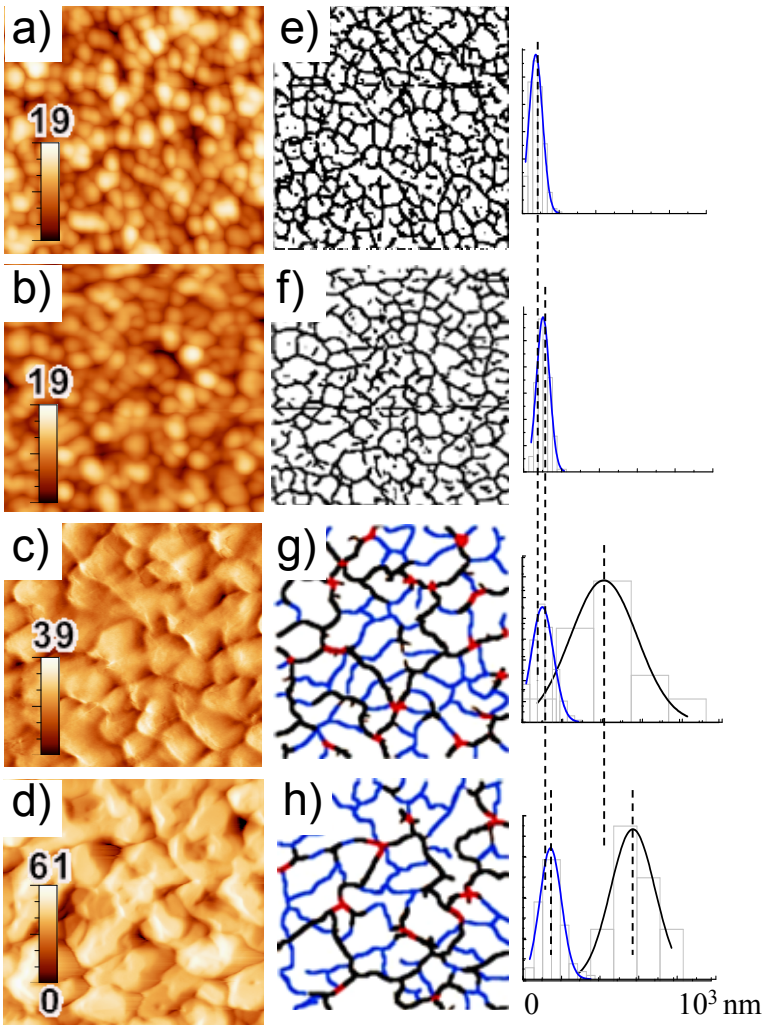

Figure 3.10 1×1 μm^2-AFM images of 200 nm-thick polycrystalline Au films with annealing times of (a) t_a = 0s (as-grown), (b) 3×10^2 s, (c) 3×10^3 s and (d) 1.2×10^4 s. (e-h) Tessellated surface in which the white, black [blue] and red regions/curves depict the inner areas of the surface features, the external [internal] GBs and surface discontinuities, respectively. *Right*: size distributions of the different types of coexisting surface features, where the curves/regions are colored accordingly the type of considered surface feature. The plots at the right show the size distributions ascribed to each type of surface feature, in the form of histograms. For small surface entities, each category has a width of 10 nm, whereas for larger entities the width is 100 nm. The curves over the histograms correspond to the best Gaussian fitting. Dashed lines are eye-guides for the shift of the mode of the normal distributions, which corresponds to the average surface entity size.

Thus, Figures 3.10(e) to 3.10(h) correspond to contour maps or tessellations of the AFM images. As observed, AFM tessellations are composed by contours of dissimilar color. Each color highlights a specific morphological domain of the surface or a type of boundary, so that:

- White regions depict the areas of surface features,
- Black curves delimit the grain boundaries delimiting them (external GBs),
- Blue curves show the internal GBs delimiting the grains inside larger features identified as grain bundles or structures, and
- Red points/curves point to surface discontinuities (grooves and holes).

In addition, at the right-side of each contour map the size distributions of the different surface features coexisting in each sample are plotted.

Figures 3.11(a) to 3.11(c) plots the variation of surface statistical parameters: roughness ω (Figure 3.11a), the in-plane size λ of the surface features (Figure 3.11b, left-side axis), out-of-the-film plane grain size $\lambda_{\perp}$ (Figure 3.11b, right-side axis), and the slope $\hat{m}$ at the flank bottoms of surface features (border slope hereafter, Figure 3.11c).

Due to the heterogeneity in the surface features the statistic parameters are defined for dissimilar length scales using a set of indices referred to: [*no index*] —generic information obtained on the AFM images before being ascribed to a particular surface feature; sub-index *g* —local data measured on the grain-size scale (e.g., ω_g —intra-grain roughness, λ_g —grain size and $\hat{m}_g$ —slope at the grain borders in Figures 3.11(a), 3.11(b) and 3.11(c), respectively); sub-index *s* —analogous information but referred to multigrain structures (ω_s, λ_s and $\hat{m}_s$ in Figures 3.11a, 3.11b and 3.11c, respectively); and sub-index *d* —data acquired on surface discontinuities ($\hat{m}_d$ in Figure 3.11c).

The grain boundaries (GBs) between touching features emerge toward the surface at gap regions confined laterally by the surface feature borders. In order to distinguish between internal GBs (those with $\hat{m} \leq \delta m$) and external ones ($\delta m < \hat{m} < m_{tip}$), threshold border slope values were defined. For inner GBs, the threshold slope value $\delta m = 0.15$ was chosen (as discussed in §3.1.2). Beyond, the surface discontinuities are characterized by $\hat{m} \geq m_{tip}$, where $2m_{tip} \approx 1.2–1.3$ corresponds to the effective aspect-

ratio of the AFM tips measured on the surface of the roughest sample (i.e. m_{tip} is the appraisable maximum slope).

The morphology evolution of the annealed films is described below in terms of: (*i*) grain growth and coalescence through t_a-dependence of λ and (*ii*) grain deformation via the t_a-dependences of $\hat{m}$ and ω since $\Delta\lambda$ ascribed to the grain deformation is much lower than the dispersion in λ due to the grain growth.

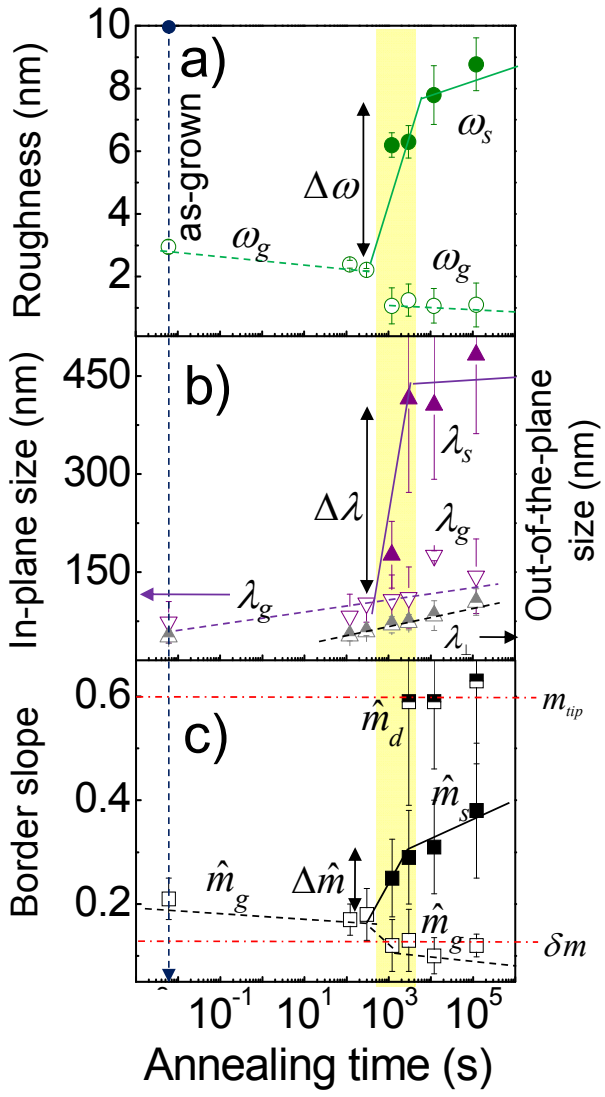

Figure 3.11 Evolution of statistical morphology parameters at different length scales: (a) roughness, (b) in-plane and out-the-plane sizes [λ —left and $\lambda_\perp$ —right axis, respectively] of the surface features, and (c) border slope $\hat{m}$.

As a result of the thermal annealing, two morphology regimes separated by a narrow transition (yellow bar in Figures 3.11a-3.11c) are distinguished: the early and late regimes.

The *Early regime* (Figure 3.10b) corresponds to short annealing times ($t_a \leq 3\times10^2$ s). In this regime, the as-grown morphology is roughly preserved. The grains grow (λ_g increases) and expand laterally. Thermally activated diffusion enables that the gaps between them become shallow (as the gap depth, that is $\propto\omega$, decreases) and smoother ($\hat{m}_g$ drops).

The *Transition regime* (Figure 3.10c) corresponds to intermediate annealing times (3×10^2 s $< t_a <$ 1.2×10^4 s). In this regime the film morphology changes (a melted-like morphology emerges), as revealed by the large variations of the statistical parameters $\Delta\omega$, $\Delta\lambda$ and $\Delta\hat{m}$. The fact that λ rises from λ_g up to $4\lambda_g$ suggests that this change is related to the peer-to-peer coalescence of the surface grains (understood here as a type of grain welding) into irregular-shaped structures (i.e., $\lambda \equiv \lambda_s$) rather than to normal or abnormal grain growth phenomena. This suggestion is supported by the following evidences and/or arguments: (*a*) Sections of internal GBs, which would correspond to the external GBs of the departing grains before coalescing, can be distinguished on the structure surfaces (blue curves in the upper inset of Figure 3.10c). This evidence is corroborated by the fact that the size of the areas delimited by the internal GBs shows a dependence on t_a similar to that found in the *Early regime* for $\lambda_g(t_a)$, which suggests that such areas correspond to the inner grain surfaces. (*b*) The different surface features —once classified them in grains/structures (features without/with internal GBs)— exhibits unimodal size distributions around λ_g and λ_s, respectively. (*c*) The irregular shapes of the large structures (as shown by the contour maps —compare upper insets in Figures 3.10(a) and 3.10(d) suggest that the growth mechanisms by atomic exchange between grains that compete to each other in which the shapes of the surviving grains are preserved (e.g., Ostwald-ripening [90]), play a minor role on the formation of such structures.

The *Late regime* (Figure 3.10d) occurs once the grain coalescence is completed (for t_a $> 1.2\times10^4$ s). In this regime the film surface is covered by large irregular structures, which are well separated to each other by external GBs and surface discontinuities. Internal GB sections are still visible on the surfaces of such structures, revealing their granular origin. In this regime, the statistical parameters exhibit behaviors opposed at different length scales: the large structures stop growing (λ_s remains constant) and shrink laterally generating deeper and sharper gaps (both ω_s and $\hat{m}_s$ increase). As a

result of the shrinking of the large structures, uncovered regions of the film bulk appear occasionally. By other hand, the inner grains slightly grow (λ_g continues rising) and the gaps between them tend to disappear ($\hat{m}_g$ decreases) such that structure tops are smoothed (ω_g remains low).

On the other hand, the grain growth kinetics reveals that whereas the shapes (in particular the λ_g / $\lambda_\perp$ -ratio with $\lambda_g \propto t_a^{0.14\pm0.02}$ and $\lambda_\perp \propto t_a^{0.10\pm0.01}$ as estimated from Figure 3.11b) of the surface grains is roughly preserved (λ_g / $\lambda_\perp$ = 1.7 ± 0.3) during thermal annealing, the structures are formed preferentially along the film surface (λ_g / $\lambda_\perp$ = 1.7 → 4.4), which indicates that the grain coalescence during the *Transition* (Figure 3.11c) involves mainly surface processes. This assertion is supported by the fact that the coarsening exponents $p = Log(\lambda_g) / Log(t_a)$ [p = 0.14 (in-plane) and p = 0.10 (out-of-the plane)] are lower than p = 1/4 (exponent predicted for an ideal surface grain growth [4] —see discussion below); and it is in accordance with the low annealing temperature (T_a = 100 °C) since higher temperatures are required to activate bulk recrystallization processes. Indeed, a similar morphology evolution to that obtained here was found for thinner (30 nm-thick) polycrystalline Au films subjected to dynamic annealing using temperature ramps [91]. The morphology of a 200-nm thick film growing by VW should correspond to a post-closure growth regime. In fact, it is widely observed that polycrystalline metal films of thicknesses even in the range of 15-40 nm have a post-coalescence surface morphology, i.e., the films are formed by considerable flat surfaces with channels. However, the experimental evidences observed in this study suggest that the surface grains keep the tendencies to coalesce and percolate that are typical of a VW coalescence stage indeed for film thicknesses in the range of 200 nm. These delayed tendencies of the surface grains can be addressed by the structure zone model, whose assumptions are summarized in Figure 3.12.

In brief, the Structure Zone Model states that during continuous film formation after nucleation, the film microstructure is generally dependent on four basic processes, shadowing, surface diffusion, bulk diffusion, and desorption. The last three are quantified by diffusion and sublimation activation energies. Shadowing is a phenomenon arising from the geometric constraint imposed by the roughness of the growing film and the line-of-sight impingement of arriving atoms.

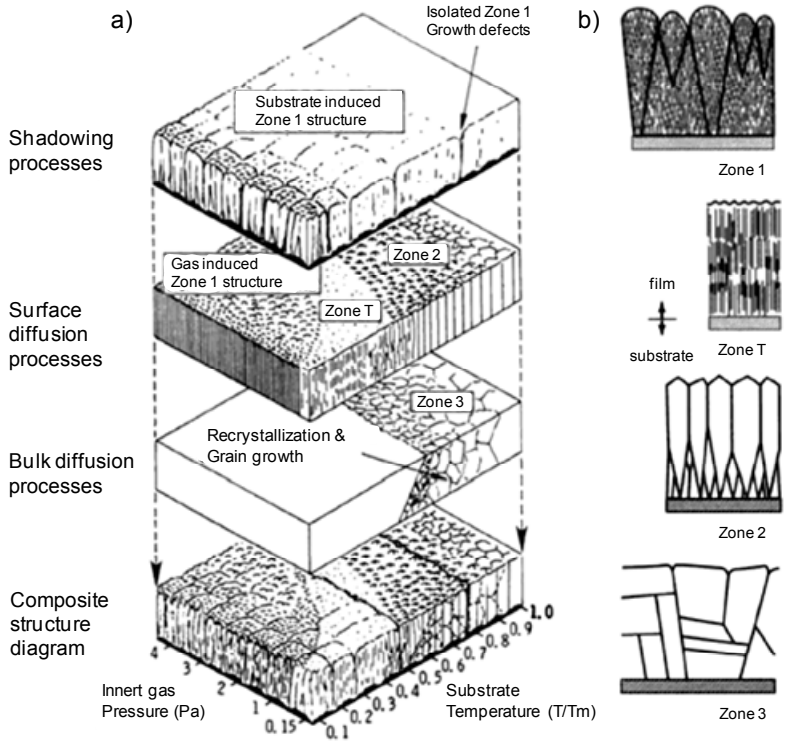

Figure 3.12 (a) schematic representation showing the superposition of physical processes which establish structural zones as stated by the structural zone model proposed by J.A. Thornton in "High rate thick film growth", *Annual Review of Materials Science* 7, 239–260 (1977). (b) Characteristics of the four basic structural zones in cross section. Adapted from J. M. Lackner *Bulletin of the Polish Academy of Sciences* 58, 281 (2010).

In this model, the description of the evolving structural morphologies in three structural zones (Zone 1, 2, 3 or SZMs, Figure 3.12a) can be accomplished by introducing the concept of "reduced" temperature" i.e., the ratio of the growth temperature T_{growth} to the melting point of the film $T_{melting}$. The formation and microstructure of the structural zones can be described as following (Figures 3.12a and 3.12b):

- Zones of quenched growth, where surface diffusion is moderate (temperature activated), here we have:

Zone 1, which consists of columns typically with tens of nm in size, separated by voids a few nm across. The columns have poor crystallinity (many defects) or are amorphous. In thicker films they become superimposed upon this structure an array of cones with wider voids between them. The cones terminate in domes at the surface and the size of the domes increase with film thickness. **Zone T**, that contains defected columns similar to those of Zone 1, but the voids and domes are absent.

- Zones of thermally activated growth and diffusion:

Zone 2, which consists of columns having tight grain boundaries between them and having a characteristic diameter which increases with $T_{growth}/T_{melting}$. Crystalline columns are less defected than in Zone 1 and T and are often facetted at the surface. **Zone 3**, in which the film is annealed just during deposition resulting in more isotropic, equiaxed crystallite shapes. Film surfaces are often smooth, but grain boundaries can develop grooves.

From such description, we can identify the surface morphology of our Au/SiO_x/Si(111) films on the zones 1 and T [92], that predicts for our deposition conditions (namely, $T_{growth} \approx 0.28\ T_{melting}$ and $F = 10^2 \times$ typical deposition rate) a film microstructure characterized by grains stacked in columns with the surface grains being belatedly generated by secondary nucleation phenomena.

In short, we can conclude from our results regarding to the coalescence and grain growth induced by post-deposition annealing at moderate temperatures, that the behavior of the layer of surface grains is equivalent to that of a free-standing thinner film with thickness $d \approx \lambda_{\perp}$, due to the continuity between the crystalline structure of film bulk and the surface grains is broken for thicknesses $>\lambda_{\perp}$. In our study, the polycrystalline film bulk below the surface layer allows us to minimize any potential influences of the substrate on the morphology evolution of the annealed films.

3.2.3 Evolution of the film texture by XRD and AFM during annealing

The out-of-plane texture was examined by XRD in the $\theta - 2\theta$ configuration. As observed in Figure 3.13, Au films have a preferred [111] out-of-plane orientation (label ● in Figure 3.13), with a 87 ± 13 %, as determined by comparison between the intensity of the peaks of the $\theta - 2\theta$ and the intensity of the same peaks in a reported powder diffraction. Other out-of-plane orientations observed were: (200) (label ■), (220) (label ♦), and (311) (label ▲) in 2 ± 1 %, 8 ± 3 %, and 3 ± 1 %, respectively. Such films were grew on a single-crystalline Si(111) wafer as a substrate (label ○). As observed in the inset of Figure 3.13, the full width at half maximum (FWHM) of the Au(111) peaks is reduced as annealing proceeds. The fitting of the peaks was achieved by pseudo-Voigt

functions. As stated by Scherrer's equation (Equation 2.1b), it implies an increase in the out-of-the plane grain size from ~50 to ~100 nm for ~10^3 seconds of annealing (see scaling in Figure 3.12b), taking into account that the width of the single-crystalline peak of Si(111) is 0.01.

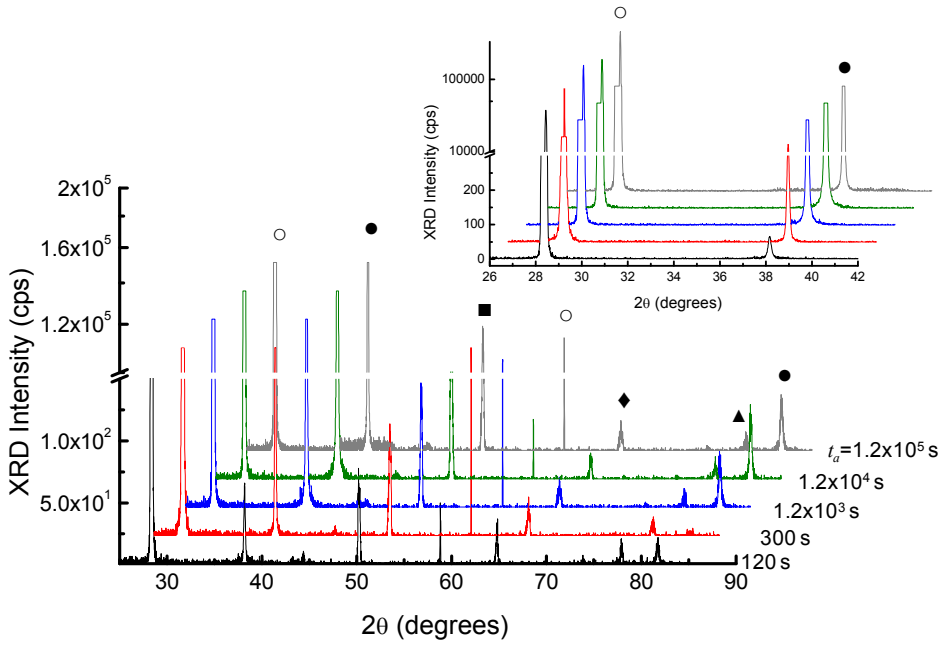

Figure 3.13 (a) $\theta/2\theta$ scan of a polycrystalline Au films annealed during several times. Labeled peaks are: (○) Si(111), (●) Au(111), (■) Au(200), (○) Si(222), (♦) Au(220), (▲) Au(311), (●) Au(222). The inset shows a zoom taken around the preferred (111) orientation of Si substrate and Au film, showing the thinning of the Au(111) peak, which becomes narrow as the annealing progresses [it is indicative of an increase in the out-of-plane grain size as estimated by Scherrer, see Fig. 3.12(b)].

Since the out-of-the-plane Au[111] orientation of the grains, $M(m, \phi)$-based analysis assumes that for large enough single-crystal grains in which the surface tension does not control their shapes, the azimuthal distribution of their facets (identified through the slopes describing their tilts to Au[111]) is connected with the in-plane orientation of the grains, and thus with the in-plane texture of the film by making statistics over representative AFM images. On the basis of these premises, the $M(m,\phi)$-based analysis has been previously used to study the in-plane texture (termed there as surface orientation map, SOM) in nanostructured systems [87, 93] and polycrystalline films [53] at space scales far below the DRX lateral resolution limit. Details concerning AFM image processing to compute $M(m,\phi)$ are reported elsewhere [55]. On the other hand, DRX ϕ-scan analysis uses (in our case) the azimuthal distribution of the population of 18.4°-tilted Au(420) planes to investigate the film in-plane texture at X-ray spot-size scale.

The azimuthal profiles $M(\bar{m},\phi)$, where $\bar{m}$ corresponds to the mode value of each distributions, are included in Figure 3.14 (right-hand lower plots) to compare with the corresponding DRX ϕ-scan spectra. Figure 3.14(a) discloses that during the deposition a random in-plane texture is generated (i.e., a ring-like structure emerges), which is preserved for $t_a \leq 3\times10^2$ s (*Early regime* in Figure 3.14b).

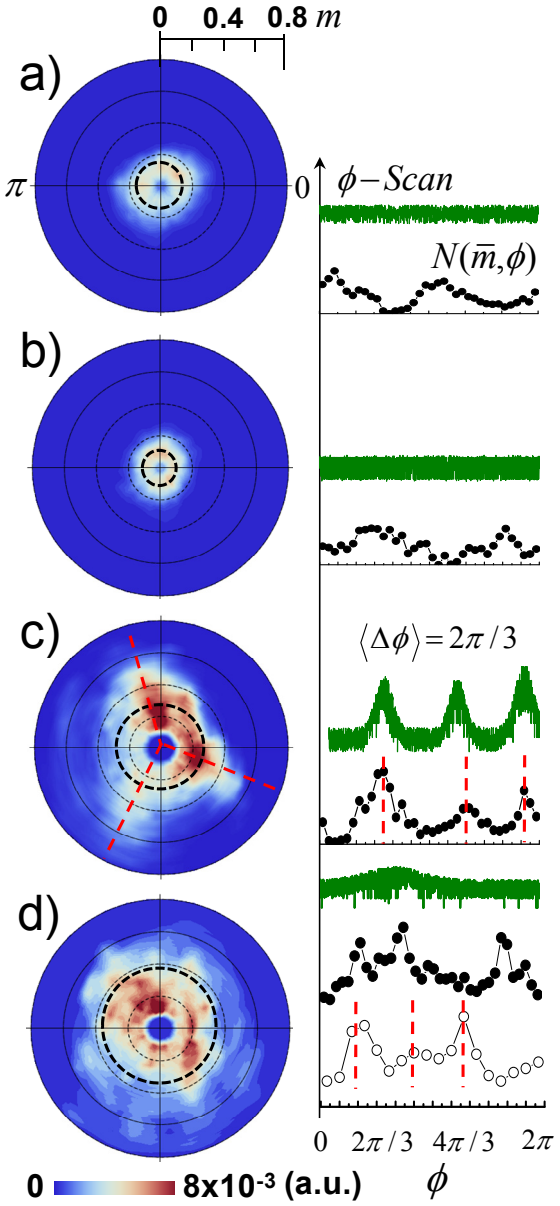

Figure 3.14 (Left-hand) Normalized ϕ-dependence of the slope distribution $M(m, \phi)$ for 200 nm-thick polycrystalline Au(111) films annealed at different times: (a) t_a = 0s (as-grown), (b) 3×10^2 s, (c) 3×10^3 s and (d) 1.2×10^4 s**.** (Right-hand) XRD ϕ-scan spectra around Au(420) planes [upper spectrum], and ϕ-profiles $M(\bar{m},\phi)$ acquired at inter- (●) and intra-structure (○) scales.

During the coalescence of the surface grains (*Transition* in Figure 3.14c) a 3-fold axis in-plain texture is suddenly formed as revealed by the profile $M(\bar{m},\phi)$, where three broad bands spaced $\langle\Delta\phi\rangle = 2\pi/3$ are distinguished. This result indicates plausibly that coalescence involves the rotation of the in-plane orientations of the neighboring grains (process termed **reorientation** hereafter) in order to minimize the misorientation between them and/or to decrease the GB contribution to the system energy. DRX ϕ-scan shows that the formation of such an in-plane texture is a massive phenomenon that spreads up hundreds of microns. Once completed the grain coalescence (*Late regime* in Figure 3.14d), the 3-fold axis in-plane texture is roughly preserved at nanometric scale inside single structures (lower profile). However, it worsens progressively at mesoscopic scale as several structures are considered (the bands in $M(\bar{m},\phi)$ are not longer evenly spaced —intermediate profile) and disappearing at macroscopic scale (the ϕ-scan spectrum shows a broad band —upper profile).

The progressive disappearance of the in-plane texture as the inspected area is larger suggests the existence of different in-plane reorientation mechanisms operating to dissimilar scales (in particular those responsible for the irreversible intra- and reversible inter-structure reorientation) and discards the possibility that the large surface structures (in Figure 3.10d) result from an grain growth based upon texture selection processes [94]. The fact that the polycrystalline film bulk isolates mechanically the surface layer from the stiffener Si substrate (as discussed above) makes possible the reorientation giving rise to the in-plane texture, which would be frustrated otherwise given the higher shear modulus of Si. Besides, the fact that the bands are wider (with full width at half maximum, FWHM~$\pi/6$) than those of single-crystal Au (FWHM < $\pi/45$) reveals the poor crystalline quality of the in-plane texture. This result suggests that the reorientation of the surface grains that underlies the in-plane texture involves the formation of pseudo-coherent GBs (with no-negligible misorientation angles $\theta \leq$ ½FWHM) rather than a perfect fit between the coalescing grains.

A detailed inspection of the DRX ϕ-scan bands (in Figure 3.14c) that correspond to the 3-fold axis in-plane texture is displayed in Figure 3.15(a).

Different kinds of pseudo-coherent GBs are possible:

(a) Low-angle GBs with $\theta = 0 - 4^{o}$: in this kind are included coherent GBs or no-GBs (for the specific case of $\theta = 0$). The development of this type of grain

boundaries involves a complete grain reorientation in order to give rise to a quasi-perfect fit (at nearest-neighbour atoms) of the GBs.

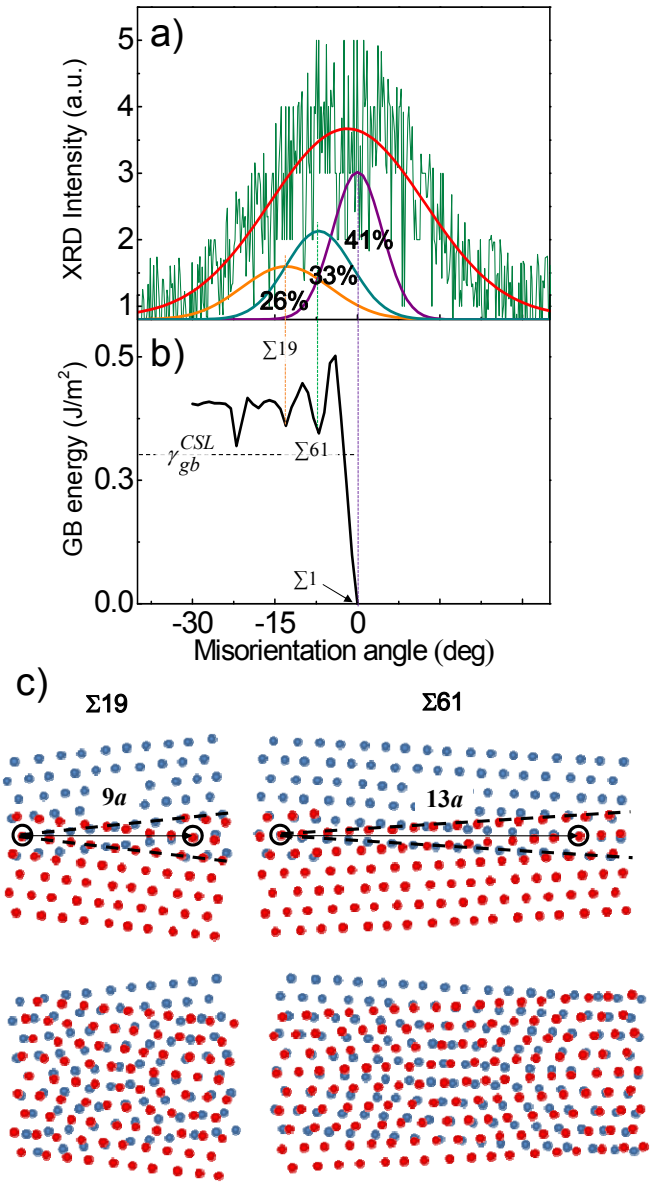

Figure 3.15 (a) Fit of a DRX ϕ-scan band to pseudo-Voigt peaks ascribed to the relative populations (labeled in %) of three types of pseudo-coherent GBs: Σ1 (θ = 0º), Σ61 (7º) and Σ19 (13º); (b) θ-dependence of γ_{gb} computed for Au(111) using EAM [J. Mei, J.W. Davenport, and G.W. Fernando, *Phys. Rev. B* **43**, 4653 (1991)]; and (c) (*top*) atomic configurations of the CSL GBs whose fitting periodicities are indicated in atomic spacing, *a*. (*bottom*) Superposition of lattices in CSL configurations forming Moirée patterns (enlarged with respect to the image of the top). The symbol "Σ" corresponds to the ratio between the number of lattice points in the lattice cell of a CSL and the number of lattice points in a unit cell of the generating lattice.

(b) Pretty "fitting" kind of GBs in coincident site-lattice (CSL) configuration: in this kind are included those GBs that are developed when relative orientations between grains have special angles so that if we rotate two lattices on top of each other some lattice points of the top lattice coincide exactly with some lattice points of the lower lattice, forming a Moirée pattern as observed in Figure 3.15(c). To reach those orientations, partial grain reorientations are required. As observed in Figure 3.15(b) for the case of Au films, the partial grain reorientations occurs towards GB configurations with long-range fitting periodicities. The lowest energy configuration Σ1 denotes a perfect (or nearly perfect) single crystal. These fitting periodicities are showed as sketches in Fig. 3.15(c) that correspond to local minima of the dependence of GB energy (γ_{gb}) on the misorientation angle θ displayed in Figure 3.15(b).

To estimate the contribution of each kind of GB to the in-plane texture, the DRX ϕ-scan band was fitted to pseudo-Voigt peaks ascribed to three GB populations: low-angle GBs ($\Sigma 1$), $\Sigma 61$ and $\Sigma 19$ whose positions were fixed to $\theta = 0^0$, 7^0 and 13^0, respectively. Because the DRX ϕ-scan band is wide, the pseudo-Voigt is similar in (>80%) to a normal-like distribution. The solid line in Figure 3.15(a) represents the convolution of the peaks corresponding to the best fit, which was obtained for relative populations of each kind of GB of $\cong 41\%$ ($\Sigma 1$), 33% ($\Sigma 61$) and 26% ($\Sigma 19$).

The θ–dependence of γ_{gb} computed for Au(111) was obtained by molecular dynamic simulations using the embedded atom model (EAM) proposed by Mei *et al.* [70] for fcc metals. In this model, the energy of an atom is expressed by $E_i = F_\alpha\left(\sum_{i\neq j}\rho_\beta(r_{ij})\right)+\frac{1}{2}\sum_{i\neq j}\phi_{\alpha\beta}(r_{ij})$ (where F_α is an embedding function that represents the energy required to place atom *i* of type α into the electron cloud, r_{ij} is the distance between atoms *i* and *j*, $\phi_{\alpha\beta}$ is a pair-wise potential function, and ρ_β is the contribution to the electron charge density from atom *j* of type β at the location of atom *i*), as detailed described in References [95, 96]. As observed in the Figure 3.15(b), two types of CSL GB-configurations with $\theta \leq \pi/12$ are available: at $\theta = 7^0$ ($\Sigma 61$) and $\theta = 13^0$ ($\Sigma 19$). The average energy obtained is $\gamma_{gb} = 0.34$ J/m^2, as indicated by the dashed line in Figure 3.15(b). The value of γ_{gb} obtained for Au(111) is in good agreement with

independent simulations using EAM potentials reported by Wen and Zhang (γ_{gb} = 0.3 J/m^2), which supports the validity of the EAM simulations employed [97].

We observe small shifts in the $\theta - 2\theta$ XRD peaks, suggesting the presence of residual stresses during film annealing. Because such displacements are small, we use the highly accurate $Sin^2(\psi)$ method to determine residual stresses. The results obtained are depicted in Figure 3.16 which shows [inset in (a)] the Au(111) X-ray peak used for the stress analyses in the Au/SiO$_x$/Si(111) system.

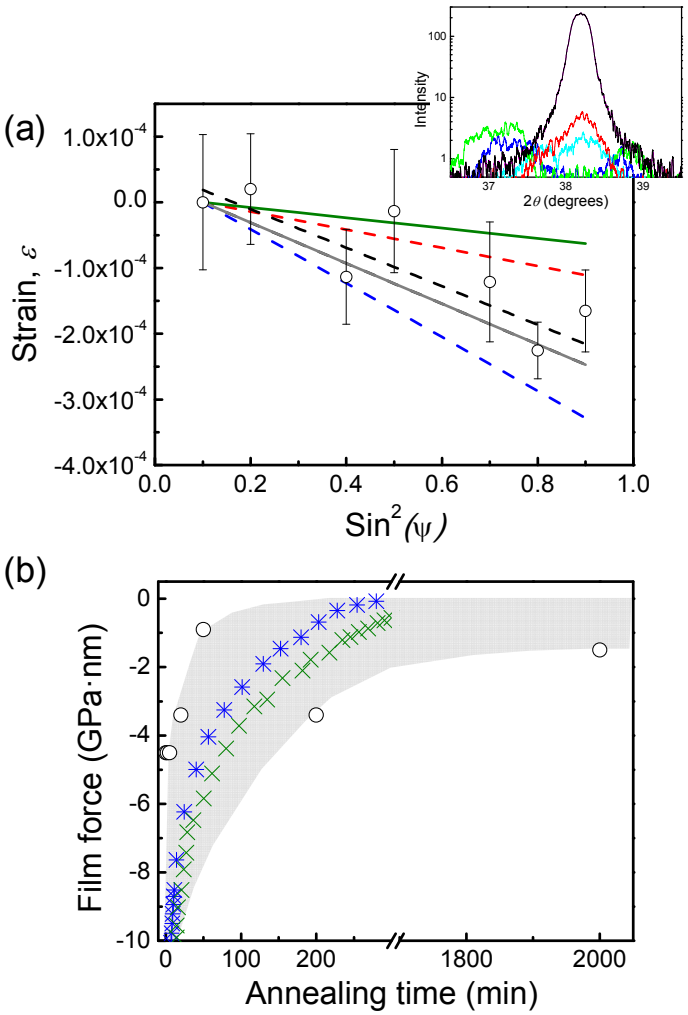

Figure 3.16 X-ray stress analysis measurements on Au(111)/SiO$_x$/Si(111) films. (a) *d-Sin^2(ψ)* distributions for polycrystalline Au films annealed during several times. Open circles show the *d-Sin^2(ψ)* for t_a =1200 s. In order to improve visibility, the rest of the growth times were represented by dashed lines representing the linear fitting. of the residual strain measurements, as: (blue) t_a =120 s, (grey) 3000 s, (red) 12000 s, (green) t_a =1.2x10^5 s. (*inset*) Au(111) reflections for various sample tilts ψ. Peaks shift are observed. (b) Film force values taken from the residual stress data (open circles). Labels (×) and (*) correspond to film force values taken from XSA analysis on Au polycrystalline films measured *in-situ* by the capacitance (R. Abermann and R. Koch, *Thin Solid Films* **129**, 71 (1985)) and cantilever beam methods (J. Leib, R. Mönig, and C.V. Thompson, *Phys. Rev. Lett.* **102**, 256101 (2009)), respectively. Dashed region corresponds to the fitting error estimated from data dispersion.

The Au(111) reflections was measured for various tilt angles ψ measured with respect to the scattering plane (see §2.5.3). The Bragg peak is seen to exhibit a tilt-dependent shift; which allows us to determine the $d - Sin^2(\psi)$ relation [or d distribution (§2.5.3)]. In Figure 3.16(a), the $Sin^2(\psi)$ distribution of a film annealed during t_a = 1200 s is displayed as open circle data, whereas for the rest of the annealed films the linear fittings are showed by dashed curves in order to improve visibility. For all the samples the inspected the strain is seen to decrease while increasing $Sin^2(\psi)$, which suggest the presence of residual compressive stress (negative slope). The results of the stress values (in the form of film force $\sigma \times$ *film thickness* , with film thickness = 200 nm) are showed in Fig. 3.16(b), and they are in accordance with film force values taken from experiments on Au polycrystalline growth in which the stress was determined *in situ* by capacitance and cantilever beam-based methods ("×" and "*" labels, respectively) [98, 99].

CHAPTER 4

PEER-TO-PEER COARSENING: INTRINSIC STRESS GENERATION AND RELAXATION DURING POLYCRYSTALLINE THIN FILM PREPARATION

4.1 Coalescence and stress generation during thin film preparation

During the development of a polycrystalline thin film, the interactions between surface entities like islands, mounds and grains modify the patterning of the thin film surface. Therefore, to prepare thin films with a controlled (desired) morphology by surface engineering and nanostructuration processes, it is interesting to identify the origin, nature, spatial distribution and evolution of the grain-to-grain interactions. Such interactions can cause grain coarsening (i.e., the increase in the surface entity size) by grain growth and coalescence. The former accounts for the atomic exchanges involved in: (normal grain growth) the homogeneous increase in the grain sizes by capture of atoms from the flux, the background density of mobile species or pseudo-amorphous regions; and (abnormal one) the inhomogeneous increase in the average size of a subset of grains that grow drawing atoms from the rest one. The abnormal grain growth is induced by hierarchical differences in sizes, slopes, neighbor numbers, and orientation; the atomic exchange being that caused by size differences (that is the driving force prevailing at early growth stages at lower coverages) is denominated Ostwald ripening so far. On the other hand, the coalescence identifies a *peer-to-peer* grain coarsening where the surface entities share material to each others rather than exchanging them. In this chapter, we will focus on grain coarsening by peer-to-peer coalescence, whereas the coarsening by an abnormal grain growth of the type generic Ostwald ripening extended to late growth stages is investigated in section §5.

Peer-to-peer coarsening causes the merging of two or more surface entities by diffusion of grain boundaries (Figure 4.1a). Larger single-crystal grains (or crystallites) are formed when coalescence occurs with a perfect matching between the crystalline orientations of the departing grains. Otherwise non-coherent multigrain (and then polycrystalline) structures are formed in which the small grains inside are separated by low-angle inner grain boundaries (Figure 4.1b. Coalescence can involve several mechanisms such as mass transport by: edge, surface, and GB diffusions; elastic interactions; and defect generation.

For solid bodies elastic interactions cause the development of strains in their structure. Such a strain describes the deformation of a body in terms of relative displacement of its parts.

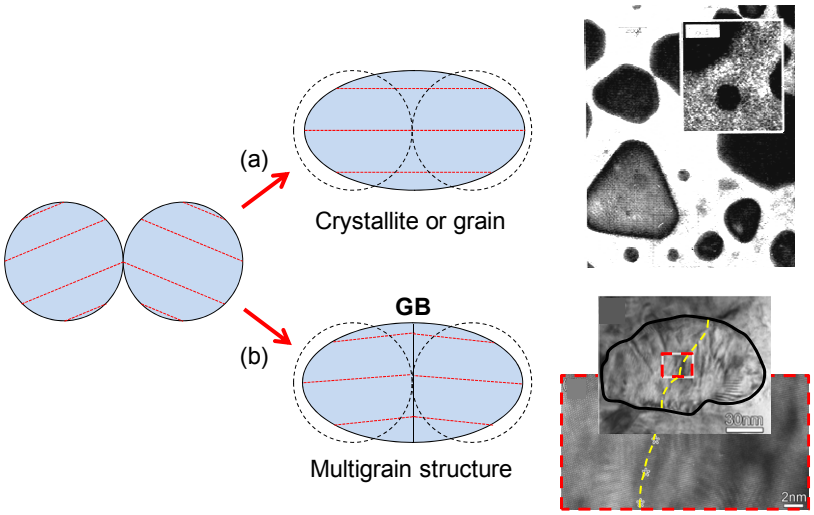

Figure 4.1 Coalescence between two individual grains, with the development of: (a) a single-crystalline grain (larger crystallite, with no inner boundaries) (b) or a multigrain (polycrystalline) structure in which the small departing grains are separated by internal grain boundaries (GBs). Graphs at the right side of the figure show examples of real surface entities. (*upper graph*) TEM image of an Au/mica surface (the inset show a magnification of an specific area) showing single-crystal grains of Au. The graph was adapted from H. Poppa *et al., Journal of Vacuum Science and Technology* **8**, 471 (1970). (*lower graph*) TEM image of a Ni multigrain structure (enclose by a black line). An inner GB is highlighted by the dashed yellow line. The inset corresponds to a HRTEM image of the area enclosed by the red rectangle. The graphs were adapted from Y. B. Wang *et al.*, *Appl. Phys. Lett.*, **92**, 011903 (2008).

Concerning crystalline solids, the generation of strain ε implies the elastic deformation of the crystalline structure, e.g., the modification of the unstrained lattice parameter (see §2.5.1). The application of external loads σ distributed along the surface of a continuous body produces an internal stress field that, by using the Hooke's law, results in the generation of an internal strain field.

Stresses can be originated by external perturbations (e.g. applied loads) and/or interactive forces between the constituent entities of the solid body (i.e., intrinsic forces), the total (macroscopic) stress (σ_Σ) a linear combination being of the intrinsic ($\sigma_{intrinsic}$) and extrinsic ($\sigma_{extrinsic}$) contributions, $\sigma_\Sigma = \sigma_{intrinsic} + \sigma_{extrinsic}$. The relation between σ and ε can be expressed by constitutive equations like the Hooke's law, $\sigma = M\varepsilon$ with M being the elastic modulus (units of N/m^2). Among extrinsic stresses, there are: (a) stress by applied mechanical loads; (b) by thermal expansion mismatch at the interface of dissimilar materials $\sigma_{thermal} = M(\alpha_f - \alpha_s)(T_{deposition} - T_{operation})$ with α_f and α_s denoting the film and substrate, respectively; and (c) by lattice mismatch, i.e. the difference between the lattice parameters of the film (a_f) and substrate (a_s), in hetero-thin film/substrate systems. By other hand, intrinsic stresses are mainly caused by the distortions of the crystalline lattice induced by defects (the surface being the major of

them); such that the stress is the restoring force of the lattice toward the minimum energy state. Intrinsic stresses are harder to prevent because they are caused by the same processes that take place during the film growth. As a consequence, a great amount of works can be found in the literature concerning methods to avoid and/or control the magnitude and spatial distribution of the intrinsic stress.

4.1.1 Intrinsic stress generation during film growth

During the growth of polycrystalline thin films, the evolution of the intrinsic growth stress, which has here its origin in the minimization of the system energy through the balance between surface and GB energies, exhibits several transitions (compressive→tensile→compressive, Figure 4.2a) as the film thickness increases during deposition experiments [100] or the grain size raises for post-deposition annealing both under high mobility conditions (growth or annealing temperature > $T_{melting}/4$) [18, 100]. The evolution of the growth stress was monitored by *in-situ* stress measurements taken in polycrystalline films of materials belonging to a large set of systems, namely: (b,c) ductile metals likes Ag and Al, (f) refractory metals –Ti, (d, e, g) massive semiconductors with different dopings such as p- and n-doped Si and p-doped Ge (Figures 4.2b to 4.2g). In all these systems the compressive-tensile-compressive behavior has been obtained.

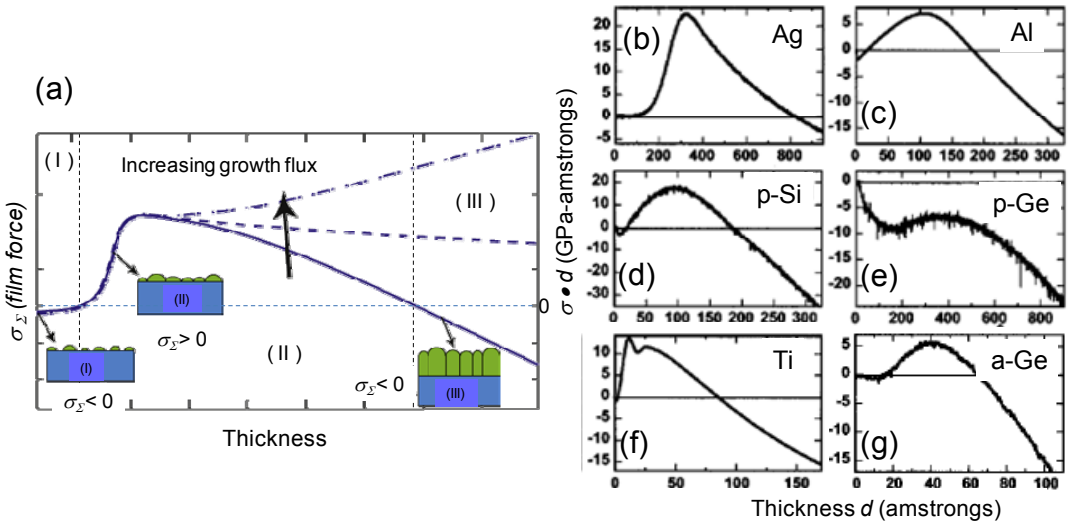

Figure 4.2 (a) Macroscopic intrinsic stress evolution during thin film growth. Labels (I), (II), and (III) and related insets correspond to several growth stages indicated in the text, which are separated also by dashed llines. Stress thickness (or film force = $\sigma \cdot d$) vs thickness (d) during deposition of: (b) Ag, (c) Al, (d) p-Si, (e) p-Ge, (f) Ti, and (g) a-Ge. Figures were adapted from J.A.Floro *et. al.*, J Appl Phys **89**, 4886 (2001) and J.S.Tello *et. al.*, J Mec Phys Solids **56**, 2727 (2008).

In an attempt to understand the origin of such transitions, they were correlated with the growth stages of a thin film, which are: (I) *nucleation*, (II) *coalescence and percolation* and (III) *film closure and growth.* It is widely admitted that during the stages (I) and (II), the surface tension and the cohesive forces between close entities generate compressive and tensile stresses, respectively, with significant changes in the film morphology [101, 102]. However, the repulsive interactions that generate the compressive growth stress observed upon the film closure (post-coalescence stress hereafter) is less understood, this being currently matter of an intense debate [103, 104]. Several models on the post-coalescence stress have been proposed so far in order to elucidate the origin of the repulsion between entities at this stage [103, 105, 106], which are summarized in Table 4.1. Briefly, an early model postulated that both compressive stresses generated during the stages (I) and (III) have the same origin: the Laplace pressure caused by the surface tension, which is counterbalanced in (II) by the cohesive forces between grains. Later, Chason and coworkers proposed that the compressive stress in (III) results from surface downhill currents leading an excess of adatoms into the entity boundaries (GBs) to be inserted.

A third model points out to the elastic deformation field that experiences a surface on which a density of adatom has been deposited as the cause of the post-coalescence compressive stress [107]. The debate arises owing to the difficulty to find a model that addresses consistently the following experimental evidences, labelled from (*i*) to (*iv*) and summarized in Figure 4.3:

(*i*) and (*ii*) —*Compressive nature and reversibility*: In high surface mobility conditions, the post-coalescence stress is: (*i*) compressive [101-107] and (*ii*) flux-dependent, this dependence being reversible [101-104, 106, 107]. It means that the compressive stress relaxes asymptotically or even becoming tensile if the deposition flux is stopped and it is regenerated once the flux is resumed, as observed in Figures. 4.2(a) and 4.3(c,d).

(*iii*) —*Multigrain-like morphology*: The post-coalescence morphology seen by high-resolution microscopy is formed by irregular-shaped multigrain structures — also identified as grain bundles (in which shallow internal grain-boundaries and non-coherent facets are visible) separated to each other by deep grooves and film discontinuities [83, 104]. This evidence requires being able to distinguish between different types of intergrain regions.

Growth stage	Growth stress model /Author(s)	Model details
Pre-coalescence	**Capillary model or "Locked-down model"** Mays et al., (1968) Laugier et al., (1981) Adopted by: Abermann and Koch (1986) Cammarata et al., (2000) Floro et al., (2001)	$\sigma \propto -2f / \lambda$ (where f is the Laplace pressure caused by the surface tension acting on the grains, and λ is the grain size) 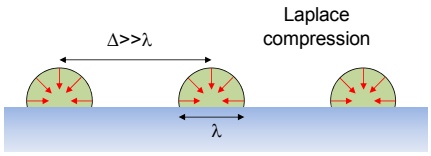 - Capillary-induced growth stress - Neglect the effect of deposition flux and mass transport
Coalescence	**"Cohesive zone model" (grain zipping)** Hoffman (1976) Adapted by: Nix and Clemens (1999) Freund and Chason (Same principle)	$\sigma_N \propto M\Delta / \lambda$ (where M is the biaxial modulus) 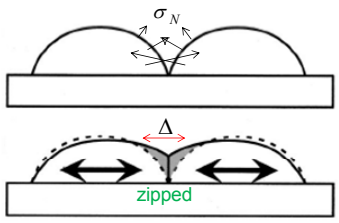 - Short range cohesive forces of attraction between grains causing attractive forces (tensile stress) - Neglect the effect of deposition flux and mass transport
Postcoalescence	**"Adatom insertion models"** Chason et al., (2007)	$\mu = -\Omega(\sigma_N + \gamma_s \kappa)$ (where Ω is the atomic radii, σ_N the normal stress, γ_s the surface energy and κ the local curvature) 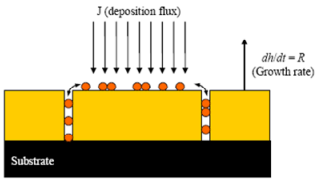 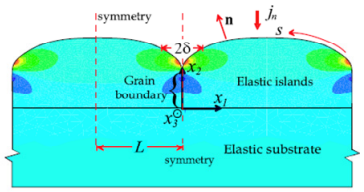 - Adatoms are inserted into the grain boundaries driven by gradients in the chemical potential along the grain boundary μ. - As observed in the figure (bottom) the resulting stress map is so that along grain boundaries are under compression despite flanks along the valley are under traction

Table 4.1 Several models explaining the evolution of the intrinsic growth stress during thin film growth stages.

(*iv*) —*In-plane texture generation*: The formation of such structures involves the generation irreversible (at short-range) and reversible (at long one) of in-plane texture via grain reorientation as revealed by the surface-orientation-map analysis and x-ray diffraction in ϕ-scan geometry, respectively (§3.3.2) [83].

Beyond the merits and deficiencies of the models proposed to date (briefly described above and summarized in Table 4.1), all of them fail to explain satisfactorily the evidences (*iii*) and (*iv*). Then, new evidences and models are needed to explain the complex interplay of attractive/repulsive interactions between surface entities causing coalescence/grooving during thin film development.

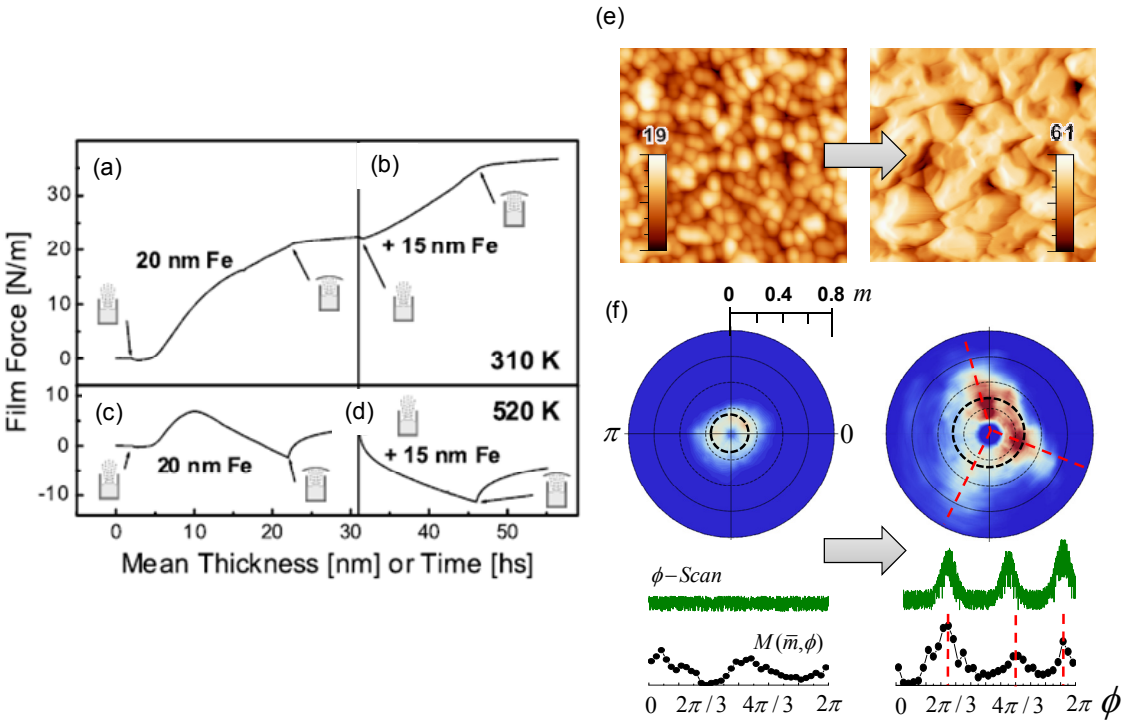

Figure 4.3 Summarize of the relevant experimental evidences to take into account for the building of a successful intrinsic stress model. —*Compressive nature and reversibility (evidences i and ii)*: (a-d) Film forces evolving during the deposition of 20 nm Fe onto oxidized Si(001) substrates at 310 K (a) and 520 K (c); after a growth interruption of 15 min an additional 15 nm layer was deposited at 310 K (b) and 520 K (d); tensile (compressive) stress is positive (negative). Images took from Koch *et al.*, Phys. Rev. Lett. **94**, 146101 (2005). —*Multigrain-like morphology* (*evidence iii*): (e) AFM images of Au polycrystalline thin films of d=200 nm in film thickness, growth at T = 373 K on SiO_x/Si(111) films. The left-side image shows the surface morphology before annealing, whereas the right-side one shows the surface morphology after annealing at 373 K during 1.2×10^4s. Images took from Figure 3.11 —*In-plane texture generation* (*evidence iv*): (f) Surface orientation maps (polar plots) and X-ray ϕ-scans showing the in-plane texture of Au polycrystalline films before and after annealing (during 3×10^3s). As observed, a 3-fold in-plane texture is developed during annealing. Images took from Figure 3.14.

4.2 Model for coalescence by stress relaxation/generation

In order to address the experimental evidences described in sections §3.3-§3.4 in terms of the interactions between grains and/or structures (recapitulating them: thermal annealing-induced morphology changes typify by single-crystal small grains that expand laterally making shallow the GBs up to coalesce into in-plane textured larger structures, which in turn shrink making deeper GBs), we propose a growth model considering the expansion and the shrinkage of the surface features like the results of the attraction and the repulsion between them, respectively.

4.2.1 Canonical system geometry

The geometric and/or physical meanings of the main parameters involved in our model are illustrated in Figure 4.4. We idealize the morphology of the polycrystalline film as formed by an array of round-shaped elastic grains (whose elastic constants are summarized in Table 4.1), which are separated to each other by a network of narrow gaps (with average gap width Δ << grain size λ).

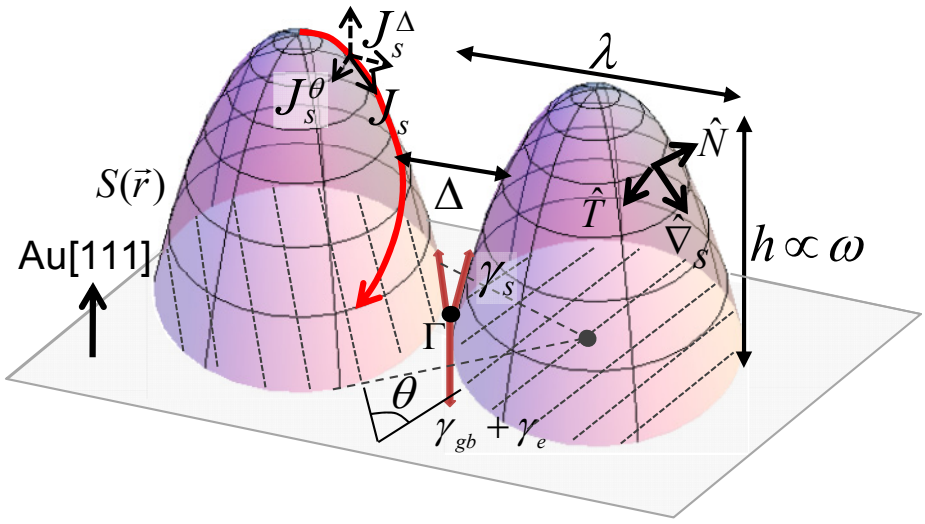

Figure 4.4 Sketch of two interacting grains illustrating the main physical and geometrical parameters considered in the model.

These grains interact to each other via: (*i*) long-range interactions (ruled by the surface tension) through the gap that extends a depth $h \propto \omega$ down to the grain junction (Γ point), where the neighbouring grains become into contact to each other. (*ii*) Short-

range interactions at the GBs (contact forces) that extend beyond the grain junction through the polycrystalline film bulk. This description allows us to identify the gap as the region in which the GBs emerge toward the surface. The model assume a cross-section of interaction between grains through of the gap of $\alpha\lambda\omega/2$, where $\alpha = \pi/3$ denotes the in-plane contact angle for a compact array of grains. As sketched in Fig. 4.4, the interactions are described using a local system of three orthogonal unit vectors defined at each site of the film surface $S(\vec{r})$, where $\vec{r}$ denotes the position vector on the film plane; these are: $\hat{N}$ —normal vector to the surface, $\hat{T}$ —tangent vector to the level curves $S(\vec{r}) \equiv const.$, and $\hat{\nabla}_S$ —the surface gradient vector.

Type of constant	Constant	Value
Elastic	Young modulus, E	79 GPa
	Poisson ratio, v	0.44
	Shear modulus, G	27 GPa
Structural and geometrical	Atomic volume, Ω	12.5×10^{-3} nm^3
	Pixel size, δr	2 nm
	Average misorientation between grains on randomly textured Au(111), $\overline{\theta}$	15º
	Appraisable maximum slope, m_{tip}	0.6 ± 0.1
	Threshold border slope, δm	0.15 ± 0.05
	Intragrain roughness, ω_g	1.8 nm
Thermodynamic constants	Surface energy, γ_s	1.54 J/m^2
	Mean coincidence-site-lattice GB energy for our Au(111) films, computed by EAM, γ_{gb}^{CSL} (in agreement with *)	0.34 J/m^2

Table 4.2 Parameters used our growth model. (*) J. Mei et al., Phys. Rev. B **43**, 4653 (1991) and Y. N. Wen et al., Solid State Commun. **144**, 163 (2007).

4.2.2 Plausible multiscale interactions between surface entities

In order to address for the experimental evidences observed in section §3.3 [also described above as evidences (*i*) – (*iv*)], a model including several interactions between surface grains was proposed. Two types of interactions between neighboring surface grains were considered: *longitudinal interactions* (along the surface normal direction), and *azimuthal* ones (along the in-plane direction), which appears at different stages of the thin film growth.

In the *Early growth regime* small surface grains are separated enough from each other so that $\Delta >> \lambda$. Then, in this early regime interactions between surface grains are not observed. The compressive stress that arises in this early regime is usually attributed to the action of surface tension and/or interface stress.

In the *Precoalescence regime* $\Delta << \lambda$, and grains are close enough so that long-range Van der Waals forces appear. Attractive forces of traction between the opposite faces of the close grains arise as a consequence of the tendency of the system to reduce its surface energy. Such interactive (attractive) forces, of the kind of cohesion, generate a normal tensile stress σ_N (Figure 4.5), which in a general form can be expressed as:

$$\sigma_N \propto -(\hat{\nabla}_s 2\gamma_s)\hat{N} > 0 \qquad (4.1),$$

(where $2\gamma_s$ denotes the surface energy saved as a result of the perfect coalescence between two grains, Table 4.1) on the grain faces within the gap region. Note that in Equation 4.1, γ_s (the surface energy in Joule/area-unit) could be understood as surface tension force, and then the gradient of γ_s corresponds to the dot product $\hat{\nabla}_s \cdot 2\vec{\gamma}_s$. Such definition implies that $\sigma_N \propto \hat{\nabla}_s \vec{\gamma}_s$ for isopotential surfaces and $\sigma_N \propto -(\hat{\nabla}_s \cdot 2\vec{\gamma}_s)\hat{N}$ for surfaces with potential gradients. Equation 4.1 defines the ***longitudinal interactions*** between grains included in our model.

It is worth to mention that Equation 4.1 is close in spirit and similar to previous cohesive zone models proposed to describe attraction between grains, in which the tensile stress is defined by $\sigma_N(\delta) \propto \Delta(z)\exp\left(1-\left[\Delta(z)/\Delta\right]\right)/\Delta$ [63, 64], where $\Delta(z)$ is the height- (z) dependent gap width. However, Eq. 4.1 enables a better description by including a z-dependent energetic term $\hat{\nabla}\gamma_s\hat{N}$ in the expression, allowing to incorporate the contribution of other terms relevant mechanisms to the attractive process. Thus-generated σ_N produces a phenomenon of gap closure starting from the bottom (where σ_N reached its maximum value) with the formation of new GB sections as the grain junction shifts up.

Two complementary mechanisms of stress accommodation and/or relaxation contributing to the gap closure are available, as stated by:

$$\sigma_N = \frac{M}{\lambda}\left[\frac{\Delta}{2} - \Omega\frac{\Delta}{\omega}\int_0^{t_a} J_s^{\Delta}\partial t\right] = \frac{M}{\lambda}\left(\frac{\Delta_r}{2}\right) \quad (4.2),$$

Equation 4.2 includes two terms in order to account for elastic and nonelastic contributions to the stress accommodation/relaxation phenomena:

- The first term in Equation 4.2 considers the elastic contribution, which enable the gap closure through a ***grain boundary zipping*** (Figure 4.5) by inducing a longitudinal strain $\Delta/\lambda = \sigma_N/M$ within the grain bulk ($\Delta/2$ per grain) with an elastic energy cost $\propto M\omega\Delta^2$ {where $M = E/(1-\nu)$ is the biaxial elastic modulus for isotropic mediums, E is the Young modulus and ν the Poisson ratio}.
- The second term in Equation 4.2 considers the nonelastic contribution, which enable the gap closure through a ***gap filling*** via surface downhill currents $J_s^{\Delta} = -(D_s/\Omega k_B T)\vec{\nabla}_S\mu$ biased by the stress-modified surface chemical potential $\mu = -\Omega(\kappa\gamma_s + \sigma_N)$ [64] (Figure 4.5). J_s^{Δ} flows in the direction in which the density of the strained medium decreases, i.e., from zones under compression→ unstressed zones (e.g., grain tops)→ zones under traction. Ω is the atomic volume, D_s the collective surface diffusion coefficient defined according to the Fick's laws and κ denotes the local curvature of the film surface.

For films with high mobility (such that $\lambda^2/D_s << t_a$), the relaxed fraction of σ_N is proportional to the product between the transported mass by J_s^{Δ} expressed in number of atoms [$(\pi\lambda\Delta/6)\int_0^{t_a} J_s^{\Delta}\partial t$ where $\pi\lambda\Delta/6$ is the top aperture of the gap region] and the equivalent gap narrowing per transported atom $\delta\Delta \approx 6\Omega/\pi\lambda\omega$. In terms of GB motion, a gap narrowing of $\delta\Delta$ is equivalent to a shift up of the grain junction by $\hat{m}\delta\Delta \approx 12\Omega/\pi\lambda\Delta$. The right-hand expression in Eq. 1 indicates that the grain zipping accommodates only the residual part of the stress $M\Delta_r/2\lambda$ that is not relaxed by J_s^{Δ}, with an elastic energy cost of $M\omega\Delta_r^2 = (\pi\lambda\omega/6)\gamma_e^{\Delta}$ (see e.g. Equation 3 in Ref. [63]) where γ_e^{Δ} denotes the elastic energy per gap cross-section unit ascribed to the longitudinal strain.

Besides the longitudinal interactions through the gap between neighboring grains, ***azimuthal interactions*** (i.e., interactions in the azimuthal direction) have to be considered in the light of the evidences in Figure 3.14(c), which point out to the development of a 3-fold axis in-plane texture) suggesting the reorientation of the grains during the coalescence.

Consequently, the scenario of longitudinal interactions presented above is completed as follows: As the gap closure proceeds (at a rate $\Omega J_s^{\Delta} \sim D_s / \Delta$) through the mechanisms of gap filling and grain zipping (in Equation 4.2), a torque arises on the buried sections of the opposite faces of the neighbouring grains (just below of the grain junction) due to the angular misfit (described in terms of the misorientation angle θ) between their in-plane orientations.

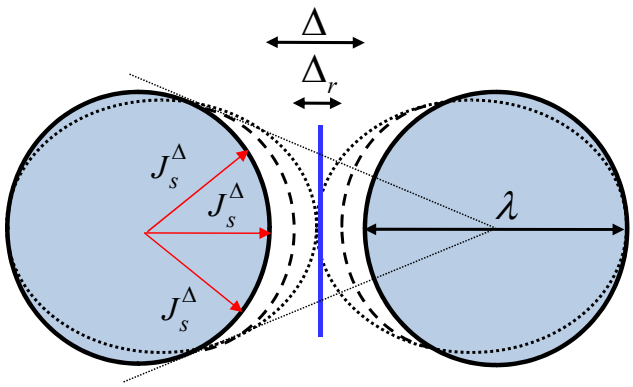

Figure 4.5 Top view schematic representations of the mechanisms of relaxation by downhill surface currents J^{Δ}_s and accommodation by strain Δ_r of the growth stress generated during the grain coalescence in the normal direction. Dashed [dotted] grain contour shown the morphology transformations of the grain shapes (the original ones being depicted by solid lines) as a result of the nonelastic [elastic] deformations. (b) Lateral view of such mechanisms. Red arrows represent normal force vectors, whereas blue ones correspond to work (energy) done, respectively (see also Equation 4.4 and Figure 4.7).

Such a torque promotes the reorientation of the grains via the generation of a shear stress $\sigma_s \propto -\nabla_\theta(\gamma_{gb}/\lambda)\cdot\hat{T}$ —with ∇_θ the surface gradient vector in the azimuthal direction, in order to reduce the GB energy $\gamma_{gb}(\theta)$ through the formation of pseudo-coherent GBs (Figure 4.6). Thus-generated σ_s is then accommodated/relaxed by means of two complementary mechanisms, as stated by:

$$\sigma_s = G\left(\frac{\theta}{2} - \Omega\frac{36\Delta}{\pi^2\lambda^2}\int_{\omega\Delta/D_s}^{t_a} J_s^{\theta}\partial t\right) = G\left(\frac{\theta_r}{2}\right) \qquad (4.3),$$

As in the case of Equation 4.2, Equation 4.3 also includes two terms in order to account for elastic and nonelastic contributions to the stress accommodation/relaxation phenomena:

- The first term in Equation 4.3 considers the elastic contribution, which promotes grain reorientation by inducing a ***shear strain*** of the kind of torsion within the grain bulk with a twist angle per grain of $\theta/2$ and an energy cost $\approx G\omega(\lambda\theta/2)^2$ (where G is the shear modulus).
- The second term in Equation 4.3 corresponds to the nonelastic contribution, which enables grain reorientation by modifying the surface chemical potential as $\mu = -\Omega\left[\kappa\gamma_s + \sigma_N - \rho(S')\gamma_{gb}(\theta)\right]$ in the azimuthal direction. $\rho(S')$ denotes the density of adsorption sites along the grain perimeter $S'=\lambda\theta/2$, whose form changes as the gap closes such that for a mean-field approach a time-averaged $\langle\rho(S')\rangle = \pi\lambda\omega/6\Omega$ is used. From thus-modified μ, a lateral component $J_s^\theta = -(D_s/\Omega k_B T)\bar{\nabla}_{S'}\mu = -(\pi D_s\omega/3\Omega k_B T)\nabla_\theta\gamma_{gb}\hat{T}$ of the surface current, which induces a ***grain rotation*** [95, 96], is generated.

Equation 4.3 puts together information provided by previous studies [108-110] in agreement with molecular dynamic and phase field simulations [95, 96, 111, 112], that demonstrates the key role played by the grain reorientation in processes of coalescence and normal grain growth for polycrystalline systems, and in particular for Au films [95, 110]. In this context, the model assumes elastic deformations of pure torsion involving shear strain gradients along the grain thickness (see a description of basic kinematics of torsion in Reference [113]), on the basis of considering a $\lambda_\perp$-thick shallow layer of surface grains (as discussed above) with circular cross-sections. In this assumption, the surface grains are: (*i*) azimuthally coupled to each other (according to data in Figure 3.14c) and, (*ii*) clamped at the bottom by the randomly in-plane textured bulk of the polycrystalline film.

On the other hand, the fact of considering a lateral component $\vec{J}_s^\theta$ implies that the net surface current $\vec{J}_s = \vec{J}_s^\Delta + \vec{J}_s^\theta$ flows (for the case of tensile stress $\sigma_N > 0$) from unstressed grain tops toward the GBs (direction of $\vec{J}_s^\Delta$) along curved trajectories to right

or left in dependence on the $\vec{J}_s^{\theta}$ direction (as sketched in Figure 4.6). These trajectories would give rise to an inhomogeneous filling of the gap, which produces a non-uniform advance of the grain faces whose in-plane orientations change consequently. Since the $\vec{J}_s^{\theta}$-induced grain rotation involves surface currents rather than GB self-diffusion and/or bulk diffusion phenomena (with $D_s \sim 10^{-2} >> D_{gb} \sim 10^{-14} >> D_{bulk} \sim 10^{-25}$ cm^2/s at 100 ^{o}C, respectively [114-116]), this process happens faster (with rates $\leq$15 ^{o}/h) than that expected[18].

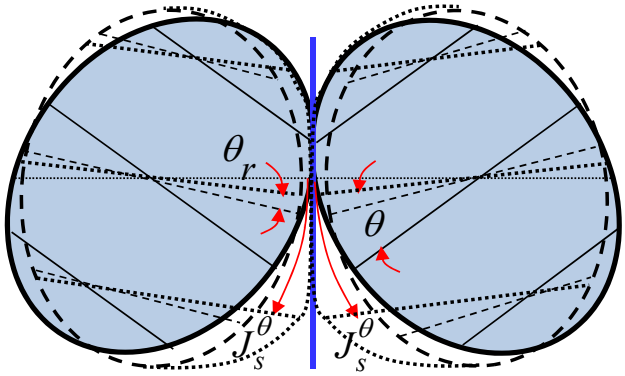

Figure 4.6 Top view schematic representations of the mechanisms of relaxation by lateral surface currents J_s^{θ} and accommodation by strain θ_r of the growth stress generated during the grain coalescence in the azimuthal direction. Dashed [dotted] grain contour shown the morphology transformations of the grain shapes (the original ones being depicted by solid lines) as a result of the nonelastic [elastic] deformations.

The J_s^{θ}-relaxed fraction of σ_s (second term in Equation 4.3) is estimated as the product between the mass transported by J_s^{θ} expressed in number of atoms [$\frac{1}{2}\omega\Delta\int_{\omega\Delta/D_s}^{t_a} J_s^{\theta}\partial t$ where $\omega\Delta$ is the lateral aperture of the gap region] and the rotated angle per transported atom ($\approx 72\Omega/\pi^2\lambda^2\omega$ —details in Ref. [95]). The λ-dependence of the relaxed fraction defines a critical size $\lambda_0 = \frac{6}{\pi}\sqrt{2\Omega\frac{\Delta}{\theta}\int_{\omega\Delta/D_s}^{t_a} J_s^{\theta}\partial t}$ for the grain rotation that corresponds to the size of the largest grain in which J_s^{θ} is high enough to fully relax σ_s during the annealing time, and so $\sigma_s \equiv 0$ for subcritical grains (those

[18] A grain rotation rate of 2.4 ^{o}/h involving GB self-diffusions was estimated for 66 nm-sized grains within the bulk of a polycrystalline Au(111) film (K. E. Harris *et al.*, *Acta Mater.* **46**, 2623 (1998)); whereas for high mobility GBs with enhanced dislocation/disclination activity, a higher rotation rate of 10 ^{o}/h was reported in P. Liu *et al.*, *Scripta Mater.* **64**, 343 (2011).

with sizes $\lambda < \lambda_0$). Note that there is not analogous critical grain size for the fully relaxation of σ_N through J_s^{Δ}. For supercritical grains (with $\lambda > \lambda_0$), the ability to rotate decreases as $\propto 1/\lambda^2$ —in agreement with the simulations in [96]; and so the non-relaxed fraction of σ_s (i.e., $G\theta_r/2$ with θ_r being the residual misorientation angle — right-hand term in Eq. 4.3) is accommodated elastically by torsion with an energy cost of $G\omega(\lambda\theta_r/2)^2 = (\pi\lambda\omega/6)\gamma_e^{\theta}$, where γ_e^{θ} denotes the elastic energy per gap cross-section unit ascribed to the shear strain.

Interaction balance: Once defined the different contributions to the elastic energy ($\gamma_e = \gamma_e^{\Delta} + \gamma_e^{\theta}$), the balance of the surface-tension forces involved in the interactions between neighbouring grains can be described along the out-of-the-film plane direction as:

$$\gamma = 2\gamma_s \sin[\arctan(\hat{m})] - \gamma_{gb}(\theta) - \gamma_e \qquad (4.4),$$

with $\gamma_e^{\Delta} = 6M\Delta_r^2/\pi\lambda$, $\gamma_e^{\theta} = 0$ for $\lambda \le \lambda_0$ and $\gamma_e^{\theta} = 3G\lambda\theta_r^2/2\pi$ otherwise; where the λ-dependences of Δ_r and θ_r are given through Equations 4.2 and 4.3, respectively. Such a balance defines: (*a*) the resulting force between interacting grains $\gamma \neq 0$ (where $\gamma > 0$ means attraction, and repulsion otherwise); and consequently (*b*) the condition of mechanical equilibrium $\gamma = 0$ that determines the steady profile $\partial_t S(\vec{r}) = 0$ of the gap region for a selected value $\hat{m}_0$ of the border slope such that $2\gamma_s \sin[\arctan(\hat{m}_0)] = \gamma_{gb} + \gamma_e$, as observed in Figures 4.5(b) and 4.7.

The attraction ($\gamma > 0$) occurs when the surface energy $\{2\gamma_s \sin[\arctan(\hat{m})]\}$ of the opposed $\hat{m}$-sloped faces of two neighbouring grains is higher than the energy involved in the formation of an in-between GB $[\gamma_{gb}(\theta) + \gamma_e]$. Otherwise, the repulsion ($\gamma < 0$) between grains prevails. The gap shape evolves under these interactions until the equilibrium profile (with slope $\hat{m} = \hat{m}_0$) is reached.

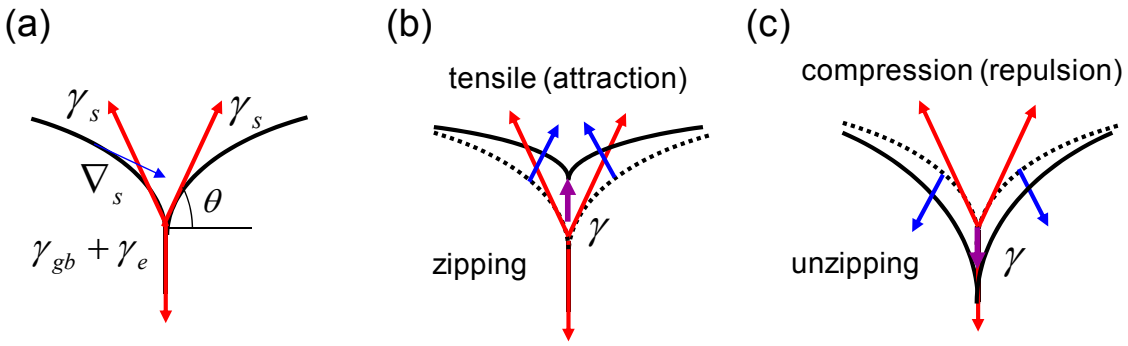

Figure 4.7 Force balance at grain boundaries. (a) Sketch of the force balance. (b) Attractive forces domain, generating zipping and (c) repulsive ones do, causing unzipping.

Depending on the $\hat{m}_0$ value, two limit situations can be outlined (Figure 4.8): (*i*) a "complete" gap closure (denominated also grain coalescence) producing a negligible border slope $\hat{m}_0 \to 0$; and (*ii*) a non-contact for small grains (or "grooving" regime) for larger ones when $\gamma_{gb}(\theta)+\gamma_e > 2\gamma_s$, which implies an unreachable equilibrium profile ($\hat{m}_0 \to \infty$) and so the grains are separated to each other leaving uncovered regions of the film bulk. For practical purposes, the grain coalescence is supposed when we are not able to distinguish between joined grains (by drawing a well-resolved complete GB). This is equivalent to have $\hat{m}_0 < \omega_s / 5\delta r$ (the discernible minimum slope) with ω_s and $5\delta r$ denoting the intra-structure roughness and lateral resolution of the AFM measurements at GB (note that five δr-sized pixels are required at least to resolve the profile of a gap region), respectively.

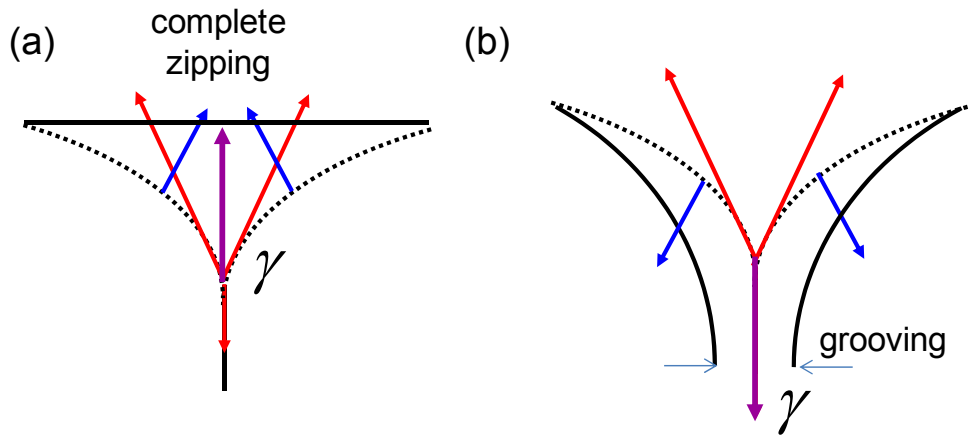

Figure 4.8 Limits of grain-to-grain interactions. (a) Complete gap closure. (b) Non-contact (grooving). In both cases, dashed (solid) lines represent initial (final) grain shapes, respectively, whereas blue, red and violet arrows represent normal, work (energy) and total work vectors, respectively.

On the other hand, the appraisable maximum slope is limited by the AFM tip aspect-ratio ($\approx 2m_{tip}$), such that the non-contact/grooving condition can be assumed for $\hat{m}_0 \approx m_{tip}$. At this point, it should be stressed that the balance in Equation 4.4 is only suitable for $\hat{m}$ ranged between $\omega_s / 5\delta r$ and m_{tip}.

4.2.3 Interpretation of the experimental results in the light of the proposed model

By using Equations 4.2, 4.3 and 4.4, the size-dependence of the elastic energy γ_e accumulated as a consequence of the interactions between surface features can be expressed as:

$$\gamma_e(\lambda) = \gamma_e^{\Delta}(\lambda) + \gamma_e^{\theta}(\lambda) = \frac{6M\Delta_r^2(\lambda)}{\pi\lambda} + \frac{G\lambda\theta_r^2(\lambda)\cdot\psi(\lambda-\lambda_0)}{2\pi} \tag{4.5}$$

In Equation 4.5, several terms can be identified:

- ***Longitudinal interactions*** described by $\Delta_r(\lambda) = \Delta\cdot\beta'(\lambda)$, where the fitting function $\beta'(\lambda) \propto 1 - 2(\Omega/\omega)\int_0^{t_a} J_s^{\Delta}\partial t$ (according Eq. 4.2) denotes the non-relaxed fraction of the normal stress by surface currents. The dependence of β' on λ results from the implicit λ-dependence of J_s^{Δ}. Thus-defined $\beta'(\lambda)$ fulfils the following condition: $\beta'(\lambda) \le 1$ with $\beta'(\lambda\to\infty)\to 1$, which accounts for the length-scale dependence of the surface currents J_s^{Δ}. If $\lambda \gg \sqrt{D_s}$, the atoms comprising the J_s^{Δ} currents will not reach the gap between neighbor grains, and therefore $\beta'(\lambda\to\infty)\to 1$. In this case, the normal contribution of the gap closure phenomenon would occur mainly by grain zipping (i.e., without gap filling).
- ***Azimuthal interactions*** described by $\theta_r(\lambda) = \theta\cdot\beta''(\lambda)$, where the fitting function $\beta''(\lambda) \propto 1 - 72(\Omega\Delta/\pi^2\theta)\int_{\omega\Delta/D_s}^{t_a}(J_s^{\theta}/\lambda^2)\partial t$ (according Equation 4.3) denotes the non-relaxed fraction of the shear stress, its dependence on λ being a consequence of the λ-dependence of J_s^{Δ}/λ^2. Similarly to the case of

zipping/filling, $\beta''(\lambda) \leq 1$ with $\beta''(\lambda = \lambda_0) = 0$ and $\beta''(\lambda \to \infty) \to 1$. Again, these conditions takes into account for the length dependence of the grain rotation phenomenon: if $\lambda \gg \sqrt{D_s}$, the atoms comprising the J_s^θ currents will not reach the gap between neighbor grains, and therefore $\beta''(\lambda \to \infty) \to 1$. Then, the azimuthal contribution to the gap closure phenomenon would occur mainly by grain torsion (i.e., without grain rotation). By other hand, for grains with sizes $\lambda \leq \lambda_0$ (subcritical grains) it is assumed that is small enough so that grain reorientation only occur by rotation (i.e., J_s^θ would be able to explore the overall grain perimeter), and therefore $\sigma_s = \beta'' = 0$.

- $\psi(\lambda - \lambda_0)$ corresponds to the step function defined as: $\psi(x) = 1$ for $x \geq 0$ and $\psi(x) = 0$ otherwise. It is assumed that both $\beta'(\lambda)$ and $\beta''(\lambda)$ depend smoothly on λ. The dependence is plotted in Figure 4.9(a).

The solid curve $\gamma_e(\lambda)$ corresponds to the best fit of the experimental data (symbols) carried out under the following criteria: (*i*) according to the model, the surface of the as-grown Au film is formed by small grains with sizes $\lambda_{\text{as-grown}} << \lambda_0$, which can rotate freely ($\gamma_{gb} \approx 0$) such that —from the equilibrium condition— we get $\gamma_e(\lambda_{\text{as-grown}}) = 2\gamma_s \sin[\arctan(\hat{m}_{\text{as-grown}})]$ with $\lambda_{\text{as-grown}}$ and $\hat{m}_{\text{as-grown}}$ being measured by AFM (Figures 3.11f and 3.11g) and γ_s computed by EAM [70]. This assumption is kept for all the subcritical grains (those with $\lambda \leq \lambda_0$ that do no accumulate shear strain, $\gamma_e^\theta \approx 0$). *(ii)* λ_0 is taken as the largest length scale in which the 3-fold axis in-plane texture persists along the annealing (see Fig. 3.14d). *(iii)* The equilibrium condition for supercritical grains becomes $\gamma_e(\lambda > \lambda_0) = 2\gamma_s \sin[\arctan(\hat{m})] - \gamma_{gb}^{CSL}$, where γ_{gb}^{CSL}=0.304 J/m^2 is the mean GB energy averaged from the relative populations ascribed to each kind of GB (Fig. 3.15a) once considered their respective energies (namely: $\gamma_{gb}(\theta = 0^\circ)$, $\gamma_{gb}(7^\circ)$ and $\gamma_{gb}(13^\circ)$ —Figure 3.15b) computed by EAM [70].

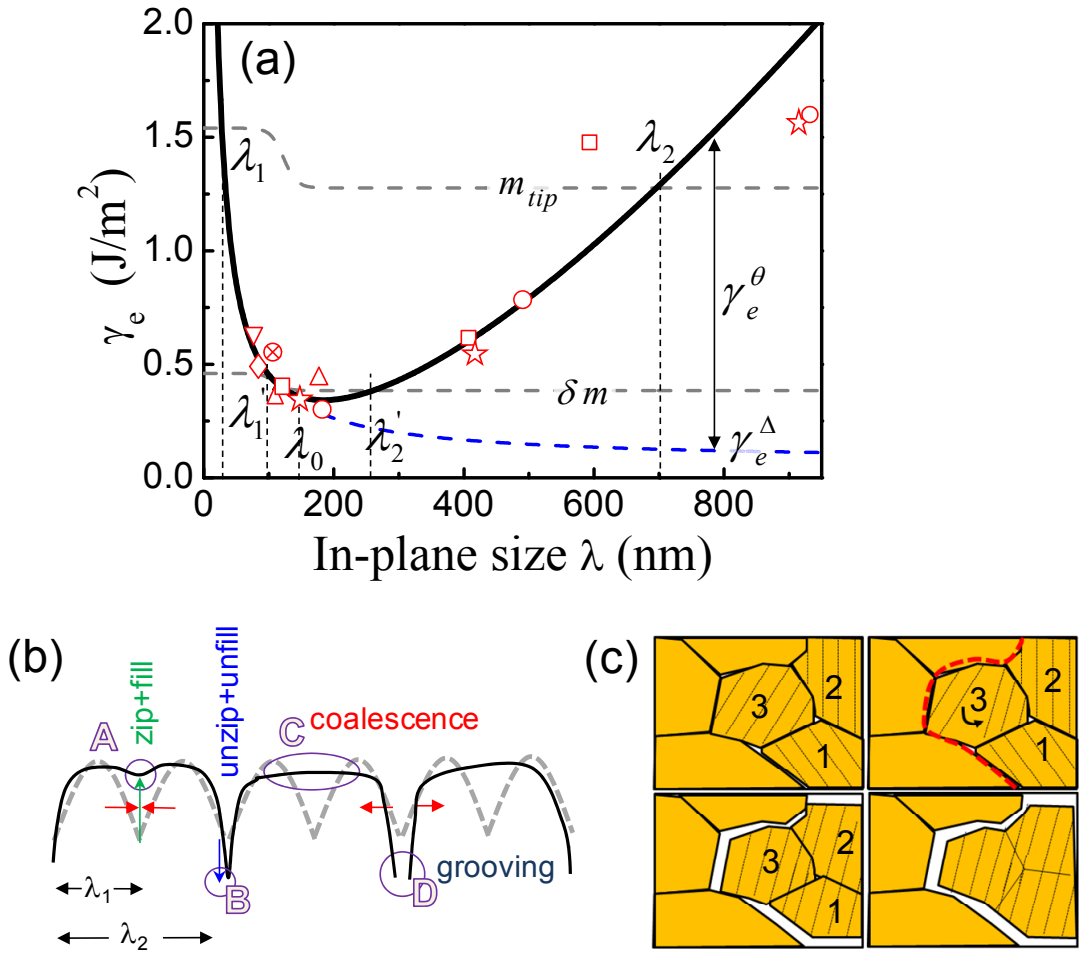

Figure 4.9 (a) λ– dependence of $\gamma_e(\lambda)$. The solid curve represents the best fit of the experimental results to the proposed model. The symbols correspond to the data measured at different length scales in 200 nm-thick polycrystalline Au films with annealing times of (▽) t_a = 0 s (as-grown), (⊗) $t_a = 1.2\times10^2$ s, (◇) $t_a = 3\times10^2$ s, (□) $t_a = 3\times10^3$ s, (☆) $t_a = 1.2\times10^4$ s and (○) $t_a = 1.2\times10^5$ s. (b) Sketch of the evolution of a surface profile (the dashed/solid curves correspond to pre-/post-coalescence profiles) in which the morphology transformations that prevail at different length scales are indicated (see description in the text). (c) Top view of the mechanism happening in (b), where grain labeled 1, 2, and 3 coalesce by the inside bundling-outside grooving mechanism. The arrow in the upper right frame corresponds to the grain reorientation phenomena. The white regions between grains correspond to zones where the substrate is exposed.

The λ-dependences of Δ_r and θ_r (the fitting parameters) are calculated from considerations (*i*) and (*iii*). As expected, such dependences fulfil the asymptotic conditions $\Delta_r(\lambda \to 0) \to 0$ $[\theta_r(\lambda \le \lambda_0) = 0]$ and $\Delta_r(\lambda \to \infty) \to \Delta$ $[\theta_r(\lambda \to \infty) = \theta]$ that point out to the fact that the longitudinal [shear] stress is relaxed or accommodated mainly via surface currents or strain generation in small ($\lambda \to 0$) and large ($\lambda \to \infty$) grains, respectively.

The asymptotic condition $\lambda \to \infty$ allows us to estimate the mean values of the gap width $\langle \Delta \rangle$ and the misorientation angle $\langle \theta \rangle$ between surface features. The dashed horizontal lines in Fig. 4.9(a) correspond to the coalescence (labelled "δm") and non-contact/grooving ("m_{tip}") conditions as defined in the previous section. Their intercepts with the curve $\gamma_e(\lambda)$ [explicitly, λ_1 (λ_1') and λ_2 (λ_2') for the line "m_{tip}" ("δm")] define the interaction regimes between the surface features as a function of their sizes. The morphological parameters $\langle \Delta \rangle$, $\langle \theta \rangle$ and the λ – intercepts obtained from the fit are summarized in Table 4.2.

Morphological parameters	
λ_0	136.0 nm
λ_1	27.7 nm
$\lambda_1^{'}$	98.0 nm
$\lambda_2^{'}$	256.1 nm
λ_2	697.5 nm
$\langle \Delta \rangle$	0.45 nm
$\langle \theta \rangle$	3.2 º

Table 4.3 Summary of the morphology parameters obtained from the numerical fit of the experimental data to our model (except λ_0 that corresponds to an input parameter estimated from results in Fig. 4.9a).

4.2.4 Interpretation of the $\gamma_e(\lambda)$ dependence

Figure 4.9(a) allows us to interpret the experimental data in Figures 3.12 to 3.15 in the light of the proposed model, as follows (the description is assisted by the sketch in Figure 4.9b):

(I) For grains smaller than the critical size for the formation of grain boundaries $\lambda_g \le \lambda_1$ {such that $\gamma_e(\lambda_g) \ge 2\gamma_s \sin\left[\arctan\left(m_{tip}\right)\right]$, which means a unreachable equilibrium condition}, the gap between grains is too wide ($\Delta \sim \lambda$) to be filled and/or zipped. The grains do not interact to each other (non-contact regime), and

then a compressive growth stress arisen from the surface tension on isolated grains. $\lambda_1 =$ 27.7 nm (in Table 4.2), estimated from the fit agrees with the sizes (ranged between 20-30 nm) of the isolated grains (before these become in contact to each other) measured in $\approx$20 nm-thick films growing according to VW mode [83, 91, 117]. This regime is outside the scope of our study as the grain size for all our samples is $\lambda_g > \lambda_1$.

(II) For grains with sizes $\lambda_1 < \lambda_g < \lambda_0$ {such that $\gamma_e(\lambda_g) < 2\gamma_s \sin\left[\arctan\left(m_{tip}\right)\right]$ — available equilibrium}, the pre-equilibrium $\gamma > 0$ as γ_e drops with λ_g according Equations 4.4 and 4.5. This means the attraction between the opposed faces of neighbouring grains predominates giving rise to a progressive gap closure (transformation A (see below) in Figure 4.9b) by gap filling and grain zipping plus free rotation in the case of in-plane misorientation. Indeed, the existence of downhill currents J_s^{Δ} flowing toward the GBs (gap filling) and/or the fact that grains are under residual in-plane traction (grain zipping) are consistent with the morphology evolution obtained for the *Precoalescence regime* (Figure 3.12c and Figure 3.14c). The gap-closure rate with λ estimated from Equation 4.5 becomes $\partial\hat{m}_0 / \partial\lambda \approx (1/2\gamma_s)\partial\gamma_e / \partial\lambda$ for $\hat{m}_0 << 1$, which means that $\hat{m}_0$ exhibits a similar behaviour to that of γ_e vs. λ, i.e., $\hat{m}_0$ drops as $\hat{m}_0 \propto \Upsilon / \lambda$ (with $\Upsilon = 3M\langle\Delta\rangle^2 / \pi\gamma_s$) down to Υ / λ_0.

Consequently, when $\Upsilon / \lambda_0 < \hat{m}_0 \leq \delta m$, which is fulfilled for $\lambda_1' \leq \lambda_g < \lambda_0$ with $\gamma_e(\lambda_g) \leq 2\gamma_s \sin\left[\arctan\left(\delta m\right)\right]$, the coalescence of the grains that interact through the gap is supposed (transformation C in Figure 4.9b). As a result of such coalescence, the surface structures with sizes $\lambda_s = n\lambda_g >> \lambda_g$ are formed and the gaps that are still visible on the structures between the coalesced grains become internal GBs. The fact that the highest normal stress generated during the coalescence $\sigma_N < M\langle\Delta\rangle / \lambda_0 \approx 225$ MPa —with $\langle\Delta\rangle \approx 0.45$ nm being computed from the asymptotic conditions once the data is fitted (Table 4.2)— is lower than the Au tensile strength (≈ 250 MPa [118]) confirms the model's assumption concerning to the minor role played by the bulk plastic deformations on the stress relaxation. Note that the threshold border slope ($\delta m \approx 0.15$) used to define the coalescence condition was fixed to a slightly higher value than that

corresponding to the discernible minimum slope ($\omega_s / 5\delta r$=1.25 nm/10 nm=0.125) described in the previous section, which allows us to investigate the morphology evolution of the inner grains.

The main repercussion of the formation of the surface structures is the fact that two different length scales of interaction appear: whereas the intra-structure interactions are controlled by the single properties of the inner λ_g -sized grains, the structures interact to each other as a homogeneous whole of size λ_s exhibiting the mean properties of the set of grains forming them. This difference resides in the better mechanical coupling between inner grains through the shallow internal GBs than that taking place between the structures through deeper external GBs. The experimental data measured at different length scales for a single sample (as shown in Figures 3.11e to 3.11g) are plotted in Figure 4.9(a) like different points all them displayed using the same symbol (i.e., one symbol per sample).

(III) For surface entities (grains and structures) with sizes $\lambda_0 < \lambda < \lambda_2$, the increase in γ_e accounts for the progressive loss of the ability to relax fully the in-plane misorientation via J_s^{θ}-induced rotation of the coalescing features. The non-relaxed part is then accommodated by shear strain with the subsequent energy cost. Thus, as the elastic energy is accumulated, pre-equilibrium $\gamma < 0$, which implies that the repulsion between the opposed faces of the close features prevails. Such repulsion would induce a shrinking of the interacting features giving rise to deeper and sharper gaps between them (transformation B) and the worsening of the 3-fold axis in-plane texture due to the shear-strain release. Note that this description is in good agreement with the morphology evolution obtained during the *Late regime* (Figures 3.11d to 3.14d) for the surface structures. The shrinkage of the structures results foreseeable from partial unzipping processes (major effect) and uphill currents J_s^{Δ} (minor one) emptying the external GBs. The shrinking rate $\{\partial \hat{m}_0 / \partial \lambda = [(1+\hat{m}_0{}^2)^{3/2} / 2\gamma_s]\partial \gamma_e / \partial \lambda \approx R(1+\hat{m}_0{}^2)^{3/2}$ with $R = 3G\langle\theta\rangle^2 / 4\pi\gamma_s$ from Eq. 3$\}$ increases progressively with λ from $\partial \hat{m}_0 / \partial \lambda \approx (1+\delta m^2)^{3/2} R \approx R$ for $\lambda_0 < \lambda < \lambda_2'$ (assuming $\delta m << 1$) up to $\partial \hat{m}_0 / \partial \lambda \approx (1+m_{tip}^2)^{3/2} R \approx 1.7R$ for $\lambda \to \lambda_2$. The fact that the highest shear stress

$\sigma_s = G\langle\theta\rangle/2 \approx 2.2$ GPa generated by the mean misorientation between neighboring features, which was estimated to be $\langle\theta\rangle = 9.2^{\circ}$ (Table I), is lower than the shear strength reported for polycrystalline Au films (> 5GPa [119]) supports the model soundness.

(IV) When $\hat{m}_0$ reaches a value similar to m_{tip}, which happens for surface features with sizes higher than the critical size for the formation of surface discontinuities, $\lambda \geq \lambda_2$ {such that $\gamma_e(\lambda_g > \lambda_2) \geq 2\gamma_s \sin\left[\arctan\left(m_{tip}\right)\right]$ — unreachable equilibrium}, the structures become fully separated to each other, and the in-between GBs disappear leaving uncovered regions of the film bulk (surface discontinuities— transformation D in Fig. 4.9b). Since the shrinking of the isolated structures would counterbalance their lateral growths to avoid that these becoming in touch, λ_2 can be realized as the saturation size of such structures. Phenomena of the saturation of the feature size in bulk as well as on the surface have been reported for polycrystalline films during growth and annealing [117]. The value estimated here of $\lambda_2 = 697.5$ nm (Table 4.2) is in good agreement with that (≈650 nm [117]) found in Au/SiO_2 films with longer annealing ($t_a \approx 1.8\times10^4$ s) once the 50% of the surface grains had coalesced into the multigrain structures. Nevertheless, since the high crystalline coherence of the largest multigrain structures (with low-angle and CSL internal GBs) that would be translated in a decrease of both the tensile and shear strengths, the presence of plastic deformations generated by dislocation motion within the structure bulk cannot be neglected. As a consequence of these plastic deformations, the growth stress would be relaxed complementarily, the accumulated elastic energy would diminish, and saturation sizes λ_2 larger than that estimated here could be expected.

Beyond the local mechanical equilibrium (in Equations 4.4 and 4.5) established between neighbouring grains through a GB emerging at a $\hat{m}_0$-sloped gap region, the shrinkage of the surface structures can be understood as the result of the attraction (which is unbalanced along the structure radius) between the inner grains. Thus, for a given grain, the attraction that it experiences for the neighbouring grain closer to the structure centre is higher than the interaction with the more distant one. This asymmetry

is a consequence of the accumulation of elastic energy γ_e with λ (Figure 4.9a for $\lambda > \lambda_0$), where λ can be realized here as the interaction length rather than the grain size. The attraction is thus-weakened as the distance from the structure centre increases until becoming repulsion due to the prevalence of the opposite attraction toward the centres of the neighbouring structures. Therefore, the λ-dependence of the interactions between the surface features acts like an inside grain-bundling/outside grooving mechanism.

4.2.5 $\gamma_e(\lambda)$ dependence and experimentally obtained force per width curves

To compare the $\gamma_e(\lambda)$ dependence obtained from our model with previous reports in terms of the force-per-width curves measured experimentally, we estimate the force-per-width curve $\bar{\sigma}(\lambda)\lambda$ from the $\gamma_e(\lambda)$ energy balance described in Figure 4.9(a) as:

$$\bar{\sigma}(\lambda)\lambda = \int_{\lambda_{ld}}^{\lambda} \langle \sigma_{\Sigma} \rangle \partial\lambda \approx -\int_{\lambda_{ld}}^{\lambda} (\gamma/\lambda)\partial\lambda \qquad (4.6)$$

In Equation 4.6 $\lambda_{ld} \cong$ 65 nm corresponds to a "locked-down" grain size, i.e., a crossover grain size above with grains are pinned (constrained) by the substrate [100]. The $\bar{\sigma}(\lambda)\lambda$ curve is plotted in Figure 4.10 vs. in-plane λ and out-of-plane $\lambda_{\perp}$ grain sizes, the later taken as the equivalent thickness for the interactions between grains. Thus-obtained $\bar{\sigma}(\lambda)\lambda$ is in good agreement with that measured by Koch *et al.* for Au films by using the cantilever beam deflection method [104], and it reproduces qualitatively the force-per-width curve shapes reported for other systems [18].

Finally, it is worth to mention that the model assumes that the contributions to the stress relaxation of other mechanisms involving bulk plastic deformations like the motion and generation of dislocations from a Frank-Read source in ductile metals such as Au play a minor role (and thus negligible). This assessment is valid for both σ_N and σ_s being lower than the Au tensile and shear strengths, which were estimated for polycrystalline Au to be ≈250 MPa [118] and > 5 GPa [119], respectively by using *in-situ* AFM tip scratch methods. The values of the Au tensile and shear modules were determined here by using XSA analysis ($Sin^2\psi$ method), as described previously in §3.3.3, resulting in ≈20 MPa for tensile stress and ≈ 1GPa for the shear one. Besides,

the same values were obtained by the fitting of the $\gamma_e(\lambda)$ curve with the experimental data.

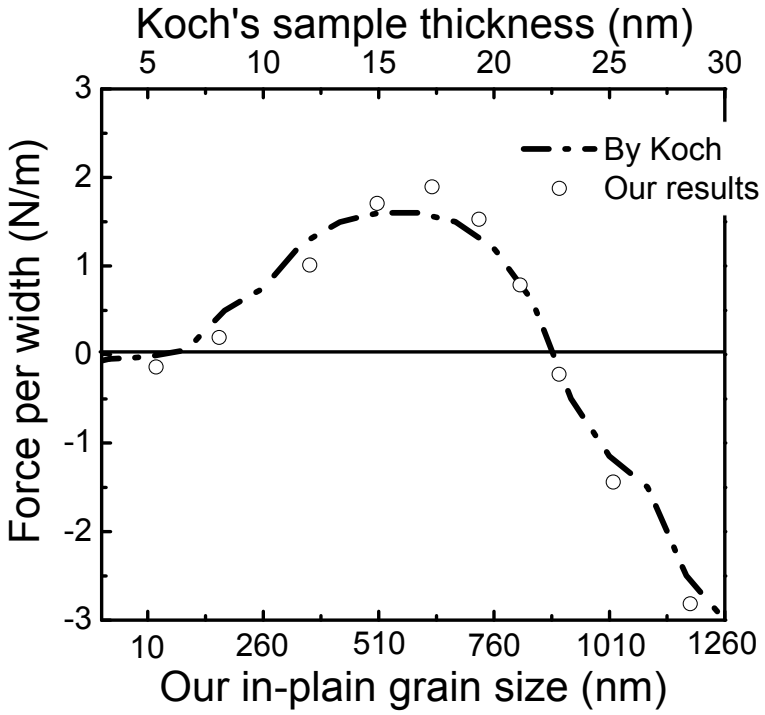

Figure 4.10 Plot of the force-per-width vs film thickness/grain size.

4.3. Time-multiscale simulations for peer-to-peer coalescence

In this section, the implications of the inside-bundling-outside-grooving model are investigated in regard to the origin, spatial distribution and evolution of the post-coalescence stress by multiscale simulation since the strain generation, the surface currents and the grain-boundary diffusion happen at very different timescales. Within this framework, the role of the flux in the stress behaviour is considered in terms of both morphology changes in the elastic deformation profiles computed by finite-element modelling and kinetic limitations (approached by partial differential equations) when the flux is of the same order "of magnitude" than the diffusion coefficients.

As described along section §4.2, our mesoscopic model for grain coalescence assumes that grain coalescence occurs by a combination of: (i) cohesive forces between grains causing the development of a growth stress with normal (long-range interactions along the radial direction $\hat{R}$) and shear (short-range interactions along the azimuthal direction

$\hat{\phi}$) contributions, and (ii) diffusive phenomena causing valley filling and grain rotation. As a consequence of these interactions, the resulting force can be determined from the balance between the involved surface-tension forces (Figure 4.11a) along the out-of-the-film plane direction ($\hat{z}$) as, $\gamma = 2\gamma_s \sin[\arctan(m)] - \gamma_{gb}(\theta) - \gamma_e(\Delta, \theta, \lambda)$ (where γ_s represents the surface energy with $\arctan(m)$ being the wetting angle at the grain junction; γ_{GB} corresponds to the GB energy depending on the misorientation angle θ between neighboring grains; and γ_e is the accumulated elastic energy during the coalescence, see Equation 4.4 for details). The key points of the inside bundling-outside grooving model to bear in mind are: (*a*) the shear-strain contribution to γ_e rises as the coalescing grains are larger (for $\lambda > \lambda_0$—a certain critical size) since their capacity to rotate drop as $\propto 1/\lambda^2$ [111]; and (*b*) since the mechanical coupling of two grains is better as the GB in between emerges at a higher height (i.e., at a shallower gap), the model assumes that the zipping of a given GB must be accompanied by the generation of shear strain within the whole crystalline volume that extends beyond the neighboring grains across GBs emerging at higher heights. As an example, whereas the zipping of the right-hand GB in Figure 4.11(a) (the shallowest) implies the generation of shear strain just within the bulk B+C, the zipping of the left-hand GB involves the whole drawn bulk (A+B+C). It means that γ_e increases (and so γ decreases) as the section of the gap to close is deeper, and the involved volume is larger. This effect would give rise to anisotropies in the σ_N strength along non-flat grain-junction contours, σ_N being higher where the gap is shallower.

4.3.1 Dynamics of stress accommodation

The stress accommodation for different degrees of σ_N anisotropy is investigated by finite-element modelling (FEM) applied on a simplified configuration of three touching (in pairs) semi-spherical grains as shown in Figure 4.11(a) (labelled A, B, and C). Such grains are not evenly spaced with each other, such that a deep gap appears between A and B, and a shallow one between B and C. The results are extrapolated to the model using periodic boundary conditions. The grains are elastically deformed by applying dissimilar normal loads σ_N^{left} and σ_N^{right} on their surface sections within the gaps A-B and

B-C, respectively. The σ_N anisotropy is defined $\chi = \max\left(\sigma_N^{rigth}\right) / \max\left(\sigma_N^{left}\right) \geq 1$ for $\sigma_N^{right} \leq 100$ MPa taken within the typical range reported for ductile metal films[19] with $\max\left(\sigma_N\right)$ being reached close at grain junctions where $-\hat{\nabla}_s$ is parallel to γ.

Figure 4.11(b-d) shows the elastic deformation profiles (*equilibrium profiles*, hereafter) that result from different χ to compare them with the initial profile (solid curve). Full sequences of the pre-equilibrium evolutions are included as complementary material[20]. The evolution of grains subjected to isotropic tensile stress ($\chi \approx 1$), which implies coalescence driven by pure radial interactions without shear strain, gives rise to an array of uniform gaps all them with the same depth (Figure 4.11b). This is because the σ_N strength to induce GB zipping increases as the gap is deeper (i.e., $\sigma_N \propto \sin^2\left[\arctan(m)\right]$; thus, the zipping between A and B prevails over that between B and C, until both gaps have the same depth.

Since the morphology for $\chi \approx 1$ in Figure 4.11(b) does not agree with those formed by irregular multigrain structures, we can rule out the radial interactions between grains (such as the traction forces and Laplace pressures) as being mainly responsible for the inside-bundling/outside-grooving phenomena. As χ rises, a bundling of the grains B and C occurs, giving rise to a multigrain structure, together with processes of unzipping for $1 < \chi < 10$ (Figure 4.11c) and grooving for $\chi \geq 10$ (Figure 4.11d) of the external GBs between structures (here A-B). A detailed inspection of the spatial distribution of the stress field inside the structures (enclosed regions in Figures 4.11b to 4.11d) reveals its dipolar geometry as depicted Figure 4.11(e). Whereas the surface continues being under traction, the zipped region comes under compression, whose strength increases as the anisotropy rises up to reach a saturation for $\chi > 20$. A dipolar field of the growth stress was proposed previously (although with a different origin) by Chason *et al.* [64] to address the insertion of leading adatoms by the gaps under traction into the GBs under compression.

[19] Maximum values of tensile stress measured in (Ag) $\sigma_N \leq 190$ MPa, (Al) ≤ 120 MPa, and (Au) ≤ 225 MPa —from J. A. Floro *et al.*, *J. Appl. Phys.* **89**, 4886 (2001) and Ref. [xx]

[20] See Supplemental Material at [*URL will be inserted by the Publisher*] for movies of the evolution of growth stress at different χ, and the relaxation by surface and bulk diffusions for the case $\chi = 4$.

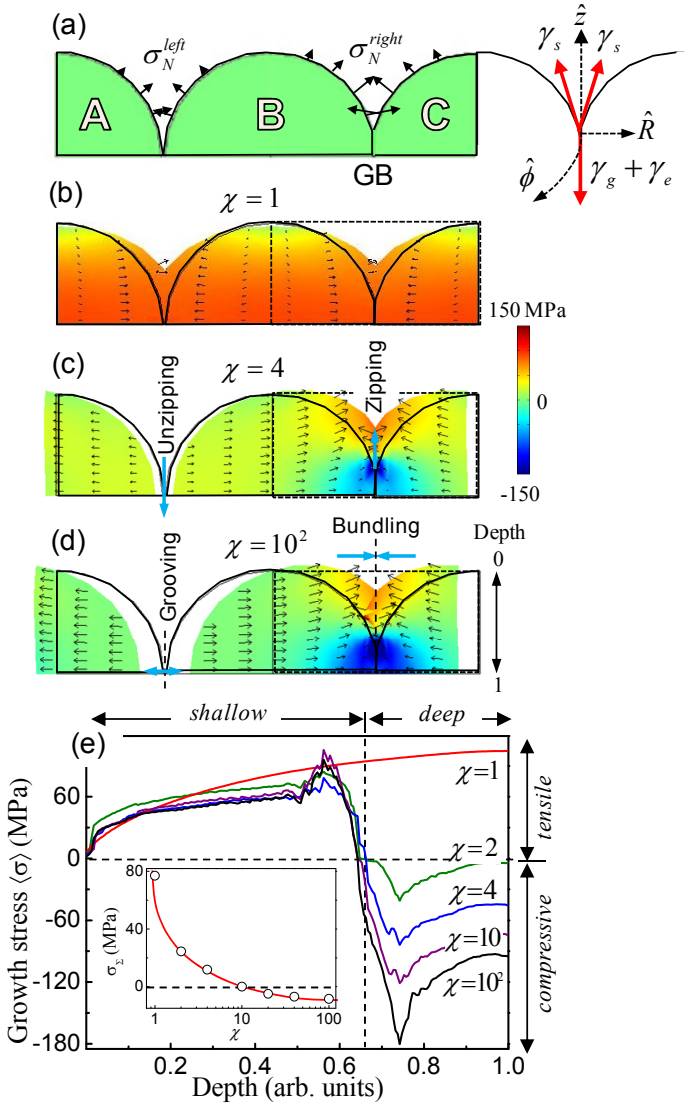

Figure 4.11(a-d) Elastic deformation profiles of three non-evenly spaced grains computed by FEM for different anisotropies χ of the σ_N stress fields resulting from the grain interactions. Right-hand sketch in (a) shows the balance between the involved surface-tension forces in Eq. 1. The arrows and the color scale in (b-d) depict the local fields of displacements and growth stress strains, respectively; whereas the solid curves correspond to the initial profile to realize the morphology changes. (e) Depth profiles of the radial-averaged growth stress ⟨σ⟩ fields within the enclosed regions in (b-d) (i.e., around GB+gap between B-C) for χ ranged between 1-10^2. Inset: χ - dependence of macroscopic stress σ_Σ [estimated as $\sigma_\Sigma \sim \int_{depth}\langle\sigma\rangle$, i.e., areas under the plots in (e)]. Profiles in (a-d) do not keep the grain proportions by AFM: the grain bulk underneath and unstressed tops are omitted to magnify GB regions.

Since the macroscopic growth stress σ_Σ (that measured through the Stoney equation) corresponds in a rough approximation to the area under the curves plotted in Figure 4.11(e) (i.e., $\sigma_\Sigma \propto \int_{depth}\langle\sigma\rangle$ where $\langle\ldots\rangle$ denotes the radial average), this can be divided into two contributions: $\int_{shallow}\langle\sigma\rangle + \int_{deep}\langle\sigma\rangle$, namely shallow tensile stress + deep compressive stress, respectively. As displayed in the inset of Figure 4.11(e), the deep

compressive stress becomes the predominant contribution for $\chi > 10$, which accounts for the compressive nature of σ_Σ during the post-coalescence, and it allows us to correlate the stress behavior with the observed phenomena of grain bundling into structures and grooving between them.

4.3.2 Dynamics of stress relaxation

Unlike the generation of the *equilibrium profiles* in Figure 4.11 that happens at atomic vibration timescale (~0.1 ps), the relaxation of such profiles by atomic currents takes place at longer times t within the range of surface (~μs-ms) and GB (~seconds-hours) diffusion timescales. Consequently, the kinetics of such a relaxation is approached by solving the following coupled mesoscopic rate equations that describe the evolution of the film surface ($S(\vec{r}_{R\phi},t) \equiv S$ —by dynamic scaling in Equation 4.5a) and film density ($\rho(\vec{r}_{R\phi z},t) \equiv \rho(\vec{r},t)$ —Equation 4.5b) in-plane $\left(\hat{R},\hat{\phi}\right)$ and out-of-plane ($\hat{z}$) directions, respectively:

$$\partial_t S\left(\vec{r}_{R\phi},t\right) = \int_{-\phi/2}^{\phi/2} F\left(\Theta\right)\partial\Theta - \kappa_s \nabla_s^2 \left(\Omega\left\{\gamma_s\left[\nabla^2 S + \left(\nabla S\right)^2\right] - \sigma\left(S\right)\right\}\right) + \eta\left(\vec{r}_{R\phi},t\right) \quad (4.5a),$$

$$\partial_t \rho = -\kappa_{GB} \nabla_{\hat{z}}^2 \left[\rho - \rho_0(\vec{r},t)\right] \quad (4.5b),$$

The considered mechanisms are:

Local advance of the surface due to the flux —First term (Equation 4.5a): The deposition flux F impinges (in general) inhomogeneously on the surface given its dependence on the incidence angle Θ and the local aperture angle $\phi(\vec{r}_{R\phi})$ —both measured from $-\hat{z}$. The angular distribution of the flux is described typically as $F(\Theta) = F_0(\cos^n(\Theta)/\psi)$ where F_0 is the plane flux, the power n gets values that depend on the flux-source characteristics [120] (e.g., for thermal fluxes originated by near-field evaporators $n = 3$; while for "forward peak" fluxes ejected from collimated massive sources $n \to \infty$ and thus $\cos^n\Theta \to$ Kronecker delta δ_ϕ) and $\psi = \int_{-\pi/2}^{\pi/2} \cos^n(\Theta)\partial\Theta$ corresponds to a normalization constant. The aperture angle is

determined by potential phenomena of shadowing ($0 \le \phi < \pi$ —geometric shadowing of grazing incident particles in the flux) and steering ($0 \le \phi < 2\pi$ —change in the trajectories of the particles by long-range attractive forces) [5].

Lateral relaxation by stress-biased Mullins-type diffusion —Second term (Equation 4.5a): $J_s = -\kappa_s \nabla_s \mu$ surface currents driven by the modified chemical potential $\mu \approx \Omega\left\{\gamma_s\left[\nabla^2 S + (\nabla S)^2\right] - \sigma(S)\right\}$ that results from the competition between the surface curvature $\propto \nabla^2 S$ —*linear Mullins term*, the local slope $\propto (\nabla S)^2$ —*Nonlinear Mullins*, and the surface stress $\sigma(S)$. Thus-defined J_s flows toward sites with higher curvatures and slopes (which implies higher densities of dangling bonds and steps, respectively) and/or under traction (those with lower film densities), as sketched in Figure 4.12(a). Edwards-Wilkinson and Kardar-Parisi-Zhang-type relaxations [namely, EW: $\nabla J_s \propto \nabla^2 S$ and KPZ: $\nabla J_s \propto (\nabla S)^2$, respectively] play minor roles at GB space scales (i.e., short-range features) [4].

Stochastic surface fluctuation by uncorrelated noise —Third term (Equation 4.5a): η includes the contributions at complementary length scales of both the Gaussian-white deposition noise $\eta_F \propto \sqrt{F_0}$ (at long-range) and the diffusive noise $\eta_D \propto \sqrt{\kappa_s}$ (short-range) arising from the probabilistic nature of the thermally-activated diffusion; the crossover between length scales being $\Lambda \approx \sqrt[4]{\kappa_s / F_0}$. Thus for a given time t', $\eta(\vec{r}_{R\varphi}, t') = \eta_D(\vec{r}_{R\varphi}, t')\Phi[\Lambda - \delta\vec{r}_{R\varphi}] + \eta_F(\vec{r}_{R\varphi}, t')\Phi[\delta\vec{r}_{R\varphi} - \Lambda]$, where $\delta\vec{r}_{R\varphi}$ denotes the perturbation spacing and $\Phi[x]$ is the unit-step function defined as $\Phi[x > 0]$=1 and =0 otherwise; such that the surface fluctuation becomes: $\delta S(\vec{r}_{R\varphi}, t') = \int_0^{t'} \eta(\vec{r}_{R\varphi}, t)\partial t$.

Relaxation of film density by GB diffusion toward the surface —Equation 4.5b: $J_{gb} = -\kappa_{gb}\nabla_{\hat{z}}[\rho(\vec{r},t) - \rho_0(\vec{r},t)] = -\kappa_{gb}\nabla_{\hat{z}}\delta\rho$ current driven by the gradient of the density perturbation $\delta\rho$ along GB with respect to that of the unstressed film/ω-rough surface/vacuum system defined as: $\rho_0(\vec{r},t) = \rho_0 / \{1 + e^{4[r_{\hat{z}} - S(\vec{r}_{R\phi},t)]/\omega}\}$ [3].

Coupling relationship: In order to convert the local perturbations of the system density to the ascribed stress-field and vice versa, we use the relation $\sigma(\vec{r},t) \propto -\nabla_r U$ between the growth stress σ and the interatomic potential U of the crystal lattice (that for fcc metals corresponds to a manybody embedded-atom potential [70]) in conditions of

small parameter perturbations $\delta a / a_0 << 1$ around the equilibrium one $a_0 \propto \rho_0^{-1/3}$ such that $U(\delta a) \propto \delta a^2$ [$\sigma \propto -\delta a$] becomes parabolic [linear] with δa and so, the Hooke's law: $\sigma(\vec{r},t) \equiv M\varepsilon = M\dfrac{a-a_0}{a_0} \approx M\left[\sqrt[3]{\rho_0(\vec{r},t)/\rho(\vec{r},t)}-1\right]$ can be applied.

Thus, the gaps deeper than the surface roughness ω are realized as rarified regions (with $\delta\rho < 0$ and $\sigma > 0$, i.e., under traction) of the films, whereas the deep regions under compression would correspond to densified regions ($\delta\rho > 0$) —Figure 4.12b. Equations 4.5a and 4.5b are computed in 1+1D by *Runge-Kutta* from the *equilibrium profiles* computed by FEM (initial conditions for times ~10^{-12} s). The calculation assumes: (*i*) in-plane radial symmetry and (*ii*) periodic boundary conditions. The obtained evolutions of the surface and film density are plotted in Figures 4.12 (a) and 4.12(b), respectively.

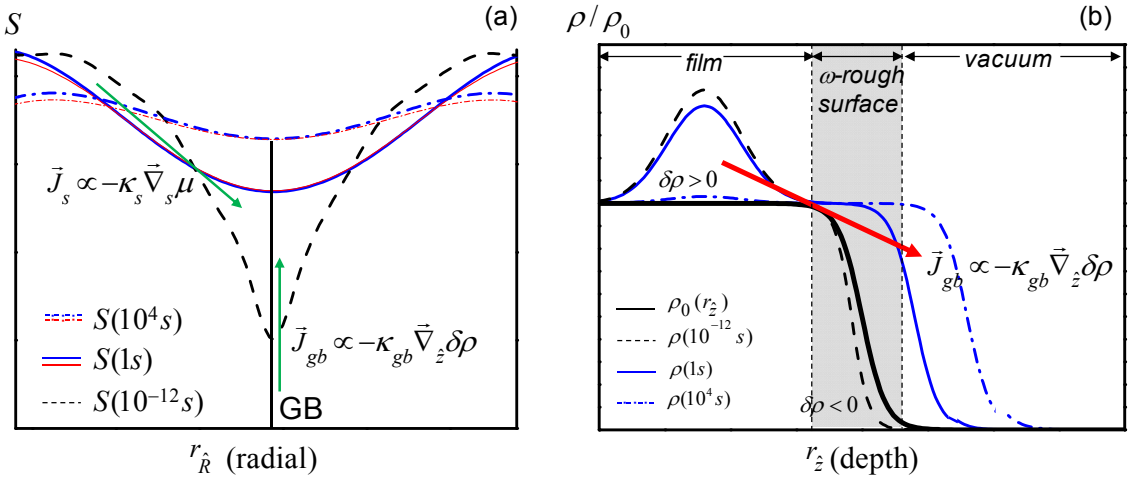

Figure 4.12 (a) Evolution of film surface driven by stress-biased Mullin-type diffusions at different relaxation times from the initial profile computed by FEM (dashed black curve for t~10^{-12}). Red (blue) curves correspond to the relaxed profiles considering linear (linear+non-linear) Mullin terms [xx]. (b) Evolution of the system-density depth profile driven by GB diffusions towards the film surface.

The partial differential equation system formed by Equations 4.5(a) and (b) are computed in 1+1D [i.e., in the plane $(\hat{R},\hat{z})$ assuming radial symmetry] by the *Runge-Kutta* method. The integration is carried out within the enclosed regions in Figures 4.11(c,d) using the *equilibrium profiles* by FEM as initial conditions, and assuming periodic boundary conditions. The physical constants for the calculation are summarized in Table 2.8. Figure 4.13(a) displays the *equilibrium profile* for $\chi = 4$ (that

corresponds to $\sigma_\Sigma > 0$), whose evolution driven by both surface and GB diffusion is outlined in Figures 4.13b and 4.13c, respectively [see footnote 12]).

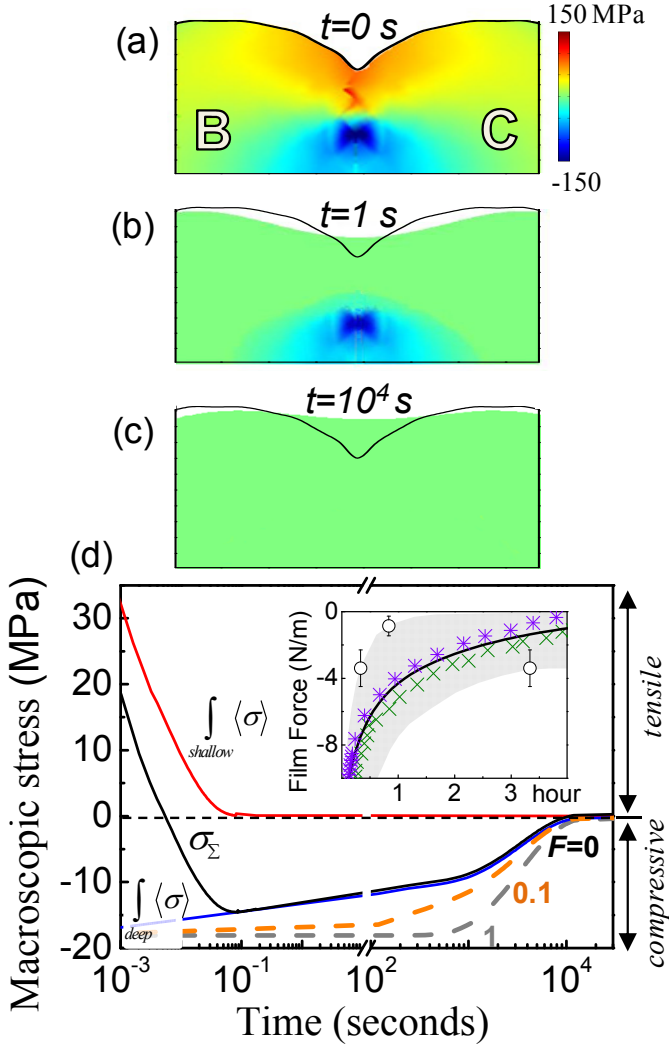

Figure 4.13 (a-c) Relaxation of the growth stress generated by interactions between the grains B and C with χ = 4 by surface (b) and GB (c) diffusions for different relaxation times once the deposition flux is stopped (F_0 = 0). The color scale denotes the strength of the stress field whereas the solid lines depict the outline of the *equilibrium profile* by FEM. (d) Evolution of $\int_{shallow}\langle\sigma\rangle$ and $\int_{deep}\langle\sigma\rangle$ contributions to σ_Σ for different F_0 as labeled. *Inset*: Fit of the simulated σ_Σ relaxation (expressed as film force $\sigma_\Sigma \cdot \lambda_\perp$ with $\lambda_\perp$ = 105 nm A. Gonzalez-Gonzalez *et al*., Phys. Rev. B 84, 155450 (2011) by Scherrer) to the residual stress data reported for polycrystalline Au films measured *in-situ* by capacitance (×, R. Abermann and R. Koch, Thin Solid Films 129, 71 (1985)) and cantilever beam methods (*, J. Leib et. al., Phys. Rev. Lett. 102, 256101 (2009)) and *ex-situ* by grazing-incidence DRX (○,A. Gonzalez-Gonzalez *et al*., Phys. Rev. B 84, 155450 (2011)). Dashed region corresponds to the data dispersion.

The relaxation of the dipolar growth-stress field is plotted in Figure 4.13(d). The fact that the surface diffusion differs in several orders of magnitude from that of GB ($\kappa_s / \kappa_{GB} \sim 10^{12}$ [114-116]) allows us to separate their contributions to the stress

relaxation by timescales. This means that during the relaxation of $\int_{shallow}\langle\sigma\rangle$ by surface diffusion happening at tens of ms (Figure 4.13d), the GB diffusion is practically frozen and $\int_{deep}\langle\sigma\rangle$ remains constant (±10%) for few seconds. The delay in the release of $\int_{deep}\langle\sigma\rangle$ is also increased by the fact that the surface diffusion moves the compression core away from the surface. Consequently, the $\int_{deep}\langle\sigma\rangle$ contribution to σ_Σ becomes higher (note the system turns out to be under compression for $t > 10$ ms).

The slow relaxation of the deep compressive stress (plotted in terms of film force $\sigma_\Sigma\lambda_\perp$ with the out-of-plane grain size $\lambda_\perp$ estimated in [62] from the Scherrer's equation) is confirmed in the inset of Figure 4.13(d) by fitting our model to experimental data reported for polycrystalline Au films, whose residual stresses were measured at RT by complementary techniques: (a) through the Stoney equation determining *in-situ* the system curvature by capacitance [99] and (b) using the standard $Sin^2\psi$ method from *ex-situ* measurements by grazing-incidence XRD [62]. $\kappa_{GB} = 5\times10^{-15}$ cm^2/s resulting from the fit shows the good agreement with those previously reported [115, 116], which supports our hypothesis of deep-compression release through GB diffusion. Nevertheless, other faster relaxations (~few min.) are also viable; e.g., Leib *et al.* [115, 116] proposed a temperature-independent relaxation based on obstacle-free dislocation glides for Au films on SiN_x/Si(100) (symbol * in the inset of Figure 4.13d).

In this scenario, the deposition flux F influences the stress behavior in two manners: (*a*) It modifies the *equilibrium profile* as a consequence of its non-uniform nature, and/or (*b*) limits partially (or totally) the mass transport-driven relaxations happening at deposition timescales $\geq 1/F_0\lambda^2$ ($\geq 1/F_0$). The first manner (*a*) would take place, for example, during growths under low-mobility conditions in which the surface diffusion is not enough to compensate higher growth rates on grain tops induced by shadowing and steering. Thus, the gaps become deeper, the grain sections under traction are larger, and the tensile stress prevails. This effect, which is counterbalanced by the surface diffusion when the flux is stopped and vice versa, would give rise to similar stress behaviour to that reported by Koch *et al.* [103] for Fe films deposited at low temperatures (T = 310 K). Conversely, (i.e., under high mobility conditions), the shallower gaps (those with higher aperture angles) receive higher fluxes than the deeper

ones, which contribute to speeding up the filling rate of the former, and to consequently increase the σ_N anisotropy that causes the deep compressive stress to strengthen (Figure 4.11e). The second manner (*b*) occurs when the flux hinders the release of $\int_{deep}\langle\sigma\rangle$ (Figure 4.13d —curves for different F_0) by moving the surface away from the compression core faster than the mass transport through GB diffusion, which is the responsible for the stress relaxation during periods of flux interruption and post-deposition ($F_0 = 0$). Note that the fact that realistic fluxes ($F_0 \ll 10$ nm/s) cannot limit the shallow relaxation by surface diffusion under high mobility conditions, it reduces the threshold σ_N anisotropy required to induce a macroscopic compressive stress down to practical values (e.g., $\chi \geq 1.5$ for $F_0 = 0.1$ nm/s after $t = 1$s —not shown) lower than the threshold of $\chi \geq 10$ by FEM for kinetically frozen systems (inset of Figure 4.11e). Different combinations of the effects described above account for the reversible dependence on the flux of the post-coalescence growth stress.

In this section we provided major findings on: (*i*) the key role played by interactions between grains (in particular those azimuthally driven by the misorientation between coalescing grains) at complementary space scales on the origin, nature, and dipolar structure of the post-coalescence growth stress; and (*ii*) how the interplay between the deposition conditions (i.e., flux and mobility) and the mechanisms of stress accommodation/relaxation determines the growth stress behaviour in regard to its reversible dependence on the flux and evolution at different timescales. The fact that the multiscale-simulated results allow a successful interpretation of the main experimental evidences reported so far supports the soundness of the proposed "inside-bundling/outside-grooving" model.

4.3.4 Role of microstructure during grain reorientation phenomena

In this section the influence of the massive stiffer substrate on the mechanical properties of polycrystalline films deposited onto will be investigated. In particular, we will analyze how the substrate constraints the relative motions of the inner parts of the films, taking into account for relative motions involved in the grain reorientation phenomena described above.

The used system geometry considered round-shaped (elastic) surface grains of average in-plane size λ and out-of-plane size $\lambda_\perp$ (along the $\hat{z}$ direction), which are attached to a buried polycrystalline columnar bulk (Figure 4.14a). The polycrystalline bulk acts as mechanical spacer, which decouples surface grains from the substrate (Figure 4.14b). The film thickness d was defined as the sum of $\lambda_\perp$ and the "bulk thickness" d_{bulk} (i.e., the depth of the columnar bulk), so that $d = \lambda_\perp + d_{bulk}$. Several bulk thicknesses were considered in our analysis, ranging from 0 to $10d_{bulk}$. In dependence of the film thickness, two limit configurations were considered: (i) $d = \lambda_\perp$ — *ultra thin film upon the coalescence*, and (ii) $d = 10\times\lambda_\perp$ —*columnar film* (Figure 4.15). As observed in Figure 3.12 (§3.3.2), for the case of Au polycrystalline films here investigated $\lambda_\perp$ values range from $\lambda_\perp$~ 50 to 100 nm (as measured by XRD Scherrer formalism). Then, these two limit configurations (i) and (ii) are available for d ~ 50 – 100 nm to d ~ 500 nm – 1μm.

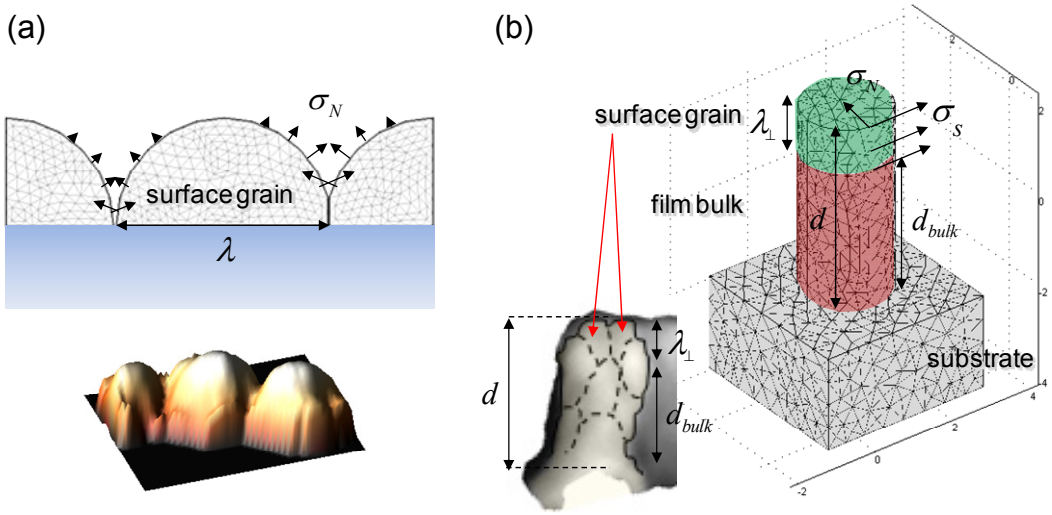

Figure 4.14 System geometry. (a) Cross-section profile of a set of three grains with grain boundaries at different heights, which are attached directly on the substrate, reproducing the surface morphology of Au polycrystalline films showed in the inset. The black arrows indicate the direction of the normal stress field applied inside the valley between grains. *Inset*: fragment of an AFM image showing three grains separated to each other through grain boundaries. The image was extracted from an Au/SiO_x/Si(111) film of d = 200 nm. (a) Green dashed region corresponds to the surface grains, whereas red dashed one to the bulk. The mesh observed correspond to the optimized Kirchhoff plate render used by the finite element algorithm to develop mechanical analyses. *Inset*: Columnar structure observed for Au/SiO_x/Si(111) films of thickness d = 200 nm . The dashed lines indicate the grain boundaries in the bulk structure. (b) two limit film configurations considered: ultra thin film (d=$\lambda_\perp$), in which no bulk grains were taken into account, and columnar film ($\lambda_\perp$ = 10λ), where thick polycrystalline bulk grain is considered. The color scheme shows the local intensity of the strain field, and arrows the direction of displacement.

As described previously in §4.2.2, surface grains are separated from each other by a network of external grain boundaries, and they interact to each other via: (*a*) *long-range interactions* through the gap down to the grain junction and (*b*) *short-range interactions* at the GBs that extend beyond the grain junction through the polycrystalline film bulk. Such interactions can promote an inside bundling-outside grooving mechanism, which can be understood as a twisted zipping in the sense that it involves concerted grain zipping and reorientation mechanisms. Our model assumes that the shear stress is only applied within the layer of surface grains since it corresponds to the "free" side of the film with the high enough mobility to allow both the mass motion and the generation of strain. It is well known that the material recrystallization starts within the regions with higher degrees of freedoms, where due to the higher entropy the energy barrier for the phase change is lower. This assumption is supported by the experimental evidences (§3.3) and model fittings (§4.2) suggesting that coalescence by inside bundling-outside grooving phenomenon only occurs for surface grains. Besides, the mechanical coupling between grains along polycrystalline columns (i.e., for columns formed by an array of vertically stacked grains) and such columns with the substrate (both separated by semicoherent grain boundaries) is stronger than the inter-columnar mechanical coupling. Potential glide effects in the GBs and the interface with the substrate are neglected.

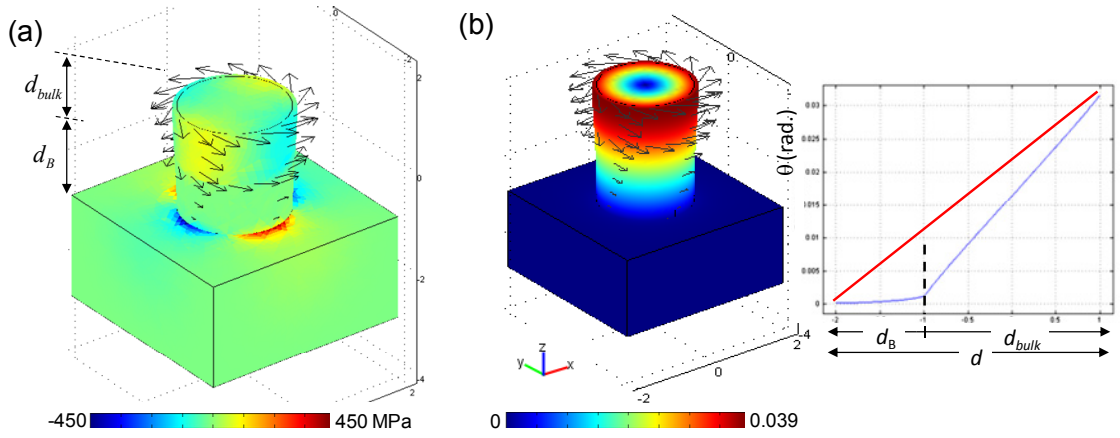

Figure 4.15 (a) FEM simulation showing the distribution of the applied shear stress along the column in a system with $d_{bulk}/d_B = 1$. The value d_B mimics the substrate depth. The color scheme corresponds to the local stress field as indicated by the color scale (including the signs of the coordinates of the stress along the *x*,*y* directions), and the length of the arrows the magnitude of the deformation caused. Shear stress is applied along the azimuthal of the surface grain, and stress in the interface film/substrate rises as a response to torsion. (b) FEM simulation showing the distribution of the shear strain along the column in the same system, together with a plot of strain vs depth dependence, showing a linear behavior with a slope change at the film/substrate interface, and the physical meaning of the effective mechanical behavior (red line) as defined in the text. The color scheme corresponds to the local strain field as indicated by the color scale.

When a shear stress is applied, it is distributed along the out-of-the plane direction, as shown in Figure 4.15(a), given rise to a torsion-like strain (with no strain at the column central axis and maximum one at borders —as displayed in Figure 4.15(b) through the columnar bulk that goes beyond the interface towards the substrate volume. A cross-section profile of the film thickness, i.e., taken along the bulk column, shows the distribution of the strain (reorientation) along the column (Figures 4.15b and 4.16a). The cross section profile was measured at a distance $\lambda / 2$ from the center of the column. As observed in Figure 4.16(a), the linear dependence of strain vs. stress ($\Delta\theta = (d_{bulk}/\lambda G)\sigma_s$ as predicted by the Hooke law) changes of slope at the film/substrate interface from a lower slope ($d_B/\lambda G_{Si}$) inside the Si substrate to the higher one ($h/\lambda G_{\mathrm{Au}}$) within the Au column. It is expected because both Au is softer than Si (i.e., $G_{\mathrm{Au}} < G_{\mathrm{Si}}$) and the Au columns have a "free" surface side such that it results feasible that the shear stress generates an out-of-plane expansion along the column axis.

The non-negligible strain observed at the stiffer Si substrate indicates that the substrate accommodates part of the applied shear stress to the surface grain. An effective shear modulus G_{eff} —i.e., the shear modulus of an homogeneous media producing a behavior similar to the so ascribed to the film/substrate system regarding to the mechanical response to the shear stress generated by the surface grain misorientation—, can be defined as $1/G_{eff} = (1/G_{Si})(d_B/(d_{bulk}+d_B)) + (1/G_{Au})(d_{bulk}/(d_{bulk}+d_B))$, as shown in Figure 4.16(a). The strain in the Au/Si interface (see Figure 4.16a for depths → h) is observed due to the elastic nature of the Si substrate.

For harder substrates (i.e. with higher shear modulus), strain along the substrate's depth is expected to be lower, and applied shear stress at the surface could induce film delamination and/or the local peeling of the film/substrate interface in local regions. This suggests that the ratio $G_{film}/G_{substrate}$ plays a significant role in the viability for grain reorientation: as the ratio $G_{film}/G_{substrate} \rightarrow 1$, the shear strain would be propagated easily along the film/substrate systems, and therefore grain reorientation would be easy to observe as larger torsion angles are reached. As observed in Figure 4.16(b), the effective shear modulus decrease as the film thickness is higher. Therefore upper and lower limits in $\Delta\theta$ correspond to the substrate and the film, here Si and Au, respectively, as observed in Figure 4.16(b). This result suggests that while thinner the film, $G_{film} \rightarrow G_{substrate}$. The theoretical value of G_{film} corresponds to the mechanical behavior for bulk materials (i.e.,

film thickness → ∞), and grain reorientation will have a low probability to occur and it will be difficult to observe.

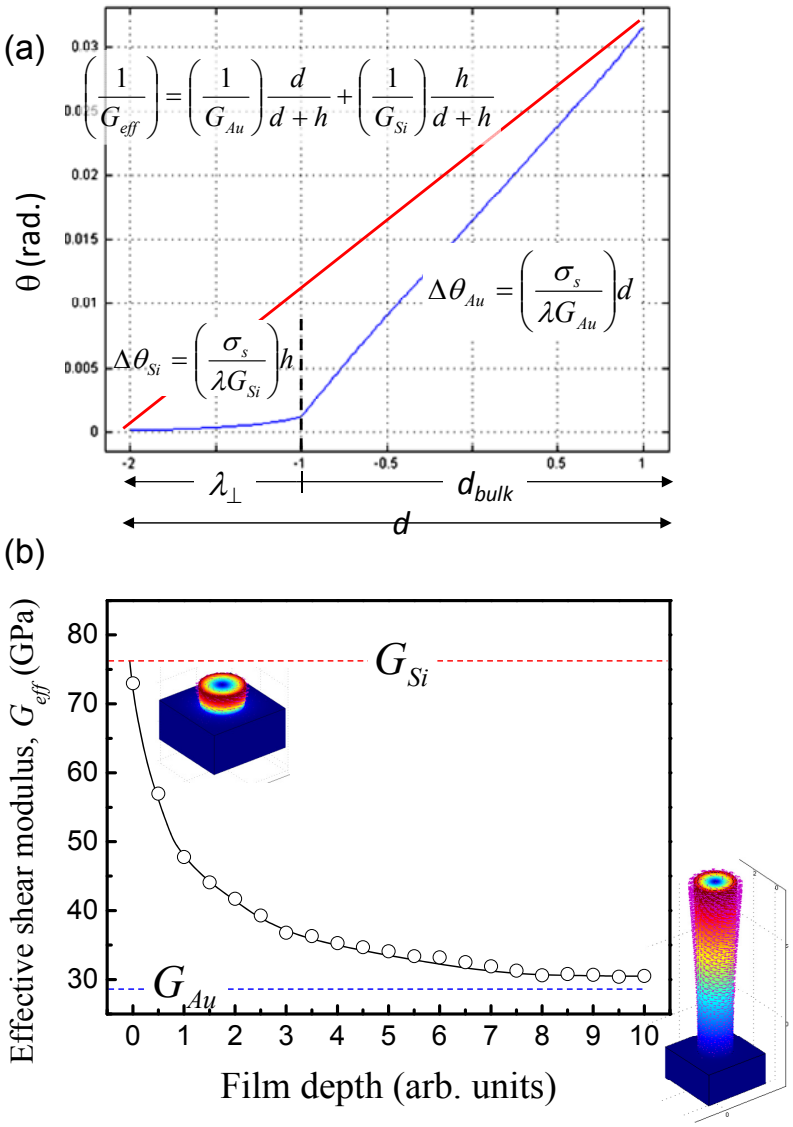

Figure 4.16 (a) Strain *vs* depth dependence showing a linear behavior with a slope change at the film/substrate interface, and the physical meaning of the effective mechanical behavior (red line) as defined in the text. (b) Evolution of G_{eff} with the film thickness. As observed, it varies between two limiting shear modulus, ascribed to the silicon substrate (stiffer material) and the Au in volume (softer material). Insets sketch several system configurations.

The change in the value of the shear modulus G as a consequence of the coupling of surface grains with a rigid substrate through an elastic film microstructure has considerable implications in the elastic energy of the system. Remembering the Equation 4.5, $\gamma_e(\lambda)$ depends linearly on G as:

$$\gamma_e(\lambda) = \gamma_e^{\Delta}(\lambda) + \gamma_e^{\theta}(\lambda) = \frac{6M\Delta_r^2(\lambda)}{\pi\lambda} + \frac{G\lambda\theta_r^2(\lambda)\cdot\psi(\lambda-\lambda_0)}{2\pi} \qquad (4.7a),$$

According to the Equation 4.5 and 4.7a, a change in G modifies the elastic energy cost for grain reorientation. Taking into account in Equation 4.7a for the columnar structure of the polycrystalline film (rather than the equiaxial shape of the surface grains considered in Equation 4.5), which implies to change G (for equiaxed homogeneous surface grains) to $\lambda G_{eff}/d$ (for inhomogeneous columns that propagate within the substrate bulk), we get:

$$\gamma_e(\lambda) = \gamma_e^{\Delta}(\lambda) + \gamma_e^{\theta}(\lambda) = \frac{6M\Delta_r^2(\lambda)}{\pi\lambda} + \frac{G_{eff}\lambda^2\theta_r^2(\lambda)\cdot\psi(\lambda-\lambda_0)}{2d\pi} \qquad (4.7b),$$

Fort the special case of polycrystalline films growing in a columnar habit by geometric shadowing or steering, $\lambda \sim d^{1/3}$ and therefore $\gamma_e^{\theta}(\lambda) \propto \lambda^{5/3}$. In this case, Equation 4.7b changes into:

$$\gamma_e(\lambda) = \gamma_e^{\Delta}(\lambda) + \gamma_e^{\theta}(\lambda) = \frac{6M\Delta_r^2(\lambda)}{\pi\lambda} + \frac{G_{eff}\lambda^{5/3}\theta_r^2(\lambda)\cdot\psi(\lambda-\lambda_0)}{2\pi} \qquad (4.7c)$$

However, as observed in Figure 4.17, it is no necessary to consider the existence of a "critical size for rotation λ_0", because it is only an approximation. Indeed, in the interval $\lambda_0 \le \lambda \le 2\lambda_0$, $\gamma_e^{\theta} \propto \lambda^2$ can be approximated by Taylor series to $\gamma_e^{\theta} \propto 4\lambda_0(\lambda-\lambda_0)$ (which corresponds to a straight line $m = 4\lambda_0$, intercept in $-4\lambda_0^2$, with a zero in $\lambda = \lambda_0$, see the pink curve in Figure 4.17). Considering that γ_e^{θ} must be ≥ 0, $\gamma_e^{\theta}(\lambda < \lambda_0) \equiv 0$ in agreement with the approximation taken in the inside bundling-outside-grooving phenomena around 300 nm. For these considerations, the mechanism of inside bundling-outside grooving phenomena is renamed as *twisted zipping*.

Figure 4.18 show a plot of the λ-dependence of the elastic energy γ_e in the lights of the assumptions of the twisted zipping model. Several regions can be identified:

I. Similar to the so described previously in §4.2.3, for grains with sizes $\lambda_1 < \lambda_g < \lambda_0$ attraction between the opposed faces of neighbouring grains predominates, giving rise to a progressive gap closure by gap filling and grain zipping plus free rotation in the case of in-plane misorientation, causing the development of multigrain structures. This region mainly corresponds to the homogeneous zipping caused by radial stress, and therefore it is not affected by modifications in the elastic energy due to changes in the shear component.

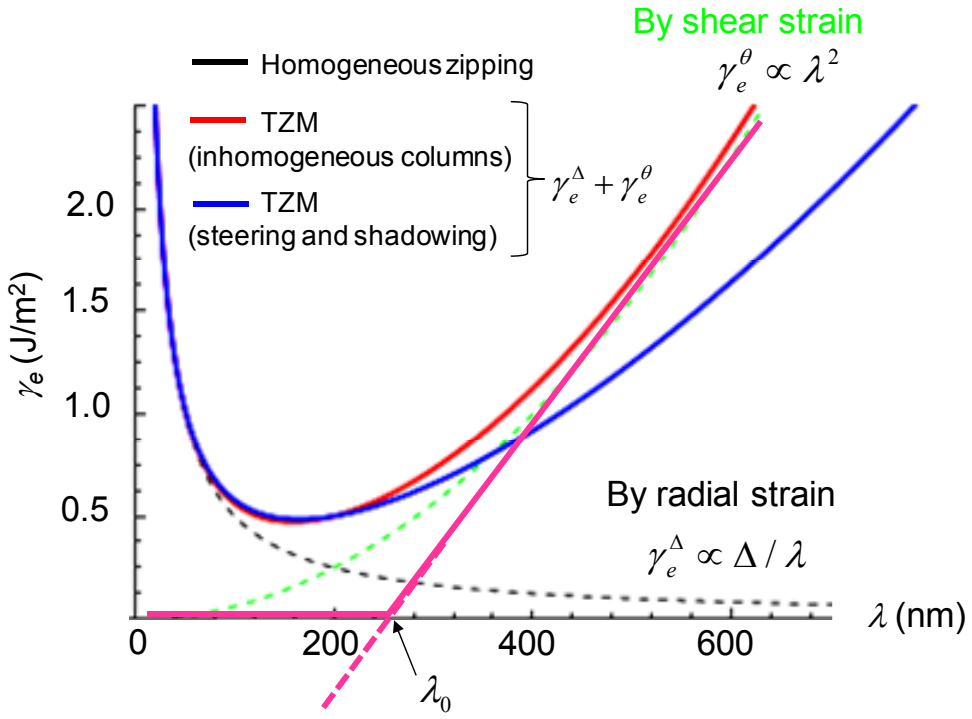

Figure 4.17 Sketch of the λ-dependence of the elastic energy with the grain size showing different contributions to compare the homogeneous zipping phenomena (black dashed curve) and twisted zipping model (TZM) as proposed previously. Also, dissimilar tendencies of the TZM are displayed, corresponding to the behaviors of the radial strain contribution to the elastic energy in the case of films formed by inhomogeneous columns ($\propto \lambda^2$) and grains grown in a columnar habit by shadowing and steering ($\propto \lambda^{5/3}$)..

II. For surface entities (grains and multigrain structures) with sizes $\lambda_0 < \lambda < \lambda_2$, the increase in γ_e accounts for the progressive loss of the ability to relax fully the in-plane misorientation via surface currents inducing the rotation of the coalescing features. The ability for grain rotation vanishes for grain sizes ~ $2\lambda_0$, when the condition $\gamma_e(\lambda_g > \lambda_2') \geq 2\gamma_s \sin\left[\arctan\left(\delta m\right)\right]$ is fulfilled. The non-relaxed part is then accommodated by shear strain with the subsequent energy

cost. In this region the dependence of the mechanical coupling between surface grains and the substrate is important. Considering shear strain propagation along the film microstructure implies that the effective shear modulus $G_{eff} \rightarrow G_{substrate}$, and the ability of the grains to twits decreases faster (red and blue dashed curves in Figure 4.18) than in the case at which shear strain is not distributed (black curve in Figure 4.18). Because the energy cost ascribed to the twist of grains that are mechanically coupled to the substrate through a "thin" film instead of a "thicker" one is higher, the λ_2 value (the size threshold for grooving) shifts towards lower grain sizes, reaching early the condition $\gamma_e(\lambda_g > \lambda_2) \geq 2\gamma_s \sin\left[\arctan\left(m_{tip}\right)\right]$. Then, reorientation between grains by torsion can be hindered even at early stages of growth.

For the case of Au/Si films investigated here, λ_2 moves from $\lambda_2 \sim 690$ nm to $\lambda_2 \sim 280$ nm ($\sim 2\ \lambda_0$) when the ratio of in-plane size to out-of-plane grain sizes is $\lambda / d_{bulk} = 1/2$. For Au ultra thin films (i.e., with surface grains attached directly to the harder Si substrate), λ_2 is even lower, reaching a value of $\lambda_2 \sim 190$ nm. In this latter case, coalescence occurs only by grain rotation. If peripheral surface currents are not able to reduce the in-plane misorientation between coalescing grains in this case, grooving occurs first, and coalescence will be inhibited. In those systems, compressive growth stress will arise even when the surface is composed by small grains with sizes of $< 2\lambda_0$. The fact that the elastic energy increases faster for low thicknesses could explain the fact that grain reorientation mechanism was not considered so far in the studies dealing with the origin of the intrinsic compressive stress during film growth. For most of the experiments describing the evolution of growth fronts the film thicknesses range from 0 to 80 nm. For such low thicknesses, the substrate pin grains against reversible (elastic) reorientation by shear strain generation.

Because torsion is inhibited for such film thicknesses, grain coalescence can occur by grain rotation phenomena. In our case, the film thickness is high (d = 200 nm), and the columnar bulk structure decouples mechanically Au surface grains from the stiffer massive Si substrate, enabling coalescence by grain reorientation due to both, torsion and rotation (as described in Equation 4.3).

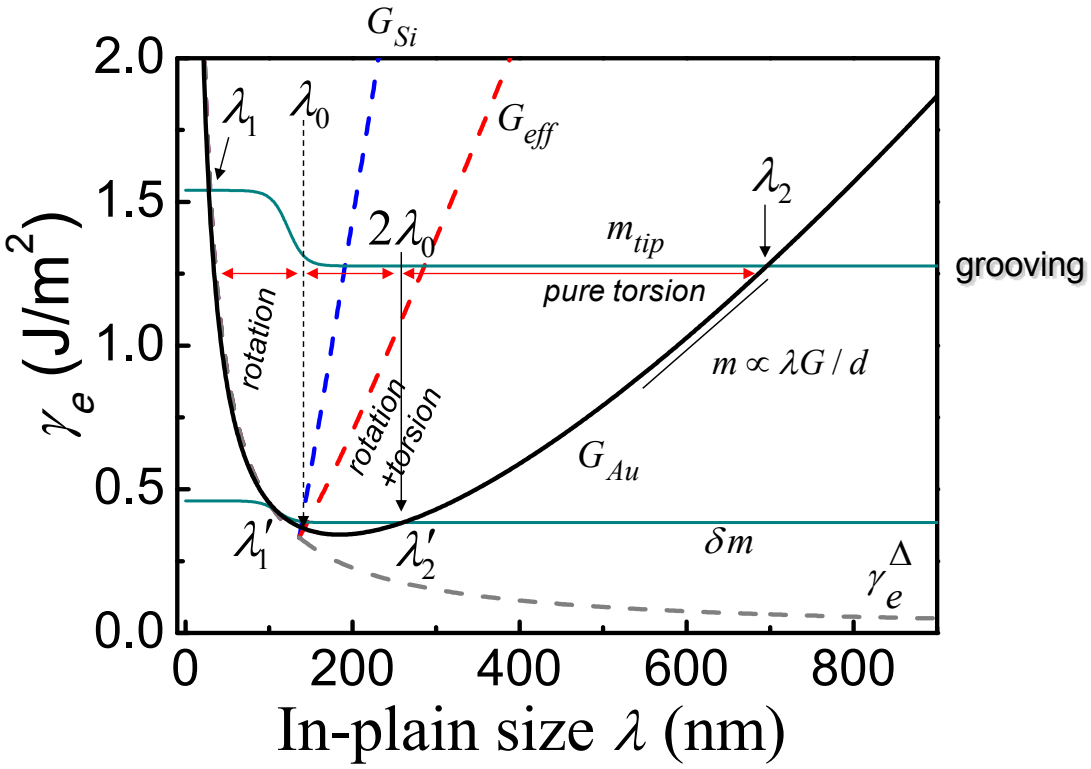

Figure 4.18 λ-dependence of the elastic energy with the grain size for a twisted zipping mechanism, which takes into account for the spreading of the grain torsion along the columnar bulk film. As compared from Figure 4.9(a) it can be observed that the consideration of a grain torsion spreading along the volume shifts the crossover grain sizes (lambdas1, 2…) to lower values than that expected if the film-substrate interactions are not considered. The meaning of the labels in the curve was previously described in §4.2.3. The horizontal lines in Figure 4.17 correspond to the coalescence (labelled "δm") and non-contact/grooving ("m_{tip}") conditions as defined in the previous section. Their intercepts with the curve $\gamma_e(\lambda)$ [explicitly, λ_1 and λ'' for the line "m_{tip}" ("δm")] define the interaction regimes between the surface features as a function of their sizes. Figure 4.17 shows the λ-dependence of the elastic energy as formulated in Equation 4.7b.

.

4.4 Conclusions of the Chapter

We report experimental findings concerning the local interactions between grains that coarsen on the surface of annealed polycrystalline Au(111) films. In the light of them, we propose a comprehensive model that addresses successful the morphological transformations observed in the annealed films and offers a plausible explication for the compressive nature of the growth stress generated during the post-coalescence. Such an explanation is based on the following evidences and/or arguments: The findings point to that the grain coarsening occurs mostly by coalescence of single-crystal grains into multigrain structures (rather than by grain growth) involving progressively mechanisms of relaxation by surface currents and accommodation by strain generation of the growth stress generated in both the normal and azimuthal directions. As the surface entities

(i.e., grains and structures) become larger, the ratio of accommodated stress to relaxed one rises with the resulting increment in the elastic energy (in particular that ascribed to the shear strain generated during the coalescence of larger misoriented structures). Consequently, the balance between the energy saved by the system as a result of the coalescence and the accumulated elastic energy at different length scales determinates the nature of the local interactions. Thus, the fact that such a balance is favorable to the coalescence at grain-size scale explains the tendency to bundle grains into structures; whereas the unfavorable balance at the size-scale of the structures accounts for the repulsion between them, and causing grooving. During grooving, sharp and deep external grain boundaries appears between multigrain structures. As deeper the external grain boundaries are, larger are the structures that they limit, because external grain boundaries have to rearrange all the grains bonded by shallow boundaries inside the multigrain structure. As a consequence, the normal stress vanishes as external grain boundaries are deeper. Therefore, for grains with contour points that are not at the same height, anisotropy in the normal stress appears.

For coalescing grains supporting several degrees of normal stress anisotropy, we observe that a grain bundling phenomenon occurs together with unzipping and grooving of the external grain boundaries between structures, promoting the development of a dipolar-shaped stress field inside structures (with shallow-tensile an deep-compressive components). The increase of the local stress asymmetry strengthens the deep compressive component (until saturation). This effect enhanced by the large differences between the adatom mobility at the surface, grain boundaries and film bulk, enables a fast relaxation of the tensile stress against the lower relaxation of the compressive one. Differences in the local curvature of the film affecting the incidence of the growth flux also improve compression in the film, because the flux enables a fast relaxation of the shallow regions of the film that supports tensile stress. Our observations would account for the compressive nature of the macroscopic growth stress during the post-coalescence and the reversible behavior of the stress during high/low mobility conditions, allowing us to address the relationship between the stress behavior and the phenomena of grain bundling and grooving during growth the Volmer-Weber-type thin films.

CHAPTER 5

HIERARCHICAL COARSENING: A LATE SLOPE SELECTION-DRIVEN OSTWALD RIPENING POLYCRYSTALLINE IN THIN FILM PREPARATION

5.1 Hierarchical coalescence: the growth by Ostwald ripening

In previous chapters we investigated the interactions between grains during coalescence. We discovered that several phenomena like grain-to-grain interactions causing stress generation and mass transport driven by chemical potential gradients relaxing such stress control the morphology evolution of film surfaces during growth an annealing. By manipulating such phenomena accordingly, we would be able to prepare nanostructurated surfaces formed by ordered arrays of nanostructures of defined sizes and shapes. For the metal films investigated to this chapter, film growth took place together with the development of (nano)faceted flanks, stabilized by (intra-)inter-layer mass transport and grain-to-grain interactive forces at grain boundaries (§4). In this chapter, we analyze how a bias for mass transport can promote a competitive growth based on Ostwald ripening, in which hierarchical processes of coarsening due to shape selection determine the film morphology evolution even for low temperatures ($0.28T_{melting}$) and large grain sizes (20-500 nm). The origin and the main characteristics of such an atypical kind of coarsening are elucidated by addressing the morphology evolution of ZnO films —described in terms of the evolution of sizes, shapes, surface slopes and morphological environments of grains—, by means of a mesoscopic approach of slope selection. The comprehensive investigation of the role played by the morphological environments (i.e. the local spatial and morphological configuration around a specific surface entity) on coarsening here proposed suppose a breakthrough for bottom-up (spontaneous) film nanostructuration techniques. Our study provides insights on relevant growth processes that can be used to design functional morphologies on demand with direct applicability in the industry. As an example, the resulting pyramidal single-crystalline grains from such a coarsening mechanism have been correlated with the enhanced UV lasing activity at room temperature of nanostructured ZnO.

5.1.1 Phenomenology of a growth ruled by Ostwald ripening

In the context of crystal growth, Ostwald ripening (OR)[21] is a well known mechanism of coarsening between surface grains, in which large grains (embedded on an ensemble of small-sized entities) grow drawing atoms from the environment (i.e. dilute space between entities with an equilibrium density of adatoms) or from smaller ones, the later shrinking (reducing their sizes) by atomic dissociation/desorption (§1.2.3) [121]. In brief, OR is mediated by mass transport phenomena. Such coarsening mechanism is an special case of the "abnormal" grain growth processes, in which a minor fraction of grains growth faster than the "normal" (small and average-sized) ones[22] [122-125].

The driving force for OR is the minimization of the total surface area of the grain ensemble, and thus the reduction of the excess of free energy (§1.1). OR can be explained by using the Gibbs-Thompson effect [124, 125]. The density of adatoms around an grain is heterogeneous with a gradient $\rho_1(x) \approx Ft(1-K_0(x/l_{liff})/K_0(\lambda/l_{liff}))$, where K_0 is a modified Bessel function of second rank, with boundary conditions: $\rho(x=\lambda)=0$ through the grain perimeter, and $\rho(x=l_{diff})=Ft$ the density that is standarized by surface diffusion. OR occurs only for separations between grains with separations $< l_{diff}$ inside depleted regions a second gradient dragging material from small grains to large ones (i.e., a biased mass transport) is established. A direct evidence of OR is the development of a bimodal grain size distribution as a result of the coarsening $\partial_t\lambda > 0$ (shrinking $\partial_t\lambda < 0$) of grains with larger (smaller) sizes than the average grain size $\overline{\lambda}$ in the l_{diff}-sized domain. The rate of grain growth (shrinking) and $\rho_1^e(\lambda)$ also depend on the atom density provided by the growth flux $\rho_1^e(F)$ [126]: for continuous growth fluxes ($F(t)=\tilde{F}=\int_{t=0}^{t=\tau}F(t')\partial t'$, with τ being the characteristic time of what?), the atom-dense background is continuously fed by F whose supersaturation $\psi_{\text{cont.}}=\ln(\tilde{F}/p(T))$ (with $p(T)$ the vapour pressure of the deposited material). This

[21] ***Used terminology*:** here "coarsening" denotes the process in which the in-plane size of the surface entities increases, without referring to the specific mechanisms (e.g., by grain growth, coalescence…) that give rise to such an increase.

[22] Ostwald ripening can be realized as a particular type of abnormal (or discontinuous) grain growth between exchanging "isolated" entities, which are in equilibrium with local adatom density of the surface, such that the coarsening (shrinkage) of the larger (smaller) entity does neither involve formation nor migration of grain boundaries. Thus, this mechanism prevails for systems with high surface-to-bulk ratios (e.g, nanostructured thin films) in which surface diffusion plays a key role on the atomic exchange. Note that in the fields of metallurgy, mineralogy and in reference to ceramics (i.e., bulky systems) the standard grain growth implies the movement of grain boundaries.

density $\rho_1^e(F)$, which is higher than $\rho_1^e(\lambda)$ can stabilize grains against dissociation [90, 125, 126], as compared in Figure 5.1(b).

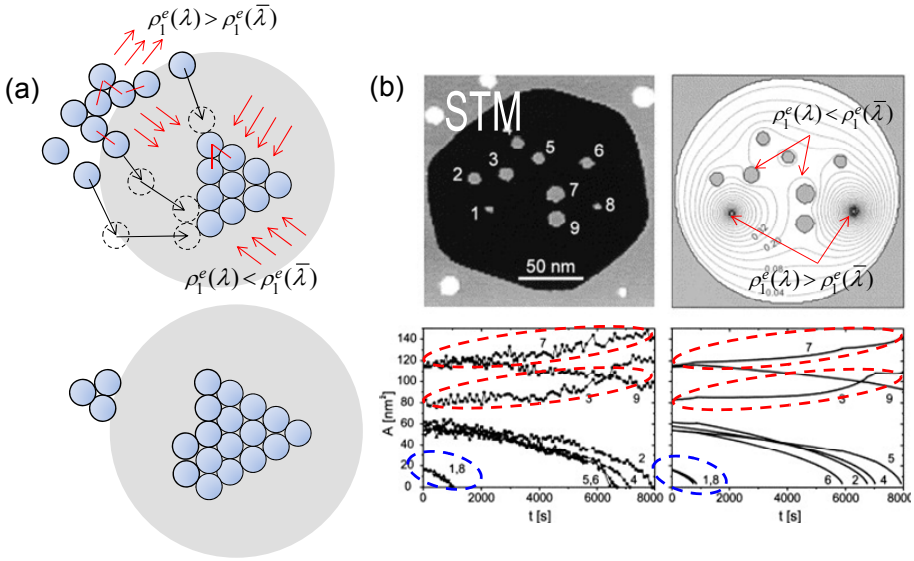

Figure 5.1 (a) Basics of Ostwald ripening. A large island growth at expense of smaller one, which shrinks until dissociation. (b) (Upper left) STM image of Ag adatom islands inside vacancy island on Ag(111) at 277 K. Upper right: calculated relative adatom density, $\varphi=(\rho-\rho_\infty)/\rho_\infty$, for a morphology modelling the experiment and assuming γ = 0.75 eV nm^{-1}. The contour lines correspond to constant values of φ, the difference between neighbouring lines is $\Delta\varphi$ = 0.06. Lower panels: experimental (left) and simulated (right) decay curves (γ = 0.75 eV nm^{-1}, $D\rho_\infty$ = 0.05 s^{-1}). Taken from G. Rosenfeld et al. *Surf. Sci.* **402-404**, 401 (1998).

Ostwald ripening requires: (*i*) that the entities exchanging adatoms are close together (with entity spacing << diffusion length) so as the capture rate of the larger entity influences on the rate of decay in size of the smaller one via local gradients of the adatom density [121-125]; (*ii*) moderate growth temperatures (typically $\geq 0.5T_{melting}$ for oxides and nitrides [124, 127]) and low adatom densities (i.e., high-mobility growth conditions) in order to promote the efficient breaking-up of the smaller entities, which takes place only for dissociation rates higher than the growth rates induced by the diffusive noise [126]; (*iii*) since OR is a relatively slow mechanism (that involves series of dissociations), it is effective just for small entities with sizes of a few tens of nanometers[23] [122, 125, 126]. On the contrary, the coarsening between larger entities

[23] Since the dissociation rate depends strongly on the local environment, series of partial dissociations are more probable than full dissociations, e.g., the full dissociation of a trimer into three monomers without involving the formation of an intermediate dimer is a rare event.

happens mainly through grain growth and/or peer-to-peer coalescence processes that involves phenomena of formation and migration grain boundary, massive rearrangement of atoms (e.g., during grain rotation) and generation of strains and inner defects with the consequent formation of non-compact entities (typically; these exhibit percolated morphologies) [28, 128]. Unlike the typical grain growth and coalescence, OR produces typically compact single-crystal entities with pseudo-equilibrium equiaxed shapes [90] since the border diffusion is faster than the dissociation, which it means that the captured adatoms can diffuse along the entity perimeter and to be attached to the nearest kinks before a new capture takes place.

5.2 Growth of polycyrtalline ZnO/InP(100) films

5.2.1 Experimental details concerning film growth and characterization

[0001]-textured ZnO films were pulsed laser deposited (PLD) on Fe-doped InP(100) substrates using a KrF excimer laser ($\lambda_{KrF} = 248$ nm, laser fluence = 4 J/cm^2 and pulse frequency = 10 Hz) focused on ZnO ceramic targets located at 6 cm from the substrate and rotated at 20 rpm. The deposit was carried out at a high vacuum chamber (with base pressure of $\approx 8\times10^{-7}$ mbar) in presence of a highly pure (99.999 %) molecular-oxygen flux (with dynamic pressure of 0.1 mbar) at a temperature of $T = 623$ K ($0.28\,T_{melting}$). The growth rate was $F = 0.08$ nm/s and deposition times ranged from $0 \le t \le 2\times10^4$ s (i.e., film thicknesses of $d = 50$-1600 nm). Afterwards, the film morphologies were investigated *ex-situ* by atomic force microscopy (AFM) [37] operating in contact mode using ultra-sharp silicon tips with nominal radius of 2 nm and aspect-ratios as high as 10 to achieve high-resolution images (§2.2). The tip miscut was estimated to be within the range of 55-60 degrees (that corresponds to a cut-off slope of $m_{tip} \ge 0.66$) on calibration samples. The tip effects on measurements by AFM on flatter morphological features are considered to be negligible, whereas the slopes detected beyond the cut-off value are ascribed to tip-induced artefacts (§2.2).

5.2.2 Surface morphology evolution during film growth

Figures 5.2(a) to 5.2(d) outline the morphology evolution of the ZnO films. We observe that for early stages of growth ($t < 2\times10^3$ s, Figure 5.2a) the morphology is dominated by a high density of small gaussian-like shaped grains that often impinge each other, termed "mounds" hereafter. For intermediate stages (2×10^3 s $< t < 1\times10^4$ s, Figs. 5.2b-c) two sets of grains are distinguishable by their shapes and sizes: large grains with partially faceted flanks (i.e., formed by vicinal surfaces with constant slopes) and a 6-fold in-plane symmetry (denominated pyramids hereafter) which are immersed within the background of mounds whose sizes decrease slightly. The density of mounds overcomes a fast decrease as the pyramids coarsen, which indicates that mounds are incorporated into the pyramid bulks. For late stages of growth (1×10^4 s $< t$, Figure 5.2d) the surface is free of mounds and it is fully covered by sub-micrometric pyramids with well-developed facets, which impinge each other forming a compact arrangement of grains. Figure 5.2(e) highlights the profiles taken over representative surface features for increasing t, showing how the grain faceting starts at the bottom regions and propagate uphill up to gives rise to a full transformation towards pyramidal structures for late stages. The 6-fold in-plane symmetry of pyramids results straightforwardly from the ZnO[0001]-texture of the films with the *c*-axis of the hcp cell along the out-of-the-film-plane direction [25, 129]. Similar morphologies to those presented here have been obtained in ZnO films grown by other vapor deposition techniques as thermal evaporation, sputtering and chemical etching [26, 130, 131].

Figure 5.3 depicts the time evolution of several statistical parameters representative of the thin film morphology, namely: (Figure 5.3a) mound and pyramid densities, ρ^m and ρ^p respectively, computed by direct counting using flooding procedures once classified the grains according their shapes; (Figure 5.3b) surface slope m of the grains (without discerning between grain types) estimated by means of a Lagrange polynomial-based image processing procedure described in sections §2.6.2 and §2.6.3 [54, 55]; (Figure 5.3c) in-plane grain-size λ estimated from the contour maps in the AFM images [54]; and (Figure 5.3d) fractal dimension ζ of the grain perimeter (see section §2.7).

Figure 5.3(a) reveals that the increase in ρ^p takes place simultaneously with the decrease in ρ^m, which points out to the transformation of mounds into pyramids at a ratio —estimated from the corresponding steady densities— of 10^2 mounds per each

formed pyramid. Figures 5.3(b) and 5.3(c) display the dynamics of faceting (the average slope increases up to reach a saturation value of $m_s = 0.41$) and coarsening ($\lambda \propto t^{1.0\pm0.1}$) of grains resulting from such a transformation. The selected slope $m_s = 0.41$, which corresponds to ZnO$\{10\bar{1}3\}$ facets, is lower than $m_s \approx 1.8$ (ascribed to ZnO$\{10\bar{1}\bar{1}\}$ facets) obtained under nearer-of-equilibrium conditions (i.e., at higher growth temperatures [131]).

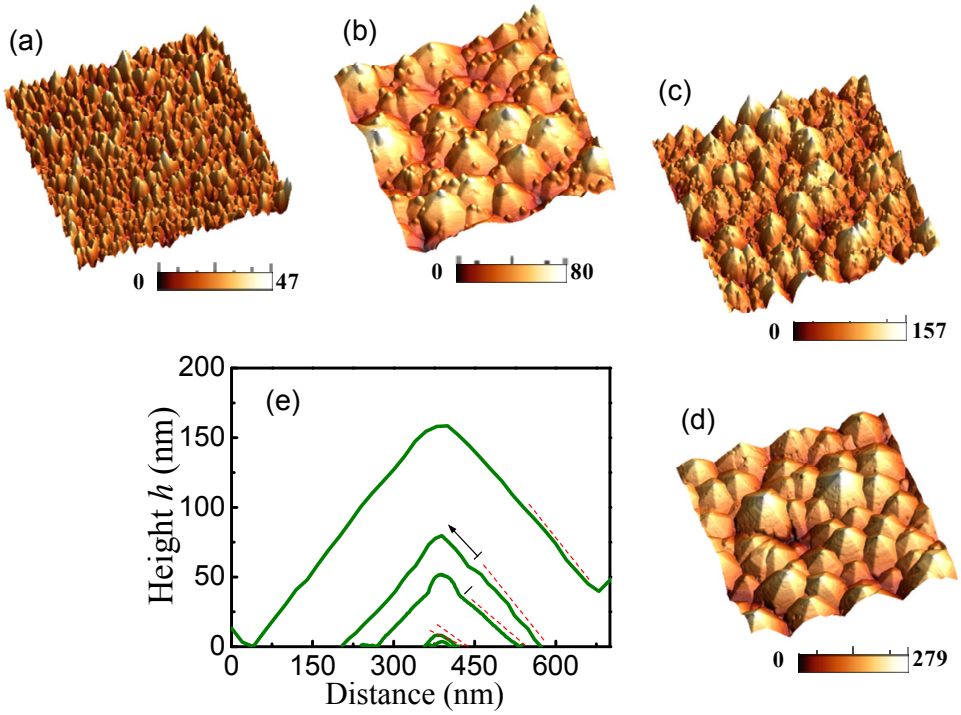

Figure 5.2 AFM images of ZnO thin films for different deposition times: (a) t =1.5×10^3 s, (b) 3×10^3 s, (c) 8×10^3 s and (d) 1.8×10^4 s. The corresponding height scales (in nm) are included as color bars. Scanned areas were: 1×1 μm^2 in (a, b) and 3×3 μm^2 in (c, d). (e) Cross-section profiles taken over representative grains for each growth regime. Arrow indicates the direction of faceting propagation, whereas dashed lines (parallel to the grain flanks) assist in realizing the slope evolution.

The obtained selected slope value m_s = 0.41 is lower than the slope threshold corresponding to the estimated tip miscut, $m_{tip} \geq 0.66$, reason why tip effects are considered to be negligible in the determination of the slopes for the surface entities analyzed here.

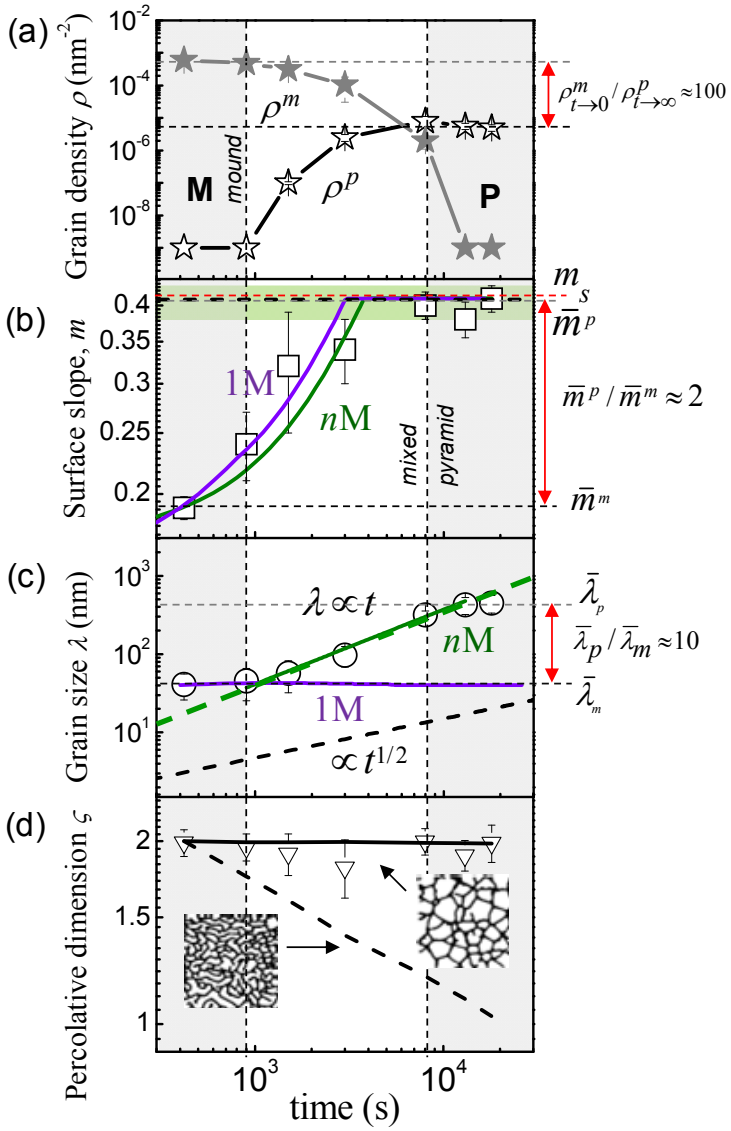

Figure 5.3 Evolution of statistical parameters representative of the film morphology, namely: (a) density of mounds ρ^m (Δ) and pyramids ρ^p (▲), (b) surface slopes m (□) with m_s denoting the selected one, (c) grain-size λ (○) and (d) fractal dimension ζ (▽). The curves correspond to: [solid ones] fitted and/or simulated results using single- (1M) or many-mound (nM) conditions; [dashed] expected and/or simulated behaviors for limit cases and/or saturation; and [dotted] lines connecting data points to guide to the eye. Insets in (d) show the percolated and compact-like morphologies (at left- and right-hand, respectively) that result from solid-on-solid simulations concerning grain growth and coalescence.

These arguments allow us to affirm that the faceting reported here corresponds to a kinetic process that results from the competition between surface currents rather a thermodynamic faceting toward facets with lower surface energies [65]. Figure 5.3(b) shows also the prediction (solid line) of the evolution of average slope values obtained from Equation 5.2 (as described below).

The fact that the compact grain shapes are preserved during the growth (note that $\zeta = 1.9 \pm 0.1$ remains constant in Figure 5.3d) for deposition temperatures as low as 0.28 $T_{melting}$ indicates that the transformation of mounds into pyramids takes place preferentially through atomic exchange by surface currents (i.e., it is an OR-type process) and thus phenomena of coalescence and/or grain boundary migration play a minor role in both the coarsening and faceting of the pyramid-shaped grains. This statement is based on the fact that the phenomena of coalescence and grain boundary migrations involve only the boundary sections between neighboring grains, such that by removing randomly these sections, percolated grains are obtained whose fractal dimensions decrease as the grains coarsen as plotted by the dashed curve in Figure 5.3(d).

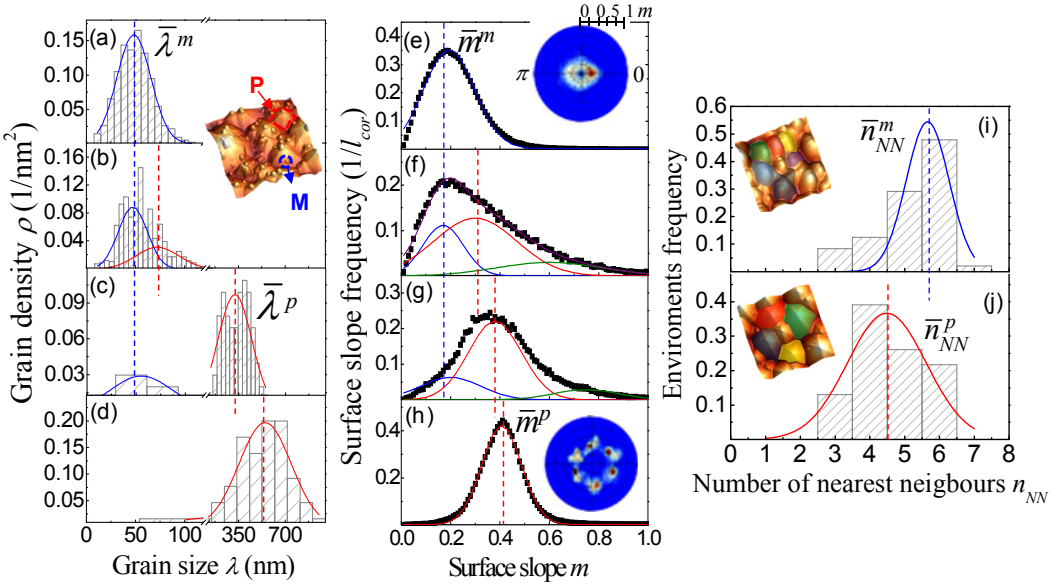

Figure 5.4 Evolution of the distribution functions $N(...)$ of morphological statistical parameters, namely: (a-d) grain-size distributions $N(\lambda)$, (e-h) surface slope distributions $N(m)$, and (i, j) environment distributions in terms of numbers of nearest neighbouring grains $N(n_{NN})$. The corresponding deposition times are: (a, e, i) t = 420 s, (b, f) 1.5×10^3 s, (c, g) 8×10^3 s and (d, h, j) 1.8×10^4 s. Insets provide complementary information: (a,b) classification by size of the grains, (e, h) surface-orientation maps $M(m,\phi)$ where ϕ denotes the azimuthal coordinate providing in-plane information, and (i, j) representative morphological environments of the population of mounds and pyramids. We believe that high-slope green-curve components in Figs. (f, g), whose means are higher than the AFM-tip cut-off ($m_{tip} \approx 0.66$-0.7), correspond to tip-induced artefacts related to the abrupt changes of the slope on the grain flanks with the uphill faceting. Note this component disappears in (h) once the faceting has propagated to the whole flanks.

In order to provide further information Figure 5.4 plots the time evolution of the normalized distribution functions $N(\ldots)$ of some statistical parameters:

(Figures 5.4a to 5.4d) the distribution of grain sizes normalized by the AFM-scanned area; (Figures 5.4e to 5.4h) the distribution of surface slopes normalized per the number

of uncorrelated areas in which can be subdivided the AFM image once interpolated[24]; and (Figures 5.4i to 5.4j) the distribution of morphological environments in terms of the number of nearest neighboring grains n_{NN}. The corresponding insets provides insight on: (Figures 5.4a to 5.4b) the classification by size of the grains giving rise to the multimodal λ-distribution; (Figures 5.4e to 5.4h) the evolution of the azimuthal ϕ-dependence of the distribution of surface slopes $M(m,\phi)$ (§2.6.4) obtained from small areas of the surface, with a maximum density of 6 grains [55]; and (Figures 5.4i to 5.4j) the representative morphological environments of the populations of mounds and pyramids in which the nearest neighbors of the central grains have been distinctively colored.

As a consequence of the transformation of the mounds into pyramids, a larger grain-size contribution (which is ascribed to the population of pyramid-shaped grains —red curve in Figure 5.4b) emerges from unimodal distribution displayed in Figure 5.4(a) (blue curve) that corresponds to the mound population. Further atomic exchange results in a shift of the λ-distribution of the pyramids toward larger sizes (i.e., the pyramids coarsen) from a decay in the mound population, which disappears for late stages (see trend in Figures 5.4a to 5.4d). Once the resulting pyramids become larger than 100 nm, both the faceting of their flanks toward ZnO $\{10\bar{1}3\}$ planes (realized as a shift of the m-distribution toward $m \to m_s \approx 0.41$) and the grain texturing (giving rise to 6-fold in-plane symmetry) take place as shown in the series of Figures 5.4(e) to 5.4(h). Besides, the data in Figures 5.4(i) to 5.4(j) indicate that the thus-formed pyramids are arrayed in less compact arrangements than the departing mounds since the average number of nearest neighboring grains decreases from $\overline{n}_{NN}^{m} = 5.8$ (mounds —Figure 5.4i) down to $\overline{n}_{NN}^{p} = 4.5$ (pyramids —Figure 5.4j). A fact to stress of these results is that the grain-size and morphological environment distributions of the pyramid population are broader than those of the mound population whereas the surface slope distribution of the pyramids is narrower than the corresponding one. This suggests that whereas the differences of grain-size and/or the morphological environments between mounds rule the inter-mound and mound-pyramid atomic exchanges (similar to the typical OR) by

[24] As discussed in §2.6.2, in order to compute the distribution of surface slopes and the feature contours, the 512 *x* 512-pixel AFM images were interpolated using or Legendre polynomials of order k=3 so as both first and second derivatives are defined everywhere. These interpolation polynomials correlated to each other 3^2 pixels of the raw images, $(512/k)^2$ being the number of areas that remain uncorrelated.

selecting which grain survives and which one perishes such that only small deviations of the grain-size and environment are possible, these differences do not appear to be important for the pyramid faceting. Instead, our results point out that the difference of the surface slopes between neighboring pyramids would play here a key role on the atomic exchange between pyramids. It is worth to mention that the surface orientation map $M(m,\phi)$ showed in the inset of Figure 5.4(h), which shows a well-shaped six-fold symmetry, was taken over and area of the surface including a small amount of grains (only one and its neighbors).

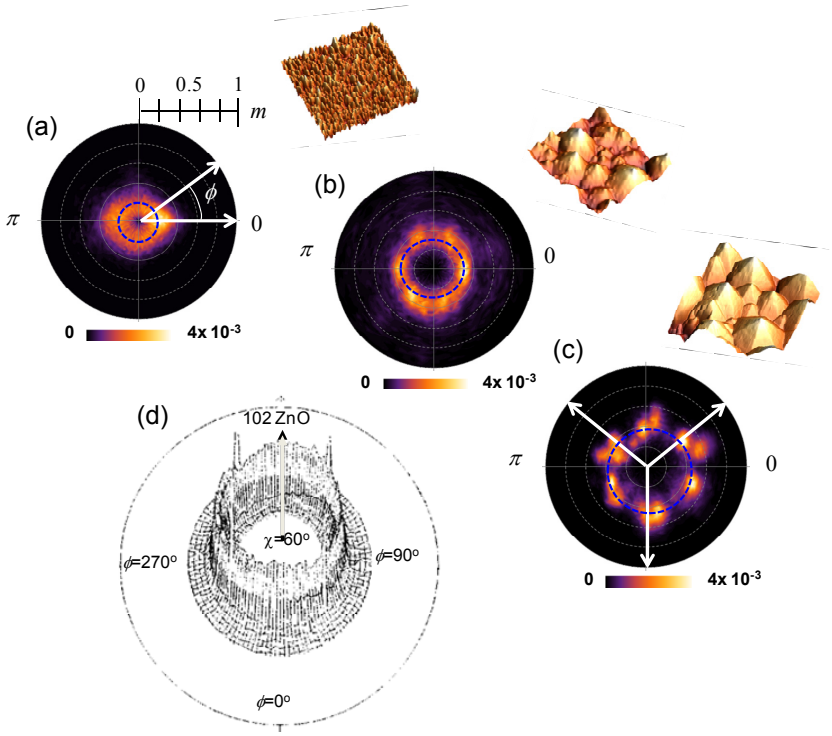

Figure 5.5 Surface orientation maps for film surfaces (showed as insets) containing several grain densities. From (a) to (c) the density of surface grains decreases. (d) XRD ϕ-scan showing the random in-plane orientation of a polycrystalline ZnO film with pyramid-like surface morphology. In XRD, the analysis is developed over mm^2 areas of the sample containing a large density of grains.

When $M(m,\phi)$ maps were taken on surface regions including a large density of surface grains, i.e., tens of grains and higher (inset of Figure 5.4e and Figure 5.5a), even for the film growth after $t = 1.8\times10^4$ s a random orientation rather than a well defined orientation is observed. This result was also reproduced from XRD ϕ-scan analyses previously developed on these solid films (Figure 5.5b). This fact suggests that grains are not oriented each other, being the correlation length for coarsening with reorientation in the order of the grain size $(500\ nm)^2 \sim 2.5\ \mu m^2$.

5.3 Model for coalescence by selected slope-driven Ostwald ripening

5.3.1 Details of the slope selection model

In the first part of the discussion, we are going to analyze the striking behavior of the slope saturation (faceting) during the formation of pyramid-shaped grains in terms of the interactions between the small grains with mound shapes. With this aim, we employ a continuum mesoscopic model of slope selection. In this model, the morphology transformation of mounds into pyramids is attributed to asymmetries in the intra- and inter-layer mass transports caused by the existence of step-edge barriers (Figure 5.6a) [4, 65]. Such an asymmetry is described in terms of the balance between the local currents, namely: uphill and downhill surface currents (denoted as J^{up} and J^{down}, respectively) to what the following mechanisms contribute: J^{up} leads the fraction of adatoms reflected by the step-edge barriers and those deposited preferentially on the upper terraces (by steering) into the ascending steps; whereas J^{down} is given by the fraction crossing the step-edge barriers (e.g., via atomic exchange) plus those deposited downwards by funnelling [4].

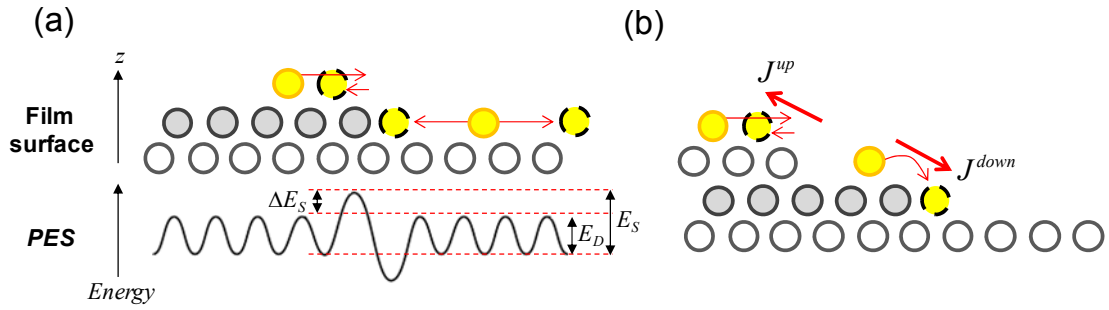

Figure 5.6 Basics of slope selection mechanism. (a) Sketch of step-edge barriers biasing surface diffusion. E_D is the activation energy for surface diffusion, E_S is the step edge Erhlich-Schwoebel barrier, and $\Delta E_S = E_D - E_S$ (b) Sketch showing processes of downhill and uphill mass transport.

In this context, the selected slope m_s corresponds to a metastable state in which the grain shapes (in particular their aspect ratios) are preserved, which means that $\partial_t m|_{m_s} \propto J^{up}(m_s) - J^{down}(m_s) \approx 0$. For small perturbations in m_s, the balance $J^{up}(m_s) = J^{down}(m_s)$ shifts to $J^{up} < J^{down}$ for $m_s + |\delta m_s|$ and $J^{up} > J^{down}$ otherwise in order to stabilize the morphological slope toward its selected value m_s (Figure 5.6b) [4, 65, 132-134].

Another approach to the same problem is to deal with the terrace growth rate. Small lower terraces with widths (1/slopes) near the selected value grow slowly (or do not), whereas upper terraces, which have larger widths, advance fast until reaching the selected terrace width, as depicted in Figure 5.7. A generalized equation at mesoscopic scale (where a continuum approach to the film surface $h(\vec{r},t)$ is pertinent, with $\vec{r}$ being a position vector within the film plane) that describes the kinetics of the phenomenon of slope selection was proposed by Johnson *et. al.* [132]:

$$\frac{\partial h(\vec{r},t)}{\partial t} = -\alpha\nabla\left(\frac{\nabla h(\vec{r},t)}{m_s^2+\left[\nabla h(\vec{r},t)\right]^2}\right)+\Phi(\vec{r},t)+\eta(\vec{r},t) \qquad (5.2),$$

In Equation 5.2, $\alpha = aFl_d^2(1+e^{-E_a/k_BT})$ is a kinetic constant that takes into account for the contribution of the atoms landing within a strip l_d of the surface around the steps to the surface currents via diffusion (whose activation energy E_a depends on the local environment). a is lattice parameter. $\Phi(\vec{r},t)$ comprises the surface relaxation mechanisms that correspond to the surface curvature-driven Mullins/Herring diffusion $\Phi(\vec{r},t) = -\kappa\nabla^4 h$ with $\kappa = D_s\rho_e^1(\overline{\lambda})\varepsilon_s\Omega/k_BT$ (where $D_s \propto e^{-E_a/k_BT}$, $\rho_e^1(\overline{\lambda})$, and ε_s corresponds to the surface diffusion coefficient, the equilibrium adatom density in a surface with an average grain size of $\overline{\lambda}$ and the surface energy, respectively). $\eta(\vec{r},t)$ encloses the uncorrelated Gaussian noise generated by stochastic perturbations of both the growth rate F and temperature T [4, 132, 135]. k_BT/Ω denotes the thermal energy per atomic volume Ω of the system during the process.

The first term in Equation 5.2, which can be rewritten as $\alpha\left[-f_1(\nabla h)+f_2(\nabla h)\right]\nabla^2 h$ with $f_1(\nabla h) = \left[m_s^2+(\nabla h)^2\right]^{-1}$ and $f_2(\nabla h) = \nabla h\cdot\partial_{\nabla h}f_1(\nabla h)$, defines the morphology evolution towards grain shapes with constant slopes (conical or pyramidal depending on the system in-plane symmetry) through the competition between two complementary mechanisms: (*i*) a *Kuramoto-Sivashinsky*-type destabilization of the surface $-\alpha\cdot f_1(\nabla h)\cdot\nabla^2 h$ [136] and (*ii*) a *Edwards-Wilkison*-type surface relaxation $\alpha\cdot f_2(\nabla h)\cdot\nabla^2 h$ [137].

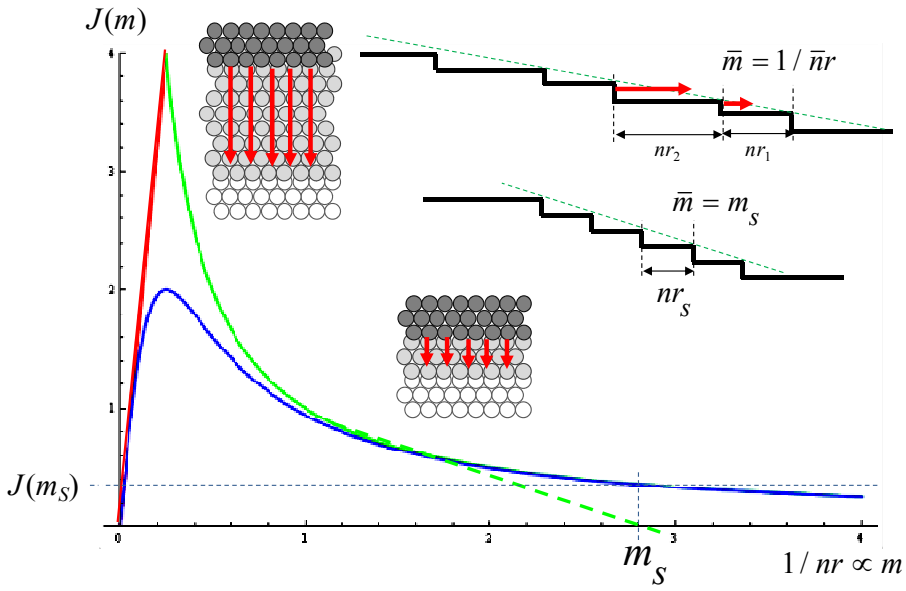

Figure 5.7 Slope dependence of the terrace growth rate. *j*(*m*) corresponds to the uphill surface current, and *m* to the local slope values at grain flanks. (*Insets*) Ball models sketching the atomistic scenario for the growth of a terrace of a fcc(111) surface. As in the cross-section profiles, it can be observed that upper terraces with large widths (low slopes) advance faster than lower steps, which have width values near the selected one.

The functions $f_1(\nabla h)$ and $f_2(\nabla h)$ describe the slope modulation of the faceting kinetics as follows: For very small slopes (with $\nabla h \to 0$), the destabilization mechanism prevails $\left[-f_1(\nabla h)+f_2(\nabla h)\right]\approx -(\nabla h)^2$ generating intense uphill currents that produce an increase in the slope at a decreasing rate $\propto \alpha/(\nabla h)^2$. The intensity of the uphill current decreases down to vanish for a facet with the selected slope $|\nabla h| = m_s$ in which the equilibrium condition between both mechanisms $\left[-f_1(\nabla h)+f_2(\nabla h)\right]=0$ is reached giving rise to a steady grain shape $h'(\vec{r})$ with $\partial_t\left[h \to h'\right]\to 0$. Conversely, for slopes $|\nabla h| >> m_s$, the capacity of relaxation of the surface prevails $\left[-f_1(\nabla h)+f_2(\nabla h)\right]\approx (\nabla h)^{-2}$ generating a weak downhill current that leads to a slow recovery of the facet with selected slope.

5.3.2 Interpretation of the results in the light of the model

Figure 5.8 displays the morphology evolution of a single mound controlled by the slope-selection mechanism as described in Equation 5.2. The initial mound shape was

taken from the experimental results and fitted to a Gaussian 3D function $h(r,0) = h_0^m e^{-(r/2\lambda_0^m)^2}$ (picture in Figure 5.8a whose profile is plotted in Figure 5.8d, blue curve) with λ_0^m = 40 nm (mound size as shown in Figure 5.3c) and h_0^m = 5 nm (mound height, from combining Figures 5.3b and 5.3c). The 2D+1 simulation shown in Figures 5.8(a) to 5.8(c) is performed for a coefficient-ratio α/κ = 0.07, which is estimated by fitting the simulated faceting kinetics to the average slope evolution plotted in Figure 5.3(b), and a selected slope of m_s = 0.41 (the experimental saturation slope).

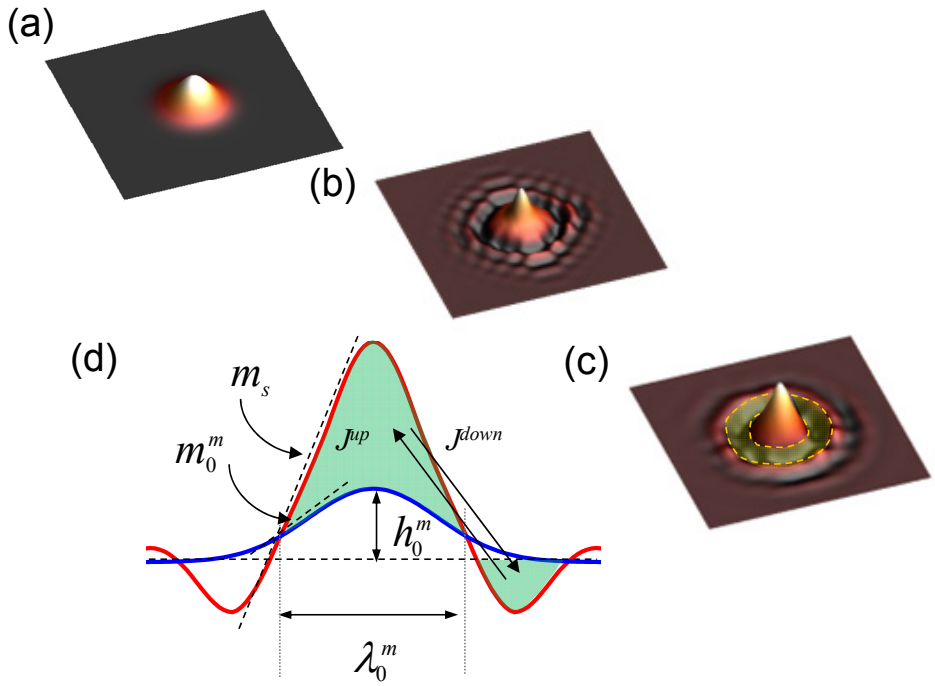

Figure 5.8 (a-c) Simulated morphology evolution of a single mound-shaped structure ruled by the slope-selection mechanism described in Equation 1. As the growth proceeds, a surrounding depletion zone is observed, as outlined in (c). (d) Cross-section profiles at different growth stages: (blue curve) initial stage in which the morphological features of the mound-shaped structure —namely: size λ_0^m, height h_0^m and the highest slope m_0^m— are depicted; and (red curve) final stage which corresponds to the profile of a conical/pyramidal-shaped structure with constant slope m_s along the flanks. Shaded regions sketch the conservative mass transport through the balance between J^{up} and J^{down} currents.

Both thus-obtained α/κ and m_s describe well the faceting kinetics in vicinal surfaces with moderate step-edge barriers as revealed from the good agreement of them with the corresponding parameters computed by kinetic Monte-Carlo simulations[25] [132]. The

[25] This κ/α ratio is in concordance with the so obtained by extrapolation of the non-linear term coefficients in the mesoscopic simulations by M. D. Jhonson *et al.*, *Phys. Rev. Lett.* **72**, 116 (1994) for the case of m_s=0.41.

final mound profile is included in Figure 5.8(d) as a red curve for comparison purposes. As the growth happens two key features of the morphology evolution are identified: *(i)* the formation of a trench-like depletion zone around the mound perimeter; and (*ii*) the development of sharp apexes at intermediate times. This latter feature arises as a consequence of that the Gaussian 3D function chosen for modeling the mound shapes has a maximum value of curvature $\propto -\nabla^2 h(\vec{r},t)$ on mound top, such as the strength of the *Kuramoto-Sivashinsky-type* mechanism is enhanced within these regions speeding up the faceting. Once the slopes within the apex regions reach the selected slope, the apex shapes remain constant. Note that these sharp apexes should not be related with those rounded ones on the pyramidal trunks in Figure 5.2(b), whose origin is the uphill propagation of the faceting.

An inspection of the series of simulated images (Figures 5.8a to 5.8c and no-shown intermediate images) confirms the fact pointed out in Figure 5.2(e) that the faceting kinetics starts at the grain bottom and propagate up via uphill currents that drain material from the depletion zone. For longer growth times (Figure 5.8c), the selected slope has propagated to the whole flank giving rise to the full transformation of mounds into conical structures as revealed by red profile in Figure 5.8(d).

The time-dependences of both the slope averaged on the grain flank and the grain size computed from the simulation for a single mound are included in Figure 5.3(b) and 5.3(c) (solid curves labeled "1M") to be compared with the experimental data. From these comparisons, we can conclude that the single-mound slope-selection model reproduces well the experimental morphology evolution of the grains (good agreement in Figure 5.3b) with regard to the faceting kinetics giving rise to the shape transformations of isolated mounds into conical/pyramidal grains; however this is unable to explain the grain coarsening behavior observed experimentally (Figure 5.3c).

Figure 5.9(a) discloses some relevant aspects of the simulated morphology evolution for a single mound that play a key role when several grains are considered. In particular, Figure 5.9(a) provides details of the profiles of the depleted zones generated around grains with different sizes λ (compare curves A and B), different selected slopes m_s (curves A and C) and kinetic coefficient-ratios κ/α differing in several orders of magnitude (curves A and D). From the profiles, two characteristic parameters (which are linked closely to the depletion kinetics) can be defined: the capture length ξ that corresponds to the distance beyond the grain perimeter where the depletion is highest

(i.e., where the profile has a minimum), and the capture rate $1/\tau$ (with τ being the characteristic draining time of the depletion phenomenon) such that the depth of the profile minimum (at ξ) for a given runtime t is $\propto t/\tau$. The dependences of these parameters on λ, m_s and κ/α are log-log plotted in Figures 5.9(b) to 5.9(c). Whereas ξ depends only on λ through the power-law dependence $\xi \propto \lambda^{\beta}$ with $\beta = 1.0 \pm 0.2$ for wide ranges of $0.1 \le m_s \le 1.0$ and $0.01 \le \alpha/\kappa \le 1000$ (see the dataset collapse in Figure 5.9b); τ is roughly independent on both λ and α/κ exhibiting a power-law dependence only on m_s (Figure 5.9(c)): $\tau \propto (m_s - m)^{\varphi}$ with $\varphi = 1/3 \pm 0.01$. In brief, larger (steeper) pyramidal-shaped grains give rise to wider (deeper) depletion zones. From these dependencies, we can throw light on the nature of the depletion phenomenon as well as on the physical meanings of both ξ and τ. The fact that τ does not depend on ξ (note that both depend on independent variables) points out to a depletion phenomenon driven by drift, i.e., by biased mass transport rather than by diffusion-limited aggregation for which $\tau \propto \xi^2$ as predicted. Thus, the drain of the captured atoms would take place through biased "random" paths that become more ballistic and less random-walk as the capturing grain is larger. It would addresses the capability of the larger grains to capture far atoms (at $\xi \propto \lambda$) at the same rate (as $\partial_{\lambda}\tau \approx 0$) than the smaller grains capture near atoms. This conclusion explains also the independence of both ξ and τ on κ/α as a consequence of the grain sizes are larger than the space-scale ($\approx \sqrt{\kappa/\alpha}$) in which the surface diffusion plays a preponderant role, which means that the diffusion becomes negligible at inter-grain scale. The value range of κ/α used for the simulations in Figure 5.9 was thus-chosen on the basis of previous reports [138-141] from which a diffusion length of ≈100 nm could be estimated for ZnO films at 623K and it is in the same order of magnitude of that employed in growth simulations of metal surfaces. Note that such a diffusion length is several times shorter than the sizes of the pyramidal-shaped grains. Once the main characteristics of the slope-selection model computed for single mounds have been discussed, a simulation considering many mounds (which compete to each other at ξ length-scale) has to be performed in order to address the grain coarsening behavior as shown in Figure 5.3(c). Figure 5.10 displays the simulations for three kinds of grain competitions:

(*i*) Figure 5.10(a): Competition in terms of the morphological environment between grains with similar sizes and surface slopes $m << m_s$ so as the grains with a number of nearest neighboring grains n_{NN} higher than the average number $\overline{n}_{NN}$ decays (shrinkage of the central mound with six neighbors —green curve in Figure 5.10d) whereas those within rarefied environment coarsen (grow of a not showed mound with four neighbors —red curve in Figure 5.10d) [125]. The results in Figures 5.4(a) and 5.4(j) showing the narrow grain-size distribution and the different morphological environments of the mound population, respectively, suggest that this type of competition acts as selection mechanism of a few mounds (those that coarsen) to become pyramidal/conical grains. This suggestion is: (a) inspired on the decrease in the average number of neighbors per resulting pyramid, which cannot be explained through a model of isotropic/compact depletion; and (b) supported by the results in Figures 5.4(a) to 5.4 (d) that reveal the break-up of the unimodal grain-size distribution into two populations (blue and red curves) whose average sizes exhibit dissimilar behaviors (remain slightly constant and increase, respectively) with the deposition time.

(*ii*) Figure 5.10(b): Competition between two grains with different sizes and similar surface slopes $m << m_s$. Once the average sizes of the two grain populations differ significantly, the competition becomes ruled by the grain sizes λ through the capture length ξ. As a consequence of the λ-dependence of ξ (Figure 5.9b), a lot of mounds are within the depletion zones of the pyramidal/conical grains while only a few of these latter are affected partially by the capture of so close mounds. Thus, the grain-size-based competition would be the responsible for the decay in the density of mounds (as shown in Figure 5.3a) and the coarsening of the pyramidal/conical grains (Figure 5.3c).

On the basis of our results in Figure 5.3(a) and 5.4(a-d), we can assume that many small mounds dissociate slowly (which implies $\partial_t \rho^m >> \partial_t \lambda^m$, i.e., the mound density drops faster than the mound shrinkage) proving the adatom flux for the quick growth of a few conical/pyramidal grains ($\partial_t \rho^p << \partial_t \lambda^p$). This assumption is supported on the fact that the ratio between the corresponding steady densities is $\rho^m_{t\to 0} / \rho^p_{t\to\infty} \sim 10^2$ (Figure 5.3a), which means that a single pyramidal grain results from the dissociation of 10^2 mounds in average. For conservative systems (like that analyzed here where the re-evaporation of the adatoms generated from the mound dissociation is neglected), the mass-conservation condition $\partial_t \chi^p = -\partial_t \chi^m$ is satisfied in terms of the densities of

adatoms $\chi^m = \frac{\pi}{4\Omega} h^m \left(\lambda^m\right)^2 \rho^m$ and $\chi^p = \frac{\sqrt{3}}{16\Omega} m_0^p \left(\lambda^p\right)^3 \rho^p$ that compose the mounds and the pyramidal grains, respectively.

By rewriting the mass-conservation condition from the assumption described above, we get an expression to calculate the coarsening rate of the pyramidal grains:

$$\frac{\partial}{\partial t}\lambda^p \approx -\frac{4\pi}{3\sqrt{3}} \frac{h^m}{m_s \rho^p_{t\to\infty}} \left(\frac{\lambda^m}{\lambda^p}\right)^2 \frac{\partial}{\partial t}\rho^m \qquad (5.3).$$

At this point, $\partial_t \rho^m$ is estimated from the scaling dependences in Figure 5.9 that indicate that the mound population is depleted beyond the pyramidal-grain perimeter $\propto \lambda^p$ by a capture length $\xi \sim \left(\lambda^p\right)^\beta$ at a rate of $1/\tau \sim (m_s - m)^{-\varphi}$ such that $\partial_t \rho^m \propto \rho^p_{t\to\infty} \rho^m_{t\to 0} \lambda^p \xi / \tau \sim \left(\lambda^p\right)^{1+\beta}$.

Now, using the kinetic relations showed until now we will obtain a power-law for coarsening. As stated in Equation 5.3, $\partial_t \lambda^p = A\left(\lambda^p\right)^{-2} \partial_t \rho^m$, and using the relation $\partial_t \rho^m = B\left(\lambda^p\right)^{1+\beta}$, we have that $\partial_t \lambda^p = C(\lambda^p)^{\beta-1}$ where C=A·B is a constant including geometrical constraints. Solving this partial differential equation, we have the scaling law $t^{1/(2-\beta)} = \sqrt[2-\beta]{\frac{C}{(2-\beta)}} \lambda^p$. Because $\rho^p_{t\to\infty} = \frac{16\Omega}{\sqrt{3} m_s \left(\lambda^p\right)^3} \chi^p$ and $\rho^m_{t\to 0} = \frac{4\Omega}{\pi h^m \left(\lambda^m\right)^2} \chi^m$, the constant C can be rewritten as $C = \rho^m_{t\to 0} / 16\Omega\sqrt{\kappa / 27\alpha}$. Therefore,

$$\lambda^p \cong \Theta \cdot t^{1/(2-\beta)} \qquad (5.4),$$

With $\Theta = \sqrt[2-\beta]{\rho^m_{t\to 0} / 16\Omega(2-\beta)\sqrt{\kappa / 27\alpha}}$.

By substituting β=1.0±0.2 in Equation 5.4, we get $\lambda^p \sim t^{1.0\pm0.2}$, which is in good agreement with the experimental coarsening rate found in Figure 5.3(c) that shows the pyramids growing as $\lambda^p \sim t^{1.0\pm0.1}$. Note this agreement proves the fact that the capture and drain within the depletion zones take place through biased mass transport as discussed above to address the independence on ξ of τ. Otherwise, by assuming a hypothetical scaling dependence $\tau \propto (\xi)^\psi \sim \left(\lambda^p\right)^{\psi\beta}$ (where ψ=2 for the case of random-

walk diffusion), $\partial_t \rho^m \sim \left(\lambda^p\right)^{1+\beta(1-\psi)}$ and so $\lambda^p \sim t^{1/[2-\beta(1-\psi)]}$ that would be in accordance with the experimental results only for $\psi \approx 0.0 \pm 0.2$.

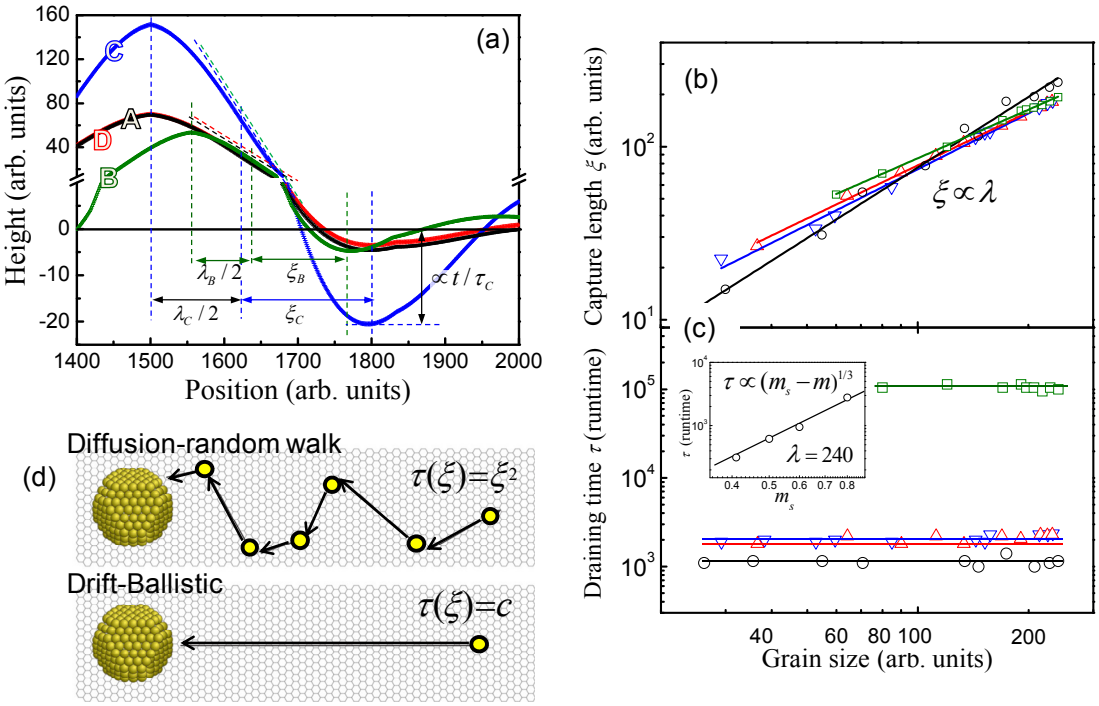

Figure 5.9 (a) Cross-section profiles of simulated mound-shaped structures after growing by a slope-selection mechanism. Curve labels and sub-indexes indicate the sets of used parameters for simulations: A→{κ/α = 0.01, m_s= 0.41, λ= 400}, B→{κ/α = 0.01, m_s= 0.41, λ= 300}, C→{κ/α = 0.01, m_s= 1.0, λ= 400} and D→{κ/α = 1000, m_s= 0.41, λ= 400}. Note that a break in the height axes has been inserted to assist in realizing the magnitudes: λ —structure size estimated from the full-width-at-half-maximum of the mound profiles, ξ —capture length defined as the distance beyond λ/2 where the profile has a minimum, and τ— draining time such as the profile depth at the minimum position becomes $\propto 1/\tau$ (i.e., t/τ for a given runtime t). λ–dependences of ξ and τ are log-log plotted in (b) and (c), respectively. In both cases, the used symbols define the sets of parameters for simulations: (○)→{κ/α = 1.0, m_s= 0.3}, (□)→{κ/α = 1.0, m_s= 1.0}, (Δ)→{κ/α = 1000.0, m_s= 0.41} and (∇)→{κ/α = 0.01, m_s= 0.41}. Solid lines in (b) and (c) represent the best fit of the simulated data to scaling dependences based on power-law functions. The inset in (c) shows the m_s-dependence of τ for the larger structures. (*d*) Sketch of random walk (*Up*) and ballistic (*Down*) –types of mass transport.

(*iii*) Figure 5.10(c): Competition between faceted grains with surface slopes close to m_s. Under these conditions, the small currents between neighboring grains are insufficient to alter both the grain density and/or the morphological environments, especially when the grains are large enough. This competition that operates between the pyramidal-shaped grains would stabilize the surface slopes toward their saturation value that corresponds with the selected slope (in agreement with Figure 5.3b) and would preserve by mass-conservation the average size of the pyramid population (Figure 5.3c). Once

the local grain slopes are stabilized, the surface of regular pyramidal structures becomes steady.

Figure 5.11(a-c) displays the morphology evolution of a many-mound surface controlled by the slope-selection mechanism described in Equation 5.1.

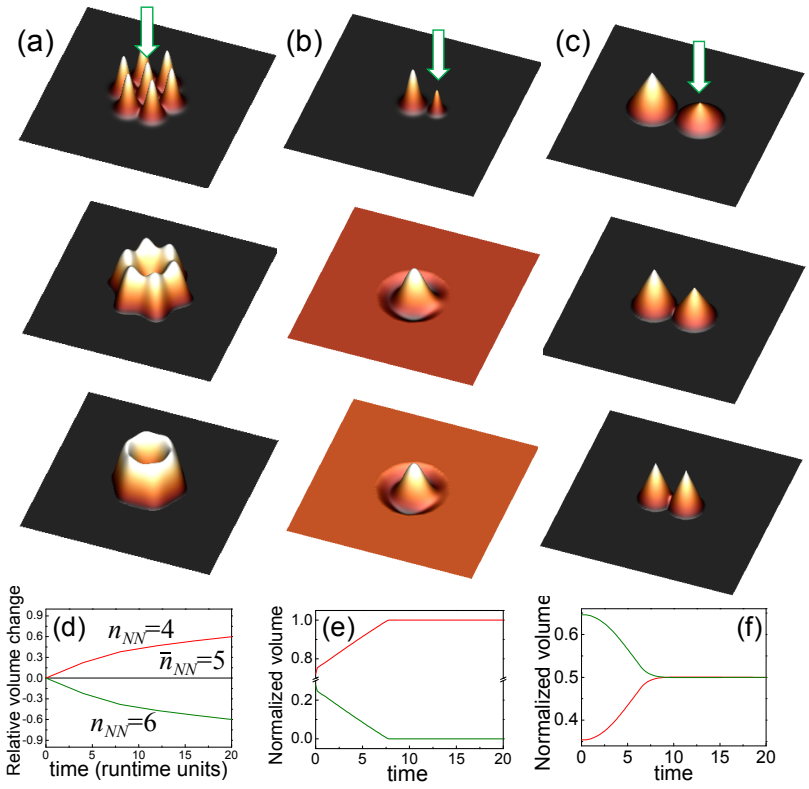

Figure 5.10 Simulated grain coarsening by competitive growth based on: (a) *Different morphological environments* (same-sized grains with $m << m_s$ and $n_{NN} = 6$ for the central grain), (b) *Grain-size differences* (dissimilar-sized grains with $m << m_s$) and (c) *Surface-slope differences* (same grain size with m's $\approx m_s$ and $\leq m_s$ for the left- and right-hand grains, respectively). The arrows point out to the involved grains with the highest relative volume-variations. Graphs in (d-f) show the time- dependence of the grain coarsening (expressed here in terms of volume changes) for the different kinds of competitive growths. Plot in (d) depicts the relative grain-volume variations (i.e., with respect to the initial grain volume) for grains that decays/grows within dense/rarefied environments with n_{NN}=6/ n_{NN}=4 assuming $\bar{n}_{NN} \approx 5$ from Fig. 3j; whereas those in (e and f) exhibit the variations normalized with regard to the considered total volumes $\sum_{\text{grain population}}$.

The initial morphology is formed initially by an array of uniform-sized mounds, in which the different morphological environments are considered by locating the mounds at random positions. Periodic boundary conditions are assumed in order to avoid finite-size artefacts. The series shown in Figures 5.11(a) to 5.11(c) corresponds to successive growth stages generated by competitive growth illustrated in Figure 5.10. The thus-

simulated surfaces are directly compared with local environments observed in the corresponding AFM-imaged morphologies, as depicted in Figures 5.11(d) to 5.11(f) and the corresponding insets[26]. The qualitative agreement between the simulated morphologies and AFM-imaged ones is apparent and so it supports the soundness of our model.

The slope-selection mechanism reported here is classified as an OR-type process on account of the following fingerprints: The grain coarsening results from the atomic exchange via surface currents between isolates entities giving rise to compact grains with pseudo-equilibrium shapes; whereas (as predicted by the SZM model [92]) potential phenomena of bulk recrystallization involving grain-boundary migration are suppressed at the used deposition temperatures ($0.28T_{melting}$).Nevertheless this classification, the slope-selection mechanism corresponds to an atypical OR regarding both the driving force for the atomic exchange between the involved entities, and the scenario in which this mechanism remains alive (it continues being operative between moderately large grains with λ = 20-500 nm at deposition temperatures as low as 0.28 $T_{melting}$). Unlike the typical OR where the exchange is driven by grain-size and/or environment difference, the exchange for the slope-selection mechanism is ruled by the kinetic stabilization of certain crystalline facets on the grain faces (i.e, by kinetic faceting).

This difference in the driving forces (in which underlies in the atypical nature of the operation conditions) has the following implications: (a) A grain with surface slopes lower than the selected slope cannot reach an equilibrium state with the surrounding flat surface independently of the adatom density on it because rather than an equilibrium adatom density (like in the typical OR), in this case there is an equilibrium grain-shape for which the downhill current becomes high enough to compensate the surface adatom depletion produced by the uphill current. (b) In the absence of surrounding flat surface for compact arrangement of grains, the exchange is driven by the slope differences between neighbouring grains. (c) In the case of that the slopes of the neighbouring grains are far below the selected one, the exchange driven by slope-difference can be interpreted straightforwardly in terms of exchange driven by grain-size and/or environment difference from the grain-size dependence of the depletion range.

[26] A feasible comparison of the simulations with the experiments is able just for small AFM-imaged regions, in which the random contribution (third term in Equation 5.1 —that is hard to reproduce by simulation given its nature) to the surface statistics is negligible.

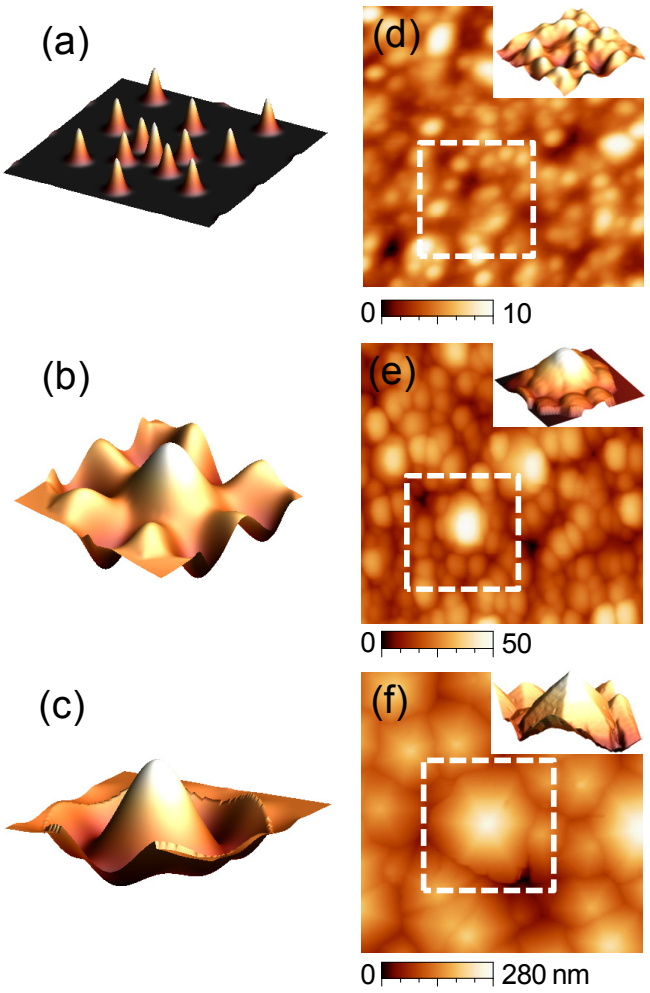

Figure 5.11 (a-c) Simulated morphology evolution of a many-mound surface ruled by the slope-selection mechanism as described in Eq. 1 to be compared with the top-view AFM-images displayed in (d-e). The direct comparison takes place with the outlined local environments, whose cross-section views are included in the corresponding Insets. Scanned areas of images [insets] were 500×500 nm^2 and 2×2 μm^2 [200×200 nm^2 and 1×1 μm^2] in (d, e) and (f); respectively. Height scales are in nm. Note that the 6-fold in-plane symmetry of the resulting pyramids are a consequence of the ZnO[0001]-texture of the films, which is irrelevant for our study that deals with the inter-grain competitive growth rather than intra-grain recrystallization.

It means that for early growth stages, the coarsening behavior produced by the slope-selection mechanism is similar to that generated by a typical OR. On the basis of these arguments, we refer to the slope-selection mechanism as a *late slope-selection driven Ostwald ripening*. Although they have been investigated in an independent manner so far, the results presented here allow us to conclude that both the Ostwald ripening and slope-selection mechanisms belong to the same universal class of processes. At this point, it deserves to be mentioned that this mechanism is responsible for the nanostructuring of the film into arrangements of pyramidal/conical single-crystalline grains, which has been correlated recently to the enhanced lasing activity of

nanostructured ZnO [142, 143]. The pyramidal/conical single-crystalline grains would play a double role in this effect: they act like gain medium (since the large binding energy, ≈60 meV, of ZnO exciton) and as well as resonant Fabry-Perot cavity (since the shapes and grain coupling [143]) to produce excitonic UV laser emission at room temperature.

5.4 Conclusions of the Chapter

In this chapter, we report experimental findings concerning the hierarchical grain coarsening on the surface of PLD-grown ZnO[0001] films and interpret them through a comprehensive mesoscopic model of slope selection. From the evolution of the shapes of the grains studied by AFM, we observe that the surface morphology transforms from small and round grains into large sized sixfold pyramids, with the development of a well defined bimodal grain size distribution. In addition, the slopes at the flanks of the grains increase until reaching a selected (preferred) one, which remains constant during the rest of the growth, while the morphological environment decreases as growth proceeds. In order to address for the experimental observations, we employ a mesoscopic (continuous) approach for selected slope model. The selected slope model states that the balance between surface currents upward and downward step edges in the flanks of the surface entities is the responsible for the selected slope formation.

From simulations considering the selected slope mechanism, we obtain that grains can growth by drawing material from smaller ones through a depleted zone if they are close enough to that the depleted zone overlap the grain structure, which explains whose density decreases as observed from experiments. Besides the process of mass transport from bottom to tops of the grain structures, together with plausible steering and geometrical shadowing effects, enable grains to develop selected slope flanks, i.e., with well defined facets. Due to the asymmetry in the growth process due to slope selection, grains with slope values near the selected one growth preferably and at expenses to the other (smaller ones). Therefore, a *late slope-selection-driven Ostwald ripening* mechanism operating under atypical conditions is identified and their main characteristics, addressed. In dependence of the morphological environment of grains, these mechanisms permit the self-organization of surface structures in thin film surfaces.

SUMMARY AND GENERAL CONCLUSIONS

Along this work I have been investigated relevant mechanisms controlling the surface morphology evolution of polycrystalline thin films during processes of film preparation. For the case of thin film systems, the elucidation of the mechanisms controlling the surface morphology evolution is one of the first steps considered for surface nanostructuration and engineering processes following bottom-up strategies (i.e., those which seek to arrange smaller components into more complex assemblies), which have a high technological impact because permit the quasi-spontaneous modification of the film morphology in a way that alter interesting functional properties of the films prepared as convenient.

Thin films were prepared by using physical vapor deposition methods, among them Thermal Evaporation, Pulsed Laser Deposition and thermal annealing. The surface morphology of the thus prepared films was characterized at dissimilar length scales by using scanning probe microscopies (i.e., atomic force microscopy and scanning tunneling microscopy, *mesoscale*), and scanning electron microscopies (*microscale*). By using own image processing procedures and statistical analyses, I extract valuable information regarding the shape transformations supported by the films during preparation, including as example the evolution of in-plane and out-of-plane grain sizes, roughness, slope values, and local in-plane orientations. By other hand, I used X-ray diffraction in order to analyze the crystalline structure of thin films.

In order to address for the experimental evidences, i.e., the evolution of both the surface morphology of thin films (as observed by microscopies), the scaling of the shape parameters, and changes in the crystalline structure, I proposed novel models of grain growth at the coarse-grained (mesoscale) level. Such models were based on dynamic scaling simulations using Langevin-type approaches (to describe surface diffusion), partial differential equation systems (to describe diffusion along defects), and finite element methods (to describe elastic phenomena). From such experimental evidences and models, I can extract the following general conclusions:

- The surface morphology of polycrystalline thin films support drastic transformations during film preparation processes under far-from-equilibrium

conditions, here considered growth/annealing temperatures as low as 0.2-0.3 $T_{melting}$ and growth rates of 1 nm/s.

- Surface morphology transformations occur by coarsening mechanisms, including peer-to-peer coalescence and hierarchical (abnormal) grain growth, which are driven by both energy minimization processes and kinetic restrictions.

Concerning peer-to-peer coalescence, we can conclude that:

- Peer-to-peer coalescence between single-crystal grains into large-sized multigrain structures occurs by local interactions between grains involving progressively mechanisms of relaxation by surface currents and accommodation by strain generation of the growth stress generated in both the normal (valley filling and grain zipping) and azimuthal (grain rotation and torsion) directions. As the surface grains become larger, the ratio of accommodated stress to relaxed one rises with the resulting increment in the elastic energy.
- The balance between the energy saved by the system as a result of the coalescence and the accumulated elastic energy at different length scales determinates the nature of the local interactions. Thus, the fact that such a balance is favorable to the coalescence at grain-size scale explains the tendency to bundle grains into structures; whereas the unfavorable balance at the size-scale of the structures accounts for the repulsion between them, and causing grooving.
- During grooving, sharp and deep external grain boundaries appears between multigrain structures. As deeper the external grain boundaries are, larger are the structures that they limit, because external grain boundaries have to rearrange all the grains bonded by shallow boundaries inside the multigrain structure. As a consequence, the normal stress vanishes as external grain boundaries are deeper. Therefore, for grains with contour points that are not at the same height, anisotropy in the normal stress appears.
- For coalescing grains supporting several degrees of normal stress anisotropy, we observe that a grain bundling phenomenon occurs together with unzipping and grooving of the external grain boundaries between structures, promoting the development of a dipolar-shaped stress field inside structures (with shallow-tensile an deep-compressive components).

- The increase of the local stress asymmetry strengthens the deep compressive component. This effect enhanced by the large differences between the adatom mobility at the surface, grain boundaries and film bulk, enables a fast relaxation of the tensile stress against the lower relaxation of the compressive one. Differences in the local curvature of the film affecting the incidence of the growth flux also improve compression in the film.
- A new model, termed *inside bundling-outside grooving* (recently renamed *twisted zipping*) account for the compressive nature of the macroscopic growth stress during the post-coalescence and the reversible behavior of the stress during high/low mobility conditions, allowing us to address the relationship between the stress behavior and the phenomena of grain bundling and grooving during growth the Volmer-Weber-type thin films.

Concerning coarsening by hierarchical processes like Ostwald ripening, we can conclude that:

- Ostwald ripening can occur not only by the Gibbs-Thompson effect, i.e., ruled by the grain size, but also by a phenomenon of slope selection in which grains with slopes near a selected slope value growth faster, favouring the propagation of such selected facet.
- Slope selection can maintain coarsening by Ostwald ripening even for large stages of growth, with the consequent development of large surface grains (~1μm in size) with well-defined shapes and facets. Therefore a *late slope-selection-driven Ostwald ripening* mechanism operating under atypical conditions (large grain sizes and low temperatures) is identified and their main characteristics, addressed by our model. In dependence of the morphological environment of grains, these mechanisms permit the self-organization of surface structures in thin film surfaces.

RESUMEN Y CONCLUSIONES GENERALES

A lo largo de este trabajo se ha investigado los mecanismos relevantes que controlan la evolución morfológica de la superficie de láminas delgadas policristalinas durante su preparación. En sistemas de lámina delgada, la elucidación de los mecanismos que controlan la evolución morfológica es uno de los primeros pasos a tener en cuenta en aquellos procesos de nanoestructuración e ingeniería de superficies que se basan en estrategias de nanoestructuración tipo "*bottom-up*" (es decir, las que tratan de organizar componentes más pequeños en ensambles más complejas), que tienen un alto impacto tecnológico ya que permite la modificación *quasi*-espontánea de la morfología superficial de las láminas de una manera que altere de manera controlada propiedades funcionales de interés.

En este trabajo, las láminas delgadas se prepararon mediante el uso de métodos físicos, entre ellos la evaporación térmica, la ablación láser pulsado y el recocido térmico. La morfología superficial de las láminas se caracterizó a diferentes escalas espaciales, mediante el uso de microscopías de proximidad (microscopía de fuerzas atómica y microscopía de efecto túnel, *mesoescala*), y microscopías de barrido electrónico (*microescala*). Mediante el uso de los procedimientos de procesado de imágenes y análisis estadísticos, se logró extraer información valiosa concerniente a las transformaciones morfológicas soportadas por las láminas durante su preparación, incluyendo como ejemplo la evolución de la variación de tamaños de grano, la rugosidad, los valores de pendiente y textura local (en el plano). Por otra parte, he utilizado difracción de rayos X con el fin de analizar la estructura cristalina de las láminas delgadas.

A fin de abordar las evidencias experimentales, es decir, la evolución tanto de la morfología superficial de las láminas, el escalado de los parámetros de forma, y los cambios en la estructura cristalina, se propusieron nuevos modelos mesoscópicos de crecimiento de grano. Estos modelos consideran: simulaciones tipo escalado dinámico basadas en ecuaciones tipo Langevin para describir la difusión superficial, sistemas de ecuaciones diferenciales parciales para describir la difusión a lo largo de defectos, y métodos de elementos finitos para describir fenómenos elásticos. De las evidencias experimentales y los modelos propuestos pude extraer las siguientes conclusiones generales:

- Durante los procesos de preparación de láminas delgadas policristalinas en condiciones fuera de equilibrio (es decir, temperaturas en el rango de 0.2-0.3 veces la temperatura de fusión y ritmos de crecimiento elevados en el rango de 1 nm/s), la morfología superficial de las láminas soporta transformaciones drásticas.

- Las transformaciones de la morfología superficial de las láminas se producen por mecanismos de "*coarsening*" (o agregación), incluyendo la coalescencia a pares entre granos y el crecimiento anormal o jerárquico, que son impulsados por procesos de minimización de energía y restricciones de tipo cinético.

En cuanto a la coalescencia entre granos, podemos concluir que:

- La coalescencia entre granos monocristalinos para formar estructuras multigrano de gran tamaño se produce mediante interacciones locales entre granos que involucran, de manera progresiva, mecanismos de relajación por corrientes superficiales y de acomodo mediante deformación elástica de las tensiones generadas durante el crecimiento; tanto en las direcciones normales (difusión hacia valles entre granos y "*zipping*" de la frontera entre granos) y las direcciones acimutales (rotación de grano y torsión). A medida que los granos superficiales aumentan de tamaño, la relación entre la tensión acomodada y la relajada aumenta, lo cual ocasiona el incremento de la energía elástica.
- El equilibrio entre la energía ahorrada por el sistema como resultado de la coalescencia y la energía elástica acumulada a diferentes escalas espaciales determina la naturaleza de las interacciones locales entre granos. Por lo tanto, el hecho de que dicho equilibrio sea favorable a la coalescencia a escalas de tamaño de grano explica la tendencia a la agrupación de granos, mientras que el equilibrio desfavorable en la escala de tamaño de las estructuras multigrano representa la repulsión entre ellos, causando la abertura de fronteras externas y la generación de discontinuidades (fracturas) en la lámina delgada.
- Durante el proceso de abertura aparecen fronteras externas profundas y agudas entre las estructuras multigrano. Cuanto más profundas sean dichas fronteras, mayor resulta ser el volumen de estructuras que limitan; ya que dichas fronteras externas han de reorganizar a todos los pequeños granos unidos por fronteras

internas poco profundas dentro de la estructura multigrano. Como consecuencia, a medida que las fronteras externas de las estructuras multigrano son más profundas, el esfuerzo normal causante de la atracción entre granos desaparece. Por lo tanto, para los granos con puntos de contorno que no están a la misma altura, aparece una anisotropía en la tensión normal.

- Para granos que coalescen soportando varios grados de anisotropía en la tensión normal, se observa que el fenómeno de agrupación entre granos pequeños para formar estructuras multigrano se produce junto con la abertura de las fronteras externas, promoviendo el desarrollo de un campo de tensiones dipolar en el interior de las estructuras (con componentes de tracción superficiales y de compresión en zonas profundas).
- El aumento de la asimetría en la tensión local entre granos refuerza el componente compresivo en zonas profundas. Este efecto, el cual es incrementado su vez por diferencias entre la movilidad de átomos tanto en la superficie, las fronteras de grano y el volumen de la lámina, permite una rápida relajación de la tensión de tracción en contra de la relajación inferior de la compresión. Las diferencias en la curvatura local de la lámina que afectan a la incidencia del flujo de crecimiento también incrementan la compresión en la lámina.
- Un nuevo modelo, denominado "*inside bundling-outside grooving*" (renombrado recientemente como "*twisted zipping*") da cuenta de la naturaleza compresiva del estrés de crecimiento en la etapa de post-coalescencia de las láminas, y también del comportamiento reversible de la tensión durante las condiciones de alta/baja movilidad, lo que nos permite explicar la relación entre el comportamiento del estrés y los fenómenos de agregación de grano durante el crecimiento de las películas delgadas policristalinas.

En cuanto al "*coarsening*" mediante procesos jerárquicos como "*Ostwald ripening*", se puede concluir que:

- El mecanismo de "*Ostwald ripening*" se puede producir no sólo por el efecto de Gibbs-Thompson, es decir, gobernado por el tamaño de grano, sino también por un fenómeno de selección de pendientes en el que los granos con pendientes cerca de una pendiente preferente o "seleccionada" crecen más rápido que aquellos que no la tienen, lo cual favorece la propagación de dicha faceta "seleccionada".

- El proceso de selección de pendiente puede mantener el "*coarsening*" por "*Ostwald ripening*" incluso para etapas tardías del crecimiento, con el consiguiente desarrollo de granos superficiales de gran tamaño (~1μm) con formas y facetas bien definidas. Un mecanismo denominado "*late slope selection driven Ostwald ripening*" operando en condiciones atípicas (grandes tamaños de grano y temperaturas bajas) ha sido identificado, siendo sus principales características descritas por nuestro modelo. En dependencia del entorno morfológico de cada grano este mecanismo puede permitir la auto-organización de las estructuras superficiales en láminas delgadas.

AGRADECIMIENTOS

Esta memoria es el resultado de un extenso trabajo llevado a cabo con la ayuda y compañía de muchas personas. Por tanto, me gustaría expresar mi más sincero agradecimiento a todos los que me han acompañado en esta etapa pre-doctoral.

En primer lugar quiero agradecer a mi director, Enrique Vasco, al que otrora lo fuera, José Luis Sacedón, y a mi tutor, Celia Polop. ¡Menudo tándem!. Y es que después de todo y con sus pros *vs* contras eso érais (ya no porque "Sace" se ha jubilado), un equipo. Y aquí mucho he de agradecer. En primer lugar, gracias por haberme brindado la oportunidad de venir a España para realizar este trabajo. En aquella hermosa y amada tierra llamada Venezuela jamás hubiera imaginado poder emprender un proyecto como este. En segundo lugar, he de agradecer la paciencia depositada en mí, destilada poco a poco para dirigir este trabajo y culminarlo con buenos resultados. Muchas experiencias aleccionadoras hemos pasado a lo largo de estos años. Entre laboratorios, ordenadores, discusiones y cafés, desde detalles técnicos hasta modelos complejos, he aprendido mucho gracias a vosotros, y no solo de Ciencia. Mis respetos y admiración para vosotros. Gracias por vuestro tiempo y por el esfuerzo invertido en mi formación como científico. En tercer lugar, y no menos importante, gracias por conseguir la financiación para mi permanencia en el instituto y para poder llevar a cabo este proyecto. Y aquí mención especial a José Luis, que invirtió dinero de algunos proyectos importantes para financiar mis primeros pasos. Sin vuestra ayuda y asistencia en la preparación de informes no me hubiera sido posible conseguir los contratos siguientes. En este sentido, gracias también a Isabel Montero por incluirme en sus proyectos de investigación, y por su disposición. ¡Ah! y no se me olvida, también gracias a María Alonso que en este asunto económico también ha aportado su grano de arena. Quedarían más cosas que agradecer, pero ya este trabajo es bastante extenso, de modo que en resumen, gracias totales.

También quiero dar las gracias al departamento de Nanoestructuras y Superficies. Mención especial para María Alonso y Ana Ruiz. Con vosotras he tenido el placer de colaborar científicamente y "distraerme" un poco de los granos redondos para aprender sobre granos en forma de pirámide. Además, vuestros consejos me han resultado siempre de utilidad. También gracias por vuestro tiempo dedicado para la preparación

de charlas en conferencias y artículos. Hemos conseguido conseguir una colaboración con otro laboratorio, y ojalá sea fructífera para el grupo de cara al futuro.

He de agradecer también a Enrique Rodríguez. Además de mi fiel escudera Jannett, fuiste el primer compañero que tuve al venir de mi querida Venezuela. Dedicaste tiempo a introducirme y adaptarme al grupo, a enseñarme los "trucos" del AFM y del SEM y me has brindado tu amistad a lo largo de estos años. Tus enseñanzas me han sido de utilidad, y algo de ellas está plasmado en este trabajo.

Gracias a José Antonio Aznárez y a José María Sánchez por vuestra ayuda en la preparación de las muestras metálicas de este trabajo. También agradezco al personal del taller del ICMM por su esmero en la preparación componentes de vacío.

Gracias a Gerardo y al Dr. Iván Oliva por su colaboración y entera disposición en la consecución de los objetivos de este trabajo. También gracias por la asistencia en el tratamiento y preparación de algunas de las muestras analizadas

A mis compañeros en el ICMM, entre los que están Enrique Navarro y Nacho. Mucho mejor el despacho animado por vuestra compañía… y ahora más aún con la nueva incorporación, ¡bienvenida, Paloma!.

A mis amigos de siempre, esos que a pesar de todo aún están y a aquellos que en algún momento estuvieron: David Bastida, María Alejandra y Kenny (y Joaquim), Alberto y Luisa, Carola, Vanessa, Otsmar, Jenny y Gabriela, Toño, Omar...

Por último y no por eso menos importante (sino más), a mis padres Norma y Antonio, a mi hermano Fernando, a mis abuelos (a ti también Francisco!), a Jannett y al que pronto ha de venir, Leonardo (que debe estar pasándosela de lo lindo en el vientre de mamá), mi familia. Gracias por soportarme!. Gracias por estar ahí para animarme siempre que lo he necesitado. Este trabajo os lo debo sin ninguna duda a todos vosotros especialmente.

Alejandro González González, Abril de 2013

Este trabajo ha sido financiado gracias a los proyectos F1-54173 (programa bilateral CSIC-Conacyt), los proyectos del Ministerio de Ciencia e Innovacion y del CICYT ESP2006-14282-C02-02, AYA2009-14736-C02-01; los proyectos intramurales especiales del CICYT PIE200960I182 y PIE201160E53, y el proyecto CCG10-UAM/MAT-5537 (DGUI Comunidad de Madrid y Universidad Autónoma de Madrid).

BIBLIOGRAPHY

[1] H. Ibach, *Physics of Surfaces and Interfaces* (Springer-Verlag Berlin Heidelberg, 2006).
[2] J. William D. Callister, *Introducción a la Ciencia e Ingeniería de los Materiales* (Editorial Reverté, S. A., 1995).
[3] H. Lüth, *Surfaces and Interfaces of Solid Materials* (Springer-Verlag, Berlin Heidelberg, Germany, 1998).
[4] A.-L. Barabási and H. E. Stanley, (Cambridge University Press, Cambridge, 1995).
[5] T. Michely and J. Krug, *Islands, Mounds and Atoms: Patterns and Processes in Crystal Growth Far From Equilibrium* (Springer-Verlag, Germany, 2004).
[6] J. V. Barth, Surface Science Reports 40, 75 (2000).
[7] F. Montalenti and R. Ferrando, Physical Review Letters 82, 1498 (1999).
[8] B. Voigtländer, Surface Science Reports 43, 127 (2001).
[9] H. Brune, Surface Science Reports 31, 125 (1998).
[10] V. A. Shchukin and D. Bimberg, Reviews of Modern Physics 71, 1125 (1999).
[11] J. Stangl, V. Holý, and G. Bauer, Reviews of Modern Physics 76, 725 (2004).
[12] M. Alexe, C. Harnagea, D. Hesse, et al., Applied Physics Letters 75, 1793 (1999).
[13] J. Xu, S. W. Hong, W. Gu, et al., Advanced Materials 23, 5755 (2011).
[14] A. Pimpinelli and J. Villain, *Physics of Crystal Growth* (Cambridge University Press, Cambridge, 1998).
[15] C. Ratsch and J. A. Venables, Journal of Vacuum Science & Technology A: Vacuum, Surfaces, and Films 21, S96 (2003).
[16] K. van Benthem, G. Tan, L. K. DeNoyer, et al., Physical Review Letters 93, 227201 (2004).
[17] M. Masuduzzaman, S. Xie, J. Chung, et al., Applied Physics Letters 101, 153511 (2012).
[18] L. B. Freund and S. Suresh, *Thin Film Materials: Stress, Defect Formation and Surface Evolution* (Cambridge University Press, Cambridge, 2003).
[19] R. Otero, J. M. Gallego, A. L. V. de Parga, et al., Advanced Materials 23, 5148 (2011).
[20] D. Alonso-Álvarez, J. M. Ripalda, B. Alén, et al., Advanced Materials 23, 5256 (2011).
[21] Y. Sun, Y.-Y. Song, H. Chang, et al., Applied Physics Letters 101, 152405 (2012).
[22] H. Jung and K.-H. Jeong, Applied Physics Letters 101, 203102 (2012).
[23] Y.-H. Ko, J.-H. Kim, L.-H. Jin, et al., Advanced Materials 23, 5364 (2011).
[24] M. Ren, B. Jia, J.-Y. Ou, et al., Advanced Materials 23, 5540 (2011).
[25] E. Vasco, J. Rubio-Zuazo, L. Vazquez, et al., Journal of Vacuum Science & Technology B: Microelectronics and Nanometer Structures 19, 224 (2001).
[26] J. Xiao, Y. Wu, X. Bai, et al., Journal of Physics D: Applied Physics 41, 135409 (2008).
[27] D. S. Wiersma, Nature Physics 4, 359 (2008).
[28] J. W. Evans, P. A. Thiel, and M. C. Bartelt, Surface Science Reports 61, 1 (2006).
[29] P. Jensen, Reviews of Modern Physics 71, 1695 (1999).

[30] R. Kassing, P. Petkov, W. Kulisch, et al., *Functional Properties of Nanostructured Materials* (Springer, The Netherlands, 2006).
[31] W. D. J. Callister and D. G. RethWisch, *Fundamentals of Materials Science and Engineering: An Integrated Approach* (John Wiley & Sons, United States of America, 2007).
[32] L. I. Maissel and R. Glag, *Handbook of Thin Film Technology* (McGrawn-Hill Book Company, United States of America, 1970).
[33] K. Reichelt and X. Jiang, Thin Solid Films 191, 91 (1990).
[34] B. Shin, in *Division of Engineering and Applied Sciences* (Harvard University, Cambridge (Massachusetts), 2007).
[35] S. Tolansky, *Multiple Beam Interferometry* (Clarendon, Oxford, 1948).
[36] R. García and R. Pérez, Surface Science Reports 47, 197 (2002).
[37] I. Horcas, R. Fernandez, J. M. Gomez-Rodriguez, et al., Review of Scientific Instruments 78, 013705 (2007).
[38] B. Cappella and G. Dietler, Surface Science Reports 34, 1 (1999).
[39] S. N. Magonov and M.-H. Whangbo, *Surface Analysis with STM and AFM: Experimental and Theoretical Aspects of Image Analysis* (Wiley-VCH, Germany, 1996).
[40] D. Sarid, *Exploring Scanning Probe Microscopy with MATHEMATICA* (Wiley-VCH, Germany, 2007).
[41] I. Ekvall, E. Wahlström, D. Claesson, et al., Measurement Science and Technology 10, 11 (1999).
[42] L. Martinez, M. Tello, M. Diaz, et al., Review of Scientific Instruments 82, 023710 (2011).
[43] J. I. Goldstein, D. E. Newbury, P. Echlin, et al., *Scanning Electron Microscopy and X-Ray Microanalysis: A Text for Biologists, Materials Scientists, and Geologists* (Plenum Press, New York, 1992).
[44] G. M. Alonzo-Medina, A. González-González, J. L. Sacedón, et al., Journal of Physics D: Applied Physics 45, 435301 (2012).
[45] Y. Matsukawa, K. Yasunaga, M. Komatsu, et al., Materials Science and Engineering: A
Symposium on High-Speed Plastic Deformation 350, 8 (2003).
46 M. Birkholz, *Thin film analysis by X-Ray Scattering* (Wiley-VCH, Great Britain, 2006).
[47] Wikipedia, (Braggs' Law).
[48] C. Teichert, Physics Reports 365, 335 (2002).
[49] M. A. Lutz, R. M. Feenstra, P. M. Mooney, et al., Surface Science 316, L1075 (1994).
[50] I. Levchenko and K. Ostrikov, Applied Physics Letters 95, 243102 (2009).
[51] M. Brehm, H. Lichtenberger, T. Fromherz, et al., Nanoscale Research Letters 6, 70 (2011).
[52] K. J. Caspersen, C. R. Stoldt, A. R. Layson, et al., Physical Review B 63, 085401 (2001).
[53] E. Palacios-Lidón, L. Guanter, J. Zúñiga-Pérez, et al., Small 3, 474 (2007).
[54] A. González-González, J. L. Sacedón, C. Polop, et al., Journal of Vacuum Science and Technology A 27, 1012 (2009).
[55] A. González-González, M. Alonso, E. Navarro, et al., Nanoscale Research Letters 5, 1882 (2010).
[56] A. González-González, C. Polop, and E. Vasco, Physical Review B 86, 045434 (2012).

[57] D. E. Sanders, D. M. Halstead, and A. E. DePristo, in *38th National Symposium of the American Vacuum Society* (AVS, Seattle, Washington (USA), 1992), Vol. 10, p. 1986.
[58] J. Yu and J. G. Amar, Physical Review Letters 89, 286103 (2002).
[59] M. R. a. S. G. M. a. S. J. L. a. M. M. a. P. H. n. a. K. Samwer, EPL (Europhysics Letters) 50, 61 (2000).
[60] F. Montalenti, M. R. SÃ¸rensen, and A. F. Voter, Physical Review Letters 87, 126101 (2001).
[61] F. Montalenti and A. F. Voter, Physical Review B 64, 081401 (2001).
[62] A. González-González, G. M. Alonzo-Medina, A. I. Oliva, et al., Physical Review B 84, 155450 (2011).
[63] J. S. Tello and A. F. Bower, Journal of the Mechanics and Physics of Solids 56, 2727 (2008).
[64] J. S. Tello, A. F. Bower, E. Chason, et al., Physical Review Letters 98, 216104 (2007).
[65] V. Borovikov and J. G. Amar, Physical Review B 72, 085460 (2005).
[66] J. Q. Broughton, F. F. Abraham, N. Bernstein, et al., Physical Review B 60, 2391 (1999).
[67] J. Fish, Journal of Nanoparticle Research 8, 577 (2006).
[68] W. K. Liu, E. G. Karpov, S. Zhang, et al., Computer Methods in Applied Mechanics and Engineering
Multiple Scale Methods for Nanoscale Mechanics and Materials 193, 1529 (2004).
[69] W. A. C. a. R. E. Miller, Modelling and Simulation in Materials Science and Engineering 11, R33 (2003).
[70] J. Mei, J. W. Davenport, and G. W. Fernando, Physical Review B 43, 4653 (1991).
[71] E. Rodríguez-Cañas, E. Vasco, J. A. Aznárez, et al., Surface Science 604, 974 (2010).
[72] J. G. Allpress and J. V. Sanders, Surface Science 7, 1 (1967).
[73] I. G. H. a. R. H. W. a. A. J. McEvoy, Journal of Physics D: Applied Physics 8, 1033 (1975).
[74] M. Higo, K. Fujita, M. Mitsushio, et al., Thin Solid Films 516, 17 (2007).
[75] H. Jaeger, P. D. Mercer, and R. G. Sherwood, Surface Science 6, 309 (1967).
[76] F. Ruffino, V. Torrisi, G. Marletta, et al., in *Applied Physics A: Materials Science & Processing* (Springer Berlin / Heidelberg, 2010), Vol. 100, p. 7.
[77] D. J. Semin, A. Lo, S. E. Roark, et al., The Journal of Chemical Physics 105, 5542 (1996).
[78] M. Levlin and A. Laakso, Applied Surface Science 171, 257 (2001).
[79] G. Polanski and H.-G. Rubahn, Journal of Vacuum Science & Technology A: Vacuum, Surfaces, and Films 14, 110 (1996).
[80] U. Höpfner, H. Hehl, and L. Brehmer, Applied Surface Science 152, 259 (1999).
[81] P. A. Campbell, L. J. Sinnamon, C. E. Thompson, et al., Surface Science 410, L768 (1998).
[82] N. Matsuki, T.-W. Kim, J. Ohta, et al., Solid State Communications 136, 338 (2005).
[83] C. Polop, C. Rosiepen, S. Bleikamp, et al., New Journal of Physics 9, 74 (2007).
[84] C. Munuera, J. A. Aznarez, E. Rodriguez-Canas, et al., Journal of Vacuum Science & Technology A: Vacuum, Surfaces, and Films 22, 1767 (2004).
[85] B. Lüssem, S. Karthäuser, H. Haselier, et al., Applied Surface Science 249, 197 (2005).

[86] A. Rastelli and H. von Känel, Surface Science 515, L493 (2002).
[87] B. Sanduijav, D. Matei, G. Chen, et al., Physical Review B 80, 125329 (2009).
[88] H. Poppa, K. Heinemann, and A. G. Elliot, Journal of Vacuum Science and Technology 8, 471 (1971).
[89] S. Ruan and C. A. Schuh, Journal of Applied Physics 107, 073512 (2010).
[90] M. Zinke-Allmang, L. C. Feldman, and M. H. Grabow, Surface Science Reports 16, 377 (1992).
[91] M. J. Rost, D. A. Quist, and J. W. M. Frenken, Physical Review Letters 91, 026101 (2003).
[92] J. A. Thornton, Journal of Vacuum Science and Technology 11, 666 (1974).
[93] Z. Zhong, W. Schwinger, F. Schäffler, et al., Physical Review Letters 98, 176102 (2007).
[94] C. V. Thompson and R. Carel, Materials Science and Engineering: B Containing papers presented at the Indo-US Workshop on Nucleation and Growth in Solids 32, 211 (1995).
[95] K. E. Harris, V. V. Singh, and A. H. King, Acta Materialia 46, 2623 (1998).
[96] M. Upmanyu, D. J. Srolovitz, A. E. Lobkovsky, et al., Acta Materialia 54, 1707 (2006).
[97] Y.-N. Wen and J.-M. Zhang, Solid State Communications 144, 163 (2007).
[98] R. Abermann and R. Koch, Thin Solid Films 129, 71 (1985).
[99] J. Leib, R. Mänig, and C. V. Thompson, Physical Review Letters 102, 256101 (2009).
[100] J. A. Floro, S. J. Hearne, J. A. Hunter, et al., Journal of Applied Physics 89, 4886 (2001).
[101] R. C. Cammarata, T. M. Trimble, and D. J. Srolovitz, Journal of Materials Research 15, 2468 (2000).
[102] W. D. Nix and B. M. Clemens, Journal of Materials Research 14, 3467 (1999).
[103] R. Koch, D. Hu, and A. K. Das, Physical Review Letters 94, 146101 (2005).
[104] J. Leib and C. V. Thompson, Physical Review B 82, 121402 (2010).
[105] R. Koch, Journal of Physics: Condensed Matter 6, 9519 (1994).
[106] E. Chason, B. W. Sheldon, L. B. Freund, et al., Physical Review Letters 88, 156103 (2002).
[107] C. Friesen and C. V. Thompson, Physical Review Letters 89, 126103 (2002).
108] V. Randle, Philosophical Magazine A 67, 1301 (1993).
[109] T. Yamasaki, Y. Demizu, and Y. Ogino, Materials Science Forum 204-206, 461 (1996).
[110] P. Liu, S. C. Mao, L. H. Wang, et al., Scripta Materialia 64, 343 (2011).
[111] D. Moldovan, D. Wolf, and S. R. Phillpot, Acta Materialia 49, 3521 (2001).
[112] D. Moldovan, D. Wolf, S. R. Phillpot, et al., Acta Materialia 50, 3397 (2002).
[113] G. Timoshenko, *Mechanics of Materials* (PWS Publications, Boston, 1997).
[114] C. L. Liu, J. M. Cohen, J. B. Adams, et al., Surface Science 253, 334 (1991).
[115] D. Gupta, Physical Review B 7, 586 (1973).
[116] D. Gupta, Journal of Applied Physics 44, 4455 (1973).
[117] C. C. Wong, H. I. Smith, and C. V. Thompson, Applied Physics Letters 48, 335 (1986).
[118] Y. Cao, S. Allameh, D. Nankivil, et al., Materials Science and Engineering: A 427, 232 (2006).
[119] J. D. Kiely and J. E. Houston, Physical Review B 57, 12588 (1998).
[120] D. B. Chrisey and G. K. Hubler, *Pulsed Laser Deposition of Thin Films* (John Wiley & Sons, Inc., New York, 1994).

[121] G. Prévot, Physical Review B 84, 045434 (2011).
[122] V. M. Kaganer, W. Braun, and K. K. Sabelfeld, Physical Review B 76, 075415 (2007).
[123] J. G. McLean, B. Krishnamachari, D. R. Peale, et al., Physical Review B 55, 1811 (1997).
[124] S. Kodambaka, V. Petrova, S. V. Khare, et al., Physical Review Letters 89, 176102 (2002).
[125] G. Rosenfeld, K. Morgenstern, M. Esser, et al., in *Applied Physics A: Materials Science & Processing* (Springer Berlin / Heidelberg, 1999), Vol. 69, p. 489.
[126] E. Vasco, C. Polop, and J. L. SacedÃ³n, Physical Review E 80, 041604 (2009).
[127] S. Aggarwal, A. P. Monga, S. R. Perusse, et al., Science 287, 2235 (2000).
[128] C. R. Stoldt, A. M. Cadilhe, C. J. Jenks, et al., Physical Review Letters 81, 2950 (1998).
[129] E. Vasco, C. Zaldo, and L. Vázquez, Journal of Physics: Condensed Matter 13, L663 (2001).
[130] Q. J. Wang, C. Pflugl, W. F. Andress, et al., Journal of Vacuum Science & Technology B: Microelectronics and Nanometer Structures 26, 1848 (2008).
[131] S.-C. Han, J.-K. Kim, J. Y. Kim, et al., Journal of Electrochemical Society 157, D60 (2010).
[132] M. D. Johnson, C. Orme, A. W. Hunt, et al., Physical Review Letters 72, 116 (1994).
[133] B. Chakrabarti and C. Dasgupta, Physical Review E 69, 011601 (2004).
[134] W. Kanjanaput, S. Limkumnerd, and P. Chatraphorn, Physical Review E 82, 041607 (2010).
[135] W. L. Chan and E. Chason, Journal of Applied Physics 101, 121301 (2007).
[136] R. Cuerno and A.-L. s. Barabási, Physical Review Letters 74, 4746 (1995).
[137] S. F. Edwards and D. R. Wilkinson, Proceedings of the Royal Society of London. A. Mathematical and Physical Sciences 381, 17 (1982).
[138] B. J. Wuensch and H. L. Tuller, Journal of Physics and Chemistry of Solids 55, 975 (1994).
[139] P. Lakshmi and K. Ramachandran, in *Bulletin of Materials Science* (Springer India, in co-publication with Indian Academy of Sciences, 2011), Vol. 34, p. 371.
[140] S. T. Tan, X. W. Sun, X. H. Zhang, et al., Journal of Applied Physics 100, 033502 (2006).
[141] A. Janotti and C. G. Van de Walle, Physical Review B 76, 165202 (2007).
[142] D. M. Bagnall, Y. F. Chen, Z. Zhu, et al., Applied Physics Letters 70, 2230 (1997).
[143] Z. K. Tang, G. K. L. Wong, P. Yu, et al., Applied Physics Letters 72, 3270 (1998).